Polarimetric Models of Circumstellar Discs Including Aggregate Dust Grains

By

Mahesh Mohan

Submitted to the University of Hertfordshire in partial fulfilment of the requirements of the degree of

Doctor of Philosophy

November 2015

Typeset in LaTeX 2$_\varepsilon$.

Except where acknowledged in the customary manner, the material presented in this thesis is, to the best of my knowledge, original and has not been submitted in whole or part for a degree in any university.

Mahesh Mohan

Acknowledgements

Firstly, I would like to thank my supervisor, Tim Gledhill, for putting up with me and my nonsense for four years. You were very patient and supportive when I needed help and kept me motivated to continue working. You also gave me the opportunity to travel the world to various conferences and meet new people. I could not have completed this thesis without you.

My sincerest thanks also go to Dr. Tom Robitaille for his continued support with Hyperion and Prof. Bruce Draine for his very helpful discussion on DDSCAT. I would also like to thank Dr. Phil Lucas and Dr. Evelyn Hesse for their continued support with very helpful discussion and proof reading.

I would also like to thank my parents, Krishna and Mohinder, for giving me the opportunity to do this PhD. You have always been supportive of my decisions throughout my time in academia and have given me the freedom to make my own path in life. For this I am grateful.

Finally, I would like to give a shout out to my friends. To the guys of Saint Audrey's (Herald and Romy), thank you for making my stay in Hatfield so entertaining and welcoming, I'll never forget that fateful 'Simon Cowell' day. To the guys of E119 (Alex, Phil and Sam), thank you for making my time at the University of Hertfordshire so memorable, I don't think I'll ever get office mates as good as you guys again. A special thanks to Phil for being Phil and so helpful over the years. To the guys of 2E68 (Billy and Charlie), thank you for the random conversations, they kept me sane during the write up. And most importantly, a massive thank you to Alessandro, Conor, Jose

and Sunil. You guys were always there for me and not just during my PhD, for the last 10 years you guys have kept me company and happy. Whether it be during our late night Skype sessions, whatsapp/facebook messages or our random meet ups, you guys have never failed to put a smile on my face, so thank you.

Abstract

The work conducted in this thesis examines the nature of circumstellar discs by investigating irradiance and polarization of scattered light. Two circumstellar discs are investigated.

Firstly, H-band high contrast imaging data on the transitional disc of the Herbig Ae/Be star HD169142 are presented. The images were obtained through the polarimetric differential imaging (PDI) technique on the Very Large Telescope (VLT) using the adaptive optics system NACO. Our observations use longer exposure times, allowing us to examine the edges of the disc. Analysis of the observations shows distinct signs of polarization due to circumstellar material, but due to excessive saturation and adaptive optics errors further information on the disc could not be inferred.

The HD169142 disc is then modelled using the 3D radiative transfer code Hyperion. Initial models were constructed using a two disc structure, however recent PDI has shown the existence of an annular gap. In addition to this, the annular gap is found not to be devoid of dust. This then led to the construction of a four-component disc structure. Estimates of the mass of dust in the gap (2.10×10^{-6} $M_{\odot}$) are made as well as for the planet ($\approx 1.53 \times 10^{-5}$ $M_{\odot}$ ($0.016 M_{Jupiter}$)) suspected to be responsible for causing the gap. The predicted polarization was also estimated for the disc, peaking at ≈ 14 percent.

The use of realistic dust grains (ballistic aggregate particles) in Monte Carlo code is also examined. The fortran code DDSCAT is used to calculate the scattering properties for aggregates which are used to replace the spherical grain models used by the radiative

transfer code Hyperion. Currently, Hyperion uses four independent elements to define the scattering matrix, therefore the use of rotational averaging and a 50/50 percent population of grains and their enantiomers were explored to reduce the number of contributing scattering elements from DDSCAT. A python script was created to extract the scattering data from the DDSCAT output files and to apply a size distribution to the data.

The second circumstellar disc investigated is the debris disc of the M dwarf star AU Mic. The disc was modelled, using the radiative transfer code Hyperion, based on F606W (HST) and JHK'-band (Keck II) scattered light observations and F606W-band polarized light observations. Initially, the disc is modelled as a two component structure using two grain types: compact silicate grains and porous dirty ice water. Both models are able to reproduce the observed SED and the F606W and H-band surface brightness profiles, but are unable to fit the observed F606W degree of polarization. Therefore, a more complex/realistic grain model was examined (ballistic aggregate particles). In addition, recent millimetre observations suggest the existence of a planetesimal belt < 3 AU from the central star. This belt is included in the BAM2 model and was successful in fitting the observed SED, F606W and H-band surface brightness and F606W polarization. These results demonstrate the limitations of spherical grain models and indicate the importance of modelling more realistic dust grains.

Contents

Acknowledgements **v**

Abstract **vii**

List of Figures **xiii**

List of Tables **xxiii**

1 Introduction **1**

1.1 Circumstellar Discs 1

1.1.1 Protoplanetary Discs 4

1.1.2 Transitional Discs 9

1.1.3 Debris Discs 10

1.1.4 Composition of Dust Grains in Circumstellar Discs 15

1.2 Scattering of Light by Small Particles 16

1.2.1 Amplitude Scattering Matrix 16

1.2.2 Stokes Parameters 16

1.3 Optical Characteristics of Dust Grains 19

1.3.1 Size Parameter 19

1.3.2 Phase Function 20

1.3.3 Asymmetry Parameter 20

1.3.4 Cross section and Efficiency Factor 20

1.3.5 Albedo 21
1.3.6 Optical Depth 21
1.4 Spherical vs Non-Spherical Particles 22
1.4.1 Spherical Grains - Mie Theory 22
1.4.2 Non-Spherical/Irregular Grains 23
1.4.3 Approximating/Modelling Non-Compact Particles 25
1.5 Aims of the Thesis 27
1.6 Structure of the Thesis 27

2 Polarimetric Differential Imaging of HD169142 29
2.1 Introduction 29
2.2 Observations and Data Reduction 33
2.3 Very Large Telescope 33
2.3.1 Adaptive Optics 35
2.3.2 NACO 35
2.3.3 Observations 36
2.3.4 Data Reduction 37
2.3.5 Cross Correlation 39
2.3.6 Calculating the Stokes Parameters 40
2.3.7 PSF Subtraction 42
2.4 Instrumental Polarization 43
2.5 Results and Analysis 48
2.5.1 Stokes Parameters 48
2.5.2 Polarized Intensity 49
2.5.3 Polarization 49
2.5.4 Surface Brightness Profiles 52
2.5.5 Radial Stokes Parameter Images 54
2.6 Discussion 55

3 Hyperion 61
3.1 Hyperion - v.0.9.4 62

3.1.1 Dust Modelling 62
3.1.2 Disc Structure 66
3.1.3 Optimization 68
3.1.4 Computing SED and Scattered Light Images 73
3.2 Testing Hyperion 75
3.2.1 Speed Test 75
3.2.2 Scattered Light Image 75

4 Modelling HD 169142 **79**
4.1 Two Disc Model 80
4.1.1 SED 80
4.2 Three Disc Model 91
4.2.1 SED 92
4.2.2 Surface Brightness 96
4.2.3 Polarization 98
4.3 Site For Planet Formation 100
4.4 Final Disc Model 103

5 DDSCAT **109**
5.1 Validity of DDSCAT 109
5.2 Testing DDSCAT 111
5.3 Speed Test 114
5.4 Aggregate Type 115
5.5 Rotational Averaging 117
5.6 DDSCAT Wrapper 118
5.7 Testing Hyperion with DDSCAT 122

6 AU Mic **127**
6.1 Previous AU Mic Modelling 134
6.1.1 Stellar Model 134
6.1.2 Liu et al. 2004 135

6.1.3 Metchev et al. 2005 . . . 136
6.1.4 Krist et al. 2005 . . . 137
6.1.5 Graham et al. 2007 . . . 139
6.1.6 Fitzgerald et al. 2007 . . . 142
6.1.7 Discussion . . . 145
6.2 Modelling AU Mic with Hyperion . . . 145
6.2.1 SED . . . 147
6.2.2 Surface Brightness and Polarization . . . 150
6.3 Discussion . . . 155
6.4 Modelling AU Mic with DDSCAT + Hyperion . . . 156
6.4.1 DDSCAT/HDF5 Dust Model . . . 158
6.5 Final Disc Model . . . 159
6.5.1 Inner Planetesimal Belt . . . 159
6.5.2 JHK' Polarization Predictions . . . 161
6.6 Discussion . . . 165

7 Conclusion & Future Work 167
7.1 PDI Observations of HD169142 . . . 168
7.2 Modelling of HD169142 . . . 169
7.3 Integrating DDSCAT and Hyperion . . . 170
7.4 Future Work . . . 172

A Appendix 175
A.1 Mass calculations for HD169142 four component disc . . . 175
A.2 DDSCAT Extraction Script . . . 177

References 187

List of Figures

1.1 SED of β Pictoris (Vandenbussche et al., 2010). The image shows PACS (70-160 μm) and SPIRE (250-500 μm) (Vandenbussche et al., 2010), IRAS (IRAS source catalogue), SCUBA 850 μm (Holland et al., 1998) and SIMBA 1200 μm (Liseau et al., 2003) data. 2

1.2 YSO calssification for a low-mass YSO (i.e. T Tauri) (Armitage, 2010). 7

1.3 ALMA millimeter imaging (combination of the 1.3 mm and 0.87 mm data) of HL Tauri (Brogan et al., 2015). The disc is estimated to have a semimajor axis of 70 ± 15 AU at a distance of 140 pc (Mundy et al., 1996; Kwon, Looney & Mundy, 2011). 8

1.4 Top: Shows model protoplanetary discs for six epochs (Dullemond & Dominik, 2005). Bottom: SED plot for GM Aur (Najita et al., 2007). The black solid line shows the observational IRS spectra (Furlan et al., 2006) IR and the black diamonds show optical and IRAS photometry (Kenyon & Hartmann, 1995), 2MASS near-IR (Cutri et al., 2003) and IRAC photometry (Hartmann et al., 2005). The blue solid line represents a Kurucz stellar model. The hashed regions represent the uper and lower quartiles of the Taurus classical T Tauri star (CTTS) median SED (D'Alessio et al., 1999). 10

1.5 Image in polarized light of the transitional disc HD 142527 (Canovas et al., 2013). The image has had a Sobel filter applied to it to enhance disc edges. The arrows indicate the spiral features of the disc. 11

1.6 Infrared imaging of HR 4796A taken on the spectro-Polarimetric High-contrast Exoplanet REserach (SPHERE) instrument on the Very Large Telescope (VLT). The disc has a mean angular radius of 70 AU (Telesco et al., 2000). 12

1.7 HST optical imaging of AU Mic (Top at 0.606 μm (Krist et al., 2005)) and β Pictoris (Bottom at 0.57 μm (Apai et al., 2015)). 14

1.8 Left: Fomalhaut HST optical (0.6 μm) Kalas et al. (2008) (left/blue side of the image) and ALMA (350 GHz) (Boley et al., 2012) (right/orange side of the image) composite image. Right: Shows the entire HST optical imaging of Fomalhaut Kalas et al. (2008) with a zoomed view of Fomalhaut b between 2004 and 2006. The disc extends to approximately 20" in the North and 11" in the West. The semimajor axis of the belt is traced out 133-158 AU (inner and outer boundary of the belt respectively). 15

1.9 Visual representation of the Stokes parameters. 18

1.10 Left: Scanning electron microscope (SEM) imaging of a porous interplanetary dust particle (Brownlee, Tomandl & Olszewski, 1977). The bar is equivalent to 1 μm . Right: SEM imaging of Calcium Aluminum Inclusion (CAI) like porous particles (Brownlee, Joswiak & Matrajt, 2012). 24

2.1 Top: ISO observations showing IR Spectra from 4 Herbig Group Ib objects: HD 100453, HD 135344, HD 139614 and HD 169142 (Meeus et al., 2001). This plot shows that these objects do not produce the 10 μm silicate feature. Bottom: Shows the best fit model spectra over the 11 μm range for HD 169142 van Boekel et al. (2005). Once again there is no evidence for silicate band emission, but there is a clear 11.2 μm PAH emission feature. 32

2.2 Left: UKIRT H-band polarimetry (Kuhn, Potter & Parise, 2001). The image shows the polarization vectors where the length of the vectors are proportional to the polarization fraction. The image is scaled as 0".0814 pixel^{-1}, therefore giving a spatial scale of $\approx$ 5".2. Right: UKIRT J-band polarimetry (Hales et al., 2006). A centrosymmetric pattern is marginally resolved around the disc. 33

2.3 Left: H-band VLT imaging of HD169142 in polarized light (Quanz et al., 2013). Image shows the final $Q_{\rm r}$ scaled with r^2. Right: Image showing 7 mm VLA (Osorio et al., 2014) contours over H-band VLT (Quanz et al., 2013). 34

2.4 Image of the VLT. 34

2.5 Illustration the optical elements of the NACO System (Witzel et al., 2011). 36

2.6 Illustration the a typical mask used in a dual beam imaging polarimeter. Top: shows the mask with equally spaced parallel bars. Bottom: shows the results of the Wollaston prism dividing the incoming light into ordinary (O) and extraordinary (E) ray images[2]. 37

2.7 Image showing the cross correlation shift and add process. 40

2.8 Image showing the result of the cross correlation process. The maximum value of the image determines the centre of the image. The image has been expanded by a factor 20 to increase the accuracy of the cross correlation process which results in a 6720 x 1880 image. 41

2.9 Final Stokes I images for HD 169142 (top) and HD 161743 (bottom) in the H (left) and $K_{\rm s}$ (right) band. The central region of the images have been masked out due to saturation of the pixels. The colour bar represents the pixel count. 44

2.10 Final Stokes Q (left) and U (right) images for HD 161743 in the H (top row) and $K_{\rm s}$ (bottom row). The central regions of the images have been masked out due to saturation of the pixels. The colour bar represents the pixel count. 46

2.11 Polarized intensity image of the reference star, HD 161743, in the H (top) and K_s-band (bottom) with percent polarization vectors plotted on top. The length of the vectors are proportional to the degree of polarization. 47

2.12 Final Stokes Q (left) and U (right) images for HD 169142 in the H (top row) and K_s (bottom row). The central regions of the images have been masked out due to saturation of the pixels. The colour bar represents the pixel count. 50

2.13 Azimuthal variation of the Q and U Stokes parameters for the H-band (top) and K_s-band (bottom). This shows modulation of Q and U with azimuthal angle which is expected for tangential polarization vectors (Apai et al., 2004) 51

2.14 Polarized intensity images in the H (top) and K_s (bottom) bands. The polarization angles (P_ϕ) are shown by the vectors. Artefacts from the adaptive optics systems and spider are also present in the PI image. . . 52

2.15 Azimuthally averaged percent polarization for the H (left) and K_s (right) bands 53

2.16 Radially averaged SBP of HD 169142 in polarized light for the H (top) and K_s (bottom) bands. 59

3.1 Left: Disc density structure for a flared disc created in Hyperion. The dust grain parameters can be seen in Table 3.1. Right: The disc density structure made by Pascucci et al. (2004). The contours shown provide 0.10, 0.19, 0.28, 0.38 and 0.48 percent of the maximum. 68

3.2 Scattering within a constant density sphere. Both models contain the same density of grains, but the bottom image has forced first scattering enabled while the top image has it disabled. 70

3.3 Temperature map for a flared disc model. Left: shows PDA disabled. Right: shows PDA enabled. 71

3.4 Speedup time for N cores compared serial execution for a flared disc model. The error bars on the plot represent the average values of the 10 executions the speedup time would reside in. 76

3.5 Scattered light (top) and percent polarization (bottom) images using the disc/dust parameter from Table 3.1. An initial photon count of 5×10^6 was used. 77

4.1 Kurucz model fits to the SED of HD 169142. Data includes IUE LWP and SWP and BVRI data from van der Veen, Habing & Geballe (1989) 81

4.2 A simple illustration of a disc model consisting of a wafer thin inner disc and a flared outer disc as used by Grady et al. (2007). 82

4.3 A synthetic SED comparing the single disc and two disc flared model from Table 4.2. 83

4.4 The top image shows how the position of the inner radius of the inner disc affects the SED. The bottom image shows how the inner raidus of the annular gap affects the SED. 84

4.5 Model SED fits to the observational data (red). The data includes spectra from ISO, 2Mass and IRAS. 88

4.6 Temperature map and density structure of a two disc model 90

4.7 Two disc model: current best fit SED model, created in Hyperion, to the observed data. 91

4.8 Top: Final Q_{r} image from Quanz et al. (2013). The image is scaled with r^2 to compensate for the decrease in stellar flux. The cross indicates the position of the star and the central pixels have been masked out due to saturation. Bottom: A simple illustration of the three disc mode (Osorio et al., 2014). 92

4.9 SED plots for the dust model combinations described in Table 4.6. . . . 94

4.10 Parameter tests for β and p. The left image shows how β affects the SED. The right image shows how p affects the SED. 95

4.11 Current SED modelled from the parameter tests conducted.The parameters summarized in Table 4.7. 96

4.12 Parameter tests for the flaring parameter (β) and surface density power law exponent (p). Plot shows how varying p for a fixed β changes the surface brightness power law exponent for the scattered light image at 1.1 μm 97

4.13 Top: Synthetic surface brightness image at 1.1 μm (left) and 1.65 μm (right). Bottom: azimuthally averaged surface brightness image of the outer disc (disc 3). Left: shows the power law exponent for the 1.1 μm image between $65 - 230$ AU. Right: shows the power law exponent for the 1.65 μm image between the range $120 - 200$ AU (red) and $120 - 174$ AU (green). 98

4.14 Parameter tests for the flaring parameter (β) and surface density power law exponent (p). Plot shows how varying p for a fixed β changes the surface brightness power law exponent in polarized light at 1.65 μm . . 99

4.15 H-band modelling of the HD 169142 disc. Top left: Polarized intensity image, Top right: linear polarization image, Bottom left: radially averaged polarized intensity image and Bottom right: radially averaged linear polarization image. 101

4.16 Left:Zoomed in view from $40-70$ AU for varying values of the dust mass in the contained in the annular gap. Right: best fit dust mass for the annular gap comparing the model SB profile (black X) to the observed SB profile (red +). 102

4.17 Final SED image for the 4 disc model for HD 169142. 104

4.18 Final surface brightness and polarized intensity images for the 4 disc model for HD 169142 at 1.65 μm 105

5.1 Polarization fraction vs scattering angle. The values for polarization are the modulus values of $|Q/I|$. The coloured lines represent DDSCAT where, blue = 4945, purple = 10395, green = 33552, red = 523984 dipoles. The black line is Mie calculations for $x = 3$ (top), 5 (middle), 7 (bottom) respectively. The refractive index is taken to be $m = 1.33 - 0.01i$ (dirty water-ice grains). 112

5.2 Polarization fraction vs scattering angle. The values for polarization are the modulus values of $|Q/I|$. The coloured lines represent DDSCAT where, blue = 4945, purple = 10395, green = 33552, red = 523984 dipoles. The black line is Mie calculations for $x = 3$ (top), 5 (middle), 7 (bottom) respectively. The refractive index is taken to be $m = 0.96 + 1.01i$. 113

5.3 Speed up time for C processors compared serial execution for an aggregate spherical dust grain consisting of 107218 dipoles. 115

5.4 Aggregate cluster models where $N = 256$. Axes $\mathbf{a}_1$, $\mathbf{a}_2$ and $\mathbf{a}_3$ denote the principal axes with the largest, intermediate and smallest moment of inertia (Shen, Draine & Johnson, 2008). 117

5.5 Degree of Polarization vs scattering angle for the three ballistic aggregate models. These models were run for the 256 cluster models ($a_{eff} = 1.095$ μm) where the dust grains are modelled as pure silicates at a wavelength of 1.4 μm 118

5.6 Figure showing the target orientation in the Lab Frame (Draine & Flatau, 2013). 119

5.7 Difference, in percentage, between the scattering matrix elements for a pure silicon dust grain model. 120

5.8 Degree of polarization for a population of BAM2 silicate grains (left) and a population of BAM2 silicates and their enantiomers, for different size parameter $x = 0.6$ (top) and $x = 4$ (bottom). 121

5.9 Difference, in percentage, between the scattering matrix elements for a pure silicon dust grain model comprised of 50% silicon and 50% silicon enantiomers. 122

5.10 Scattered light (top) and percent polarization (bottom) images using the disc/dust parameter from Table 5.10. An initial photon count of 5×10^6 was used. 125

6.1 Images showing radial (top) and vertical (bottom) substructure within the AU Mic disc (Liu, 2004). Top: the data has been smoothed with a Gaussian kernel and each pixel has been multiplied by its distance to the star to highlight the substructure. Bottom: the plot has been expanded vertically by a factor of 5 and has been smoothed with a Gaussian kernel. 129

6.2 Image slice $12.''0 \times 4.''0$ showing radial substructure within the AU Mic disc (Metchev et al., 2005). The bar is 10".0 (100 AU) in length with each tick representing 10 AU. The labelling convention is the same as the one used by Liu (2004). 130

6.3 Image showing radial substructure within the AU Mic disc (Krist et al., 2005). 131

6.4 Stokes I image of the AU Mic disc in the F606W band. The orientation of the vectors plotted indicate the direction of the electric field and the size of the vectors are proportional to the degree of polarization (Graham, Kalas & Matthews, 2007). 131

6.5 Image showing the radial substructure in the AU Mic disc in the F606W, J, H and K' bands (F07). 132

6.6 1.3 mm ALMA image of the AU Mic disc (MacGregor et al., 2013). The ellipse in the bottom left corner represents the beam size (8×7 AU). . 133

6.7 AU Mic SED fits for (Liu et al., 2004). 135

6.8 SED and surface brightness fits for Metchev et al. (2005). The surface brightness image has H and R-band (Kalas, Liu & Matthews, 2004) data plotted. 137

6.9 Surface brightness plot of the SE side of the AU Mic disc in comparison to the disc model produced by Krist et al. (2005). 138

6.10 Model fits to the surface brightness and polarization data. The plot shows three models fitted to the data, Porous ice, HG and zodiacal dust (GKM07). 140

6.11 An illustration of the disc model used by F07. The illustration shows the compact and porous grain disc models. The disc models are split into an inner disc consisting of millimetre size grains and the outer disc consisting of micron size grains. 142

6.12 Surface brightness profiles for AU Mic in the F606W, H-band (left) and J and K' band (right) (Fitzgerald et al., 2007). 144

6.13 SED parameter tests conducted for the minimum radius of the disc R_{min} (top left), flaring parameter β (top right), surface density exponent for the inner disc p_{inner} (bottom left) and outer disc p_{outer} (bottom right). . 148

6.14 Best fit synthetic SED models created in Hyperion for the compact grains (top) and porous grains (bottom). 149

6.15 Surface brightness parameter tests conducted for the flaring parameter β (left), surface density exponent for the inner disc p_{inner} (right) and outer disc p_{outer} (bottom) in the H-band. 151

6.16 Plots showing the surface brightness in the JHK' (Fitzgerald et al., 2007) and F606W (Graham, Kalas & Matthews, 2007) band for the compact grain model. 152

6.17 Plots showing the surface brightness in the JHK' (Fitzgerald et al., 2007) and F606W (Graham, Kalas & Matthews, 2007) band for the porous grain model. 153

6.18 Plots showing the percent polarization in the F606W (Graham, Kalas & Matthews, 2007) band for the compact (top) and porous (bottom) grain model. 154

6.19 Plots showing the normalized phase function (left) and the degree of polarization against scattering angle for the compact, porous, T-matrix aggregate (GKM07) and HG function. 155

6.20 Phase function vs scattering angle (top) and Polarization vs scattering angle (bottom). The grains are modelled as 50%-silicate/50%-graphite and the wavelength of the incoming light is 0.5012 μm. 157
6.21 Plots showing the normalized phase function (left) and the degree of polarization against scattering angle for non-spherical grains (BAM2) modelled using DDSCAT. 158
6.22 Illustration of the AU Mic disc model with the additional inner belt. . . 160
6.23 Plots showing the SED, surface bright (top) and percent polarization (bottom) for the BAM2 grains. Observational F606W data is taken from (Graham, Kalas & Matthews, 2007). 162
6.24 Plots showing the surface brightness in the JHK' (Fitzgerald et al., 2007) and F606W (Graham, Kalas & Matthews, 2007) band for the BAM2 DDSCAT grain model. 163
6.25 Plots showing the predicted percent polarization in the JHK'-band (Fitzgerald et al., 2007) for the BAM2 DDSCAT grain model. 164

List of Tables

1.1 Summary of the YSO classes 6

2.1 Parameters of HD169142 30

2.2 Summary of observations of the target HD169142 and standard star HD 161743 38

2.3 Summary of Instrumental Polarization values from HD161743 48

2.4 Summary of the FWHM 55

2.5 Summary of the Power Law fits 56

3.1 Input parameters for the Pascucci et al. (2004) benchmark test 67

3.2 Input parameters for the forced first scattering test 69

3.3 Input parameters for the scattered light test images 78

4.1 Summary of the parameters used for previous modelling of HD 169142 81

4.2 Single disc (Hyperion) and best fit two disc model from Meeus et al. (2010) 83

4.3 Summary of the dust grain models used 87

4.4 Summary of the combination of dust grain models used in the disc . . . 88

4.5 Model to be used in the parameter tests for the three disc model 93

4.6 Summary of the dust combinations used in the 3-disc model 94

4.7 Final parameters used for the 3 disc model 95

4.8 Final parameters used for the 4 component disc model including the annular gap 103
4.9 Summary of the power law exponent fits from the 3 disc and 4 disc models 106

5.1 Input parameters for the scattered light test images 123

6.1 Summary of stellar NextGen models (Hauschildt, Allard & Baron, 1999) used for AU Mic 134
6.2 Summary of the disc model used by Metchev et al. (2005) 136
6.3 Summary of the disc models used by Krist et al. (2005) 139
6.4 Summary of the dust grain models used by GKM07 141
6.5 Summary of the disc models used by Fitzgerald et al. (2007) 143
6.6 Best fit disc models from Fitzgerald et al. (2007) 146
6.7 Summary of the dust grain models used 147
6.8 Summary of the dust grain models for the best fit DDSCAT dust model 159
6.9 Best fit disc model from Hyperion for the DDSSCAT BAM2 grains . . 160

1

Introduction

1.1 Circumstellar Discs

Circumstellar discs occur throughout stellar evolution from protostellar accretion discs, through debris discs around main sequence stars (Hillenbrand et al., 2008) to more recently discovered dusty discs around white dwarfs (Farihi, 2011), however their origins are not always fully understood. Our solar system is a prime example of a highly evolved circumstellar disc. It contains a central star orbited by planets and smaller objects such as asteroids and comets contained in belts. These smaller objects are debris leftover from the formation of planets and fill the system with small dust grains through collisional processes. Evidence for the existence of these grains can be seen through zodiacal light, where light, from the Sun, is scattered off micron size dust grains.

It was not until the launch of the Infrared Astronomy Satellite (IRAS) in 1983 that significant evidence of similar dusty discs outside our solar system was first discovered. Initial observations from IRAS found an infrared excess around Vega, Fomalhaut and β Pictoris (Harvey, Wilking & Joy, 1984). As Vega was the first star detected with an IR excess, stars showing this trait are dubbed Vega excess stars. IRAS was able to detect excess radiation, in the wavelength passbands of 12, 25, 60 and 100 μm, above that is produced by just a stellar photosphere. The spectral energy distribution (SED) of the excess IR radiation is consistent with models where optical and UV photons, from the nearby star, are reprocessed by micron and sub-mm sized dust particles into the IR wavelength range. Figure 1.1 shows an example of the SED of β Pictoris. The IRAS, Submillimetre Common-User Bolometer Array (SCUBA) and SEST IMaging Bolometer Array (SIMBA) data points can clearly been seen to be in excess of what the stellar photosphere can produce (solid black line).

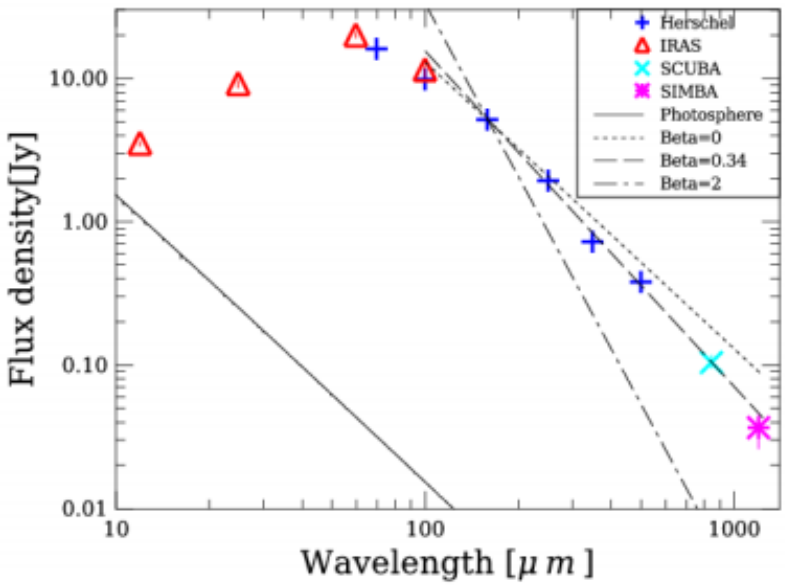

FIGURE 1.1: SED of β Pictoris (Vandenbussche et al., 2010). The image shows PACS (70-160 μm) and SPIRE (250-500 μm) (Vandenbussche et al., 2010), IRAS (IRAS source catalogue), SCUBA 850 μm (Holland et al., 1998) and SIMBA 1200 μm (Liseau et al., 2003) data.

Circumsterllar discs consist of gas, dust and larger bodies (including planetesimals)

which orbit a star primarily in a plane perpendicular to the axis of stellar rotation. Circumstellar discs have gained a large amount of attention over the last decades as they are thought to play an important role in star and planet formation. Planet formation is thought to occur in the disc through one of two methods depending on the mass of the disc. Massive discs are thought to form gas planets via gravitational instability (Kuiper, 1951; Boss, 1997; Durisen et al., 2007; Matsuo et al., 2007) while less massive discs are thought to form planets via core accretion process (Pollack et al., 1996; Matsuo et al., 2007). Gravitational instability assumes a disc to be large enough that it's self gravity is significant enough to alter the structure of the disc and to create instabilities. In addition, if the local cooling time is very rapid then the disc can fragment into dense clumps which then contract and collapse to form giant planets (Bodenheimer et al., 1980; Laughlin & Bodenheimer, 1994). Core accretion involves a sufficiently large core triggering hydrodynamic instability in the disc, causing the gas to accrete onto the core (Perri & Cameron, 1974; Mizuno, 1980). Hydrodynamic instability occurs as the core reaches a critical mass (critical mass is dependant on the accretion rate and opacity in the envelope) (Armitage, 2010). Accretion will continue to occur until either the gas in the disc is depleted or as a result of the core creating an annular gap within the disc. This model assumes that the core grows to a sufficiently large size before the gas disc dissipates. By observing circumstellar discs, during various phases of evolution, one can examine how planetary systems within the disc are formed and how they affect the structure of the disc.

In the optical and near-IR part of the spectrum, discs can be detected in scattered light, i.e. β Pic (Smith & Terrile, 1984). Scattered light observations can help determine the size distribution of the dust grains however, in order to examine the grain shape and phase function, one must observe the disc in polarized light. In optically thin discs, where single scattering dominates, a high degree of linear polarization is expected, with the orientation of the polarized light being dependent on which plane the light is being scattered in. The degree of polarization depends on the size, shape, composition, physical structure and alignment of individual grains and their distribution along the line of sight (Graham, Kalas & Matthews, 2007).

1.1.1 Protoplanetary Discs

Formation of Protoplanetary Discs

Protoplanetary discs form as a consequence of the conservation of angular momentum during the collapse of a molecular cloud. This is triggered due to the molecular cloud being a non-homogeneous structure as its density and velocity fields show signs of structure (McKee & Ostriker, 2007) and turbulence (Shu, Adams & Lizano, 1987). The mass of the cloud is concentrated around a core and material surrounding this core falls inward through an accretion disc. The initial disc size and mass depends on many factors. The radius of the disc extends to the centrifugal radius, $R(t) \propto \Omega^2 t^3$, where Ω is the angular rotation rate of the core and t is the accretion time (Terebey, Shu & Cassen, 1984). Analysis of dense cores was performed by Goodman et al. (1993) who found the core rotation rates can vary quite significantly. The ratio of rotational to gravitational energy, β, was found to vary between $2 \times 10^{-3} < \beta < 1.4$ for 43 cores in dark clouds. The angular momentum of the collapsing core can be estimated using:

$$j_{core} \simeq \Omega_{core} R_J^2 \tag{1.1}$$

where R_J is the Jeans length. In addition, the $\Omega_{\rm break}$ of a star can be estimated in a similar manner:

$$j_{break} \simeq \Omega_{break} R_*^2 \tag{1.2}$$

where R_* is the radius of the star and j_{break} is the break-up specific angular momentum. Assuming stellar parameters, $j_{break} \ll j_{core}$. Therefore, material in the disc must lose angular momentum in order to accrete onto the star. This is known as the 'angular momentum problem'. One solution to this is to consider outflows due to magneto-centrifugal acceleration (Blandford & Payne, 1982). This process involves accelerating material near the disc's surface to become ballistic (acceleration is governed by gravitational and magnetic forces). Once the ballistic phase ends, the collimation phase will begin causing the material to deflect perpendicular to the disc via hoop stress (forces acting perpendicular to both the axis and radius of the object). In this

case, the hoop stress is due to piled-up toroidal lines. As accretion continues, due to processes such as viscous transport and internal friction, gas and dust are lost though outflows which are produced in order to conserve angular momentum. In turn, this allows the disc to spread out further.

The sources for viscous transport can be found in two different processes. Magnetic fields frozen into a fluid can create magnetic torque, therefore increasing the angular momentum of the system (Basu, 1998) and on large scales, gravitational instabilities can create spiral density waves which can cause disc disruptions (Williams & Cieza, 2011).

Accretion due to viscous transport is one of the main methods by which a protoplanetary disc loses mass. Another process which causes discs to lose mass is photoevaporation. High energy photons, such as far UV, extreme UV and X-ray, from the central star remove material from the disc in different ways. Extreme UV photons have been modelled (Clarke, Gendrin & Sotomayor, 2001) and were found to ionize and heat hydrogen in the disc to $\approx 10^4$ K. The hydrogen will leave the system, if it achieves escape velocity, as part of the stellar winds. More recently, models have included x-ray and far UV radiation (Gorti, Dullemond & Hollenbach, 2009). Both x-rays and far UV radiation are able to penetrate further than extreme UV and are able to heat material further out in the disc. Models including x-ray and far UV photoevaporation were found to remove material two orders of magnitude more than extreme UV alone (Gorti, Dullemond & Hollenbach, 2009; Owen et al., 2010). However, the mass estimated from these models ($> 10 M_{\rm Jup}$) is higher than those observed ($< 1 - 2 M_{\rm Jup}$) (Andrews & Williams, 2005; Cieza et al., 2008) indicating that this process is still not fully understood.

YSO Classification and Evolution

Initially, young stellar objects (YSO) were classed based on the slope of the spectral energy distribution (SED) between 2 and 25 μm (Lada, 1987) ranging from Class I to Class III. An intermediate class between Class I and II, 'Flat-spectrum source' class, was introduced by Greene et al. (1994). Due to the improvements in faint

millimetre detectors, a fifth class, Class 0, was also introduced (Andre, Ward-Thompson & Barsony, 1993). As the name implies, Class 0 is the earliest phase where the mass of the circumstellar envelope is greater than that of the star. A summary of the classes is given in Table 1.1.

TABLE 1.1: Summary of the YSO classes

Class	Slope	Physical Properties	Observational Characteristics
0	-	$M_{\rm env} > M_{\rm star} > M_{\rm disc}$	No optical or near IR emission
I	$\alpha_{IR} > 0.3$	$M_{\rm star} > M_{\rm env} \approx M_{\rm disc}$	Generally optically obscured
Flat Spectrum	$-0.3 < \alpha_{IR} < 0.3$		Intermediate class between I and II
II	$-1.6 < \alpha_{IR} < 0.3$	$M_{\rm disc}/M_{\rm star} \approx 1\%$, $M_{\rm env} \approx 0$	Accreting disc, strong Hα and UV emission
III	$\alpha_{IR} < -1.6$	$M_{\rm disc}/M_{\rm star} \ll 1\%$, $M_{\rm env} \approx 0$	Passive disc, no or very weak accretion

The evolution of protoplanetary discs through class 0-III can be seen in Figure 1.2. Accretion is seen in the earliest stages of star formation (Class 0 and I). In the case of Class 0 objects, they are only beginning to the accrete the bulk of its final mass. The central star is surrounded by a thick layer of optically thick gas and therefore the system is only visible at IR and millimetre wavelengths.

Class I objects have begun accreting mass from an optically thick circumstellar disc. The surrounding envelope and molecular cloud close to the central source are cleared by stellar jets and outflows. The SED in the near and far IR wavelengths can now be seen as either flat (Flat spectrum class) or rising (Class I). Once the envelope has been been depleted due to accretion, the YSO enters Class II. The SED begins to drop quite significantly in the near and mid IR. Finally, after the circumstellar disc

has been dissipated, the remaining YSO is a Class III pre-main sequence star. The lifetimes of protoplanetary discs are $\approx 3 \times 10^6$ years (Bally et al., 1998; Haisch, Lada & Lada, 2001).

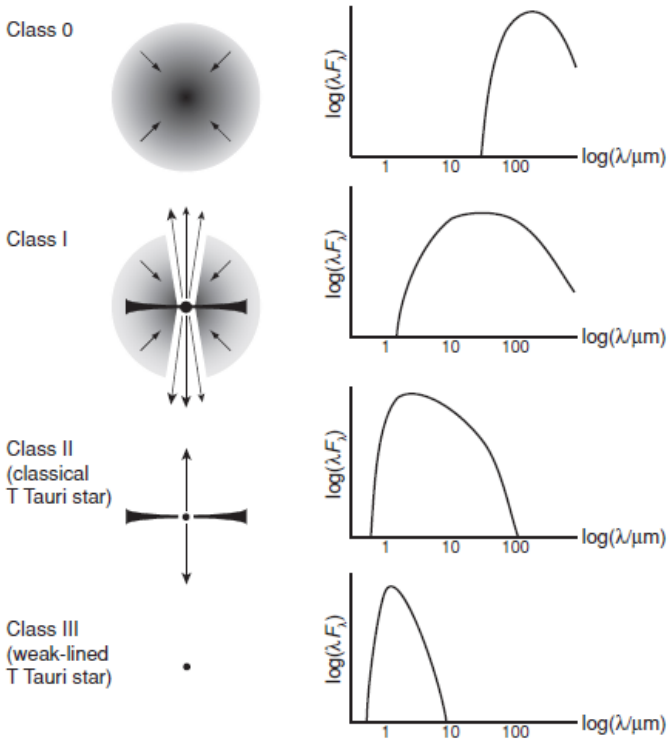

Figure 1.2: YSO calssification for a low-mass YSO (i.e. T Tauri) (Armitage, 2010).

Disc Structure

Protoplaneraty discs are often optically thick, in the IR wavelength range, due to the massive disc which surrounds the central star. The mass of the envelope is generally $\gg M_{\rm Jup}$ and due to the close proximity of material to the star, accretion can occur. Protoplanetary discs are also young, having an age < 10 Myrs (Strom et al., 1989). The structure of the disc may be affected by many processes. Continued accretion, due to internal friction or viscosity within the disc, causes the loss of material through outflows and from the accretion onto the star. Photoevaporation due to the central

star (Hollenbach et al., 1994) and external sources, such as nearby massive stars (Johnstone, Hollenbach & Bally, 1998), can begin to clear the disc. The agglomeration of dust grains, through collisions, into larger objects (i.e. planetesimals) can also create perturbations in the disc. Figure 1.3 shows a very recent millimetre image of the protoplanetary disc around HL Tauri taken by the Atacama Large Millimeter/submillimeter Array (ALMA) telescope.

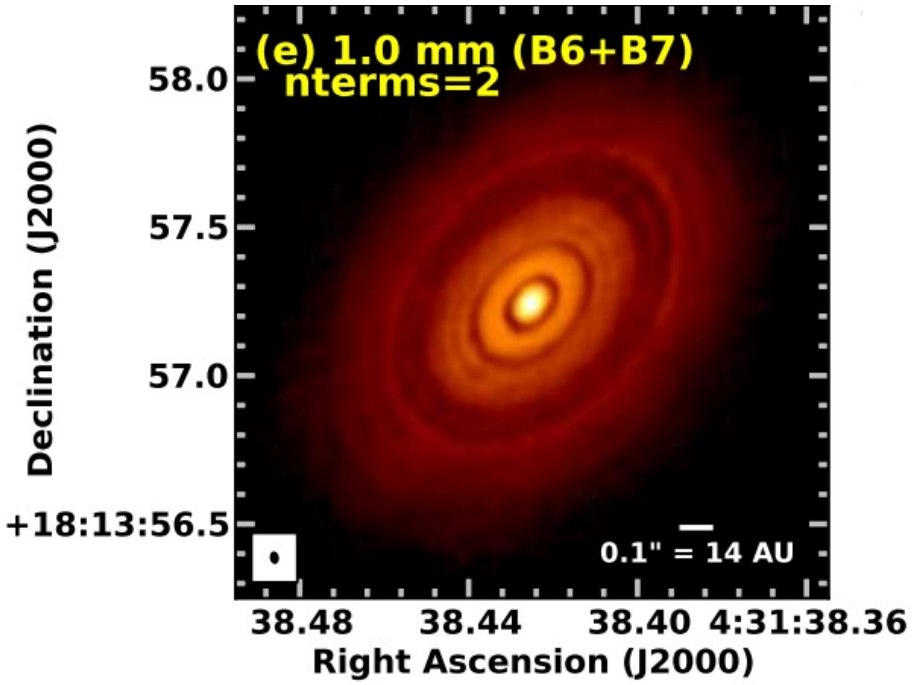

FIGURE 1.3: ALMA millimeter imaging (combination of the 1.3 mm and 0.87 mm data) of HL Tauri (Brogan et al., 2015). The disc is estimated to have a semimajor axis of 70 ± 15 AU at a distance of 140 pc (Mundy et al., 1996; Kwon, Looney & Mundy, 2011).

The image shows the protoplanetary disc with a large amount of structure. Concentric rings separated by annular gaps can clearly be seen in the disc, which are likely to have been created by planetesimals being formed in the disc. As the disc continue to evolve, large cavities begin to form and the protoplanetary disc enters the transitional disc phase.

1.1.2 Transitional Discs

Formation of the Transitional Disc

As the structure of a protoplanetary disc evolves, large central cavities of low dust density begin to form (e.g. GM Aurigae, TW Hya). These cavities can result from clearing due to the presence of a large planet as was first proposed by Strom et al. (1989). Their existence was confirmed via SED modelling and Spitzer spectra analysis (D'Alessio et al., 2006). The lack of or small near-IR excess in the SED suggests that this is due to clearing of dust in the inner disc region. This is one of the main characteristics of a transitional disc (Strom et al., 1989; Espaillat et al., 2007). These discs also show a variety of additional SED characteristics, such as exhibiting steep slopes in the mid-IR and high far-IR excesses (Muzerolle et al., 2010). Figure 1.4 shows an SED comparison between a model protoplanetary disc and transitional disc (GM Aur). The SED for the transitional disc is seen to have a lack of near-IR excess where as the protoplanetary disc SED is seen to have a very high near-IR excess. Evidence for accretion can also be seen in some discs (Calvet et al., 2005; Najita et al., 2007; Hughes et al., 2009) while other discs show no signs of it (Cieza et al., 2010; Merín et al., 2010).

Structure of the Transitional Disc

As the disc continues to evolve, the central cavity will become completely devoid of dust (no excess emission in the near-IR) and the dust grains in the disc will grow further and settle towards the midplane (Cieza et al., 2010), therefore producing additional sites for planet formation. Larger planetesimals can clear regions of the disc creating annular gaps e.g. HD 169142 (Quanz et al., 2013), HD 142527 (Canovas et al., 2013).

Figure 1.5 shows the transitional disc HD142527 in polarized light. The image shows complex and asymmetrical structures between the western and eastern side of the disc. A spiral like feature (located by the arrows) can also be seen, which could indicate the presence of a planetesimal perturbing the disc.

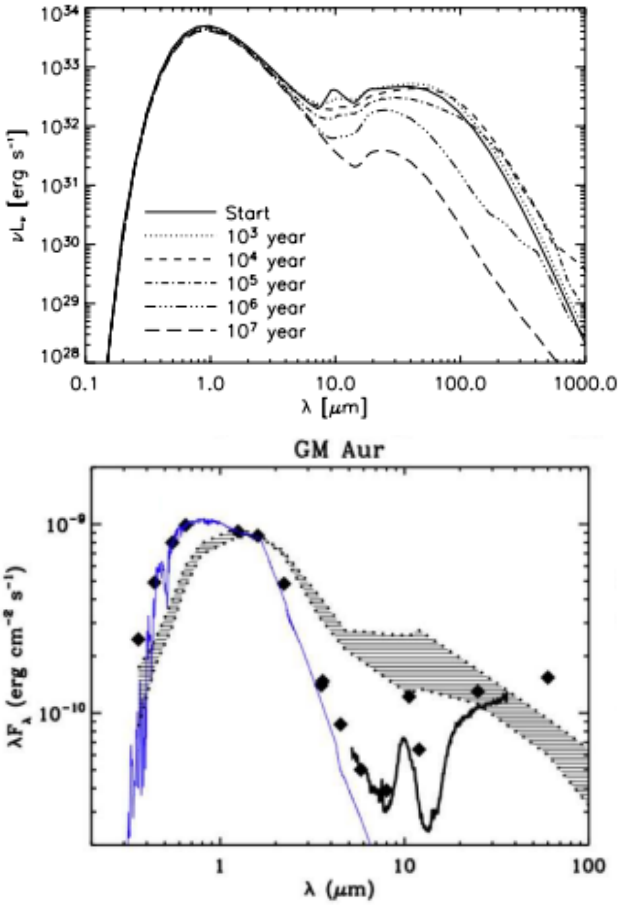

FIGURE 1.4: Top: Shows model protoplanetary discs for six epochs (Dullemond & Dominik, 2005). Bottom: SED plot for GM Aur (Najita et al., 2007). The black solid line shows the observational IRS spectra (Furlan et al., 2006) IR and the black diamonds show optical and IRAS photometry (Kenyon & Hartmann, 1995), 2MASS near-IR (Cutri et al., 2003) and IRAC photometry (Hartmann et al., 2005). The blue solid line represents a Kurucz stellar model. The hashed regions represent the uper and lower quartiles of the Taurus classical T Tauri star (CTTS) median SED (D'Alessio et al., 1999).

1.1.3 Debris Discs

Formation of the Debris Disc

A debris disc is a type of circumstellar disc containing dust particles of various sizes and composition, which orbit around a star. Interest in debris discs has risen over the years due to the relationship they may have to the formation of planets and small objects such as comets and asteroids (Backman & Paresce, 1993; Zuckerman et al., 2001).

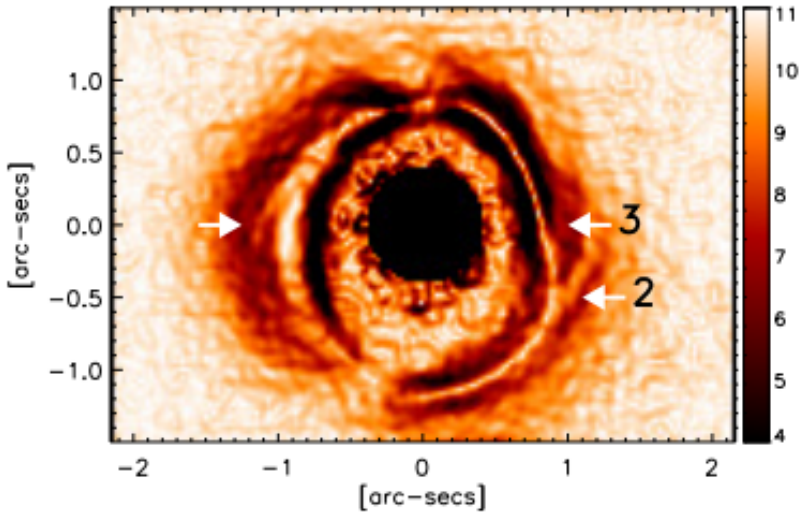

Figure 1.5: Image in polarized light of the transitional disc HD 142527 (Canovas et al., 2013). The image has had a Sobel filter applied to it to enhance disc edges. The arrows indicate the spiral features of the disc.

Debris discs are the result of the primordial gas and dust leaving the system due to processes such as acrretion, photoevaporation, radiation pressure and Poynting-Robertson (PR) drag. This is expected to occur over a timescale of $1 - 10 \times 10^6$ years (Zuckerman, Forveille & Kastner, 1995; Haisch, Lada & Lada, 2001). The lack of gas in the system means that the dust dynamics are governed through collisional means (Backman & Paresce, 1993). A gas to dust ratio > 1.0 would imply that the dust dynamics are influenced by the gas in the system (Takeuchi & Artymowicz, 2001).

Structure of the Debris Discs

The age of debris discs is much larger than the dust removal (due PR drag and collisions) timescale (Strubbe & Chiang, 2006). Smaller dust grains are expected to be driven out of the system by radiation pressure, or PR drag would decay their orbits (Harper, Loewenstein & Davidson, 1984). However, small grains are still being observed in debris discs (Graham, Kalas & Matthews, 2007). This implies that the dust grains are being replenished; one method of replenishment is through the collisions of parent bodies. Strubbe & Chiang (2006) suggest a 'birth ring' within the AU Mic disc, $r_{br} = 43$ AU, where grains of micron size are created through collisional means.

Another method of replenishment is through the catastrophic destruction of large planetesimals. In the case of the debris disc surrounding Vega, a ring comparable to our Kuiper Belt, located at 86-200 AU in the Vega system, is suggested to reproduce the observed 850 μm flux (Su, 2005).

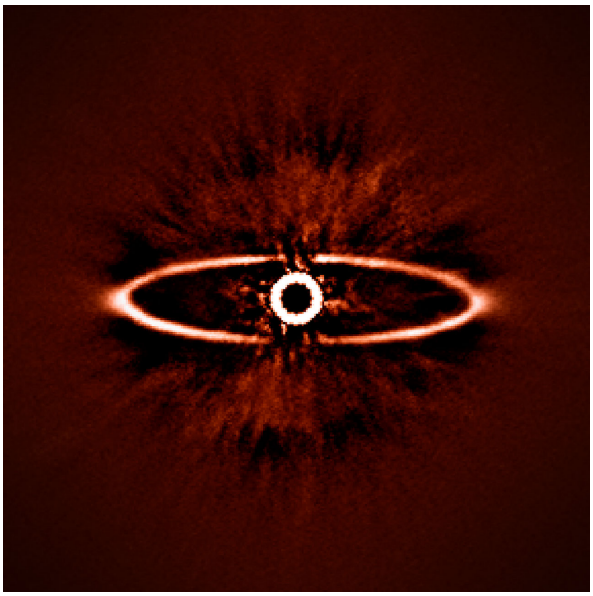

FIGURE 1.6: Infrared imaging of HR 4796A taken on the spectro-Polarimetric High-contrast Exoplanet REserach (SPHERE) instrument on the Very Large Telescope (VLT). The disc has a mean angular radius of 70 AU (Telesco et al., 2000).

Figure 1.6[1] shows very recent infrared imaging of the debris disc HR 4796A. This is one of the first images produced by the Spectro-Polarimetric High-contrast Exoplanet REsearch (SPHERE) instrument on the Very Large Telescope (VLT) and demonstrated that the device is capable of resolving ring like structures, in polarized light, and reducing the glare from the central star.

Nearby, Spatially resolved Debris Discs

AU Mic is a nearby star (9.9 pc) of type dM1e (an M-type red dwarf). The debris disc was first spatially resolved using an optical stellar coronagraph (Kalas, Liu & Matthews, 2004). AU Mic is of particular interest because of its proximity to us and

[1] ESO/J.-L. Beuzit et al./SPHERE Consortium

the fact that it is an edge-on system. β Pic is an A5 V star at a distance of 19.28 pc. The nearly edge on disc was first observed with an optical CCD coronagraph (Smith & Terrile, 1984). β Pic has a Galactic space velocity that suggests a common origin with AU Mic (Kalas, Liu & Matthews, 2004) implying that both stars belong to the same group of nearly 20 stars, the β Pictoris moving group (Zuckerman et al., 2001), that may have separated due to the differences in their Galactic space velocities. Although there is a large difference in stellar mass between AU Mic and β Pic, we see that, to first order, the mid-plane surface brightness distributions are nearly identical (Kalas, Liu & Matthews, 2004). In β Pic, radiation pressure forces quickly push out the small grains and in AU Mic we see a similar effect which is due to stellar winds. However, the midplane of the AU Mic disc exhibits a blue colour gradient between the F606W - H photometric bands at a radius larger than 50 AU (Krist et al., 2005; Metchev et al., 2005). The β Pic disc's mid-plane shows a red colour gradient between the F435W - F606W and F435W - F814W bands (Golimowski et al., 2006) suggesting differences in the grain composition, grain size distributions or minimum grain size between the AU Mic and β Pic discs.

Figure 1.7 shows HST imaging of both AU Mic (Krist et al., 2005) and β Pictoris between 1997 and 2012 (Apai et al., 2015). The β Pic disc is imaged from ≈ 7 AU in optical light (0.57 μm) and despite the disc orbiting the star and the presence of a large planet (orbital period $\approx 18 - 22$ years), the disc shows very little change between the two epochs. Very recent polarimetric observations, with the Gemini Planet Imager, of β Pic has further constrained the orbital parameters of the planet to a semimajor axis $= 9.2^{+1.5}_{-0.4}$ AU (Millar-Blanchaer et al., 2015).

Fomalhaut is another well resolved disc as it is relatively close to us at 7.7 parsecs. Unlike AU Mic and β Pic, which are edge-on to our line of sight, observations taken from the ACS on the HST show that Fomalhaut is surrounded by a narrow dust belt inclined at 24^o to our line of sight (Kalas, Graham & Clampin, 2005). Therefore the azimuthal disc structure can be measured. The ACS shows that the disc has large irregularity in its azimuthal brightness distribution. This warped structure led to the

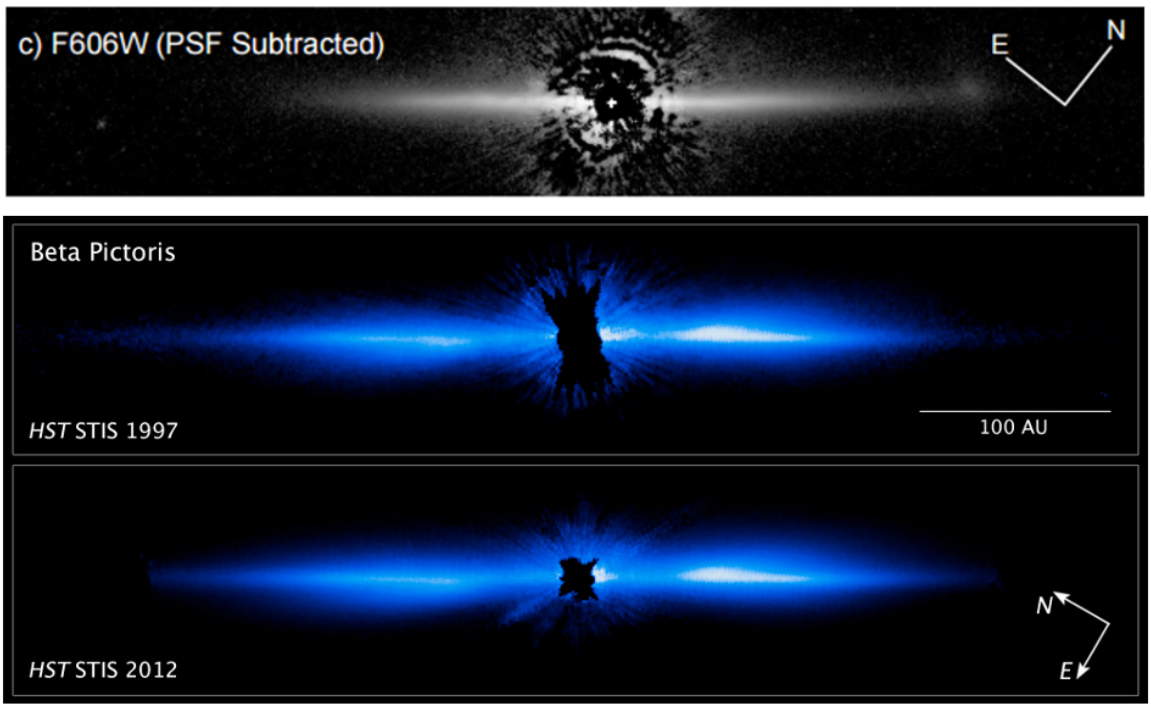

FIGURE 1.7: HST optical imaging of AU Mic (Top at 0.606 μm (Krist et al., 2005)) and β Pictoris (Bottom at 0.57 μm (Apai et al., 2015)).

prediction that a planet exists inside the belt. The exoplanet, named Fomalhaut b, was observed in the optical wavelength range by the HST (Kalas et al., 2008). There was, however, some dispute as to whether the flux in the visible wavelength was due to the planet or rather due to a dust cloud (Janson et al., 2012). Combining previous observations of Fomalhaut with recent HST/STIS imaging (Kalas et al., 2014), a four epoch (2004, 2006, 2010 and 2012) observation over eight years was produced. The point source (Fomalhaut b) is seen to have a very eccentric orbit heading northwest.

Figure 1.8 shows the debris disc around Fomalhaut imaged by the Hubble Space Telescope (HST) (Kalas et al., 2008) and ALMA (Boley et al., 2012). Both the HST and ALMA data a show ring like structures in the debris disc and one of the exoplanets (Fomalhaut b) responsible for these structures is directly imaged (Figure 1.8) in the optical wavelength (0.6 μm).

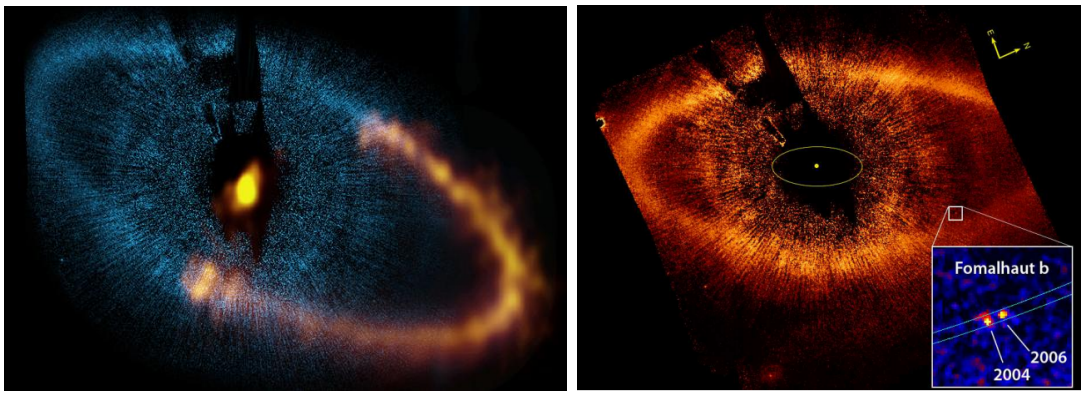

Figure 1.8: Left: Fomalhaut HST optical (0.6 μm) Kalas et al. (2008) (left/blue side of the image) and ALMA (350 GHz) (Boley et al., 2012) (right/orange side of the image) composite image. Right: Shows the entire HST optical imaging of Fomalhaut Kalas et al. (2008) with a zoomed view of Fomalhaut b between 2004 and 2006. The disc extends to approximately 20" in the North and 11" in the West. The semimajor axis of the belt is traced out 133-158 AU (inner and outer boundary of the belt respectively).

1.1.4 Composition of Dust Grains in Circumstellar Discs

The exact composition of circumstellar disc grains is still uncertain. One element which is accepted as a component of interstellar dust is silicon. This is due to the observed strength of the 9.7 μm emission line which is caused by Si-O stretch and the 18 μm line due to Si-O-Si bending (Mathis, 1990). This observed strength implies that approximately more than 50% of ISM grains must be composed of amorphous silicate, possibly in the form of olivine (Shen, Draine & Johnson, 2008). Another element which plays a large role when constructing dust grains is carbon. Carbon, however, can take several forms and determining which form it is in within the dust grain can be tricky. The forms we will consider are crystalline graphite and amorphous carbon. In large carbonaceous grains (number of atoms $> 10^5$), we would expect to see the carbon atoms arranged in a graphite like structure (Draine, 2003b). Observational evidence for the existence of carbon in dust grains can be seen from:

1). Observations from the Wide-field Infrared Survey Explorer (WISE) of all the known circumstellar discs in the Tarus complex of dark clouds in which Esplin, Luhman & Mamajek (2014) found a strong absorption line near 22 μm, which are suggested to be due to either graphite or Polycyclic aromatic hydrocarbons

(PAHs)

2). Observations of six stars in reflection nebulae and six Vega excess stars (Smith, Clayton & Valencic, 2004) which show signs the absorption at 3.4 μm, which is associated with the C-H stretching mode

3). Laboratory tests show that the emission lines (Tielens, 2008), in the interstellar medium (denoted Class A sources in Tielens (2008)) and circumstellar discs (denoted Class B sources), seen at 3.3, 6.2, 7.6, 8.6, 11.3 and 12.7 μm which are associated with the vibrational modes of PAHs.

1.2 Scattering of Light by Small Particles

1.2.1 Amplitude Scattering Matrix

The amplitude scattering matrix characterizes the relation between the incident (E_i) and scattered (E_s) electric fields for scattering by an arbitrary particle. The relation is a linear function and can be described in terms of the parallel ($E_\parallel$) and perpendicular ($E_\perp$) components of the electric fields:

$$\begin{pmatrix} E_{\parallel s} \\ E_{\perp s} \end{pmatrix} = \frac{e^{ik(r-z)}}{-ikr} \begin{pmatrix} S_2 & S_3 \\ S_4 & S_1 \end{pmatrix} \begin{pmatrix} E_{\parallel i} \\ E_{\perp i} \end{pmatrix} \tag{1.3}$$

where k is the wave number, r is the distance from the particle, $E_{\parallel i,s}$ are the electric field parallel to the scattering plane and $E_{\perp i,s}$ is the electric field perpendicular to the scattering plane for the incident and scattered light respectively, $S_j(\theta, \phi)$ are the amplitude scattering matrix elements and z is the distance in the z-axis. This definition was taken from Bohren & Huffman (1983), however other definitions, with varying terms outside the amplitude scattering matrix exist.

1.2.2 Stokes Parameters

In order to determine the polarization observed from scattered light, it is necessary to define a set of values which can describe the scattered light. The Stokes Parameters

are four quantities which denote 'radiant energy per unit time, unit frequency interval, unit area'. The absolute phase of the wave does not enter into the definition. We will use the 4-vector M with components labelled: (I, Q, U, V). The Stokes parameters of light scattered by a particle are defined, in complex notation, as the time averages of $E_{\parallel S}$ and $E^*_{\parallel S}$ (Bohren & Huffman, 1983):

$$I_S = \langle E_{\parallel S} E^*_{\parallel S} + E_{\perp S} E^*_{\perp S} \rangle \tag{1.4}$$

$$Q_S = \langle E_{\parallel S} E^*_{\parallel S} - E_{\perp S} E^*_{\perp S} \rangle \tag{1.5}$$

$$U_S = \langle E_{\parallel S} E^*_{\perp S} + E_{\perp S} E^*_{\parallel S} \rangle \tag{1.6}$$

$$V_S = i\langle E_{\parallel S} E^*_{\perp S} - E_{\perp S} E^*_{\parallel S} \rangle \tag{1.7}$$

where $i = \sqrt{-1}$. Here are some examples of the Stokes parameters:

- (1,0,0,0)I - unpolarized light (with intensity I)
- (1,1,0,0)I - 100% linearly polarized light with **E** parallel to the scattering plane
- (1,-1,0,0)I - 100% linearly polarized light with **E** perpendicular to the scattering plane
- (1,0,1,0)I - 100% linearly polarized light with **E** at $+45^o$ to the scattering plane
- (1,0,-1,0)I - 100% linearly polarized light with **E** at -45^o to the scattering plane
- (1,0,0,1)I - 100% right circular polarization (negative helicity)
- (1,0,0,-1)I - 100% left circular polarization (positive helicity)

where **E** is the electric field. Visual representations of the Stokes parameters defined above can be seen in Figure 1.9[2].

[2]http://spie.org/x32376.xml

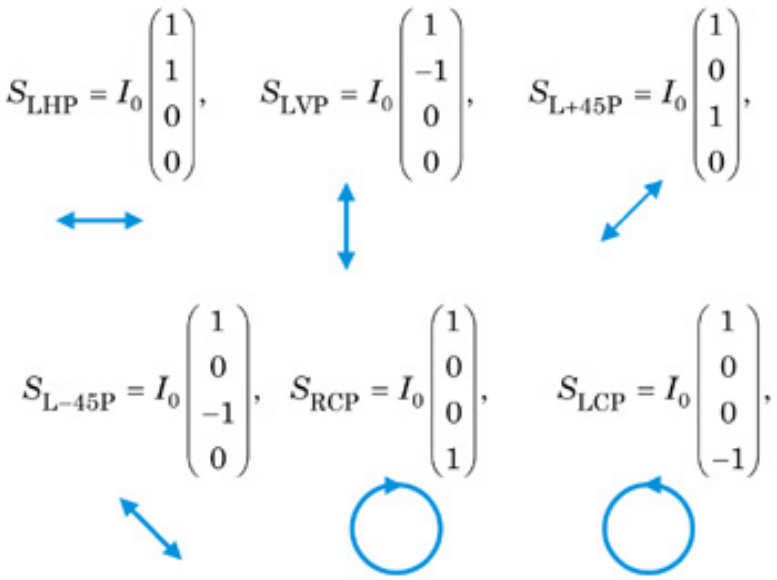

FIGURE 1.9: Visual representation of the Stokes parameters.

The degree of polarization and polarization angle are defined as:

$$P = \frac{(Q^2 + U^2 + V^2)^{1/2}}{I} \tag{1.8}$$

$$P_\phi = \frac{1}{2} \arctan \frac{U}{Q} \tag{1.9}$$

With the assumption that the incident light is unpolarized, $S_{31} = S_{41} = 0$ and only single scattering occurs, then Equation 1.8 can be simplified to:

$$P = \frac{Q}{I} \tag{1.10}$$

The scattering properties of a dust grain can be described using a 4x4 Mueller matrix S_{ij}. The matrix relates the Stokes parameters of the incident light with the

Stokes parameters of the scattered light by (Bohren & Huffman, 1983):

$$\begin{pmatrix} I_s \\ Q_s \\ U_s \\ V_s \end{pmatrix} = \frac{1}{\mathrm{k}^2 r^2} \begin{pmatrix} S_{11} & S_{12} & S_{13} & S_{14} \\ S_{21} & S_{22} & S_{23} & S_{24} \\ S_{31} & S_{32} & S_{33} & S_{34} \\ S_{41} & S_{42} & S_{43} & S_{44} \end{pmatrix} \begin{pmatrix} I_i \\ Q_i \\ U_i \\ V_i \end{pmatrix} \tag{1.11}$$

where (I_s, Q_s, U_s, V_s) is the scattered Stokes vector and (I_i, Q_i, U_i, V_i) is the incoming Stokes vector. It should be noted that the Matrix elements are dependent on the scattering angle θ and the azimuthal angle ϕ ($S_{ij}(\theta, \phi)$).

1.3 Optical Characteristics of Dust Grains

1.3.1 Size Parameter

The size parameter allows one to see how the size of the particle compares to the wavelength of light and can be defined as:

$$x = \frac{2\pi a}{\lambda} \tag{1.12}$$

where a is the semi-major particle dimension and λ is the wavelength of the incident light. Therefore, x provides a clear method of determining which size regime the scattering process resides in, these being:

- Rayleigh scattering - which applies to small, dielectric (non-absorbing) particles ($x \ll 1$)
- Mie scattering - this covers both absorbing and non-absorbing scattering solutions for arbitrary size particles
- Geometric optics - this applies to particles which are large in comparison to the incident wavelength ($x \gg 1$)

The method of interest is Mie Theory as it gives the freedom to scatter from arbitrary sized spheres (van de Hulst, 1957). This will further be discussed in detail in Section 1.4.1.

1.3.2 Phase Function

The phase function is a normalized measure of the angular distribution of scattered light intensity at a given wavelength into unit solid angle. For a single particle, with unpolarized light, this is defined as (Bohren & Huffman, 1983):

$$p = \frac{1}{C_{sca}} \frac{\mathrm{d}C_{sca}}{\mathrm{d}\Omega} \tag{1.13}$$

and is normalized as:

$$\int_{4\pi} p \, \mathrm{d}\Omega = 1 \tag{1.14}$$

where $\mathrm{d}C_{sca}/\mathrm{d}\Omega$ is the differential scattering cross section, which specifies the angular distribution of the scattered light, and C_{sca} (will be defined in Chapter 1.3.4) is the scattering cross section.

1.3.3 Asymmetry Parameter

The asymmetry parameter describes whether the light scattered will be in the forward or backwards direction (Bohren & Huffman, 1983).

$$g = \langle cos\theta \rangle = \int_{4\pi} p \; cos(\theta) \; \mathrm{d}\Omega \tag{1.15}$$

where θ is the scattering angle. Positive values indicate more forward scattering while negative values indicate more backward scattering. If a particle scatters light isotropically or if the scattering is symmetric around 90°, then $g = 0$.

1.3.4 Cross section and Efficiency Factor

The absorption and scattering cross sections, respectively, are how much of the incident light is removed due to absorption (C_{abs}) or scattering (C_{sca}). The sum of the absorption and scattering is known as extinction (C_{ext}):

$$C_{ext} = C_{abs} + C_{sca} \tag{1.16}$$

The efficiency factor is a dimensionless value which tells us the efficiency at which the incident light beam is scattered, absorbed or removed:

$$Q_{ext} = \frac{C_{ext}}{G} \tag{1.17}$$

$$Q_{sca} = \frac{C_{sca}}{G} \tag{1.18}$$

$$Q_{abs} = \frac{C_{abs}}{G} \tag{1.19}$$

where G is the cross-sectional area of a particle, projected onto a plane perpendicular to the direction of incident light beam. For a sphere of radius a, $G = \pi a^2$.

1.3.5 Albedo

The single scattering albedo is defined as a measure of the reflectivity of a material and can be calculated by:

$$\omega = \frac{C_{sca}}{(C_{abs} + C_{sca})} = \frac{C_{sca}}{C_{ext}} \tag{1.20}$$

where ω can range between $0 \leq \omega \leq 1$.

1.3.6 Optical Depth

The optical depth measures how transparent a medium is to radiation passing through it and, over a distance l, is defined as:

$$\tau_\nu = \int_0^l \kappa_\nu dx \tag{1.21}$$

where κ is the opacity in units of m^{-1}. This translates to the initial intensity of light (I_0), after passing through a medium with an optical depth equal to τ_ν, being reduced as:

$$I = I_0 e^{-\tau_\nu} \tag{1.22}$$

Debris discs are usually optically thin, therefore single scattering will dominate and little or no circular polarization is to be expected.

1.4 Spherical vs Non-Spherical Particles

1.4.1 Spherical Grains - Mie Theory

If we consider a spherical or randomly orientated non-spherical particle, then the total angle integrated scattering cross section is independent of the polarization state of the incoming photon. This simplifies the angular dependence of the scattering event. A polarization reference vector, **M**, is chosen such that $\phi = 0$, therefore the scattering event occurs in 1 plane. The scattering matrix (Equation 1.11)then simplifies to:

$$\begin{pmatrix} I_s \\ Q_s \\ U_s \\ V_s \end{pmatrix} = \frac{1}{k^2 r^2} \begin{pmatrix} S_{11} & S_{12} & 0 & 0 \\ S_{12} & S_{22} & 0 & 0 \\ 0 & 0 & S_{33} & S_{34} \\ 0 & 0 & -S_{34} & S_{44} \end{pmatrix} \begin{pmatrix} I_i \\ Q_i \\ U_i \\ V_i \end{pmatrix} \tag{1.23}$$

If we consider a spherical particle, then symmetry allows us to simplify the amplitude matrix (Equation 1.3)to:

$$\begin{pmatrix} E_{\parallel s} \\ E_{\perp s} \end{pmatrix} = \frac{e^{i\mathrm{k}(r-z)}}{-i\mathrm{k}r} \begin{pmatrix} S_2 & 0 \\ 0 & S_1 \end{pmatrix} \begin{pmatrix} E_{\parallel i} \\ E_{\perp i} \end{pmatrix} \tag{1.24}$$

This then allows us to simplify the scattering matrix even further to a four element matrix from which only three are independent:

$$\begin{pmatrix} I_s \\ Q_s \\ U_s \\ V_s \end{pmatrix} = \frac{1}{k^2 r^2} \begin{pmatrix} S_{11} & S_{12} & 0 & 0 \\ S_{12} & S_{11} & 0 & 0 \\ 0 & 0 & S_{33} & S_{34} \\ 0 & 0 & -S_{34} & S_{33} \end{pmatrix} \begin{pmatrix} I_i \\ Q_i \\ U_i \\ V_i \end{pmatrix} \tag{1.25}$$

There are many programs which incorporate Mie Theory in scattering calculations.

Initial testing was performed on MiePlot[3], which is a Windows based program which allows one use the Bohren and Huffman Mie scattering algorithm (Bohren & Huffman, 1983) with a user friendly interface. This program is designed to introduce the concept of scattering light from spherical objects. However, using the BHMIE code directly allows more freedom to change various parameters and to directly see how the code worked. Mie Theory can also be used to approximate the scattering properties of aggregate particles via the effective medium theory (EMT). EMT was first proposed by Bruggeman (Bruggeman, 1935) and allows one to determine the scattering properties of a inhomogeneous medium/particle.

1.4.2 Non-Spherical/Irregular Grains

There is strong evidence for the existence of non-spherical dust grains throughout the Galaxy:

1). The detection of circular polarization, from optically thin discs, (Martin, 1989) which can only be produced when scattering from non-spherical/irregular shaped particles (Bohren & Huffman, 1983).

2). Far IR and sub-mm polarization in dark clouds due to aligned non-spherical grains (Lucas & Roche, 1998)

3). Polarization of starlight by the ISM (Kemp & Wolstencroft, 1972)

4). Interplanetary dust particles (Brownlee Particles) collected in the stratosphere are seen to be irregular in shape (Figure 1.10) (Brownlee, Tomandl & Olszewski, 1977)

Figure 1.10 shows examples of interplanetary dust particles, which were collected with an aircraft in the Earth's stratosphere (Brownlee, Tomandl & Olszewski, 1977; Brownlee, Joswiak & Matrajt, 2012). These particles are clearly non-spherical and irregular in shape. Although researchers are aware that realistic dust grains are not spherical, approximations are still being used to model complex grains (Sauter et al.,

[3]http://www.philiplaven.com/mieplot.html

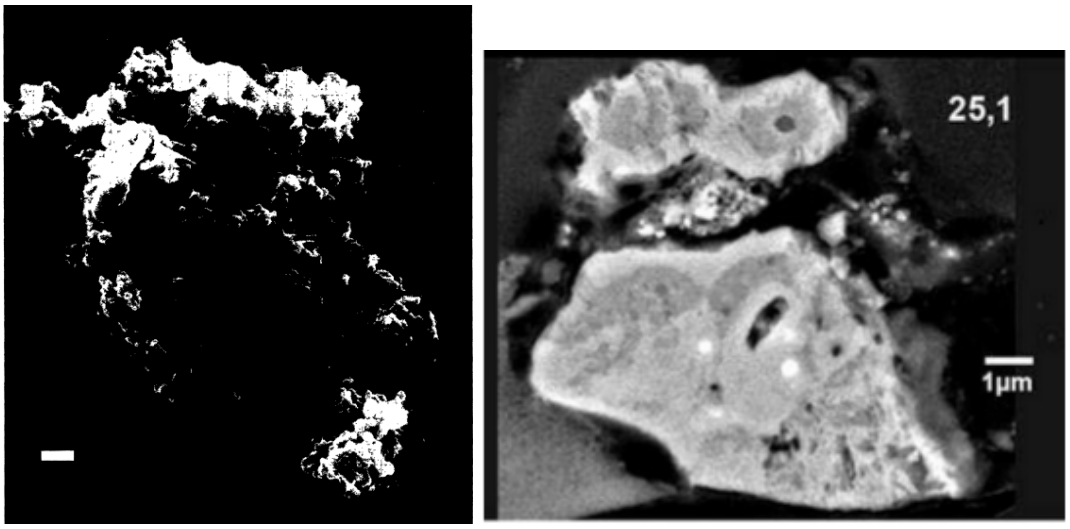

FIGURE 1.10: Left: Scanning electron microscope (SEM) imaging of a porous interplanetary dust particle (Brownlee, Tomandl & Olszewski, 1977). The bar is equivalent to 1 μm . Right: SEM imaging of Calcium Aluminum Inclusion (CAI) like porous particles (Brownlee, Joswiak & Matrajt, 2012).

2009; Voshchinnikov & Krügel, 1999). Despite its short comings, Mie Theory does provide a first-order approximation when considering the rotationally averaged scattering effects seen in non-spherical particles. In order to produce more accurate models to fit the observations, we must consider realistic dust models which will involve using non-spherical particles. The scattering of light by non-spherical particles is not something unique to astrophysics. Many other fields, such as atmospheric optics, biophysics, electrical engineering etc. require the use of modelling non-spherical particles.

In addition to circumstellar dust, cometary dust has also been modelled using aggregate particles (Kimura, Kolokolova & Mann, 2006). By comparing observed cometary comae to simulations of solar radiation scattered by cometary dust, constraints on the dust particles were made. The work is conducted under the assumption that comet formation occurs as an agglomeration process in the solar nebula (Messenger et al., 2003). This suggests that the particles grow under a ballistic cluster-cluster aggregation (BCCA) process (Wurm & Blum, 1998). The optical properties of the aggregate grains are modelled using the T-matrix method (Section 1.4.3) and are found to provide a good fit to the linear polarization and albedo.

Graham, Kalas & Matthews (2007) tries fitting various dust models to the polarimetric observations of the AU Mic disc. They conclude that their Maxwell-Garnett model requires a high porosity of 90% to 94%. This is justified by the fact that porous grains are a inevitable result from particle growth. However, they say that the method used to calculate porosity (effective medium theory was used to convert the dielectric constant to porosity (Kruegel, 2003)) was inadequate in determining the best model. They go on to suggest highly porous clusters to replicate both the peak linear polarization and phase function with the use of discrete dipole approximation (DDA) or transition-matrix (T-Matrix) methods to calculate the scattering matrix. This application of DDA will be explored in further detail in Chapter 5.

Min & Jeffers (2010) also promote the use of non-spherical particles by comparing a compact grain model with a fluffy aggregates model. They conclude their conference proceeding by stating that the optical properties of large complex aggregates and compact grains over a broad wavelength and with high values of the refractive index are now required to model debris discs.

1.4.3 Approximating/Modelling Non-Compact Particles

Analytical Multilayer Sphere

The analytical multilayer sphere (MLS) method models a sphere being comprised of shells, each with one layer of a particular material (Voshchinnikov & Krügel, 1999). The number of shells is required to be high in order to ensure sufficient mixing within the sphere.

A comparison between DDA and MLS is given in Shen, Draine & Johnson (2008). They see that the MLS method fails to provide a good approximation for the scattering and absorption by ballistic aggregate grains with high porosity and/or absorption.

Transition Matrix

This method computes the electromagnetic scattering by a single and aggregate, homogeneous and arbitrarily shaped particle. It was first introduced by (Waterman, 1965).

The Transition matrix (T matrix) method, allows one to compute scattering properties of a particle based on a direct solution of Maxwell's equations. Due to the linearity of Maxwell's equations and the extended boundary condition method, the scattered field coefficients (p and q) can be related to the incident field coefficients (a and b) by the T matrix. In matrix form, the relation between the scattered and incident field coefficients can be written as:

$$\begin{pmatrix} p \\ q \end{pmatrix} = T \begin{pmatrix} a \\ b \end{pmatrix} = \begin{pmatrix} T^{11} & T^{12} \\ T^{21} & T^{22} \end{pmatrix} \begin{pmatrix} a \\ b \end{pmatrix} \tag{1.26}$$

where T is the Transition matrix. The code is designed so that it reproduces the Mie Theory as the particle tends to a homogeneous or layered sphere. The advantage of using this method is that it calculates the orientation average of the scattering matrix. Therefore the T-Matrix method is quick, however, in the case of aggregate particles, the number of monomers used to construct the grain is limited to being small unless a large amount of RAM is available for the calculation. Mishchenko, Travis & Mackowski (1996) extensively reviewed the use of T-Matrix in calculating the light scattered from non-spherical particles.

Kimura, Kolokolova & Mann (2006) use the T-Matrix method to simulate light scattering of cometary dust whose aggregate size is much larger than the incident wavelength. Due to the memory hungry nature of the T-Matrix code, they are limited to using $N = 128$, where N is the number of monomers. Although they used a relatively simple model to construct the dust grains, they are able to match the properties of real cometary dust very well.

Discrete Dipole Approximation

Exact solutions to Maxwell's equations are known for only a limited number of geometries such as spheres, spheroids or infinite cylinders. Therefore calculating the properties of a target of arbitrary geometry will require an approximate method. The discrete dipole approximation (DDA) replaces the solid particle by an array of N point dipoles, with the spacing between the dipoles being small compared to the wavelength.

The dipoles interact with each other and the incident light, which gives rise to a set of linear equations, which are solved to obtain the dipole polarizations. The scattering properties of the target can be determined from these polarizations. This method was first introduced by Purcell & Pennypacker (1973) in which they state that a dielectric grain of arbitrary shape can be modelled by an array of N polarizable elements in a vacuum. This method will be explored in further detail in Chapter 5.

1.5 Aims of the Thesis

The main aim of this thesis is to examine the properties of circumstellar discs. This will include examining both transitional and debris discs in scattered and polarized light. Scattered light images alone can provide constraints on the dust grain size and composition, however the addition of polarized imaging will allow constraints on the phase function and percent polarization to be made. This in turn can further constrain the size, composition and structure of the dust grains. Monte Carlo modelling of these discs will also be performed to determine the grain and disc properties. Examining disc structures, such as annular gaps and clumps, can help identify and constrain the location of planetesimals in the disc. Further constraints can be made by comparing the models produced, via Monte Carlo simulations, to existing and new observational data. The final aim is to explore the use of realistic dust grains (ballistic aggregate models) in Monte Carlo simulations as spherical grains are seen to fail to simultaneously fit the observed phase function and polarization (Graham, Kalas & Matthews, 2007).

1.6 Structure of the Thesis

The thesis is structured as follows. Chapter 2 will examine the observational IR polarimetric data obtained for the transitional disc HD 169142 from the VLT. Chapter 3 will introduce the 3D radiative transfer code Hyperion, including tests conducted with the code. Chapter 4 will examine modelling of the HD169142 disc with Hyperion using conventional spherical grains. Chapter 5 will introduce the non-spherical scattering

code DDSCAT. Chapter 6 will examine modelling the AU Mic disc with Hyperion using both conventional spherical grains and ballistic aggregate grains computed with DDSCAT.

2

Polarimetric Differential Imaging of HD169142

2.1 Introduction

The structure of transitional discs in conjunction with the evolution of dust grains can tell us a large amount about the physical processes within the disc. Face on discs allow for direct observations of structures such as annular gaps or central cavities which are devoid of dust. These cavities are a key characteristic feature of the transitional disc as it indicates the possible formation of low mass companions clearing the region via tidal interactions (Papaloizou et al., 2007).

Herbig stars can be split into specific groups depending on various observational properties. The group classification was presented in Meeus et al. (2001) and splits

Herbig stars into groups based on their SED and the presence of solid state bands. Stars for which the continuum can be reconstructed by a power law and a black body are designated Group I, and stars which only need a power-law to fit their continuum are designated Group II. These groups can be further subdivided depending on whether there are solid state bands present (a) or absent (b).

The Herbig star we focus on is the group Ib star HD169142. It is an A5Ve (spectral type A, luminosity class V-main sequence, emission lines present) star (Dunkin, Barlow & Ryan, 1997a) at a distance of 145 pc (Sylvester et al., 1996). The mass of the star has been derived, through modelling of low resolution UV spectra and using theoretical pre-main sequence evolutionary tracks, to be $\approx 1.65 M_{\odot}$ (Blondel & Djie, 2006). Its age can be predicted by placing the star on the H-R diagram and comparing with theoretical pre main sequence (PMS) evolutionary tracks (Manoj et al., 2006). The age of the star is found to be 5.42 millions years old (PMS phase) (Manoj et al., 2006). Table 2.1 summarizes the basic parameters of HD 169142.

TABLE 2.1: Parameters of HD169142

Parameter	HD169142	References
R.A. (J2000)	$18^h24^m29^s.79$	-
Dec. (J2000)	$-29°46'49".22$	-
H (mag)	6.911 ± 0.038	(1)
K_s (mag)	6.410 ± 0.024	(1)
Spectral Type	A5Ve	(2)
Mass	1.65 $M_{\odot}$	(3)
Distance	145 pc	(4)
Age	5.42 Myrs	(5)

References: (1) (Cutri et al., 2003), (2) (Dunkin, Barlow & Ryan, 1997a), (3) (Blondel & Djie, 2006), (4) (Sylvester et al., 1996), (5) (Manoj et al., 2006)

The spectral energy distribution (SED) of HD169142 rises in the mid-infrared, however since it is a group Ib member, it lacks the 10 μm silicate feature (Meeus

et al., 2001; van Boekel et al., 2005). Figure 2.1 shows the SED from four Herbig group Ib objects in the wavelength range of $2 - 40$ μm. All of the objects, including HD169142, show a lack of any silicate emission bands. Moderately strong polycyclic aromatic hydrocarbon (PAH) bands have also been detected at 3.3, 6.2, 7.7, 8.7 and 11.2 μm (Meeus et al., 2001). The 11.2 μm feature can be seen in Figure 2.1. The 3.3 μm feature has also been spatially resolved by Habart et al. (2006), in which they find the emission feature is extended with a FWHM of 0.3" (43 AU). For a radial offset from the star greater than 0.3", the feature is too weak to measure its brightness profile with sufficient accuracy.

Previous ground based polarimetric imaging of this disc include H-band observations with the United Kingdom Infrared Telescope (UKIRT) (Kuhn, Potter & Parise, 2001) in which the polarization brightness fraction (polarization fraction times the mean H-band surface brightness intensity) was found to peak at 0.013 (normalized by the mean brightness as a function of distance from the central star). Although a polarized signal can be detected, Figure 2.2 shows that there is not a clear centrosymmetric pattern. They also see a slight elongation of the polarized brightness to the NE and SW. Figure 2.2 also shows the J-band observations, with the UKIRT, which marginally resolve a centrosymmetric pattern surrounding the star (Hales et al., 2006). They also see modulation in the Q Stokes parameter image when azimuthally averaging the region around the star, confirming the presence of an extended distribution of dust seen in Kuhn, Potter & Parise (2001).

HST/Nicmos coronagrphic imaging of the disc in 1.1 μm scattered light, in the range $0.57" \leq r \leq 1.4"$ (Grady et al., 2007), showed an azimuthally symmetric nebulosity surrounding the star which was consistent with a disc with inclination $\leq 20^{\circ}$ from face on. More recently (Quanz et al., 2013) observed the disc polarimetrically in the H-band as close as 0".1 to the star. They reveal that the inner region ($\lesssim 20$ AU) is depleted of scattering dust particles with an unresolved disc rim at ≈ 25 AU (Figure 2.3). They also find local brightness asymmetries at opposite sides of an annular gap between $\approx 40 - 70$ AU. Subaru/COMICS 18.8 and 24.5 μm observations (Honda et al.,

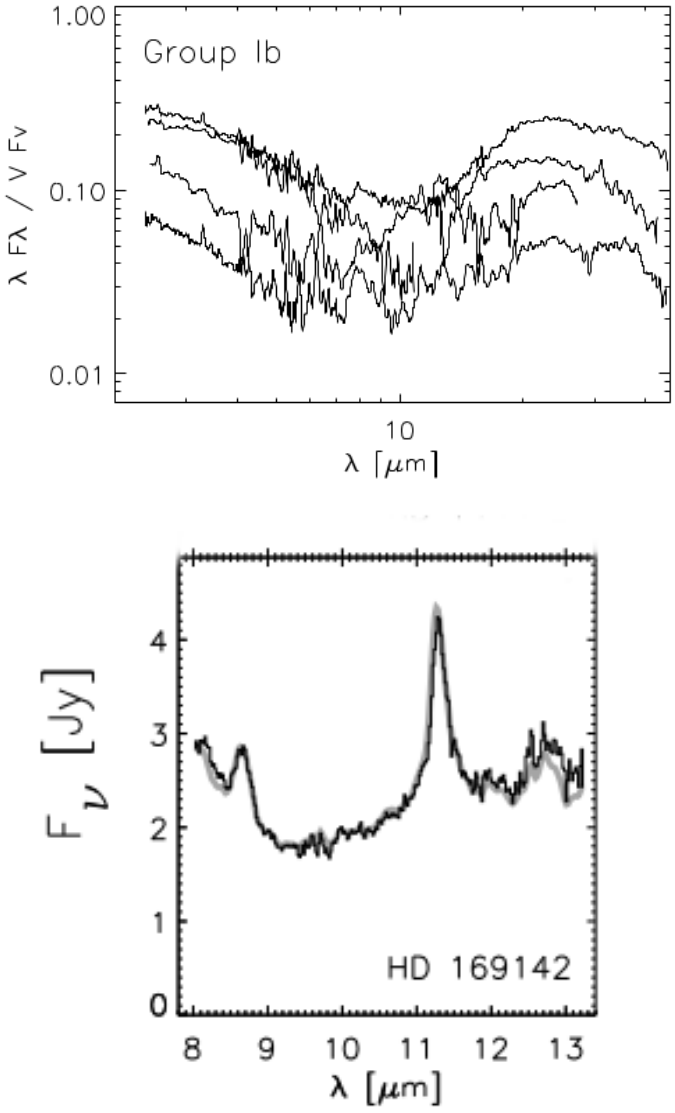

FIGURE 2.1: Top: ISO observations showing IR Spectra from 4 Herbig Group Ib objects: HD 100453, HD 135344, HD 139614 and HD 169142 (Meeus et al., 2001). This plot shows that these objects do not produce the 10 μm silicate feature. Bottom: Shows the best fit model spectra over the 11 μm range for HD 169142 van Boekel et al. (2005). Once again there is no evidence for silicate band emission, but there is a clear 11.2 μm PAH emission feature.

2012) also confirm the presence of a large gap. They suggest an inner wall of the outer disc at 23^{+5}_{-3} AU, but still require an optically thin and geometrically thick halo to produce the NIR excess. VLA 7 mm observations (Osorio et al., 2014), due to the thermal emission of large dust grains (> 100 μm), shows an inner cavity and a ring of

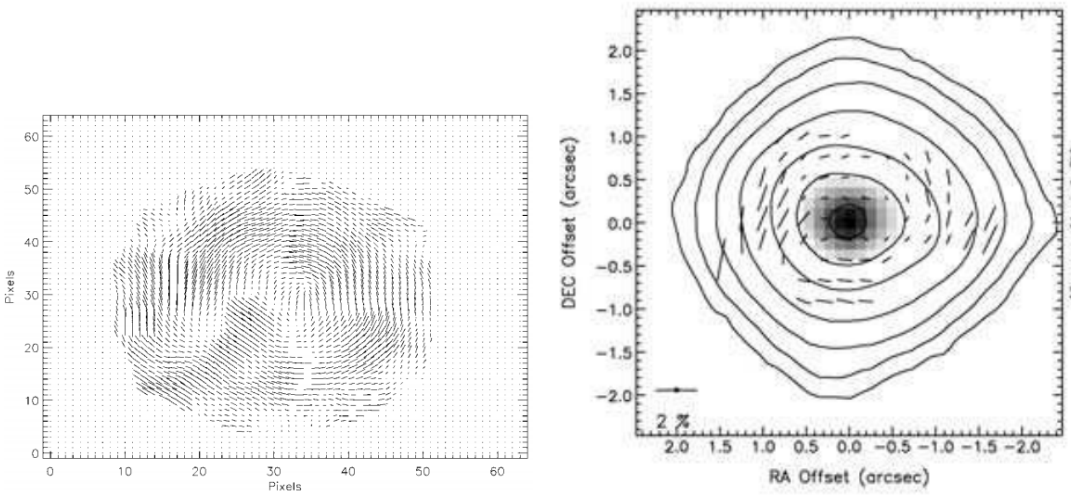

Figure 2.2: Left: UKIRT H-band polarimetry (Kuhn, Potter & Parise, 2001). The image shows the polarization vectors where the length of the vectors are proportional to the polarization fraction. The image is scaled as 0".0814 pixel^{-1}, therefore giving a spatial scale of $\approx$ 5".2. Right: UKIRT J-band polarimetry (Hales et al., 2006). A centrosymmetric pattern is marginally resolved around the disc.

enhanced emission between $\approx 25 - 30$ AU which is interpreted as the rim of an inner cavity or gap. Figure 2.3 shows this ring like feature in the H-band (Quanz et al., 2013) and 7mm observations (Osorio et al., 2014) (which appears to be asymmetric). An azimuthal asymmetry in the ring between the west and east side is seen which is linked to lopsided structures which are a consequence of trapping large dust grains. They also confirm an outer annular gap from $\approx 40 - 70$ AU inferring the presence of at least two planets or substellar objects.

2.2 Observations and Data Reduction

2.3 Very Large Telescope

The observations of HD169142 were taken on the Very Large Telescope array (VLT). It is located in the Atacama Desert (Cerro Paranal) in Chile and is run by the European Southern Observatory (ESO). Instruments cover both the optical and IR wavelength ranges. The VLT array consists of four 8.2 metre Unit Telescopes and four 1.8 metre

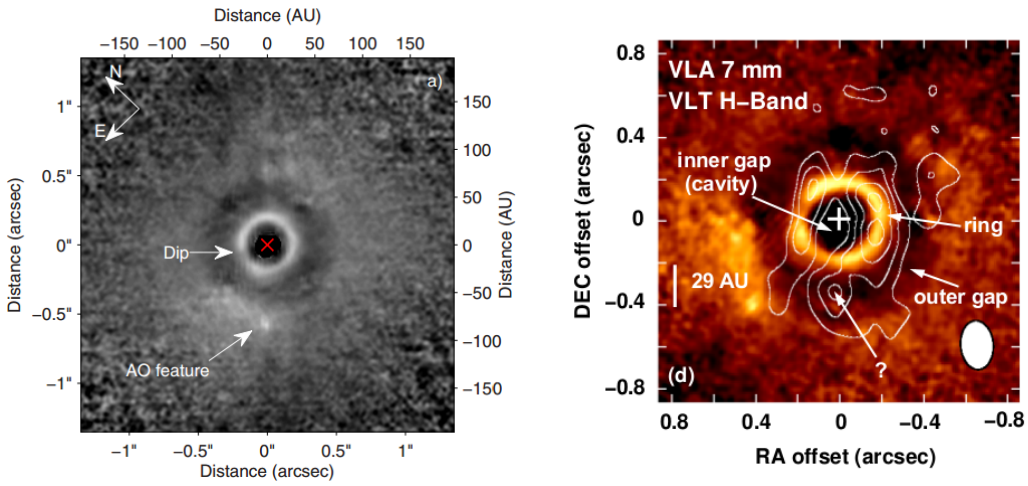

FIGURE 2.3: Left: H-band VLT imaging of HD169142 in polarized light (Quanz et al., 2013). Image shows the final Q_r scaled with r^2. Right: Image showing 7 mm VLA (Osorio et al., 2014) contours over H-band VLT (Quanz et al., 2013).

movable Auxiliary Telescopes which can work together to form a single large interferometer. Figure 2.4[1] shows both the Unit Telescopes and the Auxiliary Telescopes. Each individual Unit Telescope can be used with a large-field imager, adaptive optics corrected cameras and spectrographs.

FIGURE 2.4: Image of the VLT.

[1]http://www.astro.ethz.ch/lilly/research/vlt-muse.html

2.3.1 Adaptive Optics

Adaptive optics (AO) makes it possible to compensate for the image degradation effects that the atmosphere produces on ground-based telescope images. AO is based on a simple principle: by controlling a mirror whose surface is deformed by motors located on its rear face, the optimum image of the observed object is reshaped in real time. This concept was first explored by Babcock (1953) but was first successfully tested on the 1.52 m telescope at the Observatoire de Haute Provence (OHP) using the VLT Adaptive Optics Prototype System (also known as COME-ON) in 1989 (Merkle et al., 1989). Continuous analysis of the aberrations of the incident wavefront is used to control the deformations of the mirror.

2.3.2 NACO

The adaptive optics system on the VLT is the Nasmyth Adaptive Optics System (NAOS) which works in conjunction with the near IR Coude Near Infrared Camera (CONICA) to form the NACO system. Figure 2.5 shows an illustration of the NACO system with polarimeter module (Witzel et al., 2011). The light is focused off three mirrors before the beam is sent through the Nasmyth focus. The adaptive optics system then performs required corrections as described in Section 2.3.1. A mask, which consists of equally spaced parallel bars, is placed at the focal plane of the telescope. Figure 2.6[2] shows an example of a mask used in a dual beam imaging polarimeter.

The beam then travels to the half wave plate, which enables the observer to change the orientation of the plane of polarization with respect to the detector without rotating the Wollaston prism and without changing the field of view. One full cycle will include observations at four different plate positions in steps of 22.°5 degrees (0°, 22.°5, 45°, 67.°5), resulting in a rotation of the plane of polarization by 45° degrees between waveplate positions. The Wollaston prism divides the incoming light into two linearly polarized beams, ordinary (O) and extraordinary (E), with orthogonal polarization vectors. These two beams of light will then be imaged simultaneously onto the detector.

[2]http://starlink.eao.hawaii.edu/docs/sun223.htx/sun223.html

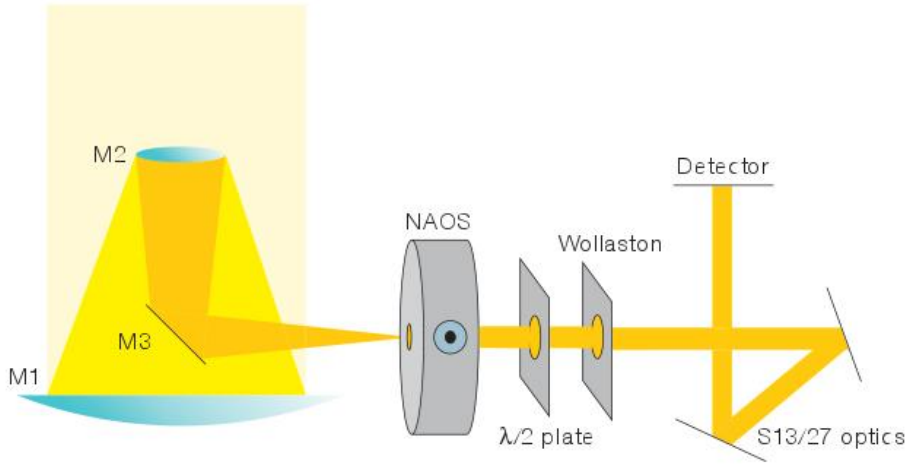

FIGURE 2.5: Illustration the optical elements of the NACO System (Witzel et al., 2011).

The masking system (not shown on Figure 2.5) is used to prevent any overlap between the O and E-images. The advantage of this system over a single-beam instrument (in which only one state of polarization is recorded on a given exposure) is that variations in sky transmission during exposures affect both states of polarization equally. This allows one to compensate for sky background changes equally between images.

2.3.3 Observations

The observations of HD169142 were carried out, by collaborators, on the 25th and 26th August 2012 in the H and K_s broad band filters on the VLT with the NACO instrument. Exposure times were set to 10 seconds for the H band and 20 seconds for the K_s band with the number of integrations (Ndits) set to 7. To correct for bad pixels the target was moved along the x-axis of the polarimetry mask at three different positions between consecutive polarization cycles. To ensure the results were consistent across the three different positions on the mask, the data reduction process was performed separately for each position. This also allowed us to increase the signal to noise by stacking the three positions into one final image (noise could be due to light from sources other than our target, read noise and/or dark current noise). Therefore the total integration time per wave plate position for the H-band is 210 seconds and for the K_s-band is 420

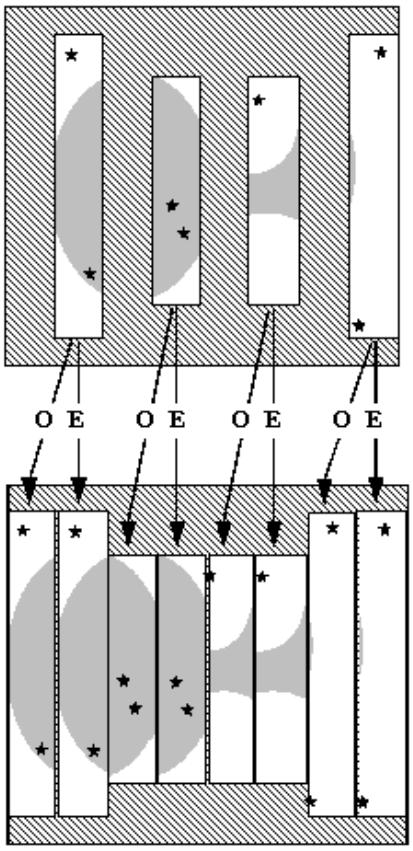

Figure 2.6: Illustration the a typical mask used in a dual beam imaging polarimeter. Top: shows the mask with equally spaced parallel bars. Bottom: shows the results of the Wollaston prism dividing the incoming light into ordinary (O) and extraordinary (E) ray images[2].

seconds. It should be noted that these long exposure times caused the central regions of the star to become saturated. Due to this saturation, photometric calibration of the images was not possible. Short exposure time observations were available (0.4 seconds for both the H and K_s-bands), however these images were excluded due to their poor signal to noise.

2.3.4 Data Reduction

Data reduction was carried out using Starlink software. Dark and flat field (these were obtained during the day as part of the VLT day time calibrations) correction used

TABLE 2.2: Summary of observations of the target HD169142 and standard star HD 161743

Target	Band	Exposure Time (s)	Ndits × Dither Positions	Air Mass	Date
HD169142	H	10	7×3	1.40	26/08/2012
	K_s	20	7×3	1.40	25/08/2012
HD161743	H	10	2×1	1.40	26/08/2012
	K_s	10	2×1	1.40	25/08/2012

applications from the CCDPACK package and calculations of Stokes parameters used the POLPACK package. It allowed us to:

1) Extract the O and E regions from the input image

2) Align the extracted O and E regions

3) Select regions of the sky which are then subtracted from the extracted regions

4) Stokes vectors are calculated as described in Section 2.3.6 for each pixel.

The O and E-images are extracted by creating a mask around the O and E region of the input frame. This mask is then used for all the half-wave plate positions to ensure that the same O- and E-regions are extracted from each frame. Polka aligns the O and E images through an image alignment procedure which is based on user defined reference points (background stars), which are used to determine the offset between images. This involves creating a set of Gaussian profiles to determine the centroid of each star. A six parameter fit is then calculated to align the O and E-images.

At least two images, taken at half-wave plate positions of 0°.0 and 22°.5, are required to estimate the degree and orientation of the polarization. This allows us to image the disc with the polarization plane rotated at 0°.0, 45°.0, 90°.0 and 135°.0. However there are benefits to imaging the disc at a half-wave position of 45°.0 and 67°.5. By imaging through a full polarization cycle, we image the disc at each plane of polarization twice. This can then provide us with a redundancy factor which will allow for internal

consistency checks to be made. Therefore, any inconsistencies between the images, which may be due to variations in sky conditions, can be corrected for.

2.3.5 Cross Correlation

While the Gaussian centroiding procedure aligned the H-band images, so that they were accurately placed on one another, well enough to produce Stokes images with features commonly seen in light scattered by small particles, the K_s-band image alignment was more problematic. There were very few reference points (background stars) in the image and the target star was also heavily saturated making it difficult to get an accurate central position. Saturation meant that pixel count would plateau across the target star, therefore making it impossible to accurately determine the peak/central point of the target. In view of this, a new alignment procedure was developed based on a cross correlation procedure written in IDL (Canovas et al., 2013).

In this case, the cross correlation process involves determining the shift between two images by progressively overlaying the images on top of one another and summing the pixel values. Figure 2.7[3] shows this process as the template (red image) progressively slides over the image. The dark pixels on the target image have a value of 1 and the light pixels have a value of 0. The centre of the image will therefore be located at the maximum value of the cross correlated image.

Firstly a template to which all the images will be aligned was required; the first O image at the half-wave plate position 0.°0 was chosen as the template. The cross correlation process included an alignment procedure which allows one to determine the shift, in pixels, between the central points of the target star. Due to the saturation of the target and lack of background stars, the Gaussian centroiding procedure was only able to align the images with a 2 pixel shift in the central position. The cross correlation process produced a better alignment (1 pixel shift) and was able to also align the K_s-band images. However, there was still room for improvement. The images were expanded by a factor of 20 along each axis through cubic convolution interpolation,

[3] www.comp.nus.edu.sg/ cs4243

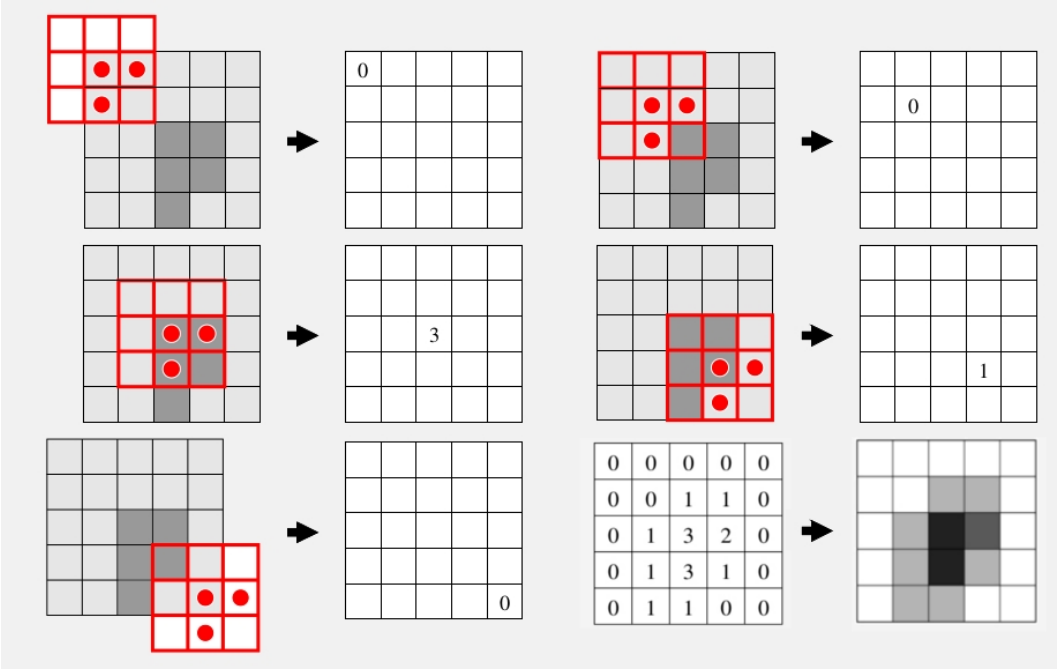

FIGURE 2.7: Image showing the cross correlation shift and add process.

which allowed us to increase the accuracy to 1/20th of a pixel. Interpolation was performed using the CONGRID function in IDL, which allows one to resample an array to an arbitrary size. The expanded images were then individually cross correlated with the template image. Figure 2.8 shows an example of the cross correlated H-band image. The maximum value determines the centre of the image and the number of pixels the image will be shifted by. Once the shift has been performed, the image was returned to its original size using CONGRID.

2.3.6 Calculating the Stokes Parameters

There are two usual methods for determining the Stokes parameters from a dual-beam polarized image. The first is called the ratio method (Tinbergen, 1996) which is less sensitive to flat-field variations and more sensitive to PSF. The second method is called the difference method which behaves in the opposite way to the ratio method. Both methods have been used with adaptive optics (NACO) imaging on the VLT (Quanz

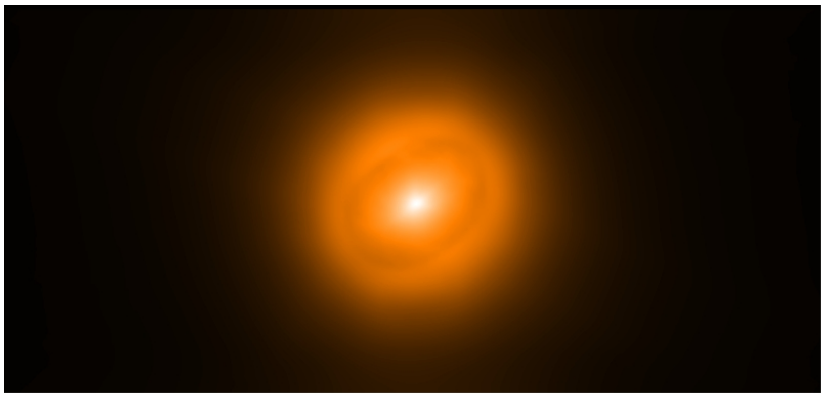

Figure 2.8: Image showing the result of the cross correlation process. The maximum value of the image determines the centre of the image. The image has been expanded by a factor 20 to increase the accuracy of the cross correlation process which results in a 6720 x 1880 image.

et al., 2011, 2013; Canovas et al., 2013). We have opted to use the difference method (Canovas et al., 2011, 2013).

A breakdown of how the Stokes parameters are determined using the extracted O and E images will be examined[4]. Using the half-wave plate position of 0° as an example, we can use Malus' Law, to define the intensities of the O (0°) and E (90°) images:

$$I_0 = I_{\rm p}.\cos^2\phi + \frac{I_{\rm u}}{2}, \tag{2.1}$$

$$I_{90} = I_{\rm p}.\cos^2(90-\phi) + \frac{I_{\rm u}}{2} = I_{\rm p}.\sin^2\phi + \frac{I_{\rm u}}{2}, \tag{2.2}$$

where $I_{\rm p}$ and $I_{\rm u}$ are the polarized and unpolarized intensities of the incoming light and ϕ is the angle between the plane of polarization and a reference direction. The total intensity is defined as the sum of $I_{\rm p}$ and $I_{\rm u}$ and can be determined by:

$$I_0 + I_{90} = I_p.(\cos^2\phi + \sin^2\phi) + I_u = I_p + I_u = I \tag{2.3}$$

The same method can be applied to summing the intensities of the 0° and 45.°0 image. By looking at the difference between the O and E images, we can determine

[4]http://starlink.eao.hawaii.edu/docs/sun223.htx/sun223.html

the Q Stokes parameter.

$$I_0 - I_{90} = I_p.\cos^2\phi - I_p.\sin^2\phi = I_p.\cos 2\phi = Q \tag{2.4}$$

If we examined the half-wave plate positions of 22.°5 and 67.°5 in a similar fashion, we can derive the U Stokes parameter:

$$I_{45} - I_{135} = I_p.\cos^2(45-\phi) - I_p.\sin^2(45-\phi) = I_p.\sin 2\phi = U \tag{2.5}$$

By using the method described above, Polka constructs a cube containing the Stokes parameters I, Q, U. It should be noted that in this thesis, only linear polarization will be examined, therefore the Stokes parameter $V = 0$. The polarized intensity (P_I), polarization angle (P_ϕ) and fractional polarization (P) were generated by using:

$$P_\mathrm{I} = \sqrt{Q^2 + U^2} \tag{2.6}$$

$$P_\phi = \frac{1}{2}\arctan\left(\frac{U}{Q}\right) \tag{2.7}$$

$$P = \frac{P_\mathrm{I}}{I_\mathrm{disc}} \tag{2.8}$$

2.3.7 PSF Subtraction

The intensity image produced by the method described in the previous subsection will include light from both the star and disc. Therefore, the point spread function (PSF) from the target star must be subtracted. This will allow us to produce an intensity image of the light scattered by the disc, which can be used in Equation 2.8 to calculate the polarization of the disc. The method we opted for was the classical PSF subtraction, where a reference star is required. Ideally, the reference star will be located on the sky relatively close to the target star (similar atmospheric effects). The reference star observed was HD 161743, which is a B9IV IR standard star (Elias et al., 1982). Its position ($17^h48^m57^s.92$, $-38°07'07".79$) is not comparable to that of the target star ($18^h24^m29^s.79$, $-29°46'49".22$), however, the air mass was consistent

between the two objects (1.40). We went through the same data reduction procedure as for HD169142 to produce the Stokes images for the unpolarized reference star.

The PSF subtraction process involves subtracting the $I_{\rm ref}$ image from the $I_{\rm target}$ image. However, the observations had different exposure times and therefore, the reference star image required flux scaling. The scaling factor would be the ratio between HD 169142 and HD 161743 at a given radius. The radius chosen was at a position where the disc's emission is not significant (annular gaps seen between 25-30 AU by Quanz et al. (2013); Osorio et al. (2014)). However we were unable to accurately subtract the reference PSF due to various problems. Figure 2.9 shows the I Stokes image for HD 169142 and HD 161743 in the H and $K_{\rm s}$ band. The saturated region was too large and spread over the annular gaps, therefore it was not possible to obtain an accurate scaling factor. An alternative method was to use an iterative process to estimate the scaling factor. This involved a trial and error process of visually inspecting the subtraction from a range of scale factors. However, this method also proved problematic as the 'spider frame' (diffraction pattern from the secondary mirror support) in the H-band images (2.9) has been projected onto the image. As the spider frames are not aligned in the HD 169142 and HD 161743 images, over subtraction results in those areas. The image were also rotated to align the spider frames, however the AO artefacts then became misaligned resulting in higher subtraction residuals in certain areas. In conclusion, it was not possible to obtain a reliable PSF subtraction given the available observational data.

2.4 Instrumental Polarization

As previously described (Chapter 2.3.6), there are two prominent methods to determining the Stokes parameters of a polarized image, these being the ratio method and the difference method. We have opted to use the difference method to determine the Stokes parameters, and this is implemented by the POLKA data reduction software.

As the name suggests, instrumental polarization is polarization which arises due to

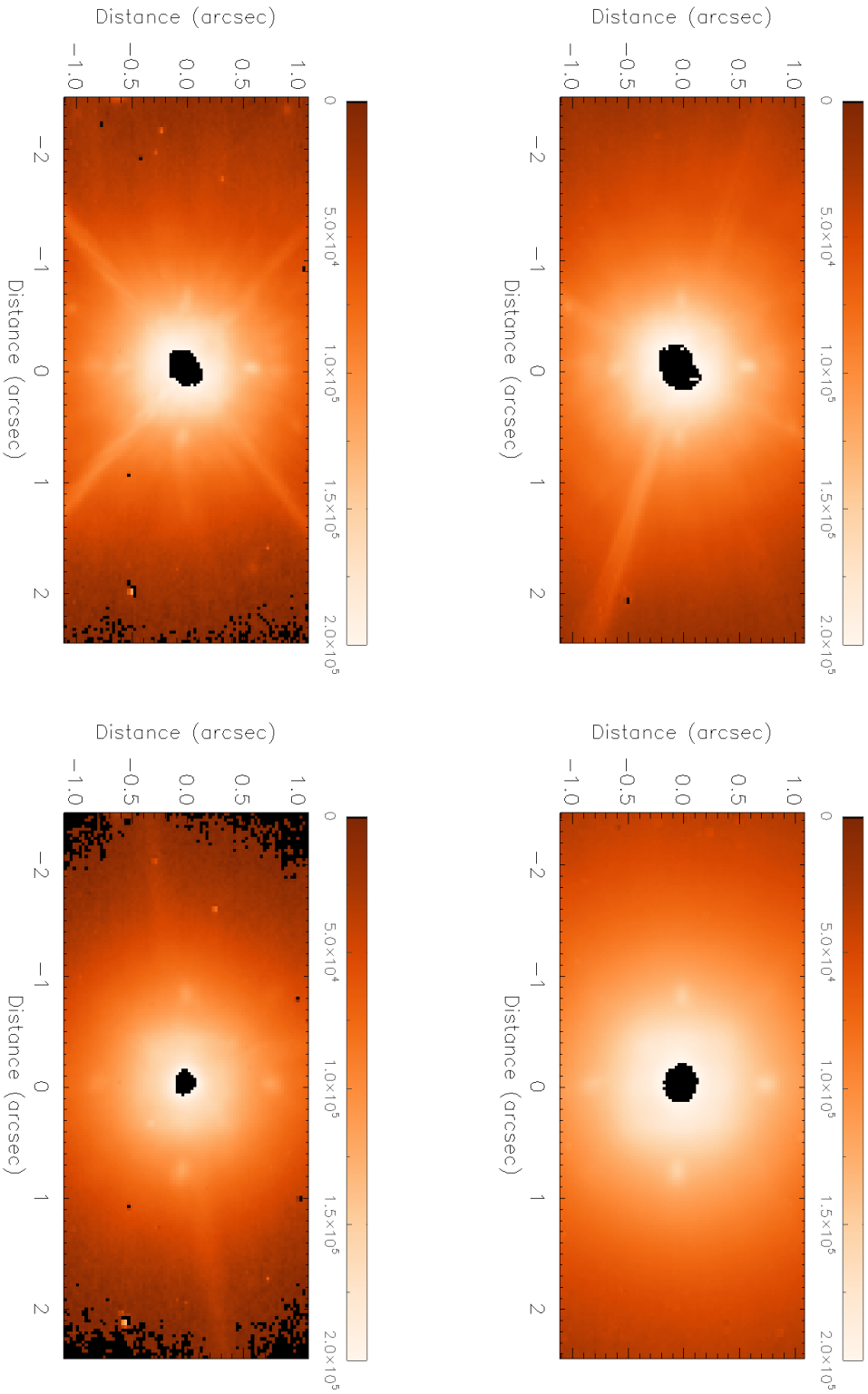

FIGURE 2.9: Final Stokes I images for HD 169142 (top) and HD 161743 (bottom) in the H (left) and K_s (right) band. The central region of the images have been masked out due to saturation of the pixels. The colour bar represents the pixel count.

the instrument. Figure 2.10 shows the Stokes Q and U parameters for the reference star HD161743. Here we see a lack of features which are commonly seen in light scattered due to circumstellar material. There is no butterfly pattern present which implies that any polarization is not due to scattering from a disc. There is also no 45°.0 rotation between the Q and the U image.

Based on lack of features, commonly seen due to circumstellar material, in Figure 2.10, an assumption is made that the polarization seen in HD 161743 is therefore due to the NACO system. The polarization of the incoming light is primarily affected by the metallic coatings of the mirrors within the telescope. Each reflection causes crosstalk between the Stokes parameters, therefore changing their values. For unpolarized light, linear polarization is generated orthogonal to the plane of incidence (Witzel et al., 2011). The magnitude of the polarization depends strongly on the angle of incidence. One way to subtract the instrumental polarization is to firstly determine the polarization produced from an unpolarized target. The polarization here will be solely due to the telescope and can then be subtracted from the Stokes images of the target star.

Figure 2.11 shows the reference star, HD 161743, in polarized light in the H and K_s-band with the polarization vectors plotted on top. Within 1.5", the vectors are aligned at a certain angle (Table 2.3). The image becomes noise dominated at distances greater than $\approx$ 1.5 arcseconds and the vector orientation becomes random. We removed the noisy measurements by requiring that the polarized intensity (PI) in a bin should be greater then its error (i.e. PI $> \sigma_{\mathrm{PI}}$), leaving the regions of aligned vectors. The average polarization and angle was then calculated by binning the remaining polarization vectors into a a single bin. This allowed us to determine the mean polarization and angle due to the telescope, which could be subtracted from the target star. The results are summarized in Table 2.3.

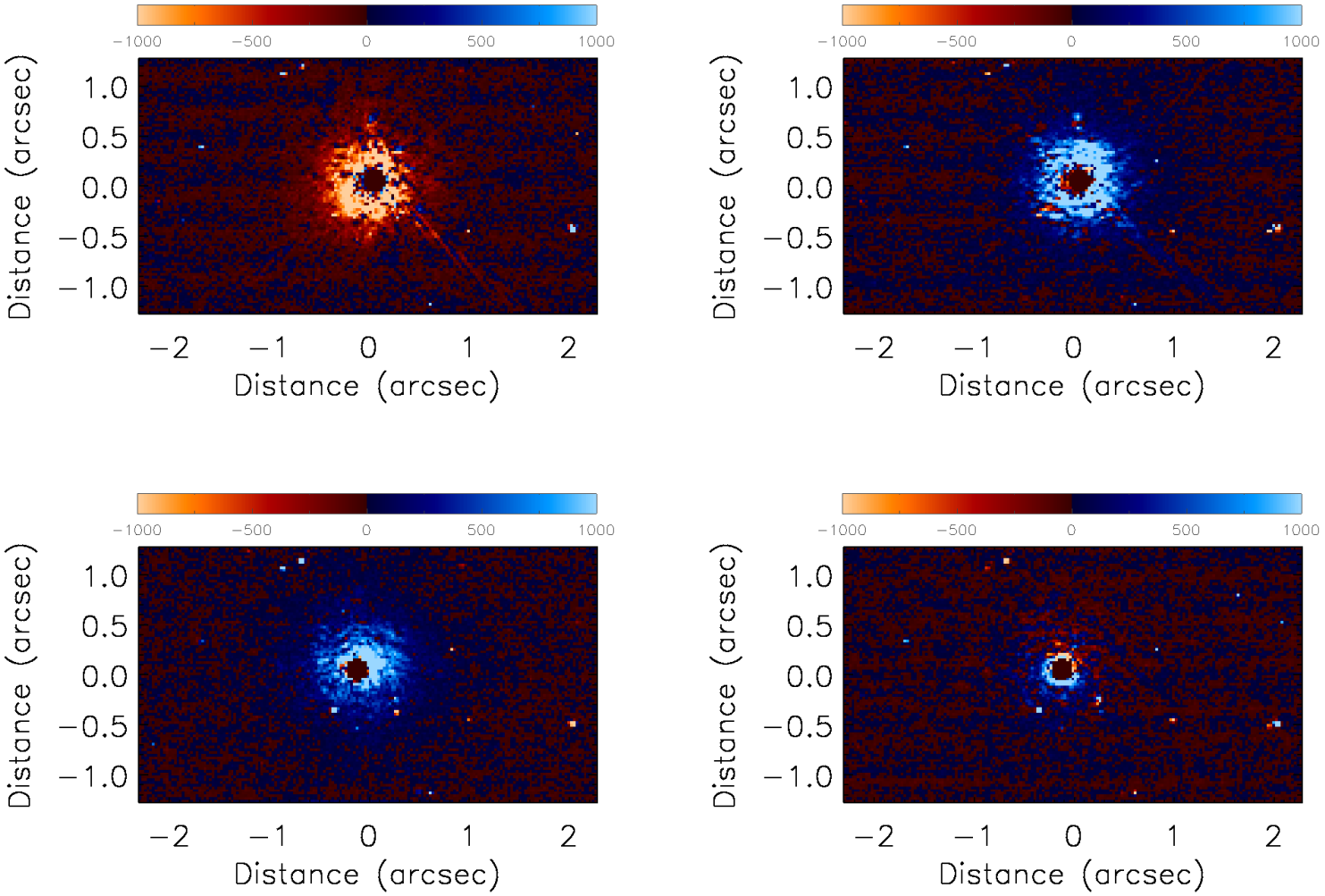

FIGURE 2.10: Final Stokes Q (left) and U (right) images for HD 161743 in the H (top row) and K_s (bottom row). The central regions of the images have been masked out due to saturation of the pixels. The colour bar represents the pixel count.

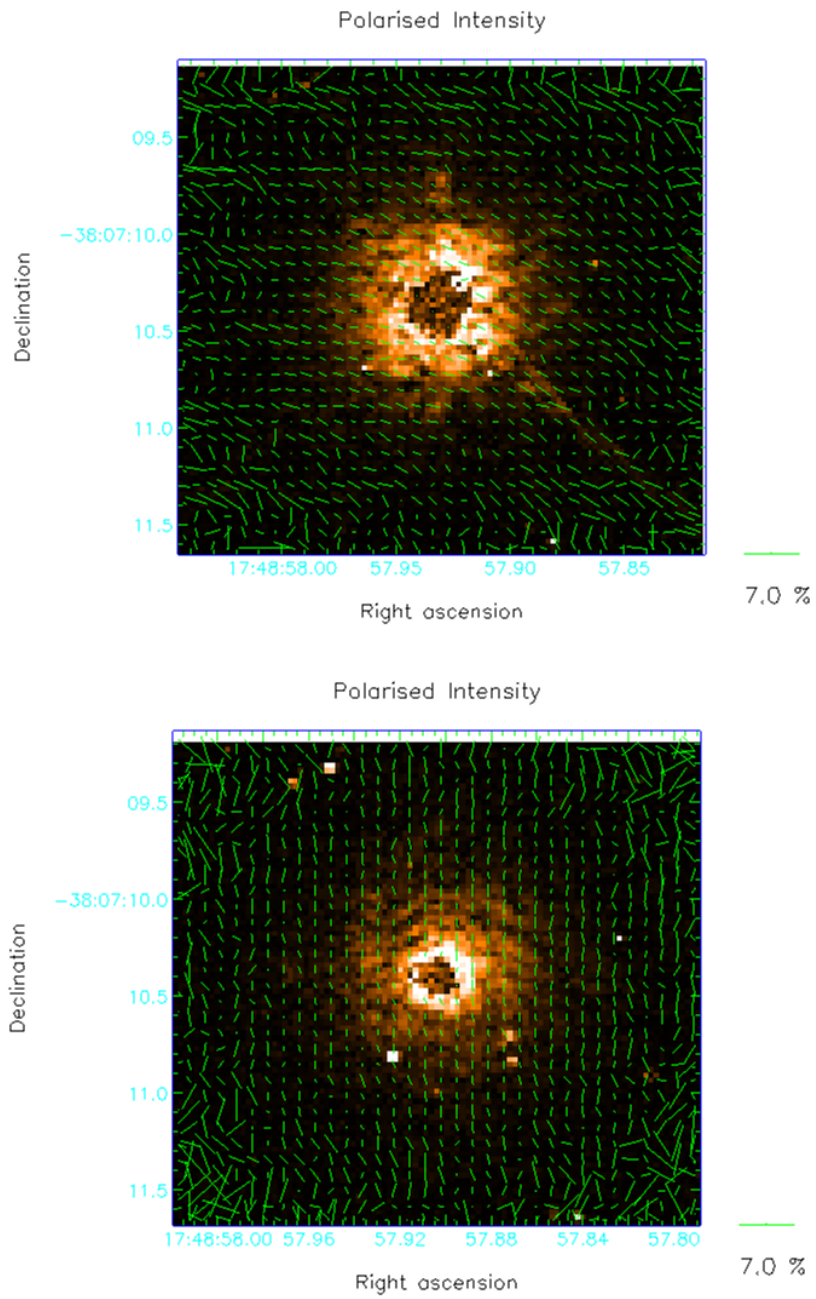

Figure 2.11: Polarized intensity image of the reference star, HD 161743, in the H (top) and K_s-band (bottom) with percent polarization vectors plotted on top. The length of the vectors are proportional to the degree of polarization.

TABLE 2.3: Summary of Instrumental Polarization values from HD161743

Band	Exposure Time (s)	Polarization (%)	Polarization Angle (°)
H	10	1.03	65
K_s	10	0.63	7

2.5 Results and Analysis

2.5.1 Stokes Parameters

After individually cross correlating each O and E image to the template image, the images are then processed through the Starlink package POLKA which produces a Stokes cube. The instrumental polarization is then subtracted from the Stokes cubes. Three Stokes cubes are produced (one for each dither position) and are stacked to increase the signal to noise. This then produces our final Stokes I images for HD 169142 and HD 161743 in the H and K-band (Figure 2.9).

There are several features present in Figure 2.9, which result from the telescope system. The spider frame is clearly visible in all the images and is orientated differently for HD 169142 and HD 161743. In addition to this, AO features can be seen as bright enhancements and radial patterns outside the saturated region. NACO uses the Shack-Hartmann based AO system which is insensitive to a checkerboard like pattern of phase error called 'waffle'. This pattern appears in the reconstructed wave front unless the wave front reconstructor (WFR) removes or attenuates it (Makidon et al., 2005). This pattern can be seen in the K_s-band HD 169142 image, which shows a square pattern around the star.

The Stokes Q and U images for HD 169142 are shown in Figure 2.12. A butterfly pattern is seen in both the Q and U images, which is a feature commonly seen when looking at light being scattered from a star with a distribution of matter surrounding it (can apply to a disc at most inclinations or a spherical shell). The 45°.0 rotation between the Q and the U image suggests a centrosymmetric polarization pattern which is a feature commonly seen in scattering due to a face-on disc (Hales et al., 2006; Apai

et al., 2004; Quanz et al., 2011).

We can further examine the butterfly pattern by plotting the radially averaged azimuthal profile (Figure 2.13) of the Q and U images. The disc has been split into 36 equal size segments to compute the azimuthal variation of the Q and U Stokes parameters. In the plots, each point represents the mean value of the image over the corresponding segment (i.e. radially averaged). The solid line represents the mean value of the entire image. The error bars are the standard deviation over the segment, divided by the square root of the number of images used. We see modulation in the Q and U Stokes parameter confirming the presence of an extended scattering disc (Kuhn, Potter & Parise, 2001).

2.5.2 Polarized Intensity

Figure 2.14 shows the polarized intensity image in the H and $K_{\rm s}$ band. The degree and angle of polarization is plotted over the PI image as vectors, which are binned 3x3 pixels. The length of the vectors are proportional to the degree of polarization. The polarization vectors were selected on the criteria that the polarized intensity $P_I > \sigma_{PI}$. The polarization vector pattern of the disc is almost centrosymmetric, indicating a nearly face on geometry, which is consistent with the sub-mm observations (Raman et al., 2006) as well as with the low $v.\sin(i) = 55$ kms^{-1} of HD169142 determined by Dunkin, Barlow & Ryan (1997a).

2.5.3 Polarization

The degree of polarization is a key tool in determining the size and properties of the dust grains in the disc. However, since we were unable to subtract the PSF due to the star, we can only obtain a lower limit on P. Figure 2.15 shows the azimuthally averaged percent polarization.

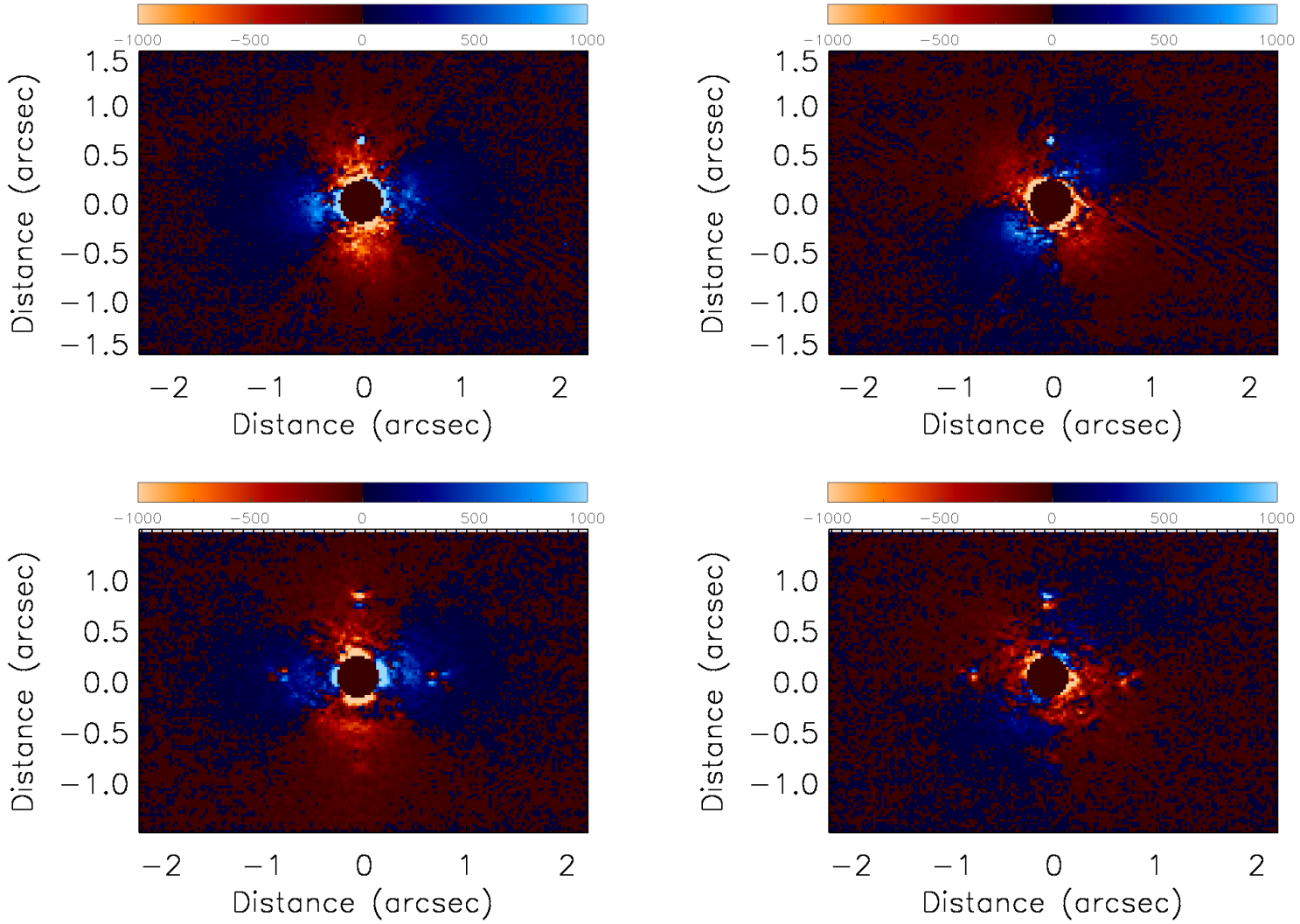

FIGURE 2.12: Final Stokes Q (left) and U (right) images for HD 169142 in the H (top row) and K_s (bottom row). The central regions of the images have been masked out due to saturation of the pixels. The colour bar represents the pixel count.

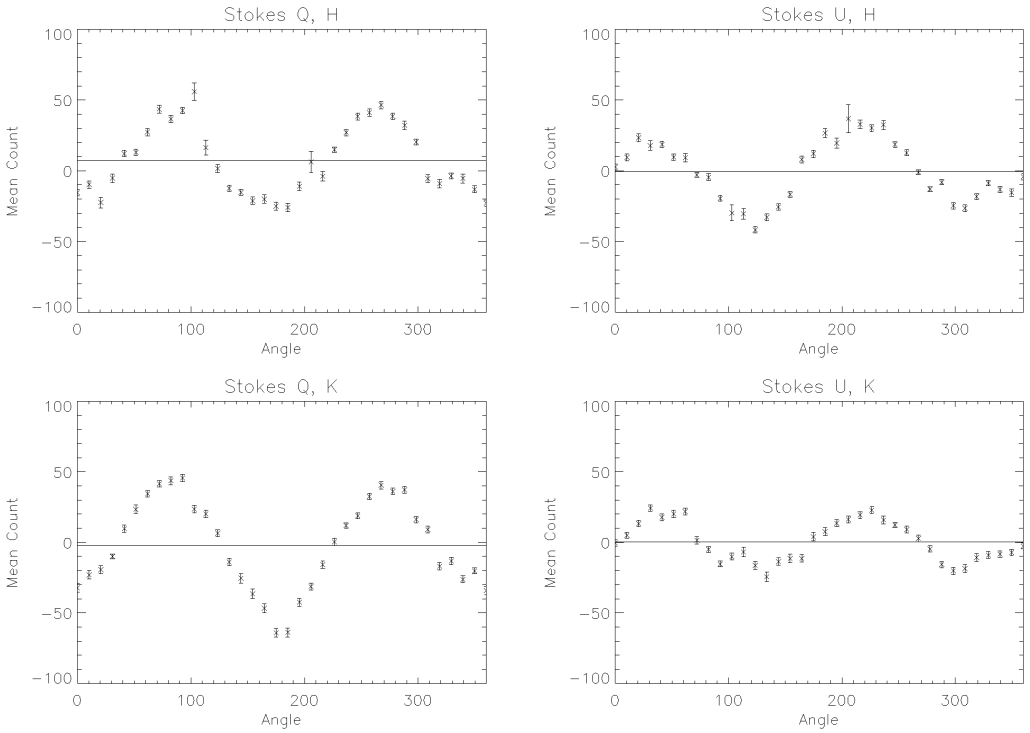

Figure 2.13: Azimuthal variation of the Q and U Stokes parameters for the H-band (top) and K_s-band (bottom). This shows modulation of Q and U with azimuthal angle which is expected for tangential polarization vectors (Apai et al., 2004)

Figure 2.15 shows a maximum polarization of 2 percent in the H-band and 1 percent in the K_s. Previous J-band imaging polarimetry (Hales et al., 2006) found the maximum polarization to be ≈ 2 percent. It should be noted that Hales et al. (2006) did not perform a PSF subtraction. One element which would be commonly seen in circumstellar discs is carbon (refer to Chapter 1.1.4) and for spherical, micron size carbon grains, the polarization would be expected to peak at ≈ 90 degrees at 45 percent polarization in the IR. However, a maximum of ≈ 2 percent is seen in the H-band and a maximum of ≈ 1 percent is seen in the K_s-band. For a face on flared disc, scattering angles close to 90° would be expected. This suggests significant dilution of the intrinsic disc polarization by the overlaying unpolarized PSF.

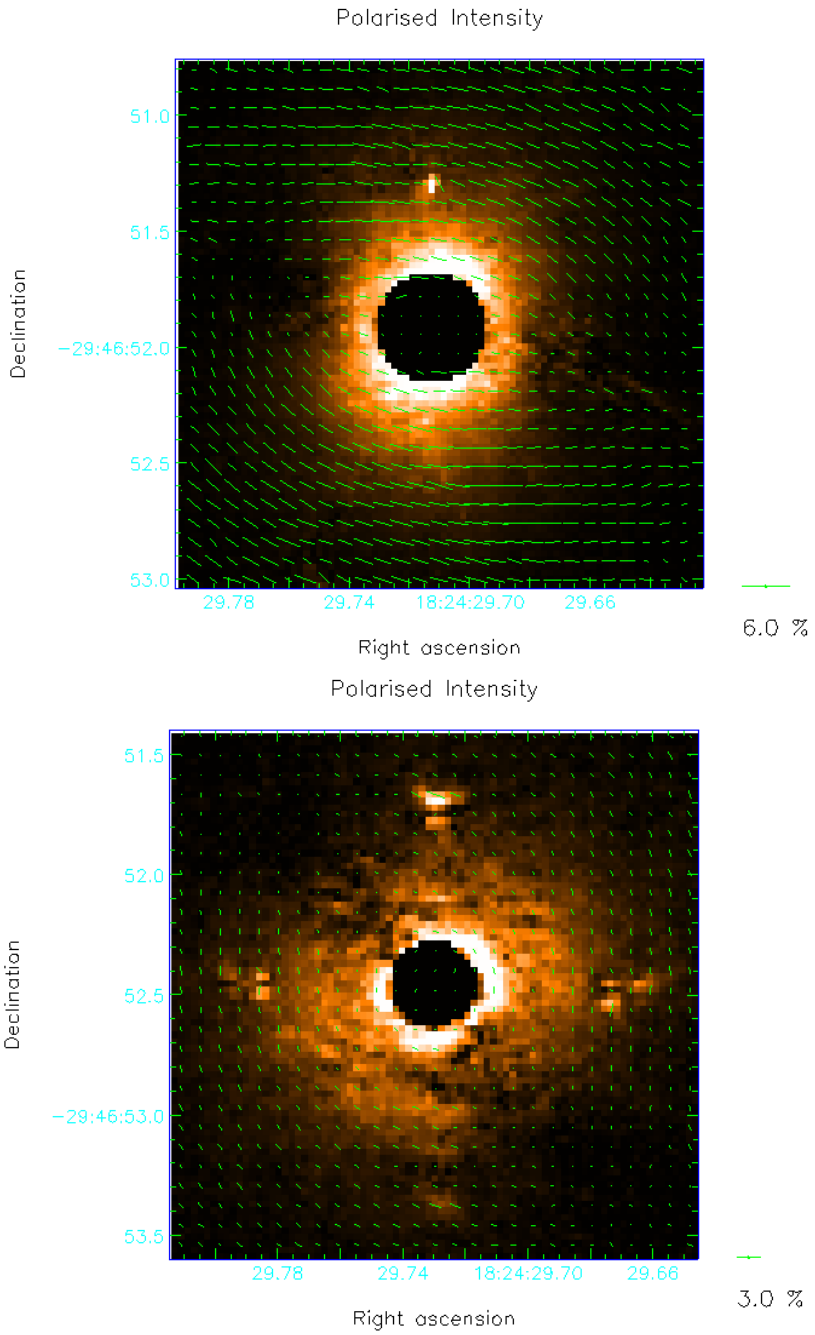

FIGURE 2.14: Polarized intensity images in the H (top) and K_s (bottom) bands. The polarization angles (P_ϕ) are shown by the vectors. Artefacts from the adaptive optics systems and spider are also present in the PI image.

2.5.4 Surface Brightness Profiles

Figure 2.16 shows the azimuthally averaged surface brightness profile (SBP) in polarized light. The disc is split into evenly spaced annuli (2 pixels wide) and each point

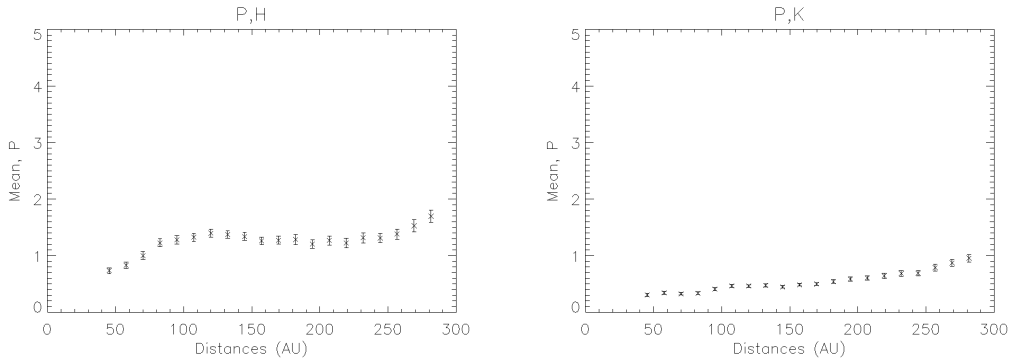

Figure 2.15: Azimuthally averaged percent polarization for the H (left) and K_s (right) bands

represents the mean value within the corresponding annulus. The artefacts seen in Figure 2.14 have been masked out before the annular averaging was computed. Single and split power laws are fitted to the data (summary is given in Table 2.5), where 1-sigma error bars are given. The errors are calculated as the standard deviation of the pixel values within the annulus, dived by the square root of the number of contributing pixels.

A broken power law SBP fit is quite common in scattered light images of debris discs (i.e. AU Mic (Fitzgerald et al., 2007), β Pic (Krivova, Krivov & Mann, 2000)). This could be due to variations in grain size due to the smaller grains being blown out to the outer part of the disc, while the inner disc retains the larger grains (Augereau et al., 2001; Liu, 2004). A broken power law is also seen to provide a better fit to the H-band polarimetric observations performed by Quanz et al. (2013). We therefore fit the single power law between 85-250 AU and the split power law between the regions of 85-120 AU and 120-250 AU. The values we obtain from our fitting (85-250 AU: -2.69 ± 0.02, 85-120 AU: -1.76 ± 0.14, 120-250 AU: -2.65 ± 0.03) do not match the previously obtained profiles from Quanz et al. (2013). They found a SBP exponent of -3.31 ± 0.11 for a single power law between $85 - 250$ AU. Using a split power law, they obtain a SBP exponent of $-2.64^{+0.15}_{-0.17}$ and $-3.90^{+0.10}_{-0.11}$ between $85 - 120$ AU and $120 - 250$ respectively.

Grady et al. (2007) finds a SBP, for the observed surface brightness (I) in scattered light, to be $\propto r^{-3\pm0.1}$ at 1.1 μm from $60 - 200$ AU. This result is also consistent with

the H-band scattered light observations taken by Fukagawa et al. (2010), who finds a SBP $\propto r^{-3.4\pm0.4}$ between $120 - 200$ AU. Overall, our power law fits are found to be shallower than the fits produced by Grady et al. (2007); Fukagawa et al. (2010); Quanz et al. (2013). This could be due to the over saturation of the PSF of the central star spreading further out into the disc.

The K_s-band observations of HD169142 in scattered light were the first performed in the wave band. Therefore there are no prior observations to compare out results to. The values we obtain from our fitting are as follows: 85-250 AU -2.45 ± 0.02, 85-120 AU: -2.35 ± 0.10, 120-250 AU: -2.38 ± 0.03). However, the K_s-band observations suffered greater waffle patterns due to the AO system (more prominent waffle pattern than seen in the H-band).

2.5.5 Radial Stokes Parameter Images

Another method to calculate the errors is to use the radial Stokes parameters. After producing the Stokes Q and U images, one is able to determine the radial Stokes parameters:

$$Q_r = +Q.\cos 2\phi + U.\sin 2\phi \tag{2.9}$$

$$U_r = +Q.\cos 2\phi - U.\sin 2\phi \tag{2.10}$$

where

$$\phi = \arctan\frac{x - x_0}{y - y_0} \tag{2.11}$$

ϕ is the polar angle of position (x, y) on the detector and (x_0, y_0) is the central position of the star. For a purely centrosymmetric pattern, Q_r is equivalent to PI and U_r should be zero (Schmid, Joos & Tschan, 2006; Quanz et al., 2013). Assuming that the removal of polarization due to the instrument was performed correctly, U_r can be

Table 2.4: Summary of the FWHM

Band	x-axis (pixels)	y-axis (pixels)
H	20.44	17.43
$K_{\rm s}$	13.17	11.20

used to estimate the errors on $Q_{\rm r}$:

$$\Delta Q_r = \frac{\sqrt{(\sigma^2_{U_r})}}{\sqrt{n_{\rm res}}} \tag{2.12}$$

ΔQ_r is the 1σ uncertainty on $Q_{\rm r}$, $\sigma^2_{U_r}$ is the variance on $U_{\rm r}$ and $n_{\rm res}$ is the number of resolution elements. The number of resolution elements can be determined by calculating the full width half maximum (FWHM), which can be seen in Table 2.4, of the PSF of HD169142. We have used this method to compute errors on the power laws which are summarized in Table 2.5.

2.6 Discussion

HD169142 is a well observed disc, with several previous observations having been conducted. The most recent of these observations were reported in Quanz et al. (2013) (IR polarimetric imaging) and Osorio et al. (2014) (7mm imaging), who revealed many sub-structures in the disc. The first structure they observe is a 'hole' devoid of dust within 20 AU of the disc. We are unable to observe this feature as the saturation of our images extends to approximately 30 AU. The saturated region also covers the ring like structure Quanz et al. (2013); Osorio et al. (2014) see at approximately 25-30 AU. The final structure which Quanz et al. (2013) sees is an annular gap between 40 and 70 AU. This annular gap is also confirmed by 7 mm VLA observations (Osorio et al., 2014). However, our observations do not show these structures. Large exposure times were used to increase the signal to noise in the outer disc at the cost of saturating the central region, so that, a large fraction of the inner disc was lost. In all cases, the

TABLE 2.5: Summary of the Power Law fits

Band	Inner Radius (AU)	Outer Radius (AU)	Power Law Exponent	Power Law Exponent (Radial Stokes)	Quanz et al. (2013)
H	85	250	-2.69 ± 0.02	-2.67 ± 0.06	-3.31 ± 0.11
	85	120	-1.76 ± 0.14	-1.76 ± 0.24	$-2.64^{+0.15}_{-0.17}$
	120	250	-2.65 ± 0.03	-2.74 ± 0.10	$-3.90^{+0.10}_{-0.11}$
K_s	85	250	-2.45 ± 0.02	-2.45 ± 0.07	-
	85	120	-2.35 ± 0.10	-2.27 ± 0.30	-
	120	250	-2.38 ± 0.03	-2.46 ± 0.12	-

saturated region extends into the second annular gap.

Deconvolution was attempted with the Lucy-Richardson (Richardson, 1972; Lucy, 1974) method algorithm in IRAF and with the convolve routine in IDL. However, both methods failed due to the standard star being affected by the waffle pattern. An attempt was made to use the stars surrounding the target star, however a suitable star was not found. This also meant that PSF subtraction was not possible, preventing an intrinsic value of P from being calculated. So unfortunately the observations were not of sufficient quality to reveal structure in the disc due to over exposure and saturation. The observations of HD169142, by Quanz et al. (2013), were also performed on the VLT with the NACO instrument. However, they used a much smaller exposure time (1 second) with 15 Ndits and 3 dither positions. While this only resulted in a total integration time of 45 seconds, their observations suffered a minimal amount of saturation due to the central star. In addition, there was no waffle pattern present in their observations.

Similar to the analysis performed by Quanz et al. (2013), both a broken and single power law SBP are examined. Quanz et al. (2013) find that a broken power law provides the best fit to their H-band observations. A broken power law was also applied to our observations to confirm Quanz et al. (2013) results, however our SBP does not match the previous results (Table 2.5) within errors.

The annular gaps observed by Quanz et al. (2013); Osorio et al. (2014) are not completely void of dust. However, they do indicate either shadowing due to the bright inner rim or clearing due to a planetary body. Biller et al. (2014) detected a faint point like source at approximately 0.11 arcsec (16 AU) at PA $\approx 0°$. While it doesn't lie within the 40-70 AU gap, it may be responsible for the clearing of the dust within the inner ring. Reggiani et al. (2014) have also detected a source at 22.7 ± 4.7 AU at PA $= 7.4° \pm 11.3°$. They also do not exclude the possibility of a second object within the 40-70 AU gap.

Unfortunately, the observations of HD169142 were unable to resolve any features (i.e. annular gaps) previously observed. Therefore, we decided to explore modelling the disc via Monte Carlo simulations to examine what disc structure and composition

would be required to produce the observed features. Before these simulations could be performed, a radiative transfer code must be chosen. The radiative transfer code we used will be examined in Chapter 3.

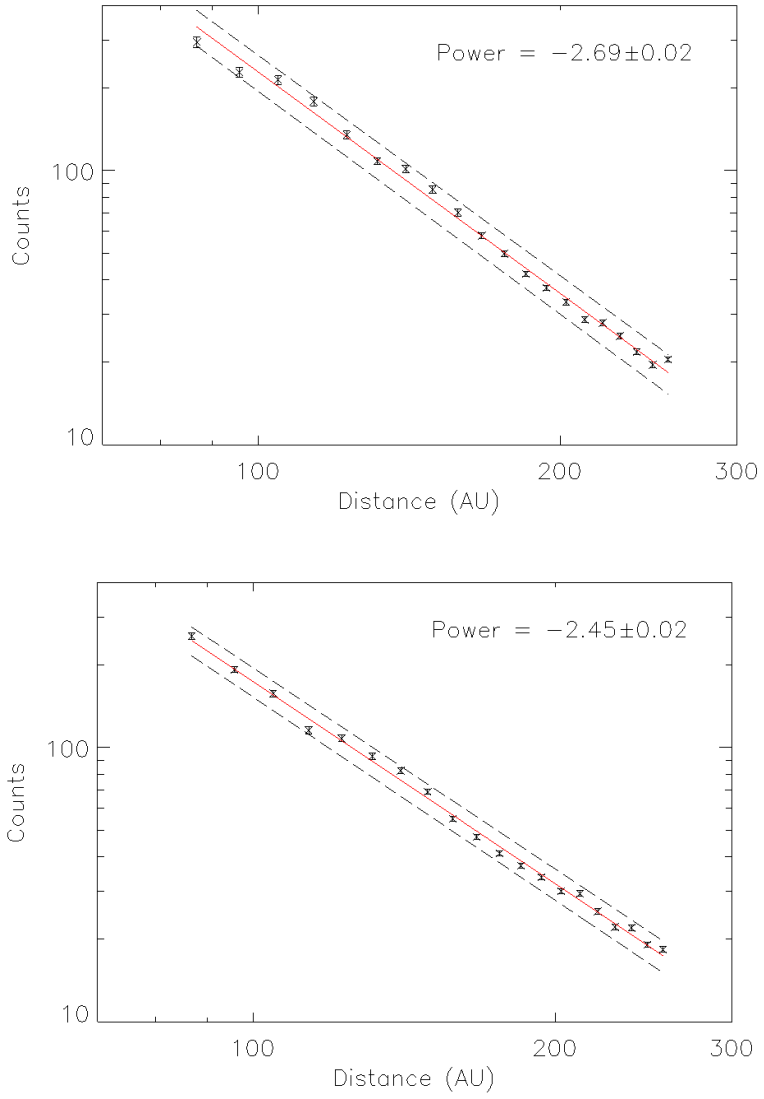

Figure 2.16: Radially averaged SBP of HD 169142 in polarized light for the H (top) and K_s (bottom) bands.

3

Hyperion

Monte Carlo simulation is a technique used to approximate the probability of certain outcomes by running multiple trials using randomly selected variables from a given distribution. In the case of light scattering from dust, radiative transfer simulations are used as they allow one to follow photons as they are scattered and absorbed within a medium defined by the user. Individual photon packets (now referred to as photons) originate at a source and travel through a medium in which the parameters of interest for each interaction are recorded. The parameter value on exit will converge to a mean when a significant number of photons are used and will therefore become statistically meaningful (Whitney, 2011). This allows one to solve the problem of radiative transfer through random sampling of probability distribution functions (pdf) rather than solving the equations directly.

3.1 Hyperion - v.0.9.4

HYPERION (Robitaille, 2011) is an open-source 3-D dust continuum Monte-Carlo radiative transfer code that is designed to be as generic as possible, allowing radiative transfer to be computed through a variety of three-dimensional grids (Cartesian, spherical or cylindrical polar, or adaptive Cartesian grids). HYPERION can compute dust temperatures, SEDs, images, and polarization maps. The code is split into two parts:

- The first part of the code consists of a Python library. These libraries allow one to create a single input file to define the model. The libraries include arbitrary three-dimensional density structures and pre-defined analytical density structures such as flared disks and ambient mediums. Post-processing tools to retrieve the observables (SEDs and images) and physical quantities (density and temperatures) are also included in the libraries.

- The second part is implemented in Fortran 95/2003 and carries out the core of the radiative transfer calculation. It takes the input file (which was set-up in the previous step) and runs the Monte-Carlo radiative transfer code to compute temperatures, SEDs, and images.

3.1.1 Dust Modelling

The dust properties read in by Hyperion are located in a Hierarchical Data Format (HDF5). In order to construct these files, the optical properties, such as the albedo, opacity and emissivities of the dust grains must first be calculated.

Hyperion has the option to use a wrapper[1] which allows one to compute dust scattering properties for spherical particles using the BHmie code (Bohren & Huffman, 1983) (modified by Bruce Draine[2]). The wrapper uses a single parameter file to compute the scattering properties of the dust grains. Within this parameter file, refractive index data for one or more chemical components can be defined.

[1] https://github.com/hyperion-rt/bhmie

[2] ftp://ftp.astro.princeton.edu/draine/scat/bhmie/bhmie.f

It is possible to define the dust particle size distribution in three ways. The first is a simple power law distribution, in which the number of particles is $\propto a^q$, where the power law (q) of the size distribution, a minimum ($a_{\rm min}$) and a maximum radius need to be defined. The second is a power law distribution with an exponential cutoff, in which the number of particles is $\propto a^q \exp(-a/a_{\rm turn})$ where a is the minimum size and a turn off size ($a_{\rm turn}$) for the distribution and a power of the size distribution must be defined. The final method is to define a two column ASCII table containing the relative number of grains as a function of size. The wrapper will then output the frequency dependent albedo (ω_ν), mass extinction coefficient (χ_ν) and the scattering matrix elements.

Once the optical properties of the dust grains have been determined, one can then begin to construct the HDF5 file. Hyperion has a number of built in procedures to aid in the construction of the HDF5 file. The procedure that will be used for spherical grains will be 'BHDust'. This works in conjunction with the BHMie wrapper to produce the HDF5 file.

Mueller Matrix

Currently, Hyperion supports scattering from spherical grains which are described by a Mueller matrix with four independent non-zero elements (van de Hulst, 1957; Bohren & Huffman, 1983):

$$\begin{pmatrix} I \\ Q \\ U \\ V \end{pmatrix}_{scattered} = \begin{pmatrix} S_{11} & S_{12} & 0 & 0 \\ S_{12} & S_{11} & 0 & 0 \\ 0 & 0 & S_{33} & -S_{34} \\ 0 & 0 & S_{34} & S_{33} \end{pmatrix} \begin{pmatrix} I \\ Q \\ U \\ V \end{pmatrix}_{incident} \tag{3.1}$$

Dust Sublimation

The sublimation of dust particles occurs as they reach a certain temperature. In circumstellar discs, dust grains would spiral into the star due to Poynting-Robertson drag (PR drag) and sublimate as they approach the star and heat up. Therefore, dust grains beyond the sublimation radius would also experience some depletion due

to sublimation. However, Hyperion does not consider PR drag and sublimation will only occur with grains in the immediate vicinity of the star. Hyperion allows three type of dust sublimation modes:

- complete removal of the dust from cells exceeding the sublimation specific energy/temperature
- reduction of the dust density in cells exceeding the sublimation specific energy/temperature.
- the specific energy/temperature is capped to the maximum value with out any change to the dust density.

The dust models computed in Hyperion were set to capping the specific energy/temperature to a maximum value of 1500K (Kama, Min & Dominik, 2009) with out any change to the dust density. This was used from here on out.

Vertical Gas and Dust Structure

Omitting external sources, circumstellar discs are heated by the central star and as a result, the vertical structure will determine how much radiation is intercepted by the disc. As previously mentioned, observation of discs in scattered light and SED observations have shown that discs are not geometrically flat and can have an associated thickness/flaring to them. The height was suggested to be result of the disc being in hydrostatic equilibrium (Kenyon & Hartmann, 1987; D'Alessio et al., 2006). If we consider gas within the disc at radius r and height z above the midplane then (Dullemond & Dominik, 2004):

$$g_z = \frac{GMz}{r^3} = \Omega_k^2 z \tag{3.2}$$

where g_z is the gravitational acceleration in the z-direction, G is the gravitational constant, M is the mass of the star and Ω_k is the Keplerian frequency. This also

assumes a negligible radiation pressure and that the gas is on a Keplerian orbit. For the disc to be in equilibrium, g_z must be equal to the pressure gradient:

$$\frac{dp}{dz} = -\rho g_z \tag{3.3}$$

where p is the pressure and ρ is the gas density. Using the equation of state for an ideal gas ($p = \rho c_s^2$) allows us to rearrange the equation to:

$$\frac{d\rho}{\rho} = -\frac{\Omega_k^2}{c_s^2} z dz \tag{3.4}$$

where c_s^2 is the speed of sound and Ω_k^2 is the Keplerian angular velocity. This can then be integrated to find the vertical pressure and density structure in the disc. If there is no vertical temperature gradient, then we obtain an isothermal vertical structure with a constant vertical scale height:

$$\rho = \rho_0 \exp\left(-\frac{z^2}{2H^2}\right) \tag{3.5}$$

where ρ_0 is the normalization constant and H is the pressure scale height (c_s/Ω_k). Using $c_s = (kT/\mu m_H)^{1/2}$ and $\Omega_k = (GM_*/r^3)^{1/2}$, the scale height can be defined as (D'Alessio et al., 1998):

$$\frac{H}{r} = \left[\frac{kTr}{GM_*\mu m_H}\right]^{1/2} \tag{3.6}$$

where k is the Boltzmann constant, μ is the mean molecular weight and m_H is the mass of Hydrogen. If we have a typical temperature profile for an irradiated disc of $T \propto r^{-1/2}$, then $c_s \propto r^{-1/4}$ (D'Alessio et al., 1998; Dullemond et al., 2007) so that:

$$\frac{H}{r} \propto r^{1/4} \quad \text{or} \quad H \propto r^{5/4} \tag{3.7}$$

By using the above definition of Ω_k, we can also define the scale height as (Kenyon & Hartmann, 1987):

$$\frac{H}{r} = \left(\frac{c_s^2 r}{GM_*}\right)^{1/2} \tag{3.8}$$

If the internal temperature of the disc $T \propto c_s^2$ falls off more slowly than r^{-1}, then the thickness of the disc will increase with radius. It is estimated that internal disc temperature of passive processing or active accretion flat discs is $T \propto r^{-3/4}$ (Adams, Lada & Shu, 1987). Since the disc was assumed to be vertically isothermal, the surface temperature will be the same as the interior and therefore the scale height $H \propto r^{9/8}$ (Kenyon & Hartmann, 1987).

It has been shown through analytical and 1D modelling (Dullemond & Dominik, 2004) that the grain settling time scale may exceed the lifetime of the disc. However, they also show that small grains (0.1 μm) can settle down to a few pressure scale heights in much less time which will result in the disc becoming flatter (this will then reduce the flaring index of the disc from the values 5/4 and 9/8).

3.1.2 Disc Structure

The disc density is defined in Equation 3.9 and 3.10. It is a flared axisymmetric disc which is described as follows:

$$\rho(R, z, \phi) = \rho_0 \left(\frac{R_0}{R}\right)^{\beta - p} \exp\left[-\frac{1}{2}\left(\frac{z}{h(R)}\right)^2\right] \tag{3.9}$$

where

$$h(R) = h_0 \left(\frac{R}{R_0}\right)^{\beta} \tag{3.10}$$

where ρ_0 is the scale factor for the disc density (g cm^{-3}), p is the surface density power-law exponent, β is the scaleheight power law exponent, h_0 is the scaleheight at R_0 and R_0 is the radius at which h_0 is defined. The structure of the flared disc model is shown in Figure 3.1 by using the parameters in Pascucci et al. (2004) benchmark as an example.

Table 3.1 summarises the dust and disc parameters used for the initial tests of Hyperion. These values were taken from Pascucci et al. (2004) who designed a benchmark test for three Monte Carlo Radiative Transfer codes. The disc is made up of spherical

Table 3.1: Input parameters for the Pascucci et al. (2004) benchmark test

Parameter	Value
Stellar Mass	1 $M_\odot$
Stellar Radius	1 $R_\odot$
Effective Temperature	5800 K
Disc Radius Range	1-1000 AU
h_0	125 AU
R_0	500 AU
Disc Flaring parameter (β)	1.125
Surface Density exponent (p)	0.125
Disc Mass	1.1×10^{-6} $M_\odot$
Minimum grain size (μm)	0.12
Maximum grain size (μm)	0.12
Number of different grain sizes	1
Number of scattering angles	181
Number of extra fine scattering angles	10
Number of chemical components	1
Gas to dust ratio	0
Wavelength range (μm)	0.01-1000
Number of different wavelengths	250
Mass fraction of the chemical components	1
Density of the grains in (g cm^{-3})	3.6

astronomical silicate grains whose optical properties are determined by (Draine & Lee, 1984).

As a sanity check, a comparison between the disc model produced by Pascucci et al. (2004) and the disc model produced in Hyperion was made to ensure that both Radiative transfer codes produced the same disc. Figure 3.1 shows that the two radiate transfer codes differ slightly in structure. This is due to the difference in how the density

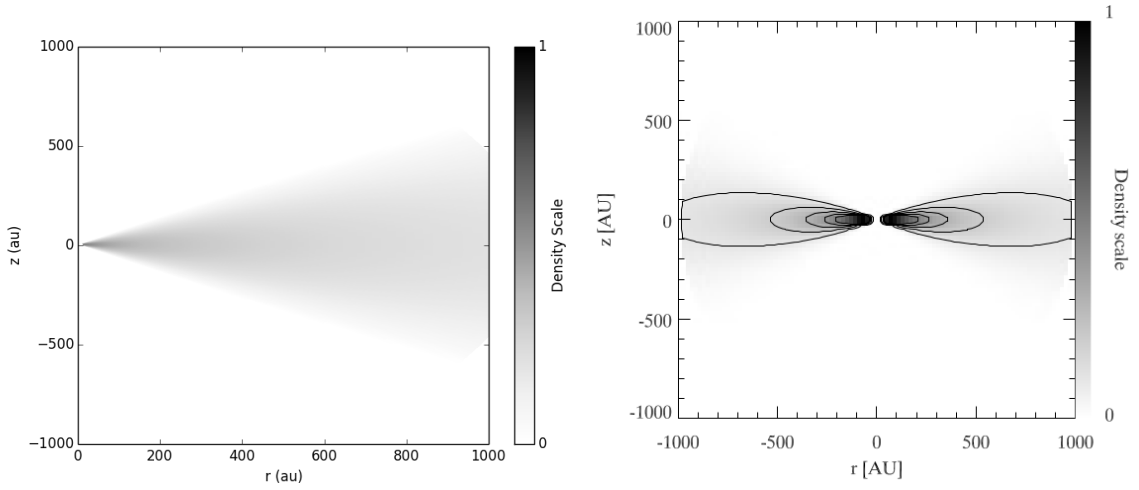

FIGURE 3.1: Left: Disc density structure for a flared disc created in Hyperion. The dust grain parameters can be seen in Table 3.1. Right: The disc density structure made by Pascucci et al. (2004). The contours shown provide 0.10, 0.19, 0.28, 0.38 and 0.48 percent of the maximum.

structure is defined. Pascucci et al. (2004) define their flared disc as:

$$\rho(R, z, \phi) = \rho_0 \left(\frac{R_0}{R}\right)^{-1.0} \exp\left[-\frac{\pi}{4}\left(\frac{z}{h(R)}\right)^2\right] \tag{3.11}$$

where

$$h(R) = h_0 \left(\frac{R}{R_0}\right)^{1.125} \tag{3.12}$$

Tests by Robitaille (2011) show that temperature and SED comparison between the Pascucci et al. (2004) disc benchmark and Hyperion are within the dispersion of the results from those conducted by Pascucci et al. (2004).

3.1.3 Optimization

First Forced Scattering

Photons in optically thin regions will struggle to interact with the surrounding medium. The majority of the photons will leave the region without any interaction, resulting in low signal to noise (S/N) in the final image. One method to increase the S/N

is to increase the number of photons, therefore increasing the probability of an interaction. This, however, becomes computationally expensive and time consuming. A method, called first forced scattering (proposed by Mattila (1970) and refined by Wood & Reynolds (1999)) forces an emitted photon to scatter. This is not an arbitrary process as each photon's energy is weighted according to the probability of scattering before escaping the grid:

$$W = 1 - \exp(-\tau_{escape}) \tag{3.13}$$

where τ_{escape} is the optical depth for a photon to escape the system. The photon is then forced to scatter at an optical depth less than τ_{escape}, sampled from:

$$\tau_{scatter} = -\ln[1 - \eta(1 - \exp(-\tau_{escape}))] \tag{3.14}$$

where η is a random number sampled uniformly from the range 0 to 1. Therefore each photon will travel an optical depth of $\tau_{scatter}$ and scatter. From here, a new scattering angle and optical depth are calculated and the photon path is tracked until it leaves the grid. If $\tau_{scatter}$ is outside the grid, then the photon is terminated. As an example, Figure 3.2 shows a scattered light image of a constant density sphere consisting of just silicate grains. The parameters are described in Table 3.2.

Table 3.2: Input parameters for the forced first scattering test

Parameter	Value
Stellar Mass	1 $M_\odot$
Stellar Luminosity	1 $L_\odot$
Effective Temperature	5800 K
Disc Radius Range	1-100 AU
Density of the grains in (g cm^{-3})	3.6

Figure 3.2 shows a comparison between forced first scattering enabled and disabled. The comparison shows that with forced first scattering enabled, every photon scatters

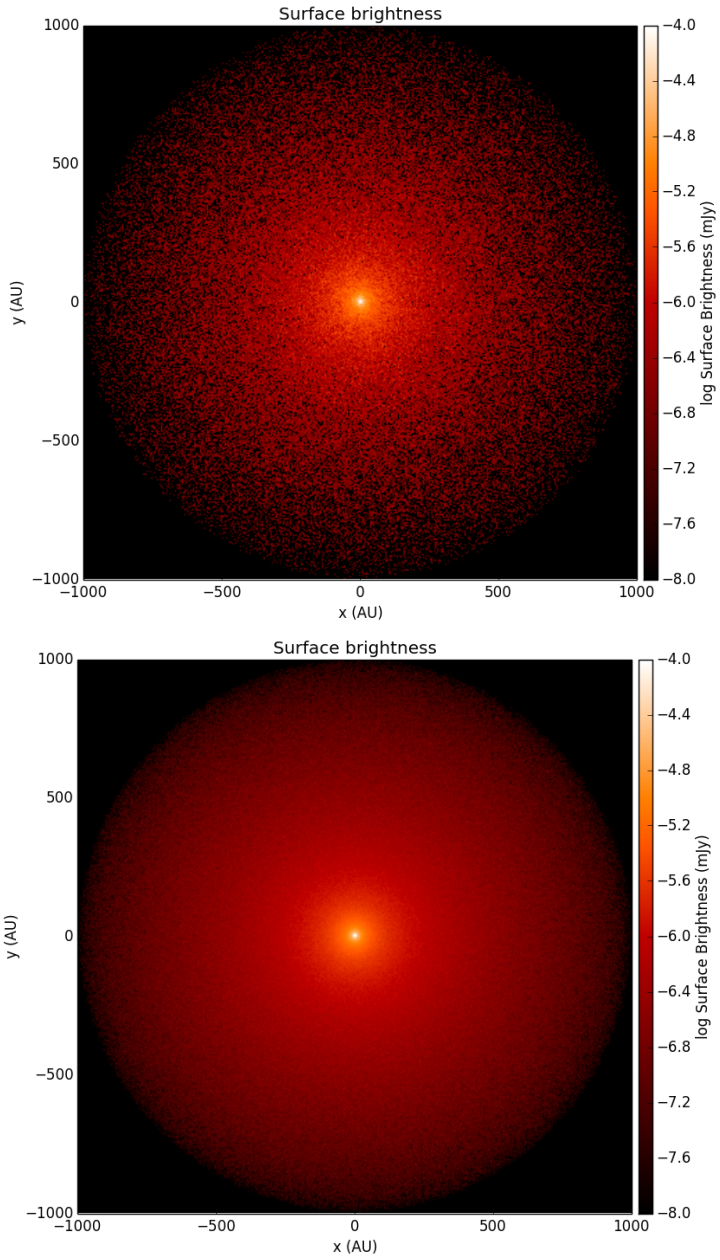

FIGURE 3.2: Scattering within a constant density sphere. Both models contain the same density of grains, but the bottom image has forced first scattering enabled while the top image has it disabled.

and the resulting image has a higher S/N ratio then with it being disabled.

Partial Diffusion Approximation (PDA)

In very high density regions, the number of interactions a photon will make before leaving the grid will be very high. It scales 'super-linearly' (Robitaille, 2011) with density making radiative transfer calculations for high density regions very time consuming and computationally expensive. Another problem which occurs is the statistical noise produced in regions optically shielded (midplane region) from radiation (Min et al., 2009). One method to deal with this problem is to define the energy transport by radiative diffusion. This will only be valid for cases where the photon's mean free path is much smaller than the length scale over which density and temperature change. The general form of the diffusion equation is defined as (Rosseland, 1924; Wehrse, Baschek & von Waldenfels, 2000; Min et al., 2009):

$$\nabla \cdot (D \nabla E) = \frac{1}{c} \frac{\partial E}{\partial t} \tag{3.15}$$

where E is the local energy density, c is the speed of light and D is the diffusion coefficient. Figure 3.3 shows a comparison between temperature maps with PDA being enabled and disabled. The disc parameters for the PDA test are summarized in Table 3.1. This model was tested with a initial photon count of 1×10^7 photons.

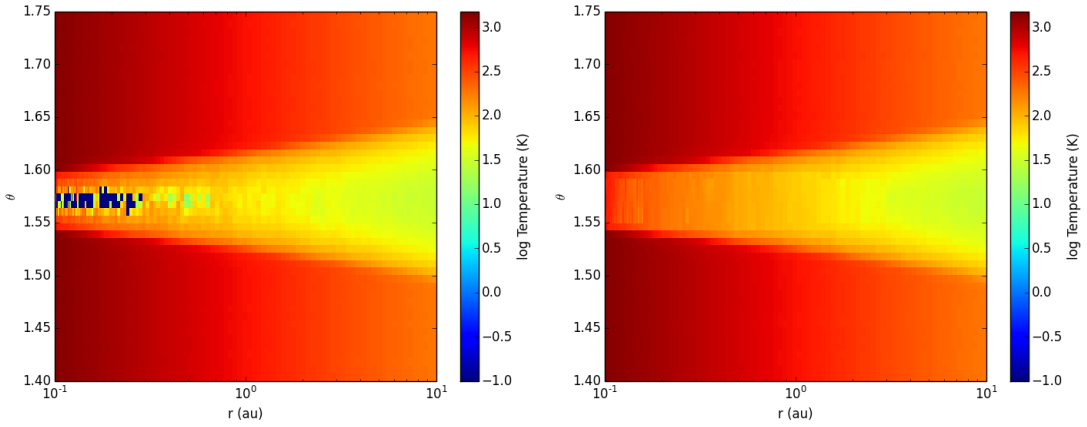

Figure 3.3: Temperature map for a flared disc model. Left: shows PDA disabled. Right: shows PDA enabled.

With PDA disabled, there are low temperature regions where the density is high.

This is due to photons being unable to penetrate that far into the high density region. In the example presented in Figure 3.3, the model failed at an optical depth ≈ 1.85. With PDA enabled, for high density regions, the local diffusion equation is solved using neighbouring cells as boundary conditions. In addition to being able to penetrate high density regions, PDA also significantly speeds up the calculation of the radiative diffusion equation in optically thick regions. For this reason, PDA will be used in the models produced from here on out.

Modified Random Walk

The standard random walk involves the net displacement of a single photon from the point source after N scatterings. Once again however, when a photon is in a high density cell, it can take a large number of interactions before a photon escapes the system. The modified random walk (MRW) solves this problem by firstly determining the distance to the closest cell edge d_{min}. The criterion whether to use MRW is:

$$d_{min} > \frac{\gamma}{\rho \bar{\chi_R}} \tag{3.16}$$

where $\bar{\chi_R}$ is the Rosseland mean opacity and γ is parameter which can be adjusted for speed or accuracy. Higher values of γ will produce more accurate results, but will require large runtimes. A sphere of radius R_0, centred on the current position of the photon, is then setup within the cell, where the diffusion equation can be solved. The solution to the diffusion equation involves sampling a random number ζ from [0,1] and using it to solve for y (Robitaille, 2010):

$$\zeta = 2 \sum_{n=1}^{\infty} (-1)^{n+1} y^{n^2} \tag{3.17}$$

As y tends to 1, larger values of n are required to maintain numerical accuracy. After determining y, the distance travelled to exit the sphere can be calculated using:

$$ct = -\ln y \left(\frac{R_0}{\pi} \right)^2 \frac{1}{D} \tag{3.18}$$

where D is the diffusion coefficient $(1/3\rho\bar{\chi_R})$, c is the speed of light and t is time taken to travel to the edge of the sphere. This simplifies the multiple interactions a photon would make by setting up a sphere within the cell, where diffusion theory is used, to move the photon to the surface of the sphere in a single step.

Parallelization

In order to effectively parallelize the code to use message passing interface (MPI), Hyperion uses the Lucy (Lucy, 1999) method to calculate the specific energy absorption rate. This is an iterative process which involves summing the optical depth to absorption of photon paths through each grid cell. It requires far fewer photons then the Bjorkman & Wood (2001) method to achieve a comparable signal-to-noise in the derived temperatures. The Lucy (1999) method is also easier to parallelize as each process can propagate photons independently, where as the Bjorkman & Wood (2001) method updates the temperature of a cell immediately each time a photon is absorbed.

Hyperion is designed so that using MPI is possible without requiring any changes to the Makefile. There are two ways to run the code with MPI enabled:

- The first is to simply define the number of nodes and cores within the python setup script. However, this method did not work on the STRI cluster.
- The second method is to use MPI versions of the grid specific binaries in the command line, e.g. The grid specific binaries '`hyperion_sph_mpi`' will run a model in a spherical polar grid in MPI. Once again the number of cores can also be defined in the command line. This method worked with the STRI cluster and was the method used throughout the work conducted in this thesis.

3.1.4 Computing SED and Scattered Light Images

Peeled Images

This process was introduced by Yusef-Zadeh, Morris & White (1984) to allow one to increase the signal to noise of an image or SED by 'peeling off' a photon in the

observers direction at every interaction. This additionally emitted photon is weighted by $P.e^{-\tau_{escape}}$, where P is the probability of the photon being scattered or re-emitted towards the observer after the interaction and τ_{escape} is the optical depth to escape the disc and reach the observer.

Raytracing

Raytracing involves determining the source function at each cell in the grid and solving the equation of radiative transfer along the lines of sight to the observer. For thermal emission, the source function is determined by the mass and temperature of the cell. Isotropic scattering only requires the specific intensity and temperature structure to determine the source function (Pinte et al., 2009). Non-isotropic scattering requires that angular and frequency dependence of the scattering components be saved. This, however, requires a large amount of memory. Therefore, the current build of Hyperion does not include raytracing for scattered light. Hyperion does, however, use raytracing for producing SED images at thermal IR wavelengths where emission is isotropic and scattering negligible.

Monochromatic Radiative Transfer

In order to compare the synthetic images produced by Hyperion to observations made at specific wavelengths, it is ideal to be able to run the Monte Carlo code at these specific wavelengths. Hyperion allows one to do this by using the monochromatic radiative transfer setting. This, however, splits the scattered light contribution into two, the first being from the source and the second being from the scattered dust emission. Photons from the source are emitted at the defined wavelength; when scattered they are peeled off and when absorbed they are removed from the system. This means photons from the scattered dust emission are computed by determining the emissivity at the defined wavelength inside each cell.

3.2 Testing Hyperion

3.2.1 Speed Test

An extensive multi-core test is conducted by Robitaille (2011) on the Harvard Odyssey cluster. It is found that the speedup from running the code on N parallel processes compared to running the code in serial follows Amdahl's law (Amdahl, 1967):

$$\text{speedup} = \frac{1}{(1-P) + P/N} \tag{3.19}$$

where P is the fraction of the code that is truly parallel. A range of N values were tested ($1 \leq N \leq 512$ in powers of 2) for two protoplanetary disc models. Both models were the same, however model 2 had 10 times as many photons for every iteration. A theoretical maximum speed up was determined for both these models at $292^{+12.3}_{-11.5}$ (256 cores) and $1604.4^{+174.8}_{-147.3}$ (512 cores) respectively. They do state that these speedup values do not hold for all models and should be taken as an example of how the code has a finite speedup limit.

A similar test was conducted on the Hertfordshire STRI cluster[3] to see how the speedup translated on a different architecture. The tests conducted on the STRI cluster were not as intensive as the tests conducted by Robitaille (2011), as N only varied from 1 - 32 in powers of 2. Figure 3.4 shows a speedup comparable to what Robitaille (2011) found. The work conducted in this Thesis used a minimum of 8 cores while running Hyperion and higher than 8 depending on the availability of nodes on the STRI cluster.

3.2.2 Scattered Light Image

Once Hyperion has been installed and the appropriate settings have been enabled/disabled, one is able to then produce scattered light images. Using the parameters described in Table 3.3, a scattered light and percent polarization image is produced (Figure 3.5) at a viewing angle of 90 degrees (disc inclination = 0 degrees) and $\lambda = 1.65$

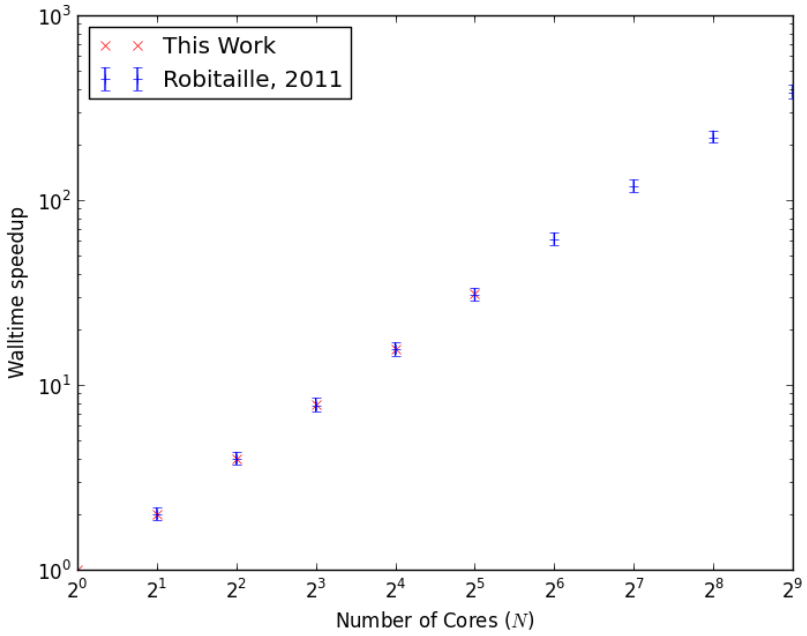

FIGURE 3.4: Speedup time for N cores compared serial execution for a flared disc model. The error bars on the plot represent the average values of the 10 executions the speedup time would reside in.

μm .

The use of forced first scattering allows one to reduce the number of photons required and therefore reduce the run time. Robitaille (2011) recommends a photon count of 10 - 100 times the number of cells in order to get a good signal to noise ratio. A spherical polar grid with dimensions (radial = 400, θ = 400, azimuthal = 1) would translate to a photon count of $1.6 \times 10^6 - 1.6 \times 10^7$. For the model described in Table 3.3, a photon count of 5×10^6 was used. Using a photon count above this did not yield better results (significantly higher S/N) for the images and only increased the run time of the code.

In addition to producing scattered light images, Hyperion is capable of producing Stokes parameters other than I. By default this is disabled to save memory, however,

[3]http://stri-cluster.herts.ac.uk

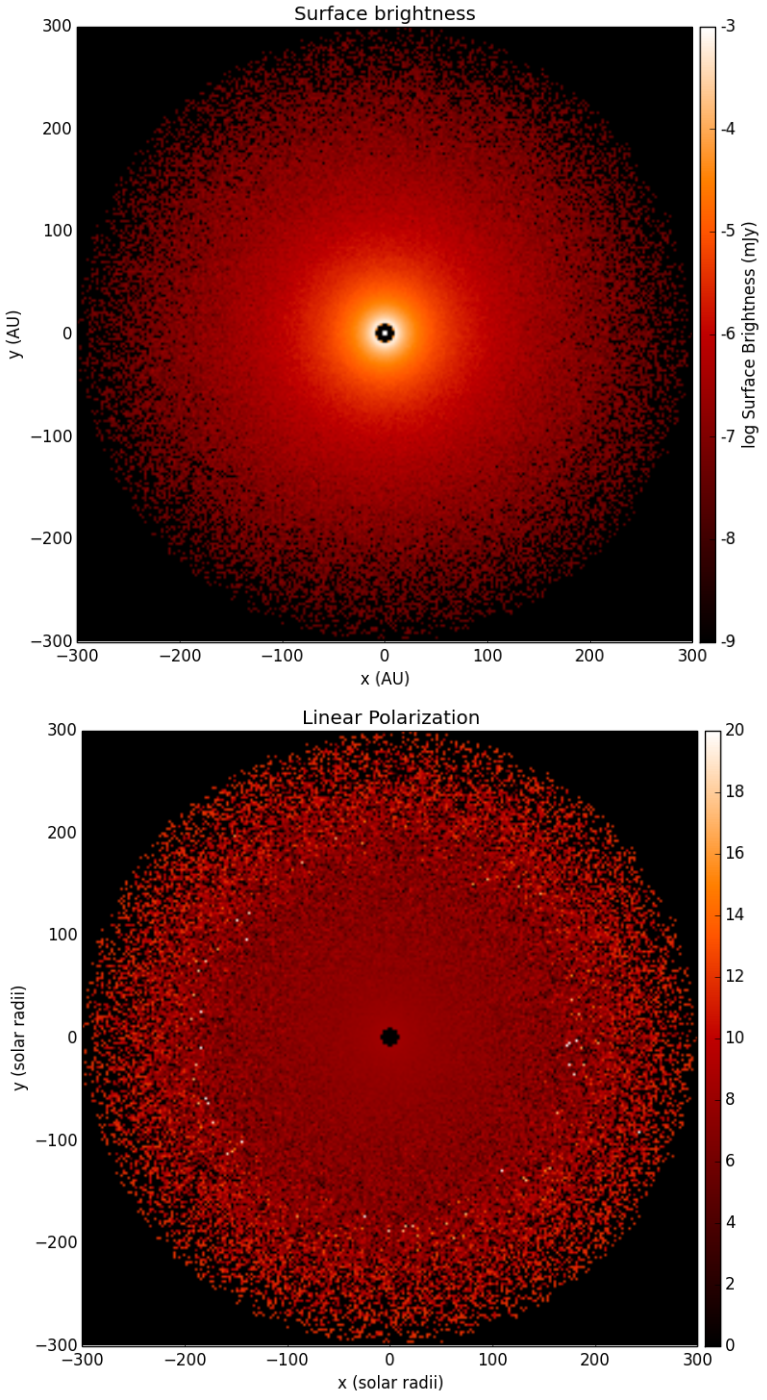

Figure 3.5: Scattered light (top) and percent polarization (bottom) images using the disc/dust parameter from Table 3.1. An initial photon count of 5×10^6 was used.

TABLE 3.3: Input parameters for the scattered light test images

Parameter	Value
Stellar Mass	1 $M_\odot$
Stellar Radius	1 $R_\odot$
Effective Temperature	5800 K
Disc Radius	10-300 AU
h_0	12.5 AU
R_0	25 AU
Disc Flaring parameter (β)	1.125
Surface Density exponent (p)	-1
Disc Mass	1.1×10^{-6} $M_\odot$
Minimum grain size (μm)	0.01
Maximum grain size (μm)	10.0
Number of different grain sizes	25
Gas to dust ratio	0
Density of the grains in (g cm^{-3})	3.6

once enabled, it is possible to produce images for all four (I, Q, U, V) Stokes parameters. From here, the linear and circular polarization can also be calculated. Figure 3.5 shows the disc described in Table 3.1 in polarized light.

4

Modelling HD 169142

As previously mentioned, HD 169142 has been well observed over a large range of wavelengths (Kuhn, Potter & Parise, 2001; Quanz et al., 2013; Osorio et al., 2014) using various techniques. Therefore, there is an abundance of observational data to help constrain computational modelling of the disc system.

Modelling of the HD 169142 system will be done with the Monte Carlo radiative transfer code Hyperion in which the SED, surface brightness and polarized intensity will be compared to observational data. In addition to this, the mass of the annular gap, and in turn the mass of the expected planet, will also be examined.

4.1 Two Disc Model

4.1.1 SED

The first step taken to constrain the disc parameters was to compare SEDs constructed via Hyperion to observational data. Each parameter in the disc model affected the shape of the SED in a unique way, therefore each parameter was tested over a range of values and in combination with other parameters to find the best fit.

Stellar Model

The spectral type of HD169142 has differed between previous studies, however the general consensus is that the star is of spectral class A. Initial spectra (Houk & Fuentes-Williams, 1982) suggested the star was a B9V star. However an absence of He I lines was seen using high resolution spectroscopy on the Anglo-Australian Telescope (AAT); therefore the spectral type was determined to be a A5Ve star (Dunkin, Barlow & Ryan, 1997b). Recent studies have produced conflicting subclass classifications. Blondel & Djie (2006) use UV spectra to best fit a model of an A7v star, while Guimarães et al. (2006) uses high resolution spectra on the FEROS spectrograph on the ESO telescope to fit a A9III/IVe model to the star (they also confirm the absence of the He I lines). This uncertainty in spectral type also extends to other parameters of the star as well. Table 4.1 shows a summary of previous observations for HD 169142.

The spectroscopic and imaging observations include: 10 μm spectra (van Boekel et al., 2005), optical spectra (Manoj et al., 2006), UV spectra (Blondel & Djie, 2006), IR spectra (van den Ancker, 1999; Acke & van den Ancker, 2004) and 12 and 18 μm imaging (Mariñas et al., 2011). Meeus et al. (2010) combined previous photometric observations: 2MASS (Cutri et al., 2003), Naval Observatory Merged Astrometric Dataset (NOMAD) (Zacharias et al., 2004) and millimeter data (Sylvester et al., 1996) with far-IR observations obtained with the Photoconductor Array Camera and Spectrometer (PACS) on the Herschel Telescope.

The conflicting values for a number of stellar parameters made it necessary to test

Table 4.1: Summary of the parameters used for previous modelling of HD 169142

Paper	Luminosity ($L_\odot$)	Mass ($M_\odot$)	T_{eff} (K)	Radius ($R_\odot$)	log(g)
van Boekel et al. (2005)	14.45	2.0 ± 0.3	8203.5	1.89	4.19
Manoj et al. (2006)	18.20	2.00	8128	2.16	4.07
van den Ancker (1999)	15.33 ± 2.17	2.28 ± 0.23	8200	1.94 ± 0.14	4.22
Meeus et al. (2010)	8.49	1.17	7800	1.60	4.10
Blondel & Djie (2006)	8.55	1.65	6464	1.60	4.25
Mariñas et al. (2011)	13.50	1.90	8128	1.86	4.18

a range of stellar models against the observed ultraviolet data from the International Ultraviolet Explorer (IUE) and BVRI data (van der Veen, Habing & Geballe, 1989). Each stellar model was represented by a Kurucz stellar model using the values in Table 4.1.

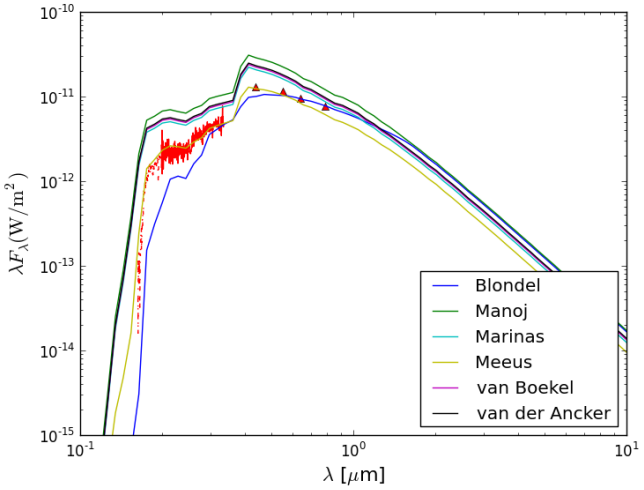

Figure 4.1: Kurucz model fits to the SED of HD 169142. Data includes IUE LWP and SWP and BVRI data from van der Veen, Habing & Geballe (1989)

Figure 4.1 shows the Kurucz stellar models against the observed UV and BVRI data. As the disc is almost face-on to the observer, there will be little to no contribution from

the disc in the UV wavelength range of the SED. Unless we consider a spherical halo surrounding HD 169142 (Grady et al., 2007; Honda et al., 2012; Osorio et al., 2014), the disc structure can be ignored for now. The parameters (Table 4.1) were input into Hyperion to produce simulated stellar SEDs. The majority of the Kurucz models do not fit the observed SED. They over estimate the UV and near IR flux, which is due to the radius and temperature of the star being too large. The Kurucz model for Blondel & Djie (2006) underestimates the UV flux, which is caused by the low surface temperature of the star (6464K). We see that the best fit Kurucz model is produced by the values presented by Meeus et al. (2010). This was therefore the stellar model adopted in our model of HD 169142.

Disc Structure

As mentioned in Chapter 2, the disc is modelled as a flared disc. UKIRT polarimetric imaging in the IR (Kuhn, Potter & Parise, 2001), spatially extended PAH data (Habart et al., 2006) and 1.1 μm imaging in scattered light (Grady et al., 2007) all suggest that beyond 0.2" (29 AU) the disc is illuminated by the star, so that a flared geometry for the disc is appropriate.

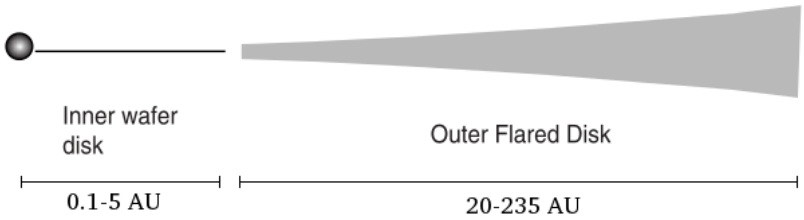

FIGURE 4.2: A simple illustration of a disc model consisting of a wafer thin inner disc and a flared outer disc as used by Grady et al. (2007).

The initial model used was a two component disc flared disc model (Table 4.2) (Meeus et al., 2010). This was proposed as a single disc fails to reproduce the observed SED. An illuminated wall is required to fit the IR flux of the SED. This can be seen in Figure 4.3 and will further be discussed in Section 4.2.1. An example of a flared two

disc model can be seen in Figure 4.2. The dust models used will be fully examined in the next section.

Table 4.2: Single disc (Hyperion) and best fit two disc model from Meeus et al. (2010)

	One Disc Model	Two Disc Model	
Parameter	Single Disc	Inner Disc	Outer Disc
r_{in}	0.1	0.1	20
r_{out}	235	5	235
p	-1.0	-1.0	-1.0
β	1.00	1.05	1.00
r_0	100	1	100
h_0	12.5	0.07	12.5
M_{dust} ($M_\odot$)	1.50×10^{-4}	2.00×10^{-9}	1.50×10^{-4}

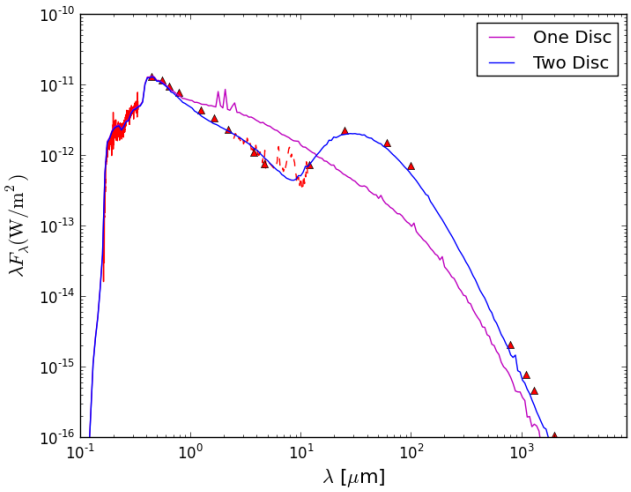

Figure 4.3: A synthetic SED comparing the single disc and two disc flared model from Table 4.2.

Figure 4.3 shows that a two component disc is required to produce an SED comparable to the observations. A single component disc over-estimates the flux between 1-30 μm due to the large abundance of dust close to the star and underestimates the

flux beyond 30 μm due to the lack of thermal emission from the dust grains at longer wavelengths. These problems can be addressed by considering a two disc model.

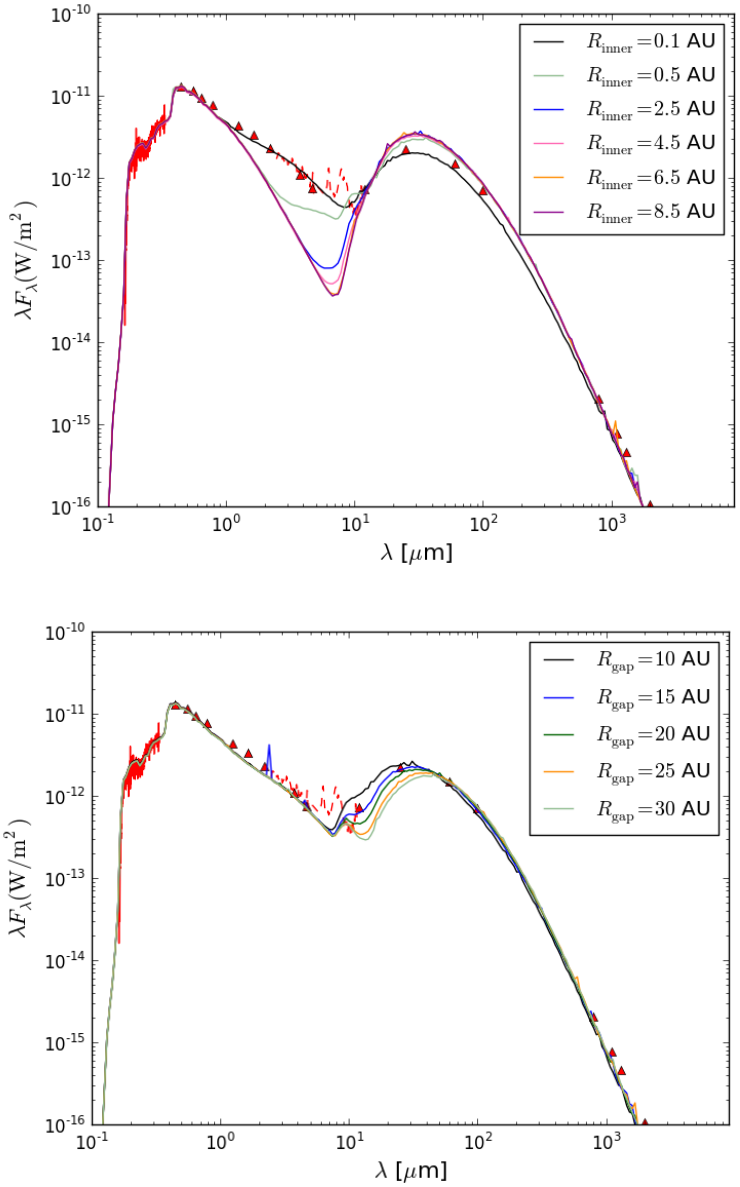

FIGURE 4.4: The top image shows how the position of the inner radius of the inner disc affects the SED. The bottom image shows how the inner raidus of the annular gap affects the SED.

The first component is a small inner disc which produces the small excess emission seen between 2-10 μm. This emission requires hot dust just below the sublimation

temperature or just at the sublimation radius. There are no observational data for this inner disc due to its proximity to the star; therefore the inner disc parameters will be set as a free parameters. It is also possible to use a combination of an inner disc and halo (Grady et al., 2007; Honda et al., 2012) to produce the excess emission in the $10 - 20$ μm range, however, a simple small inner disc and its hot wall is capable of reproducing this emission. Figure 4.4 shows how the distance to the inner disc affects the SED. Moving the inner disc further from the star reduces the flux between between 1-30 μm but increases the flux beyond 30 μm due to the increase in cool dust re-emitting at longer wavelengths. Previous modelling placed the inner disc at 0.1 AU (Meeus et al., 2001), 0.15 AU (Grady et al., 2007) and 0.1 AU + a halo (Honda et al., 2012). Figure 4.4 shows that a distance of ≈ 0.1 AU best fits the observed data.

The second component is a flared outer disc. The vertical inner wall of the second disc intercepts starlight and emits it at longer wavelengths. Honda et al. (2012) find that the emission from the wall dominates the flux contribution at 18 and 24.5μm. The position of the annular gap has been previously estimated. Grady et al. (2007) determined a good fit to the SED with a gap between 25-44 AU, Meeus et al. (2010) used a gap between 5-20 AU and Honda et al. (2012) use a gap spanning 0.2-23 AU. Figure 4.4 shows how the distance to the second disc (vertical wall) affects the SED. Moving the second disc further away shifts the mid IR peak to higher wavelengths and decreases the flux between 10-40 μm . Initial tests suggest that a distance of 15 AU fits best.

Sub-millimeter Array (SMA) observations in 1.3 mm continuum emission and ^{12}CO $J = 2 - 1$ line emission (Raman et al., 2006) in conjunction with JCMT ^{12}CO $J = 3 - 2$ line emission (Dent, Greaves & Coulson, 2005) have provided us with a good constraint on the disc inclination. Both observations are in agreement that the disc has an inclination to the plane of he sky in the region $5^\circ \geq i \leq 20^\circ$, however Raman et al. (2006) refines this to an inclination of 13° through testing of irradiated accretion disc models from D'Alessio et al. (2005).

Dust Grains

The dust grains we use are modelled as spherical grains in which the scattering properties are computed by Mie thoery (BHMie). The grains have a power law size distribution $\propto a^{-3.5}$ between minimum grain size $a_{min} = 0.01$ μm and maximum grain size $a_{max} = 1$ cm. HD 169142 is a Herbig group Ib (Meeus et al., 2001) object and one of the properties of these objects is that they do not produce a 10 μm silicate emission feature. This is also seen in Dunkin, Barlow & Ryan (1997b) who find a silicon depletion around 3 of the 4 Herbig group Ib objects. 2.1 shows the SED from four Herbig group Ib objects in the wavelength range of $2 - 40$ μm. All of the objects show a lack of any silicate emission bands. Sylvester et al. (1996) appears to see an 18 μm feature in the 20 μm spectrum, however they do note that it is noisy and it is also not seen in spectra by Meeus et al. (2001).

This could be explained through a number of processes:

- The strength of the silicate emission is related to the abundance of silicon. However, the complete omission of silicon would be anomalous in a star forming region within the ISM.

- Another explanation involves considering the size of the silicon grains. There is evidence for hot grains (2-10 μm excess) in the disc. However, if these grains are composed of silicon, then they will produce the silicon emission features. It is possible that on average, the silicate grains are too large to contribute significantly to the 10 and 20 μm features (Hanner, Lynch & Russell, 1994).

- It is possible smaller silicate grains are locked in larger grains through coagulation. If the material surrounding the silicate was sufficiently thick, then there may be no 10 and 20 μm silicate features (Meeus et al., 2001). Close to the star, the surrounding material would have to have a high sublimation temperature (e.g. carbon or iron), otherwise the mantle covering the silicon would break and expose the silicon.

Despite the lack of observational evidence for silicate dust emission, all previous

studies have used a combination of silicate and carbon when modelling the dust grains. Meeus et al. (2010) avoids the silicate emission by calculating the effective optical index with the Bruggeman mixing rule and Honda et al. (2012) replaces the amorphous silicate grains in the inner disc with dust with a higher continuum opacity (in this case carbon). This is due to them finding that the contribution of warm small (< 10 μm) amorphous silicate grains to be low, due to the flux at 10μm being very low compared to that at 20μm.

The dust models explored in this Chapter consist of 30% amorphous carbon (BE sample; Zubko et al. (1996)) and 70% astronomical silicates (Draine, 2003a) both with a power law size distribution exponent of -3.5. However, in order to prevent silicate features from being produced at 10 and 20 μm , various combinations of dust models and sizes were tested. These are summarized in Tables 4.3 and 4.4.

Table 4.3: Summary of the dust grain models used

	Astonomical Silicate		Amorphous Carbon	
	a_{min} (μm)	a_{max} (μm)	a_{min} (μm)	a_{max} (μm)
Dust 1	0.01	10000	0.01	10000
Dust 2	20	10000	0.01	10000
Dust 3	-	-	0.01	10000

Figure 4.5 shows that the dust model, for this disc structure, that fits the observed SED and does not produce any silicate emission is Model 9 (pure carbon model). It may be possible for Model 7 to fit the observed SED, but that would require moving the outer disc closer to the star. While the model with the larger (20 μm) grains does not produce the silicate emission, it underestimates the flux between 1 and 100 μm due to the lack of small grains. Therefore, it does not seem possible to recreate the SED while having silicate present in the 2 disc model.

The features present in the SED at 3.3, 6.2, 7.7, 8.7 and 11.2 μm are thought to be PAH emission. It should be noted that these features are currently not included in the

TABLE 4.4: Summary of the combination of dust grain models used in the disc

	Disc 1	Disc 2
Model 1	Dust 1	Dust 1
Model 2	Dust 1	Dust 2
Model 3	Dust 1	Dust 3
Model 4	Dust 2	Dust 1
Model 5	Dust 2	Dust 2
Model 6	Dust 2	Dust 3
Model 7	Dust 3	Dust 1
Model 8	Dust 3	Dust 2
Model 9	Dust 3	Dust 3

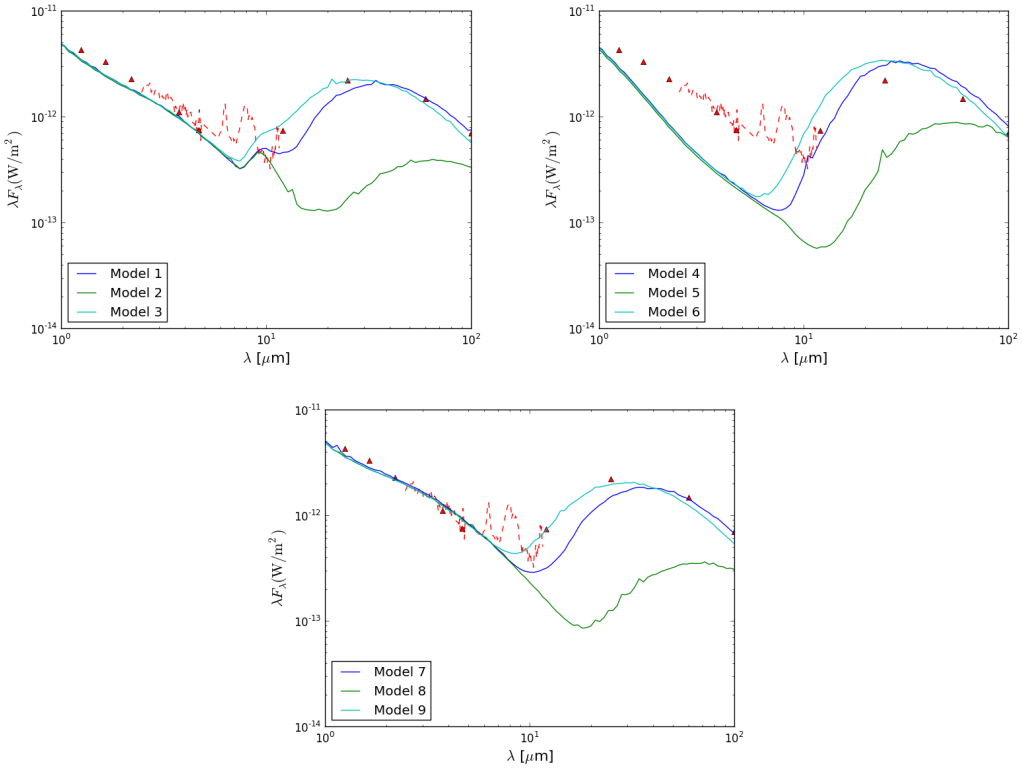

FIGURE 4.5: Model SED fits to the observational data (red). The data includes spectra from ISO, 2Mass and IRAS.

dust model. The PAH mass is estimated to only contribute to 0.0005 percent of the total mass of the disc Meeus et al. (2010) and therefore is not expected to contribute significantly to the SED or surface brightness of the disc.

Figure 4.6 shows a temperature map and density structure of the disc. It shows that the outer disc is cool, with temperatures below those required to produce the 10 μm feature. The inner disc however reaches temperatures high enough to create the silicon feature, which is why silicate can not be placed in the inner disc.

Observational Data

After testing the various disc, stellar and dust models, the model proposed by Meeus et al. (2010) (Table 4.2) was found to provide a good fit to the observational data. The observational data used to fit the SED consisted of:

- 2MASS (Green triangle) - JHK-band observations were acquired from the 2MASS database
- IRAS (Green triangle) - 12, 25, 60 and 100 μm observations were acquired from the IRAS point source catalog
- ISO (Green dash) - photospectrometry in the range of 2.469-11.621 μm were acquired from the PHT40 observations of the ISO archives.
- IUE (SWP: Red dash, RWP: red dash) - two sets of observations were made in the 0.12-0.19 μm (SWP 55483) and 0.19-0.32 μm (LWP 31285) range which were obtained from the stsci archive.
- Van der Veen (Green triangle) - BVRI data from Van der Veen et al. (1989)
- Sylvester (Green triangle) - 0.8, 1.1, 1.3 and 2.0 mm data from Sylvester er al. (1996).

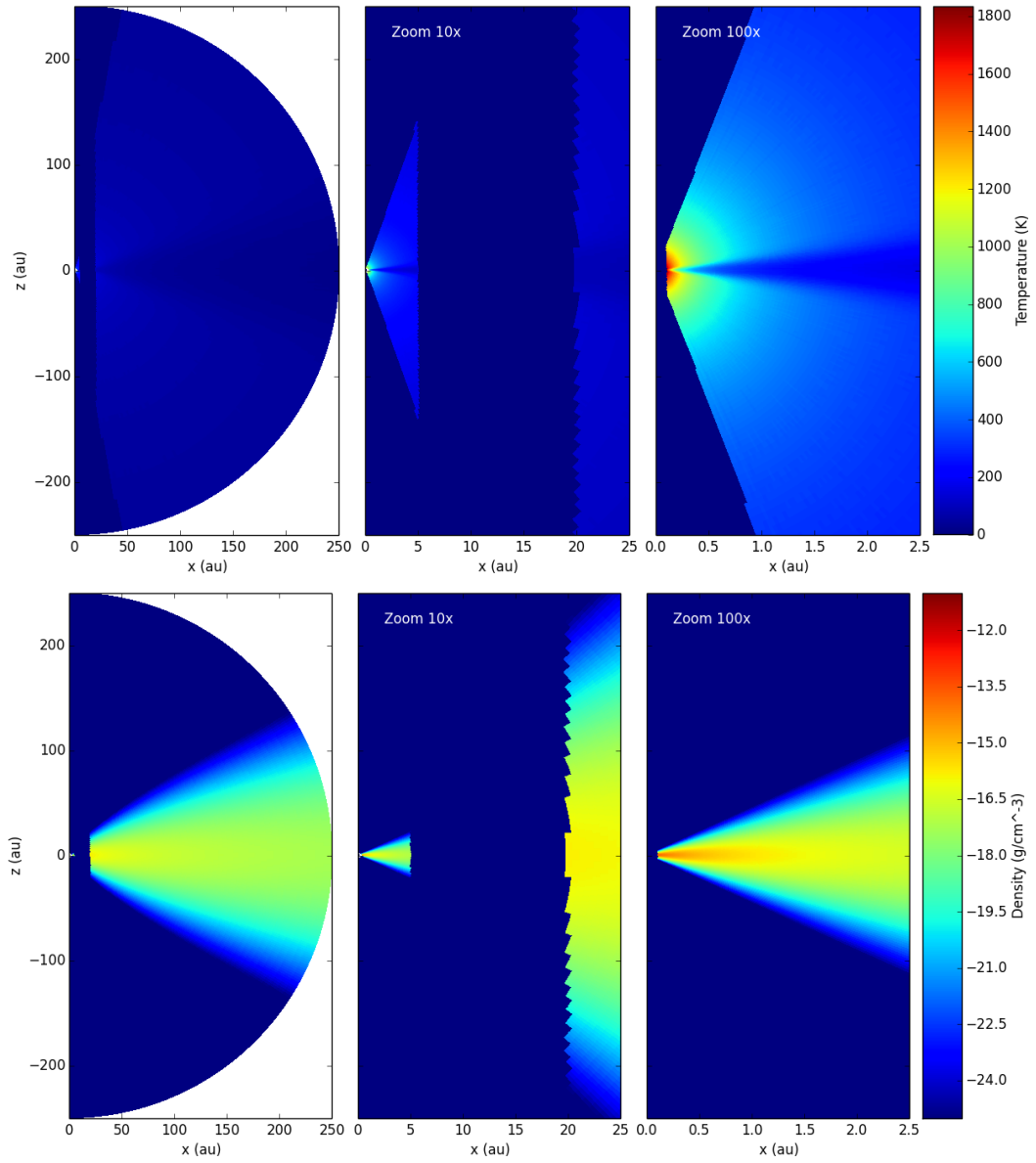

FIGURE 4.6: Temperature map and density structure of a two disc model

The best fit two disc model SED, created in Hyperion, can be seen in Figure 4.7. The dust scattering is seen to be high in the IR and far IR, this is due to the presence of large cm sized grains in the disc.

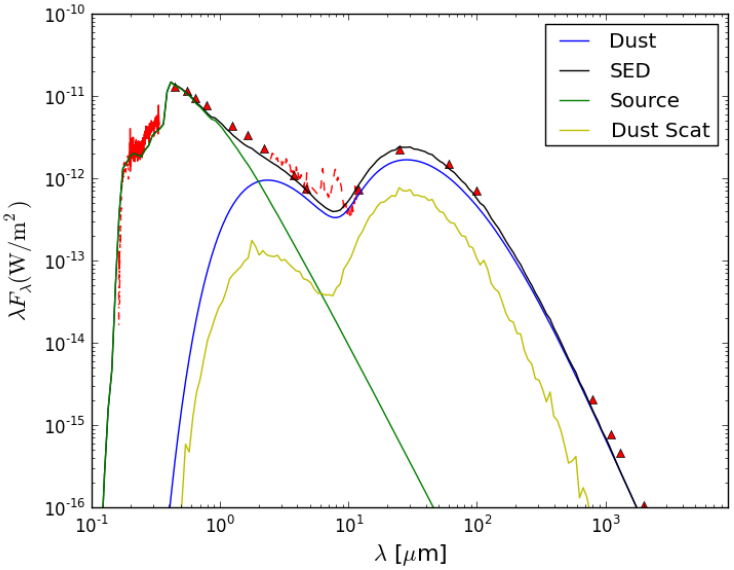

FIGURE 4.7: Two disc model: current best fit SED model, created in Hyperion, to the observed data.

4.2 Three Disc Model

The two disc model does a reasonable job at fitting the SED, however, recent VLT/-NACO H-band polarimetric imaging (Quanz et al., 2013) (Figure 4.8) has shown a second annular gap, therefore producing a three component disc. 7mm VLA observation (Osorio et al., 2014) also confirms the presence of a second gap and further constrain the disc parameters.

The position of the first annular gap can further be constrained with these observations. Quanz et al. (2013) finds a decrease in polarized light inside a rim located at ≈ 20 AU. Due to saturation of pixels, the inner disc is not visible in the image. Osorio et al. (2014) refines this position by combining the polarimetric imaging with their 7mm observations to 28 AU which is agreement with the position Honda et al. (2012) found at 23^{+3}_{-5} AU . The second annular gap is seen between $\approx 40 - 70$ AU (Quanz et al., 2013). Osorio et al. (2014) once again refines this to 42-67 AU.

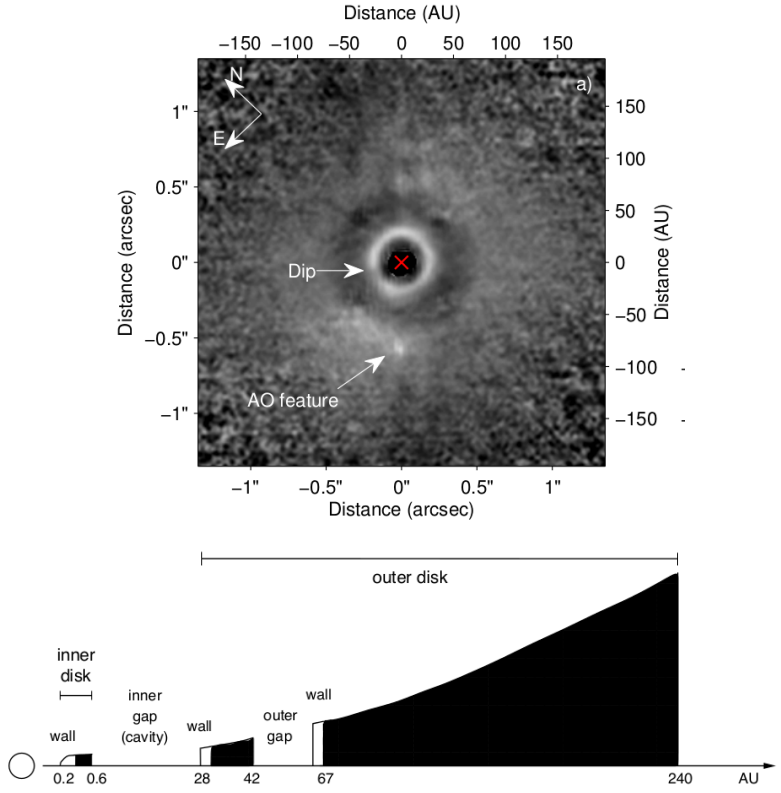

FIGURE 4.8: Top: Final Q_{r} image from Quanz et al. (2013). The image is scaled with r^2 to compensate for the decrease in stellar flux. The cross indicates the position of the star and the central pixels have been masked out due to saturation. Bottom: A simple illustration of the three disc mode (Osorio et al., 2014).

4.2.1 SED

The initial three disc model parameters are shown in Table 4.5. The model is based of the two disc model from Meeus et al. (2010) in which the outer disc has been split into with an annular gap. The mass calculation for the split outer disc can be found in the Appendix.

The observations from Quanz et al. (2013) and Osorio et al. (2014) reduced the number of free parameters to two by providing the wall positions for the outer discs. The scale height power-law exponent β and the surface density power law exponent p (disc 2 and 3) were set as free parameters so that they could be varied to fit the observational data. Testing for these values will be examined in Chapter 4.2.1.

Table 4.5: Model to be used in the parameter tests for the three disc model

Parameter	Disc 1	Disc 2	Disc 3
r_{in}	0.1	28	67
r_{out}	5	42	250
Surface Density Exponent (p)	-1.0	-1.0	-1.0
Flaring Exponent (β)	-1.05	-1.05	-1.05
R_0	1	100	100
h_0	0.07	12.5	12.5
M_{dust} ($M_\odot$)	2.00×10^{-9}	1.74×10^{-5}	1.33×10^{-4}

Dust Grain

As we now have three disc components, we can be a little bit more flexible with the dust grain modelling. Table 4.6 shows a breakdown of the dust model combinations that were tested. As previously mentioned, placing silicate in the inner disc produces the 10 μm silicate emission where it isn't observed and placing silicon in the outer disc/wall (disc 2) reduces the SED flux. However, it can now be placed in disc 3, where the contribution to the SED is low. A pure carbon model was used to model the grains in the inner disc, as it produces the correct flux in the IR (Figure 4.5).

Dust Model 1 was used in the final dust model because Dust Model 2 would require a complex process to rationalize why only the silicon grains are larger than 20 μm. Dust Model 9 was also excluded as a pure carbon model throughout the entire disc is not realistic.

Parameter Tests

The surface density power law exponent (p) has very little effect on the SED. A parameter test was conducted from $-0.5 \leq p \leq -1.5$ and we see very little change in the shape of the SED (Figure 4.10). This implies that surface density does not contribute significantly to the SED between $-0.5 \leq p \leq -1.5$. A similar parameter test was

TABLE 4.6: Summary of the dust combinations used in the 3-disc model

	Disc 1	Disc 2	Disc 3
Model 1	Dust 3	Dust 1	Dust 1
Model 2	Dust 3	Dust 1	Dust 2
Model 3	Dust 3	Dust 1	Dust 3
Model 4	Dust 3	Dust 2	Dust 1
Model 5	Dust 3	Dust 2	Dust 2
Model 6	Dust 3	Dust 2	Dust 3
Model 7	Dust 3	Dust 3	Dust 1
Model 8	Dust 3	Dust 3	Dust 2
Model 9	Dust 3	Dust 3	Dust 3

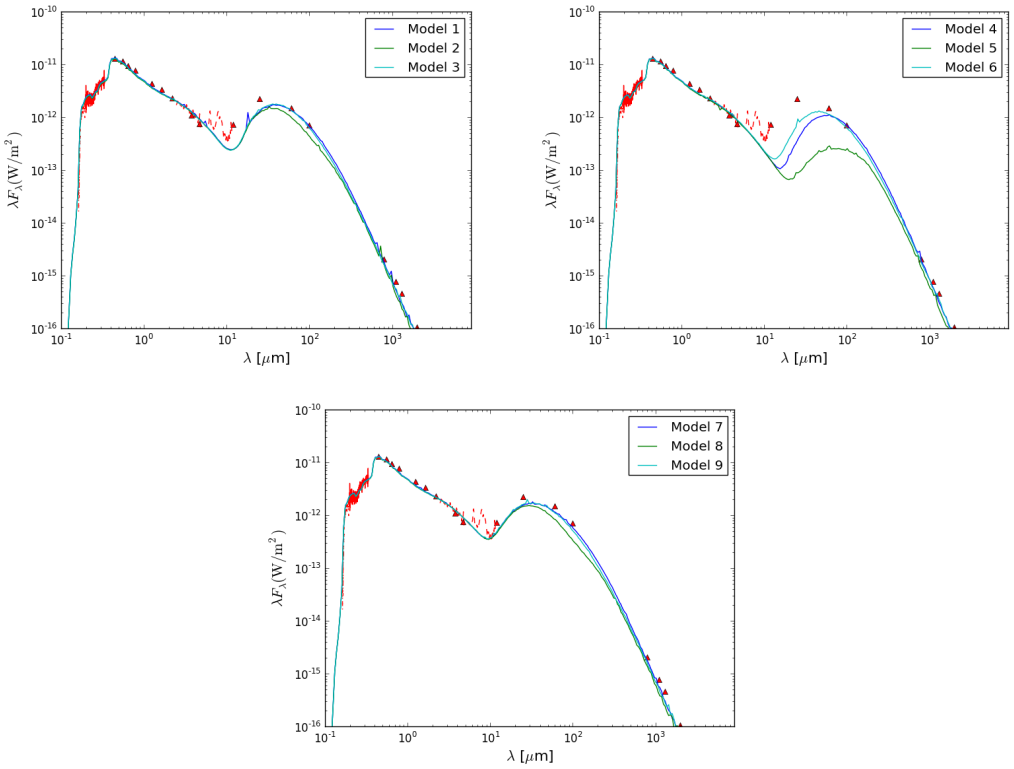

FIGURE 4.9: SED plots for the dust model combinations described in Table 4.6.

conducted for the scale height factor (β) in which it was varied from $0.5 \leq \beta \leq 1.5$. β affects the SED quite significantly (Figure 4.10). Looking at Equation 3.2, β will determine the height of the wall of disc 2. Due to R_0 being constant and greater than R at the wall, increasing β will decrease the height of the wall and therefore decrease the amount of starlight that is intercepted. Decreasing β will increase the height of the wall resulting in more starlight being intercepted. This will increase the temperature at the wall, therefore increasing the mid-IR peak.

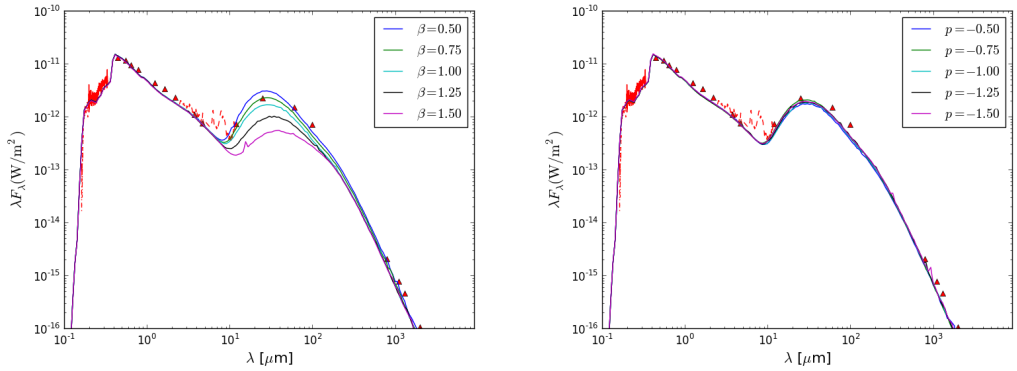

Figure 4.10: Parameter tests for β and p. The left image shows how β affects the SED. The right image shows how p affects the SED.

The current best fit disc parameters from the SED fitting can be seen in Table 4.7. This model uses Dust model 1 from Table 4.6.

Table 4.7: Final parameters used for the 3 disc model

Parameter	Disc 1	Disc 2	Disc 3
r_{in}	0.1	28	67
r_{out}	5	42	250
p	-1.00	-0.5	-0.5
β	1.05	0.8	0.8
r_0	1	100	100
h_0	0.07	12.5	12.5
M_{dust} ($M_\odot$)	2.00×10^{-9}	1.74×10^{-5}	1.33×10^{-4}

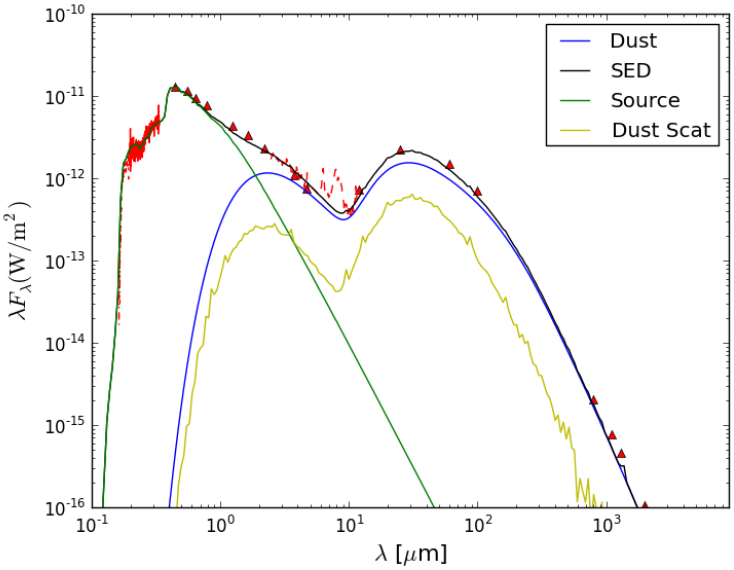

FIGURE 4.11: Current SED modelled from the parameter tests conducted.The parameters summarized in Table 4.7.

4.2.2 Surface Brightness

We can continue to constrain the disc parameters by examining the surface brightness profile of the synthetic images from Hyperion to the observed surface brightness profiles. From the SED fitting, we found that $0.7 \leq \beta \leq 0.8$ produced a good fit and that $-0.5 \leq p \leq -1.4$ had little effect on the shape of the SED.

Parameter Test in Scattered Light

There are two sets of observations that will be fitted to. The first is the 1.1 μm scattered light HST image (Grady et al., 2007). The disc is azimuthally averaged from 60-230 AU and they determine a surface brightness profile $\propto r^{-3}$. However, this range extends into the second annular gap and we therefore see a drop in intensity in our image as we approach 60 AU (Figure 4.13).

The second set of observations we examined were 1.65 μm scattered light observations (Fukagawa et al., 2010). A power law function was fitted to their H-band observations and they found a radial surface brightness $\propto r^{-3.4\pm0.4}$ between 120-200

AU. However, if the steep outskirt ($\geq$ 174 AU) is ignored, a power law $\propto r^{-3.0\pm0.2}$ is obtained.

A parameter test in the range $0.7 \leq \beta \leq 0.8$ and $-0.5 \leq p \leq -1.4$ was conducted to determine what values fit the observed surface brightness profile. The disc model used can be seen in Table 4.7. Both β and p contribute quite significantly to the slope of the surface brightness profile in scattered light. β increases the degree of flaring, therefore as it increases, the power law exponent becomes larger (slope becomes steeper). p has the opposite effect, as p increases the power law exponent becoming smaller (slope becomes shallower). This can be seen in Figure 4.12 as the power law increases as p increases.

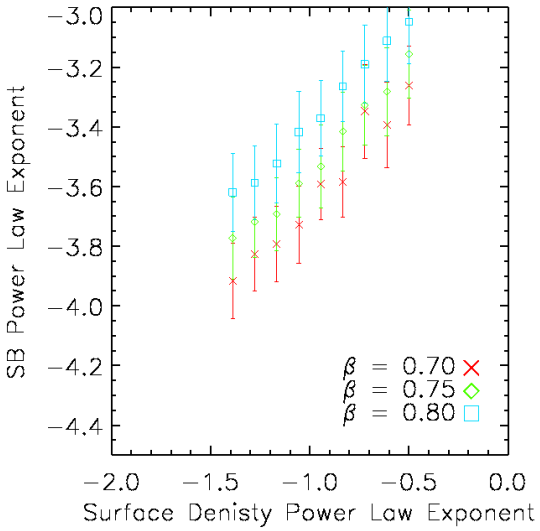

Figure 4.12: Parameter tests for the flaring parameter (β) and surface density power law exponent (p). Plot shows how varying p for a fixed β changes the surface brightness power law exponent for the scattered light image at 1.1 μm .

Figure 4.12 shows the parameter test for the 1.1 μm images, however the parameters changed the surface brightness power law exponent in the same manner for the 1.65 μm images. By fitting the synthetic disc produced in Hyperion to the surface brightness observation, p is constrained to $-0.5 \leq p \leq -0.8$ for $0.7 \leq \beta \leq 0.8$.

Figure 4.13 shows the best fit images of the surface brightness in scattered light at

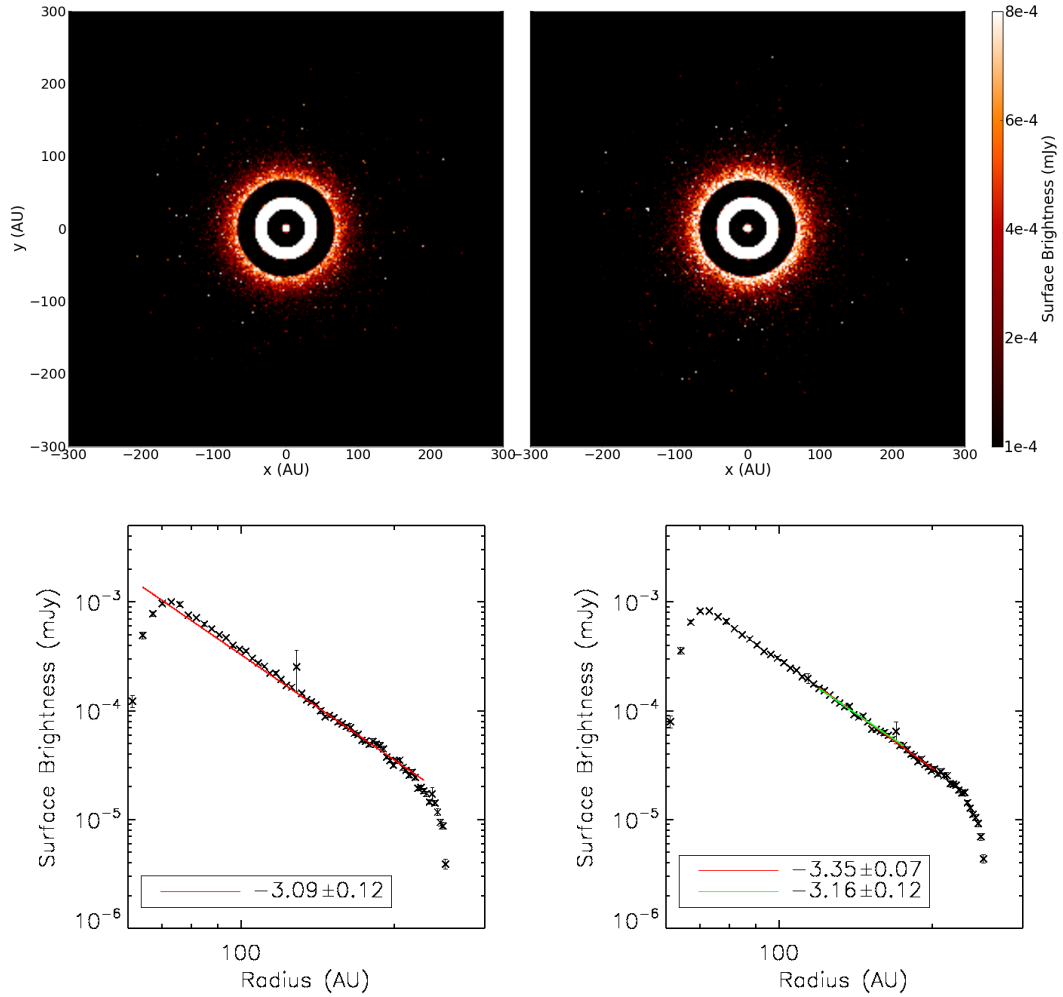

FIGURE 4.13: Top: Synthetic surface brightness image at 1.1 μm (left) and 1.65 μm (right). Bottom: azimuthally averaged surface brightness image of the outer disc (disc 3). Left: shows the power law exponent for the 1.1 μm image between $65 - 230$ AU. Right: shows the power law exponent for the 1.65 μm image between the range $120 - 200$ AU (red) and $120 - 174$ AU (green).

1.1 and 1.65 μm . It also shows the azimuthally averaged surface brightness profile and power law exponent for these images.

4.2.3 Polarization

The parameters can also be constrained by examining the target in polarized light. As previously mentioned Quanz et al. (2013) observed the star in the H-band in polarized light. They fitted a power law to their azimuthally averaged Q_r (which is equivalent to

the polarized flux) image between 85 -250 AU which shows a brightness profile exponent -3.31 ± 0.11. However, they obtain a better fit (in terms of χ^2) by considering a broken power law in the regions 85-120 AU ($-2.64^{+0.15}_{-0.17}$) and 120-250 AU ($-3.90^{+0.10}_{-0.11}$).

Parameter Test in Polarized Light

Although β and p have been constrained by the SED and surface brightness profiles, a full parameter test was conducted (same range as the surface brightness profile) in polarized light to ensure a consistent trend in the power law exponent. Figure 4.14 show that both β and p contribute quite significantly to the slope of the surface brightness profile in polarized light. β and p behave in a similar manner to how they affected the slope in the scattered light image.

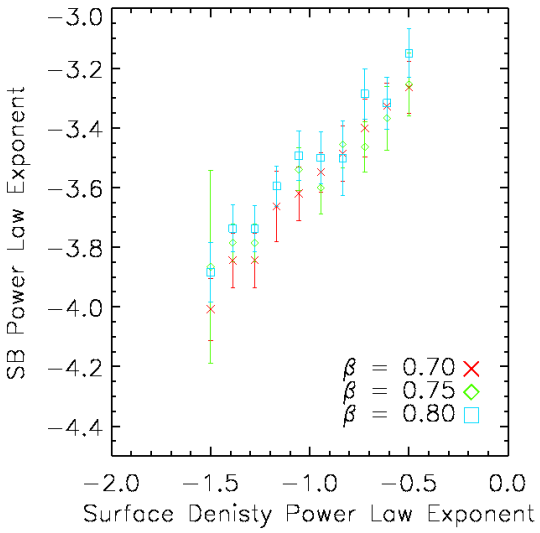

Figure 4.14: Parameter tests for the flaring parameter (β) and surface density power law exponent (p). Plot shows how varying p for a fixed β changes the surface brightness power law exponent in polarized light at 1.65 μm .

After completing a parameter test for the SED and surface brightness profile in scattered (1.1, 1.65 μm (in the radius of 120-200 AU and 120-175 AU)) and polarized light (1.65 μm), it is found that a value of $\beta = 0.8$ and $p = 0.5$ is required to simultaneously fit all three observations.

Polarimetric Imaging

Figure 4.15 shows the disc in polarized light. These images were modelled in the H-band to confirm the results produced by Quanz et al. (2013). The top images show the disc in polarized light and the degree of polarization. One feature of this model to note is the intensity of disc 2 ($28 - 42$ AU). This region has a higher intensity than disc 3 which can be attributed to the presence of pure carbon. The bottom images show the radially averaged SBP in polarized light and radially averaged percent polarization. The disc is averaged from $85 - 250$ AU and a power law exponent of -3.39 ± 0.07 is determined, which is comparable to Quanz et al. (2013) values of -3.31 ± 0.11. Quanz et al. (2013) found that they could achieve a better fit to the observations by considering a split power law between $85 - 120$ ($-2.64^{+0.15}_{-0.17}$) and $12 - 250$ ($-3.90^{+0.10}_{-0.12}$), however our tests could not produce a fit in these regions. This could indicate that a more complex disc model may be required.

4.3 Site For Planet Formation

VLT/NACO high-contrast observations in the L' (angular groove phase mask (AGPM) vector vortex coronagraph) and Gemini telescope observations in the J band (Gemini Planet Imager) reveal a source at 22.7 ± 4.7 AU (Reggiani et al., 2014). This source is also detected by Biller et al. (2014) who also observed the target in the L' band with the VLT/NACO AGPM vector vortex coronagraph.

Reggiani et al. (2014) also detects a possible object orbiting within the annular gap of $40 - 70$ AU. The object is estimated to have a mass between $0.1 - 18$ $M_{Jupiter}$ ($9.54 \times 10^{-5} - 1.72 \times 10^{-3}$ $M_\odot$). This second object is also detected by Osorio et al. (2014) at a position ≈ 50 AU to the south of the central star. It is speculated the second annular gap consists of trace circumplanetary dust emission from the protoplanet responsible for creating the gap. A total mass ($M_{dust+gas}$) using a gas to dust ratio = 100, for the source, of $0.2 - 2$ $M_{\rm Jupiter}$ is estimated from a temperature $\approx 100 - 300$ K and opacity $= 0.9 - 5 \times 10^{-3}$ cm^{-2}g^{-1} respectively (Osorio et al., 2014).

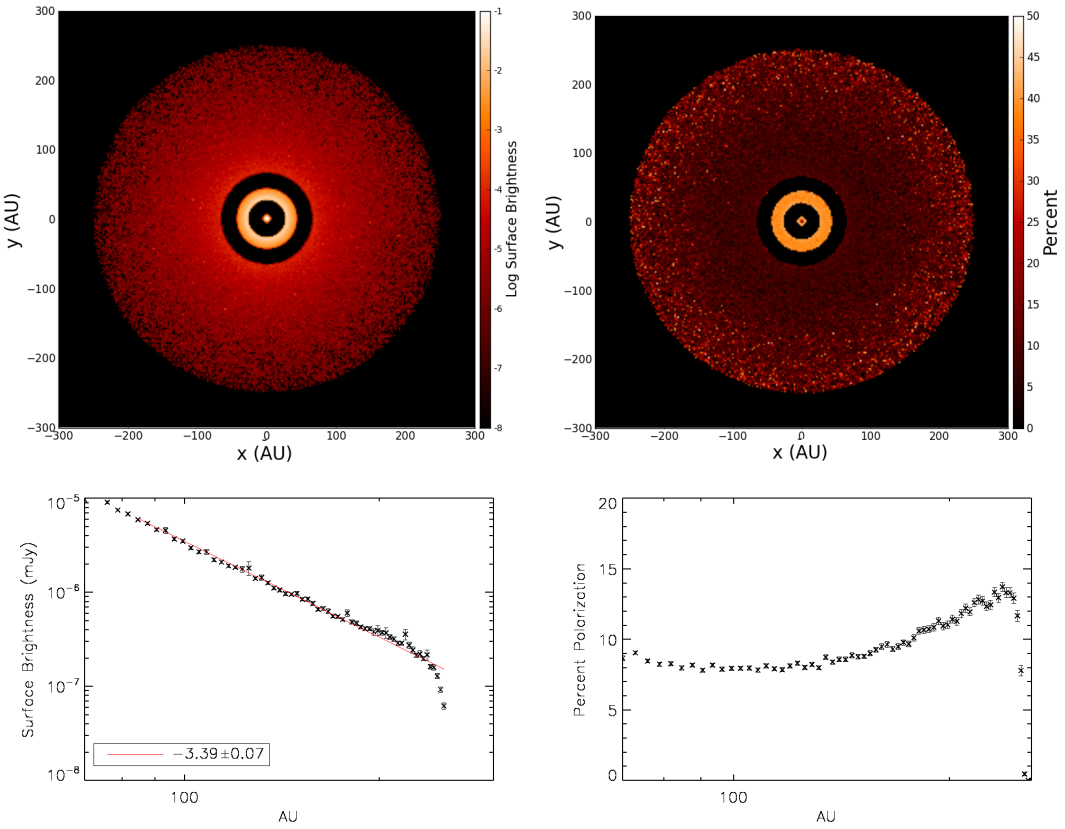

Figure 4.15: H-band modelling of the HD 169142 disc. Top left: Polarized intensity image, Top right: linear polarization image, Bottom left: radially averaged polarized intensity image and Bottom right: radially averaged linear polarization image.

Polarimertic observations (Quanz et al., 2013) show that the regions between $14.5-40$ AU (Disc 2) contributes $\approx 49\%$, $40-70$ AU (annular gap) contributes $\approx 14\%$ and $70-250$ AU (Disc 3) contributes $\approx 37\%$ to the integrated polarized surface brightness ($\approx 14.5-250$ AU). Very recently, Wagner et al. (2015) have been able to reproduce this by decreasing the dust density in the second annular gap by a factor of 0.3 or by decreasing the scale height in the annular gap by a factor of 0.86. This implies a set of possible models which could fit the polarimetric observations with the density ≥ 0.3 and the scale height ≥ 0.86.

Estimating the mass contained within the second annular gap can be done by comparing the synthetically produced surface brightness images to the observed images (Quanz et al., 2013). Before comparisons can be made, the synthetic observations were

converted to the units of magnitude/arcsec^2 via:

$$F_\mu = 10^{-m/2.5} F_0 \tag{4.1}$$

where m is the magnitude and F_0 is the zero point flux for the given photometric band. Quanz et al. (2013) observes the disc from $\approx$ 20 AU out to 250 AU. This range covers the second annular gap, in which a dip in Surface Brightness can be seen at 40 AU in Figure 4.16. A parameter test was run to estimate the dust mass contained in the annular gap. Assuming no dust clearing, a maximum value for the dust mass in the gap was calculated to be $M_{dust} = 1.74 \times 10^{-5}$ $M_\odot$. This was calculated by assuming a flared disc model described by Equation 3.2 and a total dust mass of 1.5×10^{-4} $M_\odot$ (Appendix A1).

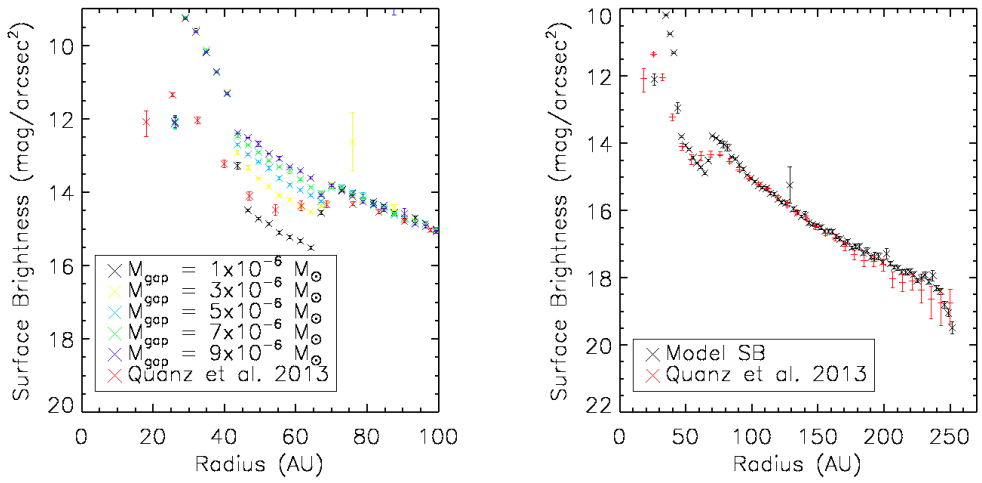

FIGURE 4.16: Left:Zoomed in view from $40 - 70$ AU for varying values of the dust mass in the contained in the annular gap. Right: best fit dust mass for the annular gap comparing the model SB profile (black X) to the observed SB profile (red +).

The parameter test shows that a dust mass $\approx$ 2.1×10^{-6} $M_\odot$ fits the surface brightness in the region of $40 - 70$ AU. Therefore, assuming a total mass of $M_{dust} = 1.74 \times 10^{-5}$ $M_\odot$ between $40 - 70$, would imply the dust mass of the planetary body to be $\approx$ 1.53×10^{-5} $M_\odot$ (0.016 $M_{Jupiter}$). This falls short of the estimated range ($0.1 - 18$ $M_{Jupiter}$) calculated by Reggiani et al. (2014), however it should be noted

that the gas mass is not included. Using a gas/dust ratio of ≈ 22-50 (Meeus et al., 2010) gives a gas mass of $3.37 - 7.65 \times 10^{-4}$ $M_{\odot}$ ($0.352 - 0.8$ $M_{Jupiter}$). Therefore, the total mass of the disc lies between $3.52 - 7.80 \times 10^{-4}$ $M_{\odot}$ ($0.368 - 0.816$ $M_{Jupiter}$). This fits within the range of the total mass calculated by Reggiani et al. (2014).

4.4 Final Disc Model

In this chapter, the disc parameters of HD 169142 are determined through comparisons of observations and Monte Carlo modelling. The best fit disc structure is somewhat consistent with previous models, however a prediction to the linear polarization and dust mass contained in the annular gap are also made. Table 4.8 shows the best fit model. The final disc is a four component disc which successfully fits the observed SED, SBP in scattered light at 1.1 and 1.65 μm (Table 4.8 and Figure 4.17 and 4.18).

Table 4.8: Final parameters used for the 4 component disc model including the annular gap

Parameter	Disc 1	Disc 2	Annular Gap	Disc 3
r_{in}	0.1	28	42	67
r_{out}	5	42	67	250
p	-1.00	-0.5	-0.5	-0.5
β	1.05	0.8	0.8	0.8
r_0	1	100	100	100
h_0	0.07	12.5	12.5	12.5
M_{dust} ($M_{\odot}$)	2.00×10^{-9}	1.74×10^{-5}	2.10×10^{-6}	1.33×10^{-4}

The primary difference in disc structure between this model and previous models is the outer disc. Comparing the disc model to Meeus et al. (2010), both are modelled as a flared disc however, the flaring exponent (β) and surface density exponent (p) are quite different. This is due to Meeus et al. (2010) only fitting the model to the SED,

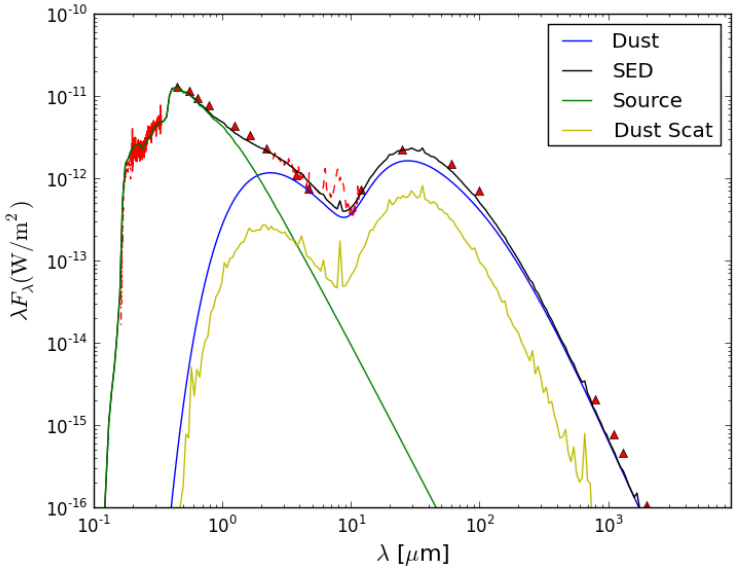

FIGURE 4.17: Final SED image for the 4 disc model for HD 169142.

while this work fits it to both the SED and SBP in scattered light and polarized light. In addition to the difference in the outer disc, the inner disc is also devoid of small silicate grains. HD 169142 is a Type Ib Herbig star and shows no signs of silicate band emission. The inner disc gets hot enough (Figure 4.6) to excite small silicate grains to produce emission bands, therefore small silicate grains are excluded from the inner disc.

The power law exponent fits are also within the errors of the observed fits for both the 3 and 4-disc model. A summary of the new results are given in Table 4.9. The Table shows that the final 4-disc model is successfully able to reproduce the observed fits.

As previously mentioned in Chapter 2.1.1, earlier studies have been uncertain on the stellar model for HD169142. This is due to the observational data the stellar models were modelled to and the presence of a halo surrounding the star. Inclusion of the IUE swp/lwp is crucial in determining the stellar model as it covers the wavelength range $0.12 - 0.19$ μm (swp) and $0.19 - 0.32$ μm (lwp). However, if a halo is modelled (Grady et al., 2007; Honda et al., 2012; Osorio et al., 2014), then the surrounding dust

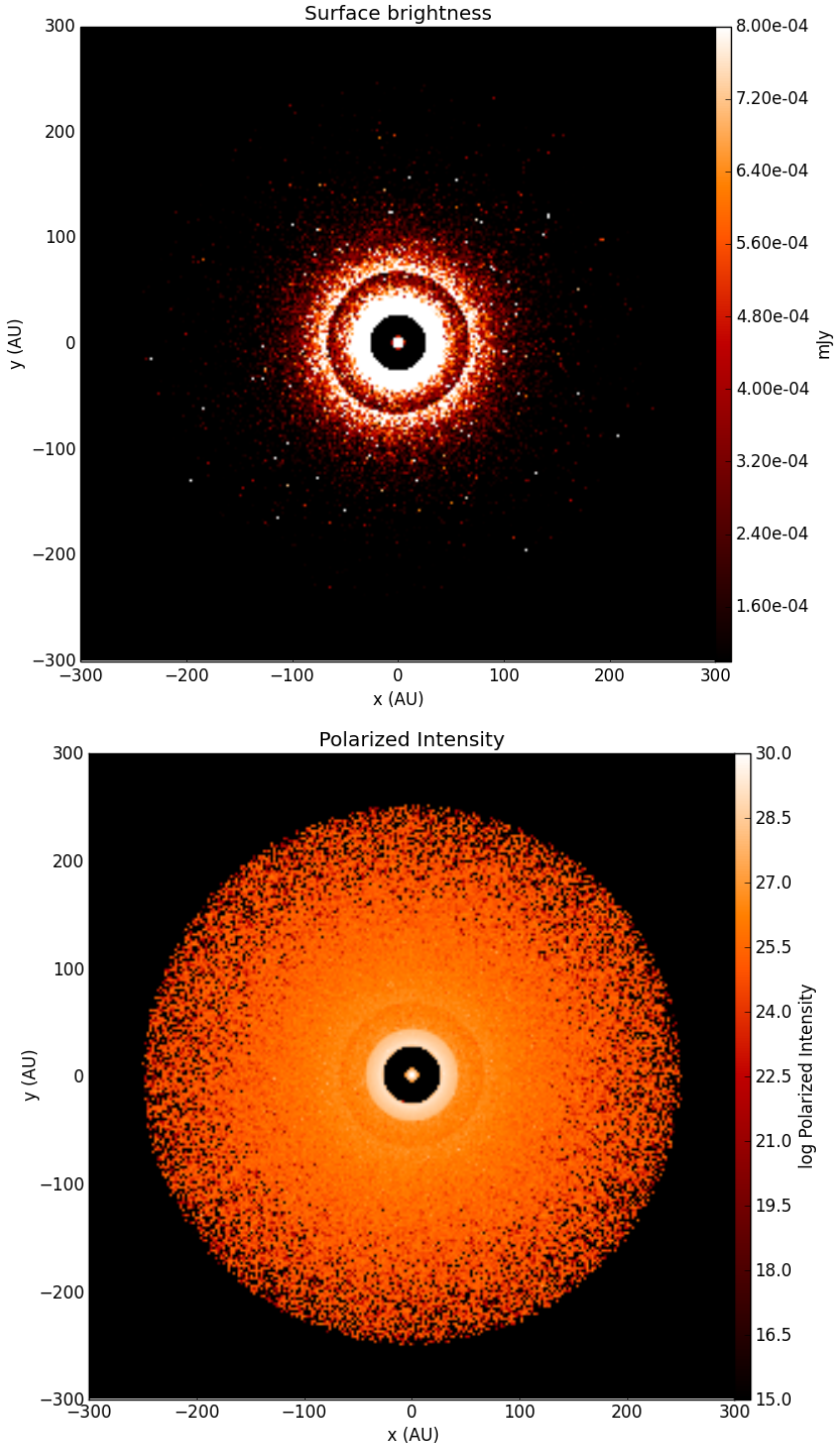

Figure 4.18: Final surface brightness and polarized intensity images for the 4 disc model for HD 169142 at 1.65 μm .

Table 4.9: Summary of the power law exponent fits from the 3 disc and 4 disc models

	Distance (AU)	Observed Fit	3 Disc Model	4 Disc Model
1.1 μm (SB) (Grady et al., 2007)	$60 - 230$	-3.0 ± 0.0	-3.09 ± 0.12	-3.06 ± 0.18
1.65 μm (SB) (Fukagawa et al., 2010)	$120 - 200$	-3.40 ± 0.40	-3.35 ± 0.07	-3.46 ± 0.15
1.65 μm (SB) (Fukagawa et al., 2010)	$120 - 174$	-3.00 ± 0.20	-3.16 ± 0.12	-3.21 ± 0.17
1.65 μm (PI) (Quanz et al., 2013)	$85 - 230$	-3.31 ± 0.11	-3.39 ± 0.07	-3.43 ± 0.13

will cause reddening/extinction. Therefore a hotter/more luminous star is required to compensate for the presence of the dust and fit the IUE data.

Grain growth is a natural consequence of ballistic aggregation of smaller dust particles. Dominik & Dullemond (2008) explored using models which balance coagulation and fragmentation in order to reproduce the wide range of dust sizes seen in observations. Similarly, Brauer, Dullemond & Henning (2008) include fragmentation in addition to radial drift to explain the abundance of micron size grains. We see this present in our disk model as a power law size distribution, ranging from micron to centimetre grains. This size distribution is required to reproduce the observed SED and surface brightness.

Grain growth is also directly related to dust settling. As grains close to the surface increase in size/mass, they will begin to experience strong drag force from the gas. This causes the grains to become decoupled from the gas and therefore settle towards the midplane. As the dust settles, the scale height and the flaring of the disc are reduced (Dullemond & Dominik, 2004). This is turn reduces the mid-IR emission from what is expected from a disc in hydrostatic equilibrium (D'Alessio et al., 2006). We see this in our disc model as our disc structure and properties are designed to simultaneously fit the SED, SB and polarization. Out parameter tests show that if the flaring parameter is too high, then the model is unable to reproduce the observed SED. We also see that our flaring parameter deviates from 9/8 and 5/4 (as mentioned in Chapter 2.3), therefore indicating that the disc is no longer in vertical isothermal equilibrium.

The inclusion of dust in the annular gap is also something that has only very recently been attempted (Wagner et al., 2015). These gaps are expected to be the result of tidal interactions with large planets; Artymowicz & Lubow (1994) compared the theoretical disc gap sizes (calculated as a function of the stellar mass) with smooth particle hydrodynamic models and found them to be in very good agreement. The SBP in polarized light of our model is compared to the observational profile found by Quanz et al. (2013). This allows us to constrain the dust within the annular gap and therefore constrain the mass of the planet most likely responsible for the gap. Our model estimates a mass of $\approx 1.53 \times 10^{-5}$ $M_{\odot}$ ($0.016 M_{Jupiter}$) which is lower than the

range calculated by Reggiani et al. (2014), however it should be noted that the gas mass is not included in this thesis. The inclusion of this extra disc does not significantly change the SED from the three disc model and it only slightly changes the power law exponent fits from the scattered light images and polarized intensity images.

5

DDSCAT

The concept of DDA was reviewed by Draine (1988) in which he produced a means to compute the scattering and absorption properties of non-spherical particles. This then led to the development of a portable fortran code called DDSCAT (Draine & Flatau, 1994). Subsequent revisions of the code have been released in the following years. The current version of DDSCAT is 7.3 (Draine & Flatau, 2013). However, during the time the work in this chapter was conducted, DDSCAT 7.1.8 was the latest version available.

5.1 Validity of DDSCAT

DDSCAT requires the parameters of the dust grain to be defined. The size of the target is characterized by an effective radius (a_{eff}), which represents the radius of a

sphere with a volume equivalent to that in the structure:

$$a_{eff} = \left(\frac{3V}{4\pi}\right)^{1/3} \tag{5.1}$$

where V is the volume of the grain which is represented by an array of N dipoles. If we let d equal the interdipole separation, then

$$V = Nd^3. \tag{5.2}$$

We can then further define a size parameter, x

$$x = \frac{2\pi a_{eff}}{\lambda}. \tag{5.3}$$

Having defined the grain structure, we can now specify the criteria for which DDA is valid. These are that d must be small compared:

1). to any structural lengths in the target,

2). the incident wavelength λ.

Calculations in Draine & Goodman (1993), Draine & Flatau (1994) and Draine (2000) have shown that the second criterion can be satisfied if

$$\frac{|m|2\pi d}{\lambda} < 1 \tag{5.4}$$

where m is the complex refractive index of the grain and must be characterized by

$$|m - 1| \leq 3. \tag{5.5}$$

Further calculations (Draine & Flatau, 2012) show that it is not appropriate to use DDA for very large values of x or m. Therefore DDA is best used for scattering by grains with size comparable to the incident wavelength.

5.2 Testing DDSCAT

The DDSCAT code is easily obtained from Draine's webpage[1] as a gzipped tarfile. Initial testing of the DDSCAT code was performed on DDSCAT7.1 which, at the time, was the latest version of the code. The tarfile included examples of irregular shaped particles which were very useful in understanding the purpose of each input file. The primary input file is the parameter file `ddscat.par`. As the name implies, this file is used to define the parameters of the target. DDSCAT is intuitively designed so that defining the target is very easy. After running the code with the given examples, the next step was to test against an exact scattering code, such as the spherical particle code BHMIE. By constructing a sphere of dipoles (using the `N_SPHERE` shape file which was supplied in the tar file), we could see whether DDSCAT could replicate the results produced by the BHMIE code.

Figure 5.1 shows a comparison between DDSCAT and BHMIE. The first plot shows scattering of dirty water-ice grains ($m = 1.33 - 0.01i$) (Graham, Kalas & Matthews, 2007) with a relatively small size parameter of $x = 3, 5, 7$. For $x = 3$ and low values of N ($N = 4945$), DDSCAT is able to accurately match the Mie calculations. As we increase N, we see an increase in accuracy. This is to be expected because as N increases, the target becomes more spherical. However, as x increases, a difference between Mie and DDSCAT calculations becomes more apparent. This difference is far greater for lower values of N (4945 dipoles), than for higher values of N (523984 dipoles) which are still able to accurately match the Mie calculations.

Figure 5.2 shows scattering from a target with $m = 0.96 + 1.01i$ and $x = 3$, 5, 7. The refractive index was chosen for the sole purpose of having a high imaginary part and to see how DDSCAT would cope with it. For $x = 3$, DDSCAT is once again able to replicate the values of BHMIE very well even for low values of N. The accuracy again increases as N increases. Once again however, as x increases, DDSCAT beings to struggle in replicating the Mie calculations. Even for high values of N, a large

[1] http://www.astro.princeton.edu/ draine/DDSCAT.html

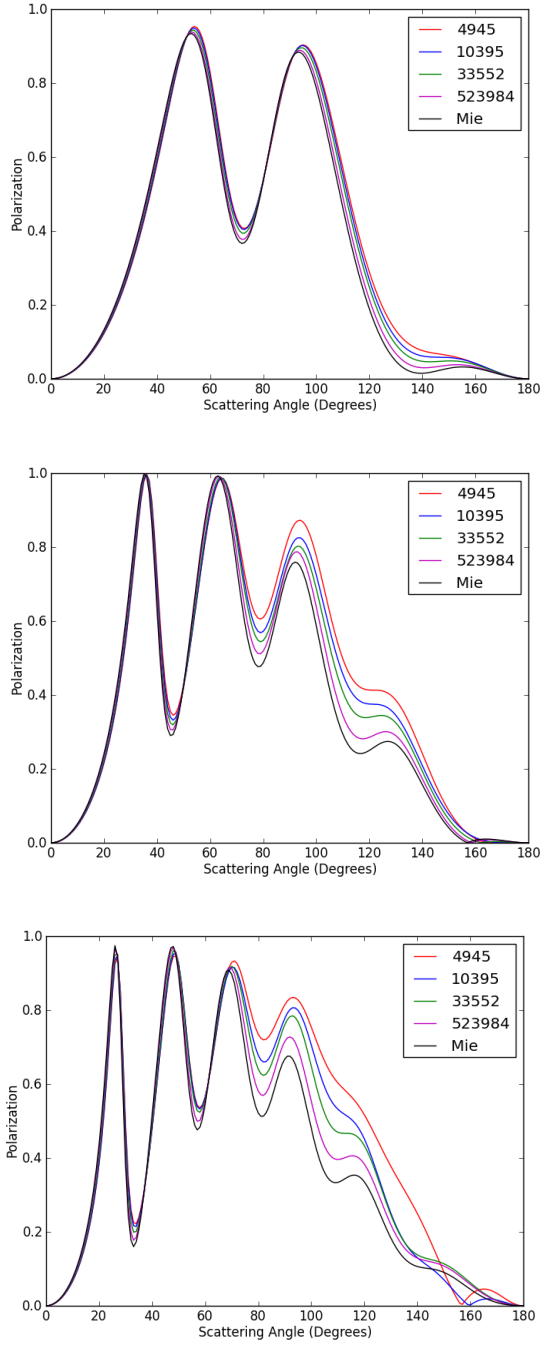

FIGURE 5.1: Polarization fraction vs scattering angle. The values for polarization are the modulus values of $|Q/I|$. The coloured lines represent DDSCAT where, blue = 4945, purple = 10395, green = 33552, red = 523984 dipoles. The black line is Mie calculations for $x = 3$ (top), 5 (middle), 7 (bottom) respectively. The refractive index is taken to be $m = 1.33 - 0.01i$ (dirty water-ice grains).

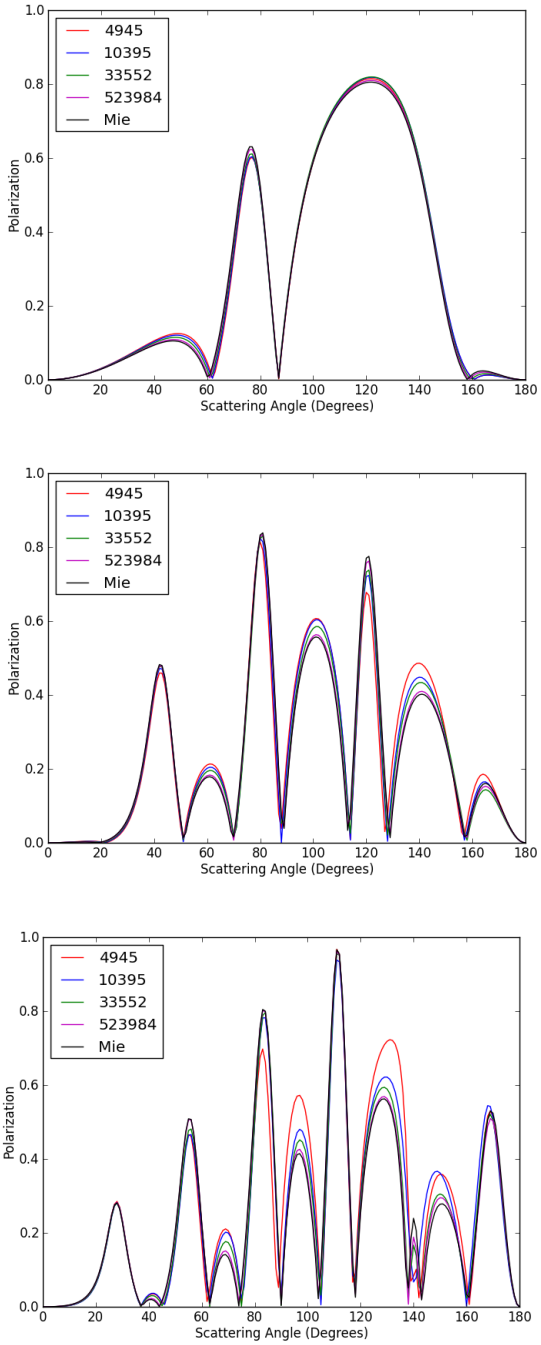

Figure 5.2: Polarization fraction vs scattering angle. The values for polarization are the modulus values of $|Q/I|$. The coloured lines represent DDSCAT where, blue = 4945, purple = 10395, green = 33552, red = 523984 dipoles. The black line is Mie calculations for $x = 3$ (top), 5 (middle), 7 (bottom) respectively. The refractive index is taken to be $m = 0.96 + 1.01i$.

difference between DDSCAT and Mie can be seen at larger scattering angles.

These tests were conducted to see whether DDSCAT was compiled correctly and to see whether it would produce sensible results. DDSCAT was successful in doing this. These tests also indicated which values of N would be appropriate to use. Using a high value of N would produce more accurate results than for low values of N, however this would become very time consuming. A value of $N \approx 100000$ was chosen to model the aggregate grains.

5.3 Speed Test

On a single desktop, these models took approximately 4 hours and 30 CPU minutes. Therefore, running these models for various wavelengths and/or size parameters would become very time consuming. However, the calculations within DDSCAT are considered embarrassingly parallel, therefore multiple orientation calculations can be done in parallel through the use of message passing interface (MPI) on a cluster. In addition to using MPI, DDSCAT allows a range of algorithms to be used for optimization. The most important of these is the choice of Fast Fourier Transform (FFT) algorithm. The user has the option to use Generalized Prime Factor FTT Algorithm (GPFA) (Temperton, 1992) or the Intel MKL routine. Tests conducted by Draine & Flatau (2012) show that the Intel MKL routine is faster than GPFA. As the MKL library was installed on the STRI cluster, this was the option used when running DDSCAT.

Once the parameter file had been finalized, a speed test could then be conducted on the Hertfordshire STRI cluster[2]. The tests conducted would examine how increasing the number of cores C would speed up the calculations (C was varied from 1 - 32 in powers of 2). Figure 5.3 shows the results of the speed test.

[2]http://stri-cluster.herts.ac.uk

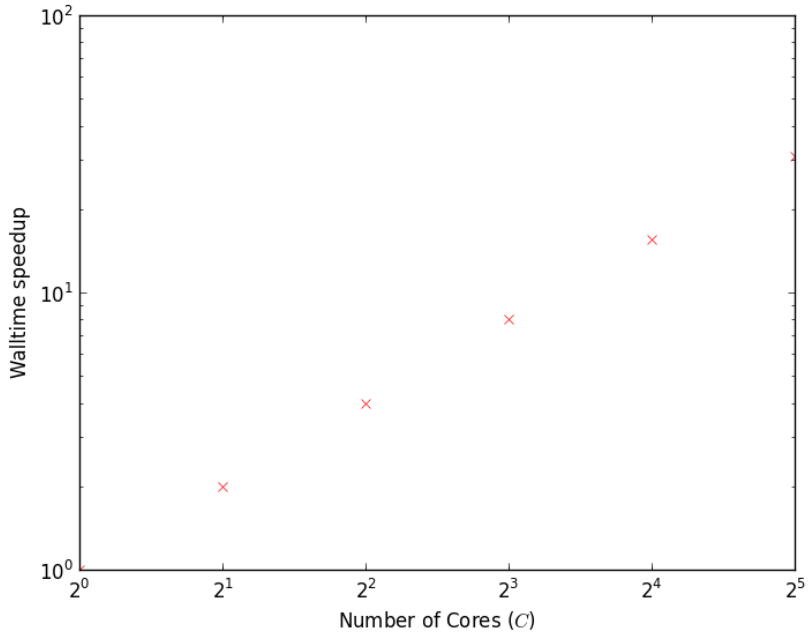

FIGURE 5.3: Speed up time for C processors compared serial execution for an aggregate spherical dust grain consisting of 107218 dipoles.

5.4 Aggregate Type

The aggregates size and shape can be characterized by assuming an equivalent ellipsoid with a fractal dimension (Blum & Wurm, 2000), filling factor and porosity (Shen, Draine & Johnson, 2008). These are defined as:

$$m \propto a_{eff}^{D_f} \tag{5.6}$$

$$f = \left(\frac{a_{eff}}{R_{abc}}\right)^3 \tag{5.7}$$

$$P = 1 - f = 1 - \left(\frac{a_{eff}}{R_{abc}}\right)^3 \tag{5.8}$$

where m is the mass of the aggregate, D_f is the fractal dimension of the growth process and R_{abc} is the characteristic size of the target ($a \leq b \leq c$ refers to the semi-major axes of the equivalent ellipsoid).

The three aggregate models of interest will be examined here and can be seen in Figure 5.4.

- Ballistic agglomeration (BA) or Ballistic particle cluster aggregation (BPCA) - this is a well known method in which monomers approach on random ballistic trajectories and stick together at the point of first contact with the pre-existing aggregate. It should be noted that a BA cluster can be formed as long as the monomers remain at the first point of contact.

The next two aggregation models were introduced by Shen, Draine & Johnson (2008):

- BAM1 (ballistic agglomeration with one migration) - this method produces clusters by having 3 or more monomers making first contact with a group of monomers consisting of less than 3 monomers. Unlike the BA case where the monomer remains at the first point of impact, BAM1 allows the arriving monomers to migrate and make contact with an additional monomer by rolling across the first contacted monomer. It should be noted that if the arriving monomer can migrate in two possible directions, then the one with the shortest distance will be chosen.

- BAM2 (ballistic agglomeration with two migrations) - this method produces clusters by having 4 or more monomers making contact with the pre-existing cluster and then making two migrations. The first migration is as for BAM1. The second migration consists of arriving monomer rolling over both the first and second sphere, therefore connecting to a third monomer. Once again the shortest path is chosen if more then one monomer is available for contact.

A list of aggregate models is available on Bruce Draine's website[3], which were used to construct realistic dust grains. The shape.dat file lists the positions of the dipoles which were constructed using a BA algorithm. The aggregation process used to construct the grains is random, therefore the R_{abc} will vary for each realization. As

[3]http://www.astro.princeton.edu/ draine/agglom.html

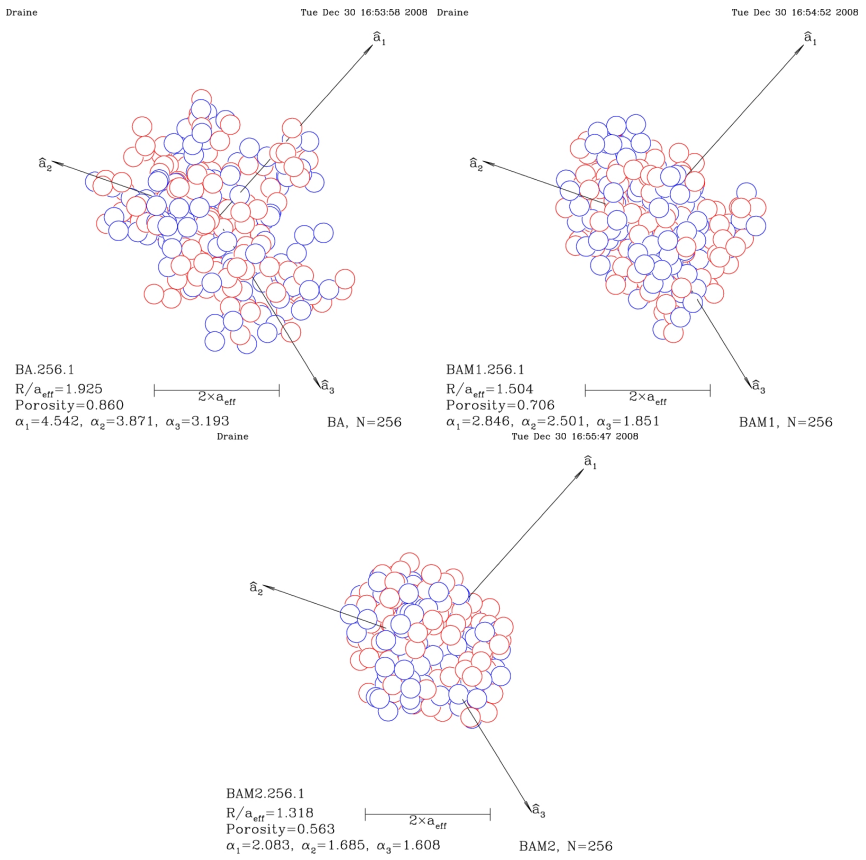

FIGURE 5.4: Aggregate cluster models where $N = 256$. Axes $\mathbf{a}_1$, $\mathbf{a}_2$ and $\mathbf{a}_3$ denote the principal axes with the largest, intermediate and smallest moment of inertia (Shen, Draine & Johnson, 2008).

the number of migrations increases, the porosity of the grain will decrease. This is due to the number of contacts each monomer has with one another. Therefore, BA will have the most porous grains, followed by BAM1 and then BAM2. Figure 5.5 shows a comparison between the three ballistic aggregate models with the number of clusters equal to 256 (each aggregate consists of 256 small equal size spheres). The aggregates are modelled as a pure silicate grain at a wavelength of 1.4 μm .

5.5 Rotational Averaging

Before the target orientation can be defined, a frame of reference must be determined. A "Lab Frame" (LF) is defined in which the incident radiation propagates in the $+x$

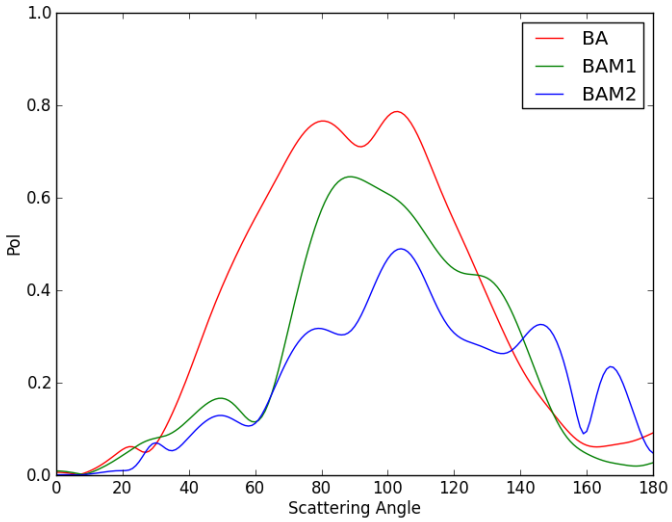

FIGURE 5.5: Degree of Polarization vs scattering angle for the three ballistic aggregate models. These models were run for the 256 cluster models ($a_{eff} = 1.095$ μm) where the dust grains are modelled as pure silicates at a wavelength of 1.4 μm .

direction. The three coordinate axes of the LF are the unit vectors $\hat{\mathbf{x}}_{LF}$, $\hat{\mathbf{y}}_{LF}$ and $\hat{\mathbf{z}}_{LF}$ ($\hat{\mathbf{x}}_{LF} \times \hat{\mathbf{y}}_{LF}$); these can be seen in Figure 5.6. The "Target Frame" is defined by the three unit vectors $\hat{\mathbf{a}}_1$, $\hat{\mathbf{a}}_2$ and $\hat{\mathbf{a}}_3$ ($\hat{\mathbf{a}}_1 \times \hat{\mathbf{a}}_2$).

The parameter file used to define the dust grain allows one to specify three angles Θ, Φ and β, which allows one to specify the orientation of the target. A higher number of orientations would provide greater accuracy in terms of averaging over the dust grain, however it becomes computationally expensive. Initial tests were conducted over 54 orientations.

5.6 DDSCAT Wrapper

One of the aims of this chapter is to create a wrapper to extract the necessary data from the DDSCAT output files, which will then be used to construct a HDF5 dust file for Hyperion to read. As previously mentioned, the wrapper will contain a script to extract the necessary data from the DDSCAT output files and to apply the specified size distribution. The next step will be to create the HDF5 dust file. The work in this

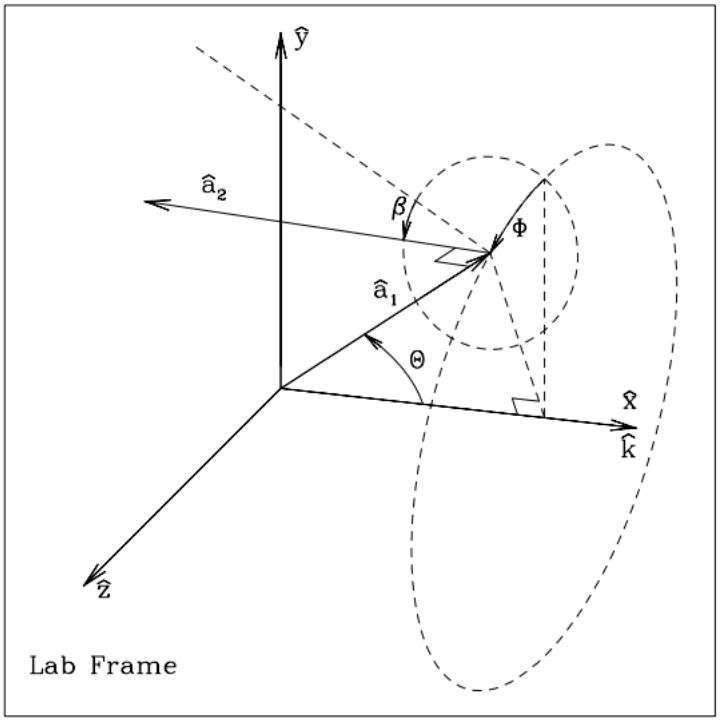

Figure 5.6: Figure showing the target orientation in the Lab Frame (Draine & Flatau, 2013).

chapter was conducted on DDSCAT 7.3.1 which is currently not publicly available.

Currently Hyperion models dust grains using a 4 element Mueller matrix and assumes that $S_{11} = S_{22}$, $S_{12} = S_{21}$, $S_{33} = S_{44}$ and $-S_{34} = S_{43}$. This assumption works for spheres, however it breaks down for irregular shaped particles which have a dependency on the angle of the grain (Φ, rotation angle of $\hat{\mathbf{a}}_1$ around k, refer to Figure 5.6) due to the grain not being symmetrical. This dependency on Φ can be removed by rotationally averaging on the grain over this angle. Averaging over a sufficient number of angles in Φ (180) reduces the difference between the scattering matrix elements leaving only four independent elements (to a first order approximation), which can be seen in Figure 5.7.

The difference between $S_{11} = S_{22}$, $S_{12} = S_{21}$ (< 1 percent) and $S_{33} = S_{44}$ (< 3 percent) is quite small. The difference in $-S_{34} = S_{43}$ however peaks at 80 percent at ≈ 105 degrees and drops below 1 percent at ≈ 110 degrees. This spike occurs at the

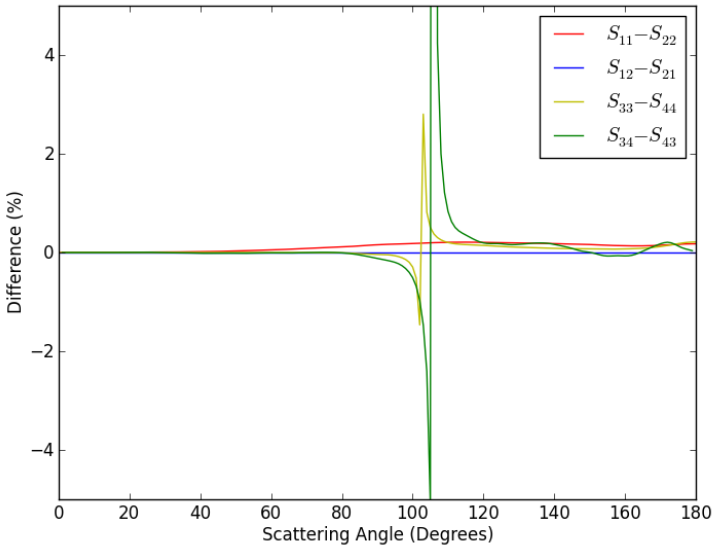

FIGURE 5.7: Difference, in percentage, between the scattering matrix elements for a pure silicon dust grain model.

peak polarization for this grain model.

The BAM2 grains also have a non-zero value for the 'zero value elements' (S_{13}, S_{14}, S_{23}, S_{24}, S_{31}, S_{32}, S_{41} and S_{42}, refer to Equations 1.25 and 1.27). Once again there are ways to reduce these 'zero' elements to become very small in comparison to the non-zero elements. The first being rotationally averaging the grains as above. Averaging over a sufficient number of angles in Φ (180) reduces the 'zero' scattering matrix elements to a very low number compared to the non-zero scattering matrix elements. The other method is to consider a population of BAM2 grains and their enantiomers. The enantiomers are produced by changing the sign of the x coordinate of every constituent sphere in the target file, which produces a mirror image of the original dust grain.

Figure 5.8 shows the difference in polarization for a population of silicate grains and a population of silicate grains and their enantiomers (50% silicon and 50% silicon enantiomers); a size parameter $x = 0.6, 4$ are used. At $x = 0.6$, the contribution from S_{31} and S_{41} is very low for both grain models. However at a $x = 4$, S_{31} and

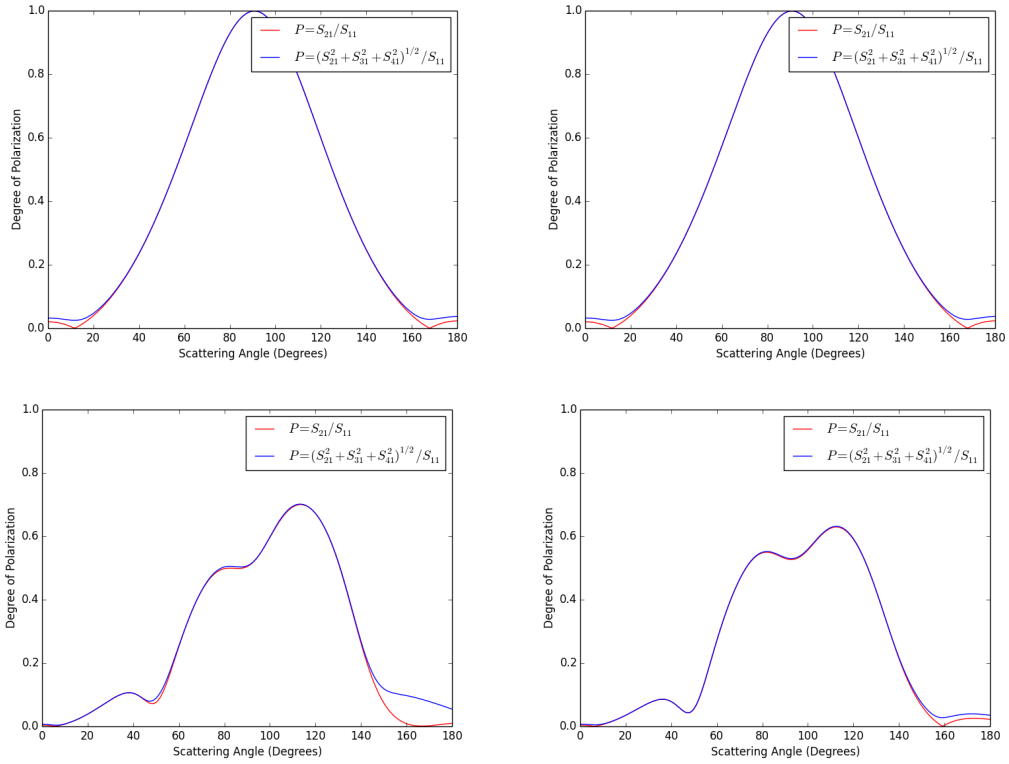

FIGURE 5.8: Degree of polarization for a population of BAM2 silicate grains (left) and a population of BAM2 silicates and their enantiomers, for different size parameter $x = 0.6$ (top) and $x = 4$ (bottom).

S_{41} increases the polarization by a significant amount ($\approx 10\%$) for the population of just silicate grains at large scattering angles. Adding the enantiomers reduces the contribution of the S_{31} and S_{41} elements ($\approx 3\%$) in comparison to the pure silicate model.

Along with reducing the contribution of these 'zero value elements', the inclusion of enantiomers also further reduces the difference between the symmetrical matrix elements ($S_{11} = S_{22}$, $S_{12} = S_{21}$, $S_{33} = S_{44}$ and $-S_{34} = S_{43}$). Figure 5.9 shows that the inclusion of enantiomers reduces difference between the matrix elements more so than using a pure silicon dust grain model. The difference between $S_{11} = S_{22}$, $S_{12} = S_{21}$ (< 1 percent) and $S_{33} = S_{44}$ (< 3 percent) is quite small. The difference in $-S_{34} = S_{43}$ however, no longer peaks at ≈ 80 percent at ≈ 105 degrees and now only peaks at ≈ 2 percent.

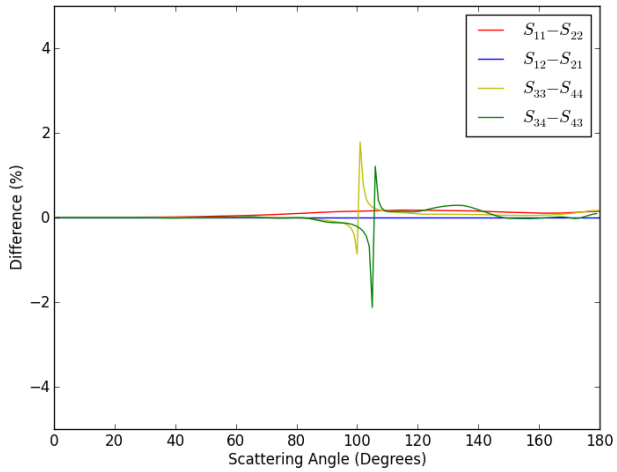

FIGURE 5.9: Difference, in percentage, between the scattering matrix elements for a pure silicon dust grain model comprised of 50% silicon and 50% silicon enantiomers.

In addition to rotationally averaging and using a 50-50 population of dust grains and their enantiomers, the debris discs are optically thin, we would only expect to see single scattering of unpolarised light. Therefore, it is possible to use only 4 scattering matrix elements to approximate, to a first order, the scattering properties of a BAM2 grain. This also means that Hyperion will require very little modifications and the HDF5 dust file can be made in a similar manner to the spherical grains. Optically thick discs on the other hand will require a minimum of 8 elements as multiple scattering will cause other scattering elements to contribute to the polarization.

5.7 Testing Hyperion with DDSCAT

Once the HDF5 file had been constructed with the scattering properties from DDSCAT, test runs could then be performed to assess whether the files had been constructed in a manner readable by Hyperion and whether the python script used to extract and apply the size distribution was working correctly. Using the disc properties from Table 5.1, a scattered light and percent polarization image is produced (Figure 5.10) at a viewing

Table 5.1: Input parameters for the scattered light test images

Parameter	Value
Stellar Mass	1 $M_\odot$
Stellar Radius	1 $R_\odot$
Effective Temperature	5800 K
Disc Radius	10-300 AU
h_0	12.5 AU
R_0	25 AU
Disc Flaring parameter (β)	1.125
Surface Density exponent (p)	-1.0
Disc Mass	1.1×10^{-6} $M_\odot$
Minimum grain size (μm)	0.01
Maximum grain size (μm)	1.00
Number of different grain sizes	10
Gas to dust ratio	0
Density of the grains in (g cm^{-3})	3.6

angle of 90 degrees and $\lambda = 1.65$ μm .

Figure 5.10 shows a test disc (Table 5.1) in scattered light and percent polarization. The images show that the HDF5 files were constructed in a readable manner and that the script successfully extracted the correct information from the DDSCAT output and applied the size distribution. The images produced in Figure 5.10 are comparable to the scattered light images produced for HD169142 (Figure 4.15 and 4.18). We see the surface brightness decrease with radius and the polarization increases towards the edge of the disc. From here, these ballistic aggregate dust grain models could be applied to an optically thin disc. Previously, the Herbig star HD 169142 and it's transitional disc was examined using spherical dust grain models. However, the disc is not optically thin throughout the entire disc (Meeus et al. (2010), Honda et al. (2012)). Therefore, rather than examining a transitional disc (multiple scattering) with the DDSCAT dust

files, a debris disc would be a more suitable target (single scattering). The debris disc used is AU Mic and will be examined in the next Chapter.

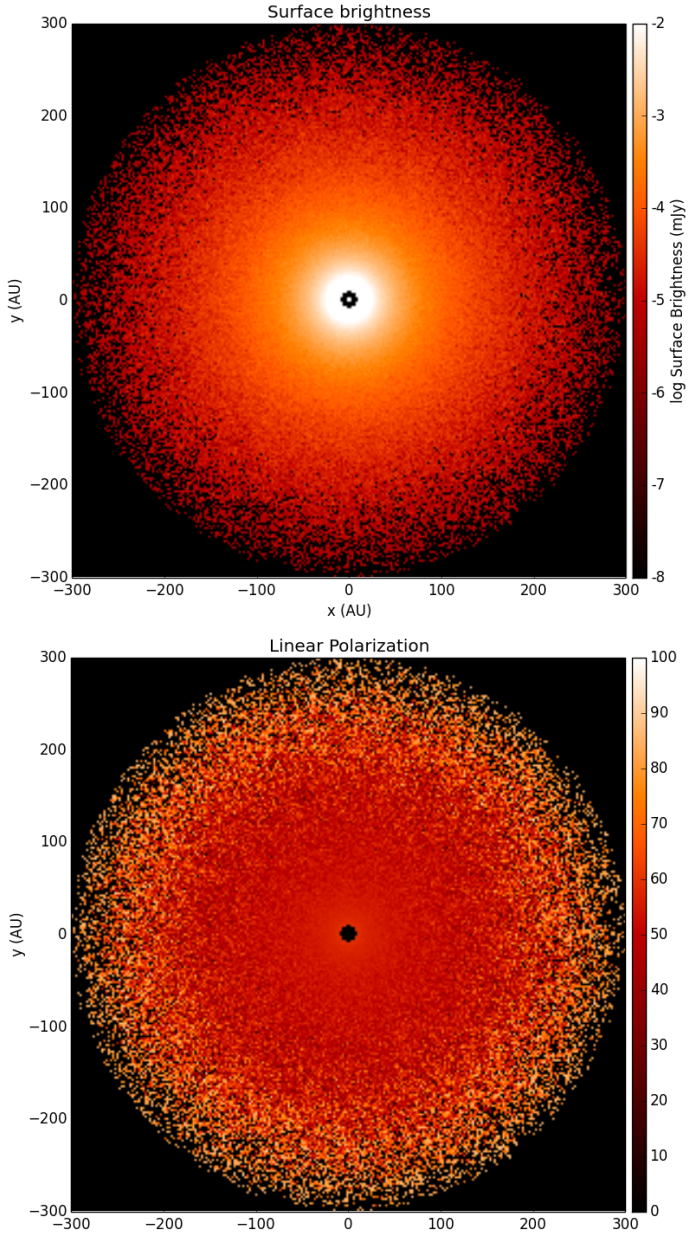

Figure 5.10: Scattered light (top) and percent polarization (bottom) images using the disc/dust parameter from Table 5.10. An initial photon count of 5×10^6 was used.

6

AU Mic

Debris discs have been imaged in scattered light for many years now, the first of these being β Pictoris (Smith & Terrile, 1984). The debris disc of AU Mic however, was first directly observed in 2003 in the R-band at the University of Hawaii 2.2 metre telescope (Kalas, Liu & Matthews, 2004). The observations were conducted with a stellar coronagraph, therefore blocking the light from the central star. From these observations, the disc was seen to be edge on and was detected from ≈ 50 AU to ≈ 210 AU. A tilt of $6^\circ \pm 3^\circ$ is also seen between the SE and NW midplane.

Prior to the observations conducted by Kalas, Liu & Matthews (2004), AU Mic exhibited signs that a circumstellar disc was present around the star. A substantial IR excess at 60 μm was seen (Tsikoudi, 1988; Song et al., 2002) which indicates thermal emission from dust grains and SCUBA 850 μm imaging (Liu et al., 2004) inferred the presence of cold dust (40 K through SED fitting).

AU Mic is of particular interest because of its close distance to us (9.94 ± 0.13 parsec from the Hipparcos Catalogue (Perryman et al., 1997)) and the fact that it is an edge-on system. β Pic is another debris disc system which has a Galactic space velocity that suggests a common origin with AU Mic (Kalas, Liu & Matthews, 2004) implying that both stars belong to the same group of nearly 20 stars, the β Pictoris moving group (Zuckerman et al., 2001), that may have separated due to the differences in their Galactic space velocities. This suggests that both systems share the same origin and were formed in the same region. Both discs show small scale structures which appear as brightness enhancements and they share an almost linearly decreasing surface brightness profile in the R-band (Kalas, Liu & Matthews, 2004). Despite these similarities the two discs vary in their colour, AU Mic is blue (Metchev et al., 2005) and β Pic is red (Golimowski et al., 2006), implying different grain sizes and distributions. AU Mic is one of the youngest members of the β Pictoris moving group with an age estimated at $12^{+8}_{-4} \times 10^6$ years (Barrado y Navascués et al., 1999; Zuckerman et al., 2001).

Following the observations of Kalas, Liu & Matthews (2004), Liu (2004) used the adaptive optics system on the Keck II telescope with the NIRC2 coronographic camera to image the disc in the H-band. An angular resolution of $0.04"/0.4AU$ was used allowing Liu (2004) to resolve the inner region ($15 - 80$ AU) of the AU Mic disc. A tilt of $2.1^\circ \pm 1.3^\circ$ between the NW and SE midplanes is also detected, which is consistent with the angle found by Kalas, Liu & Matthews (2004). They also detect radial and vertical asymmetries in the disc between the South East and North West regions. Radially, both the NW and SE show enhancements at 25 AU, however only the SE shows an enhancement at 31 AU. The enhancements at 25 and 31 AU are also located at different elevations with an additional clump displaced from the midplane in the NW side at 37 AU. These features can be seen in Figure 6.1. Liu (2004) suggests that these asymmetrical structures are due to the presence of large unseen bodies which would be due to recent planet formation. Such large bodies may perturb the dust grains, causing them to clump in ring like structures of the disc (Liou & Zook, 1999). In addition, the large bodies may create asymmetric belts through gravitational resonance with the

dust grains (Ozernoy et al., 2000).

The disc is assumed to be optically thin based on the low fractional dust disc luminosity found by Liu (2004) ($L_{disc}/L_* \approx 6 \times 10^{-4}$), the low levels of extinction (extinction of 7.84 ± 0.03 mag in the H-band) and the absence of a dark midplane in the visible and near IR which is common with optically thick edge on discs.

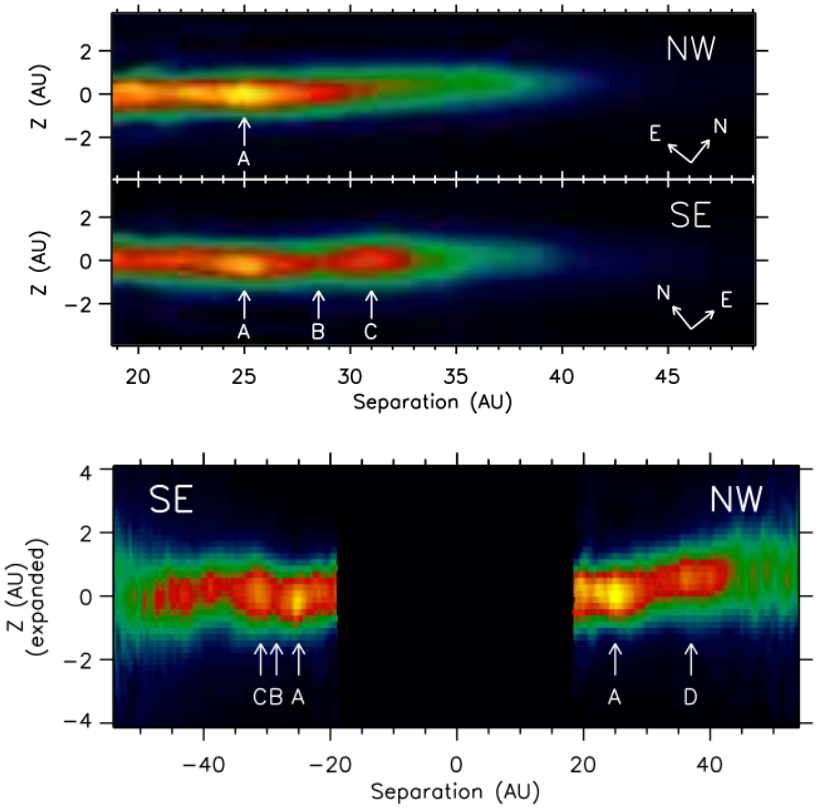

FIGURE 6.1: Images showing radial (top) and vertical (bottom) substructure within the AU Mic disc (Liu, 2004). Top: the data has been smoothed with a Gaussian kernel and each pixel has been multiplied by its distance to the star to highlight the substructure. Bottom: the plot has been expanded vertically by a factor of 5 and has been smoothed with a Gaussian kernel.

Further H-band observations (angular resolution of 0.4 AU) were performed by Metchev et al. (2005) on the Keck II telescope with the NIRC2 instrument and AO system. The disc is observed in the region between $17 - 60$ AU. Within this region, many features such as radial asymmetry, clumps and a change in the surface brightness power-law index at ≈ 33 AU are seen in the disc. These features coincide with the

the Keck II AO observations performed by Liu (2004) and can be seen in Figure 6.1. The Figure shows an asymmetrical radial structure with the brightness deficit 'B' and enhancement 'C' only being seen on the SE side. The brightness enhancement 'A' is seen in both the NW and SE side. The vertical structure also shows asymmetries as the NW side shows a local enhancement 'D' not seen on the NW side. These observations also place an upper mass limit on the possible planet in the AU Mic system (no planets are detected down to $1M_J$ at > 20 AU).

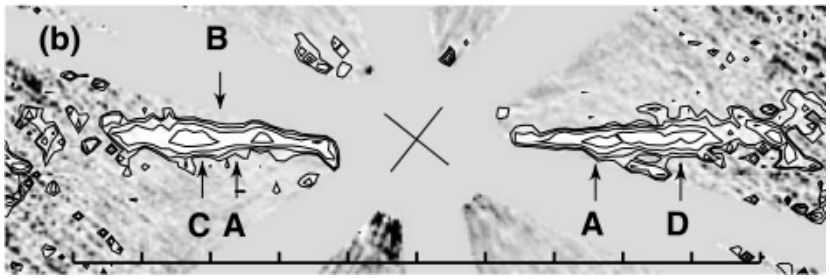

Figure 6.2: Image slice 12."0 × 4."0 showing radial substructure within the AU Mic disc (Metchev et al., 2005). The bar is 10".0 (100 AU) in length with each tick representing 10 AU. The labelling convention is the same as the one used by Liu (2004).

Using the Advanced Camera for Surveys (ACS) High Resolution Camera (HRC) on the HST, Krist et al. (2005) was able to observe AU Mic in the F606W band. Using a PSF subtraction process, they are able to see the disc from $7.5 - 150$ AU. Using the same labelling convention as Liu (2004) in the H-band, Krist et al. (2005) sees the same features present in the F606W-band (maximum 2 AU difference).

Similar to the observations performed by Krist et al. (2005), Graham, Kalas & Matthews (2007) (GKM07 from here on) used the ACS HRC on the HST to observe the AU Mic disc in the F606W band. In addition to the observations, GKM07 also made the first polarization maps in the optical wavelength of the AU Mic disc. The imaging was done of the inner 8 arcsecs radius portion of the disc. Figure 6.4 shows the results of the observations and a clear polarized signal can be seen.

Figure 6.4 shows the AU Mic disc in Stokes I with polarization vectors plotted. A pattern can be seen as the light coming from the debris disc is linearly polarized

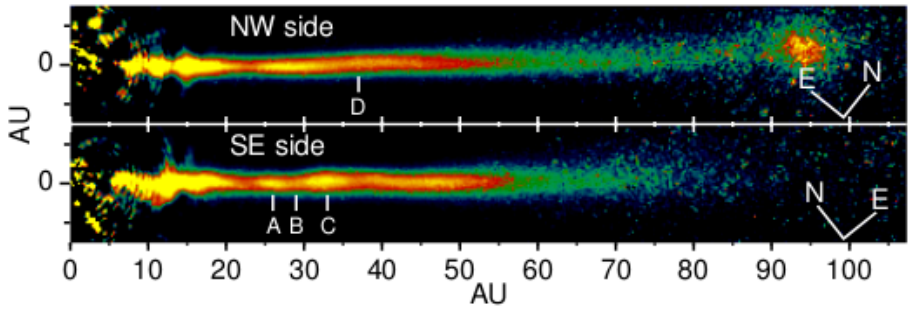

FIGURE 6.3: Image showing radial substructure within the AU Mic disc (Krist et al., 2005).

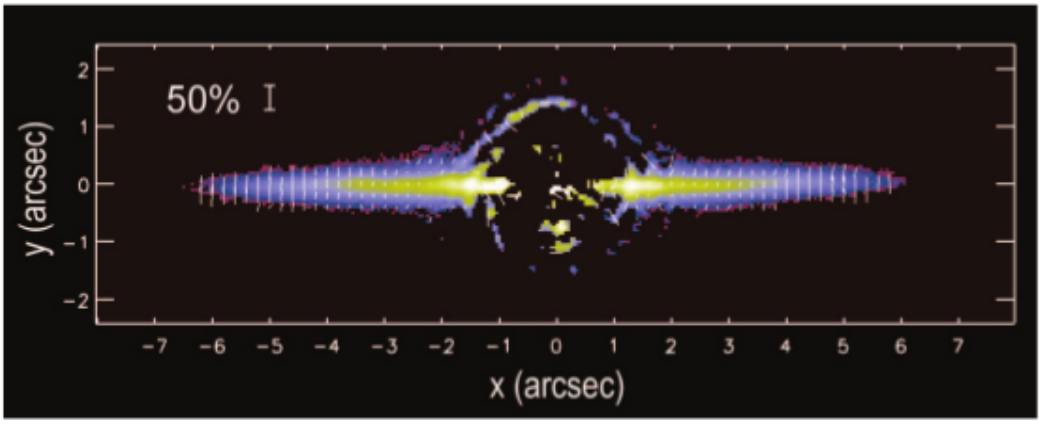

FIGURE 6.4: Stokes I image of the AU Mic disc in the F606W band. The orientation of the vectors plotted indicate the direction of the electric field and the size of the vectors are proportional to the degree of polarization (Graham, Kalas & Matthews, 2007).

perpendicular to the plane and a monotonic increase in the degree of polarization, from 0.05 to 0.40, with distance. The vectors plotted indicate the orientation of the electric field and the size of the vectors are proportional to the degree of polarization. In an optically thin disc, single scattering off small particles ($x \leq 1$) will dominate and the electric field will be orientated perpendicular to the disc. The observed degree of polarization monotonically increases, as a function of radius. This increase in polarization is likely due to the range of scattering angle decreasing along the line of sight as the radial offset increases. For silicate grains with a size parameter $x \leq 1$, the degree of polarization will peak at around 90°, therefore one would expect the degree of polarization to increase with radius as the more acute and obtuse angles are removed.

Finally at the edge of the disc, there will only be scattering at 90° which is where one would expect the highest degree of polarization to be. Another feature of the AU Mic disc GKM07 found is its blue colour in scattered light. This indicates the presence of small submicron dust grains (Kalas, Liu & Matthews (2004),GKM07).

Fitzgerald et al. (2007) (F07 from here on) performed JHK' band observations. They obtained high resolution imaging, at the Keck II telescope, of the inner 5 arcsec (8 to 60 AU) of the AU Mic disc. Their observations indicate the existence of substructure within the inner disc which can be seen in the non-uniform midplane surface brightness. The use of Adaptive Optics (AO) in addition to the coronagraph helped increase the sensitivity to the disc.

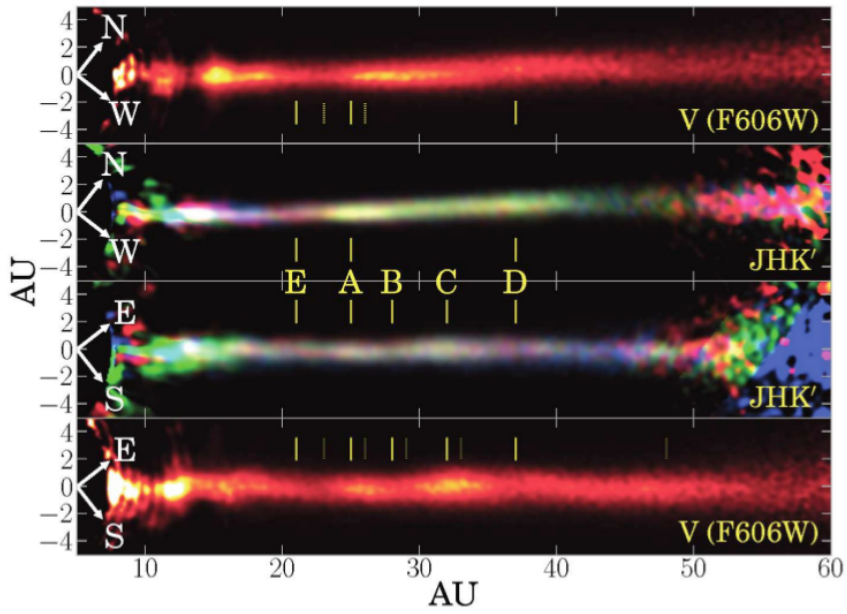

Figure 6.5: Image showing the radial substructure in the AU Mic disc in the F606W, J, H and K' bands (F07).

The substructures detected by F07 are comparable in position to those detected by Liu (2004), Krist et al. (2005), Metchev et al. (2005), however an additional feature (denoted E), initially identified by Krist et al. (2005), is also detected by F07. F07 does note that any changes in the structure seen between (Liu (2004), Krist et al. (2005), Metchev et al. (2005)) may be due to differences in the PSF subtraction process.

Millimetre observations of AU Mic have also been conducted (MacGregor et al., 2013). The observations were performed using ALMA at 1.3 mm. They confirm the presence of a dust belt extending to 40 AU and find a new unresolved central peak (Figure 6.6). One possible explanation for the peak is that it is due to the stellar photosphere; however this is ruled out due to the photosphere being much fainter, at mm wavelengths, than the central peak. In addition, the radio-wave flare decay time is very quick (order of an hour, Kundu et al. (1987)) and the ALMA observations spanned over four 2-hour long sessions. Yet the peak was observed in all four sessions, further ruling out the photosphere as a source for the peak. Another possibility suggested by MacGregor et al. (2013) is that the peak is produced by millimetre dust grains in a distinct planetesimal belt (3 AU) at temperatures up to $T \approx 75$ K.

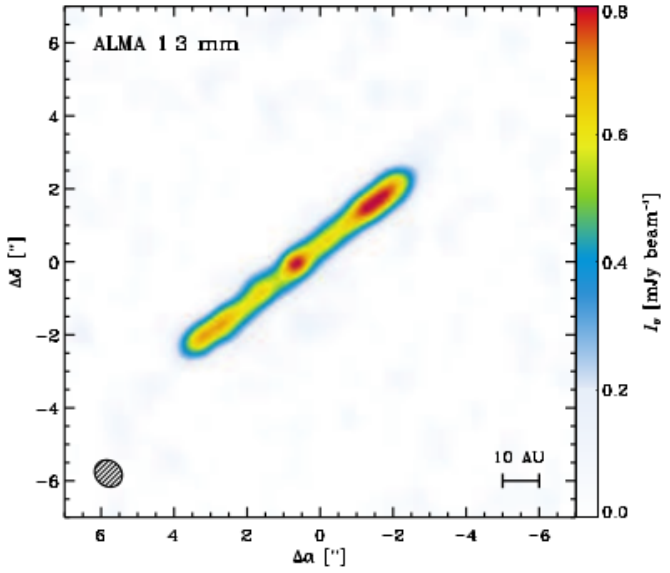

FIGURE 6.6: 1.3 mm ALMA image of the AU Mic disc (MacGregor et al., 2013). The ellipse in the bottom left corner represents the beam size (8×7 AU).

More recently, HST Space Telescope Imaging Spectrograph (STIS) Point Spread Function Template Subtracted Coronagraphy (PSFTSC) imaging of the AU Mic disc was performed over two epochs (≈ 1 year) by Schneider et al. (2014). Their observations confirm the brightness asymmetry between the NW and SE, however they are able to see the asymmetry at a distance $< 15 - 20$ AU. Additional brightness enhancements

are also seen in the SE side at 13 AU and on the NW side at 45 AU.

6.1 Previous AU Mic Modelling

As the debris disc of AU Mic is edge on ($2.1° \pm 1.3°$), the face on disc structure cannot be directly observed, however the midplane structure can be observed. This has led to a range of disc structures being used to model AU Mic.

6.1.1 Stellar Model

The spectral classification of AU Mic is consistent with an M-type star. There are however small variations in the subclass. Initial IRAS observation (Mathioudakis & Doyle, 1991) determined the star as M-type and fit a blackbody with an effective temperature of 3600 K. More recently, AU Mic was designated as M1Ve through observations on the FEROS spectrograph at the ESO telescope (Torres et al., 2006). Since the disc is edge on to our line of sight, the disc will obscure the starlight. Therefore, the disc model will also need to be considered in determining which stellar model to use. A summary of previous stellar models can be seen in Table 6.1.1.

Table 6.1: Summary of stellar NextGen models (Hauschildt, Allard & Baron, 1999) used for AU Mic

Paper	T_{eff} (K)	log(g)	Luminosity ($L_\odot$)	Mass ($M_\odot$)	Radius ($R_\odot$)
Metchev et al. (2005)	3600	4.5	0.13	0.99	0.93
Augereau & Beust (2006)	3700	4.5	0.09	0.63	0.74
Fitzgerald et al. (2007)	3600	4.5	0.12	0.89	0.88
MacGregor et al. (2013)	3720	4.4	0.11	0.60	0.80

6.1.2 Liu et al. 2004

The AU Mic disc was observed in the submm (850 μm) using the James Clerk Maxwell Telescope (JCMT)/SCUBA Liu et al. (2004). The stellar spectrum is modelled using a NextGen stellar spectrum (Allard, Hauschildt & Schwenke (2000), Allard et al. (2001)), which is normalised to the observed K-band magnitude, and the dust is modelled using a modified blackbody. The model was fitted to the observational data which include data from SIMBAD, Hipparcos catalog, 2MASS (Cutri et al., 2003), IRAS Faint Source Catalogue (Mathioudakis & Doyle, 1991) and SCANPI photometry (Helou et al., 1988). The dust emissivity is kept constant for $\lambda < 100$ μm and is proportional to $\lambda^{-\gamma}$ for $\lambda > 100$ μm (γ is the opacity index). For $\gamma = 0.8$, a modified blackbody fits the SED with a temperature, $T = 40 \pm 2$ K (1 σ error).

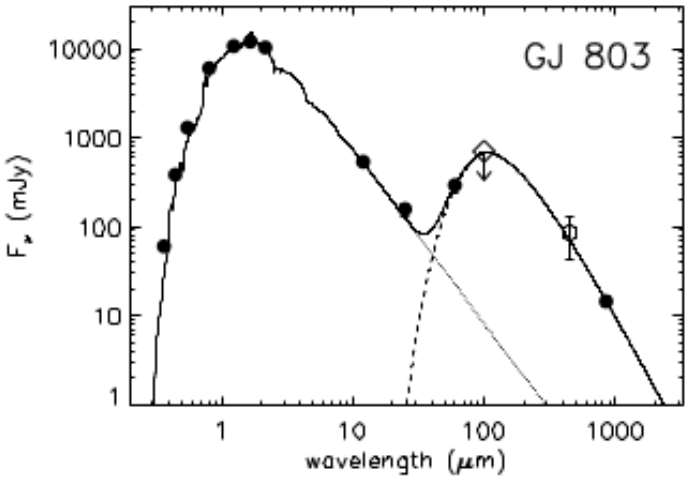

Figure 6.7: AU Mic SED fits for (Liu et al., 2004).

Figure 6.7 shows that the modified black body provides a good fit to the observational data. While this method can provide an estimate on the mass of the dust contained within the disc, it is only fitted to the SED and not the surface brightness of the disc.

6.1.3 Metchev et al. 2005

Metchev et al. (2005) used the three dimensional radiative transfer code MC3D (Wolf & Henning, 2000; Wolf, 2003) to model the SED and scattered light from the disc. The disc is modelled as a single continuous unflared (constant scale height $h = 0.8$ AU) disc with a number density profile $\propto r^{-\alpha}$, where r is the radial offset from the star and α is the power law size distribution (3.5). A maximum radius of $r_{max} = 1000$ AU is used so that the disc model covers the R-band observations (Kalas, Liu & Matthews, 2004) and the JCMT/SCUBA observations (Liu et al., 2004). This, however, left a large number of free parameters (volume density profile, inner radius r_{min}, dust mass M_{dust} and grain sizes a_{min} and a_{max}) which were determined through parameter tests. The dust grains used are spherical ISM grains composed of astronomical silicate (Draine, 2000) and graphite (Draine & Goodman, 1993). The optical properties of the grains were calculated using Mie Theory by Draine & Lee (1984). The final model used by Metchev et al. (2005) is summarised in Table 6.2.

Table 6.2: Summary of the disc model used by Metchev et al. (2005)

Parameter	Value
Dust Mass (M_{dust})	0.11 $M_\oplus$
Disc Radius($r_{in} - r_{out}$)	$10 - 1000$ AU
Grain Size ($a_{min} - a_{max}$)	$0.5 - 300$ μm
Dust power law size distribution exponent	-3.5

The SED produced by Metchev et al. (2005) was fitted to the same observational data points used by Liu et al. (2004). An extensive parameter test is conducted by Metchev et al. (2005) to determine the best fit for both the SED and surface brightness profile. From these tests, they find that by decreasing M_{dust} or by increasing the size of a_{min} or a_{max} (decreasing the number of small grains to scatter off) results in lowering the flux of the surface brightness profile. This also lowers the SED flux in a similar manner.

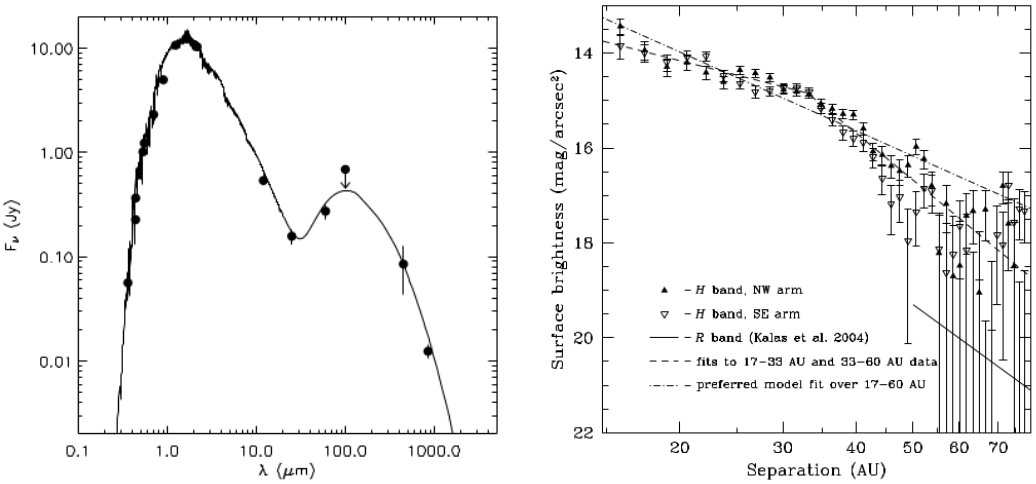

Figure 6.8: SED and surface brightness fits for Metchev et al. (2005). The surface brightness image has H and R-band (Kalas, Liu & Matthews, 2004) data plotted.

Figure 6.8 shows the MC3D disc model against the observational SED and surface brightness data points. The disc model is able to fit to the SED and confirms the mass estimate from Liu et al. (2004). Fitting the disc model surface brightness allows the dust grain size to be constrained at $> 0.5^{+0.5}_{-0.2}$ μm in the 50-60 AU. However, the model produced in MC3D is limited by the data (R and H band) as it is not sensitive to grain sizes $\gg 1$ mm, therefore an upper limit on the grain size is not determined. The data also only extends to 60 AU, beyond this the noise begins to dominate the data.

6.1.4 Krist et al. 2005

Krist et al. (2005) modelled the AU Mic disc in scattered light using their own three dimensional scattering code. The code is designed so that single scattering dominates (any multiple scattering is considered to be insignificant) and that the scattered light is modelled using a modified HG scattering phase function. In addition to this, the albedo is set to 0.5. The disc density structure is defined by an axial symmetrical equation:

$$\rho(R, z) = \rho_0 \left(\frac{R_0}{R} \right)^p \phi(z, h) \tag{6.1}$$

where R is the radius, z is the height, h is the scale height, p is the surface density exponent and $\phi(h, z)$ describes the vertical density distribution as a Lorentzian profile,

$$\phi(h, z) = \frac{1}{(1 + (z/h(R))^2)} \tag{6.2}$$

and

$$h(R) = h_0 \left(\frac{R}{R_0} \right)^{\beta} \tag{6.3}$$

where β is the disc flaring parameter. A Lorentzian profile is used because they see that the inner disc's vertical brightness profile has a sharp midplane with extended wings. Initial models were composed of three annular regions, in which the inner radius was arbitrarily set at 3 AU while the outer radius for the three regions were set as free parameters. Metchev et al. (2005) used an iterative nonlinear least squares fitting routine to determine the best fit disc parameters in both the NW and SE side simultaneously. The model fit parameters used can be seen in Table 6.3.

Despite that the minimum and maximum parameters differ, in some parameters, quite significantly, the two fits produced very similar results. The surface brightness fit can be seen in Figure 6.9.

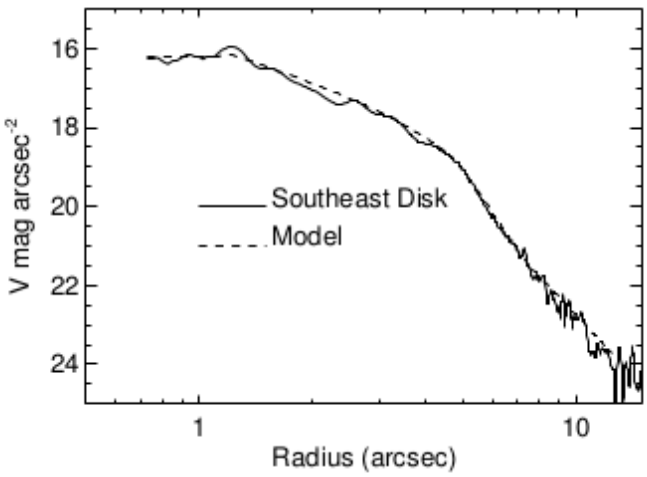

Figure 6.9: Surface brightness plot of the SE side of the AU Mic disc in comparison to the disc model produced by Krist et al. (2005).

Table 6.3: Summary of the disc models used by Krist et al. (2005)

Parameter	Minimum	Maximum
Asymmetry parameter	0.372	0.374
Zone 1		
Radius (AU)	11.70 - 48.6	11.71 - 49.1
p	-0.066	-0.053
β	0.074	0.085
Zone 2		
Radius (AU)	48.6 - 78.9	49.1 - 82.4
p	-4.66	-4.58
β	2.45	2.52
Zone 3		
Radius (AU)	78.9 - 250	82.4 - 250
α	-2.68	-2.31
β	0.01	0.59

Figure 6.9 shows that Krist et al. (2005) are able to successfully fit the radial surface brightness profile. However, it should be noted that this plot only shows the SE side of the disc. The dust model used by Krist et al. (2005) is a very simple model. Rather than using size distribution of grains, a HG function is used to model the dust across the entire disc. While this works in fitting the surface brightness, it is unlikely that this model will be able to fit the observational SED data as millimetre grains are required to fit the steep slope at the millimetre regime of the SED (Metchev et al., 2005).

6.1.5 Graham et al. 2007

GKM07 assume a single continuous disc with a surface density which follows a power law and grain properties which are uniform across the disc. They produce one dimensional surface brightness profiles by integrating along the line of sight through the disc. The disc is also optically thin in the IR (Liu, 2004), therefore multiple scattering will

not occur. Assuming the star light is unpolarized and only single scattering, GKM07 then assumes that the Stokes parameter $U = 0$.

A range of dust models are explored to simultaneously fit their surface brightness and polarization data. Initially they use a semi-empirical Henyey-Greenstein (HG) function to model the scattering by small particles. The polarization and phase function were modelled using:

$$S_{11}(\theta) = \frac{1}{4\pi} \frac{1 - g^2}{(1 + g^2 - 2g\cos\theta)^{3/2}} \tag{6.4}$$

$$P(\theta) = -p_{max} \frac{\sin^2\theta}{1 + \cos^2\theta} \tag{6.5}$$

where p_{max} is the maximum linear polarization ($0 \leq 1$), g is the asymmetry parameter ($-1 < g < 1$). Figure 6.10 shows the best fit models to the surface brightness and polarization data.

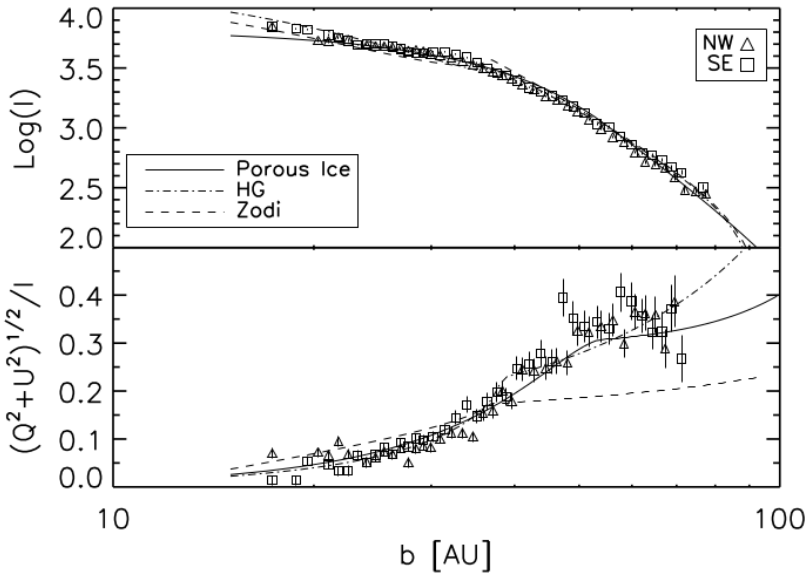

Figure 6.10: Model fits to the surface brightness and polarization data. The plot shows three models fitted to the data, Porous ice, HG and zodiacal dust (GKM07).

The HG function provides a good fit for scattering of spherical grains with a size

parameter $x \leq 1$ and only has two free parameters, allowing the function to be computationally simple to evaluate. The HG fit achieves a 'goodness of fit', $\chi^2 = 1.65$ with $p_{max} = 0.53$, $g = 0.68 \pm 0.01$ and an inner radius $r_1 = 38 \pm 0.5$ AU. However, this function assumes an outer radius of $r_2 = 92.5 \pm 4.7$ AU. If the outer radius is fixed to 200 AU, then the $\chi^2 = 1.76$ which may indicate that a single population of dust grains cannot accurately model the entire disc in scattered light. In addition to the HG function, a range of dust grain models used by GKM07 are summarized in Table 6.4.

Table 6.4: Summary of the dust grain models used by GKM07

Dust Model	Radius of the Disc (AU)	Refractive Index	p_{max}	g	χ^2
Porous water ice	$53.1(2.1) - 177.8(69.7)$	$1.03 - 0.01i$	0.94	0.81	1.6
Dirty ice	$41.6(0.8) - 100.4(3.3)$	$1.33 - 0.01i$	0.47	0.68	3.1
ISM	$35.8(0.4) - 87.1(4.4)$	MRN77	0.42	0.45	4.0
Silicate	$34.1(0.5) - 85.9(3.3)$	$1.65 - 0.01i$	0.38	0.59	4.4

Where g is the asymmetry parameter and p_{max} is the maximum linear polarization. The numbers in parentheses correspond to the 1 σ errors and MRN77 is Mathis, Rumpl & Nordsieck (1977). Porous water ice has a porosity of 91%.

The dust grains in Table 6.4 are modelled as single spherical particles using Mie theory. It is found that the χ^2 fit varies with the choice of refractive index used. The best fit in terms of χ^2 comes from the porous water ice ($\chi^2 = 1.6$) grain model which provides a better fit than the HG function and can be seen in Figure 6.10. While this model improves on the model produced by Metchev et al. (2005) by simultaneously fitting to the surface brightness and polarization, the model only considers a single size grain. Similar to the limitations the model produced by Metchev et al. (2005) suffers from, GKM07 model will not be able to model the SED due to the lack of millimetre gains in the disc.

6.1.6 Fitzgerald et al. 2007

A two region disc structure is used to model the disc. The disc is split into a inner region consisting of large millimetre size grains and an outer region consisting of small micron size grains. Figure 6.11 illustrates how the disc is split up into the two regions. A model containing small particles in an outer region was first considered by (Kalas, Liu & Matthews, 2004) as they determined that the radiation force from the star would be too weak to completely remove small grains form the system. AU Mic is an M-dwarf star which produces 3-5 orders of magnitude less radiation pressure on dust grains than from an A star (Saija et al., 2003). Therefore, the population of small grains in the outer region would outgrow the population of large grains. In addition to the stellar radiation, the inner region would be devoid of smaller grains due to aggregation of small grains to larger grains and PR drag (Krist et al., 2005).

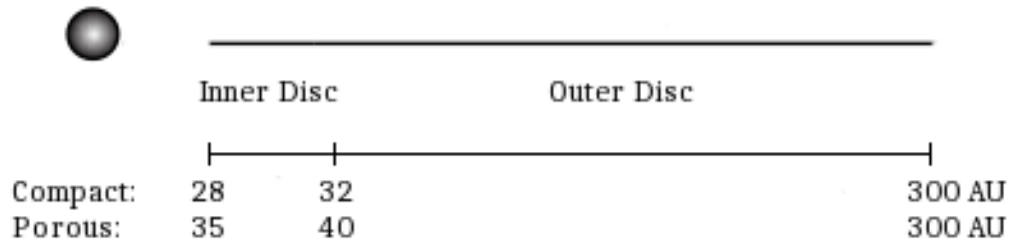

Figure 6.11: An illustration of the disc model used by F07. The illustration shows the compact and porous grain disc models. The disc models are split into an inner disc consisting of millimetre size grains and the outer disc consisting of micron size grains.

The disc models are produced using the radiative transfer code MCFOST. MCFOST uses the same equation to describe a flared axis-symmetric disc (Equation 3.2) as Hyperion does. The scale height flaring parameter (β) is set to zero to produce a disc with no flaring and a vertical density distribution which follows a Gaussian ($\sigma = 0.8$ AU).

Two dust models are also examined, these being compact spherical grains and porous spherical grains (vacuum fraction of 80 percent). The compact grains are pure silicate (Draine, 2000), while the porous grain is created using effective medium theory

(EMT) and is made up of amorphous silicate, graphite and ice (Mathis & Whiffen, 1989). The disc structure for the two models is illustrated in Figure 6.11 and summarized in Table 6.5. These models represent the best fit dust models for the F606W (GKM07) and H-band (F07) observational data.

Table 6.5: Summary of the disc models used by Fitzgerald et al. (2007)

Dust Model	Radius of the Disc (AU)	Grain Size Size Distribution	Power Law
		Porous	
Inner Disc	$35 - 40$	$3 - 6$ mm	-3.5
Outer Disc	$40 - 300$	$0.05 - 3.0$ μm	-4.1
		Compact	
Inner Disc	$28 - 32$	$1 - 2$ mm	-3.5
Outer Disc	$32 - 300$	$0.15 - 50.0$ μm	-4.1

The decision to split the disc into two regions of millimetre and micron grains comes from the radiation pressure and PR-drag removing smaller grains close to the star. In addition, smaller grains are unlikely to exist in the inner region due to their presence creating an overly steep SED at large λ. The shallow slope at the mm regime of the SED however is best fit with mm grains (Metchev et al., 2005). Very large grains ($a_{max} >$ mm) may be present in the inner region but undetectable in scattered light. The SED model produced by F07 is fitted to the data points from Liu et al. (2004), Metchev et al. (2005) and Spitzer Chen et al. (2005). Both the compact and porous disc models are examined. F07 find that both the compact and porous grain models provide a reasonable fit to the observed data points, however, Figure 6.12 only shows the SED fit for the porous grain model. An extensive χ^2 analysis was conducted to determine the best fit model parameters for both disc models in which they find the compact grain model gives $\chi = 8.6$ and the porous grain model give $\chi = 10.9$. The porous grain model can be seen in Figure 6.12.

Building on the work that GKM07 conducted, F07 performed high resolution observations in the near-IR JHK' bands on the Keck II telescope (Figure 6.5. Their observations show a break in the midplane surface brightness between 30-35 AU but no break at 15 AU which is seen by GKM07 in the F606W band. For the F606W and H-band, both the porous and compact grains provide a reasonable fit to the observed surface brightness. For polarization, the compact grains fail to reach the maximum fractional polarization of ≈ 35 percent, as seen by GKM07. The porous grains however, fit the observed polarization well, with the curve plateauing at the maximum of ≈ 35 percent at 40 AU.

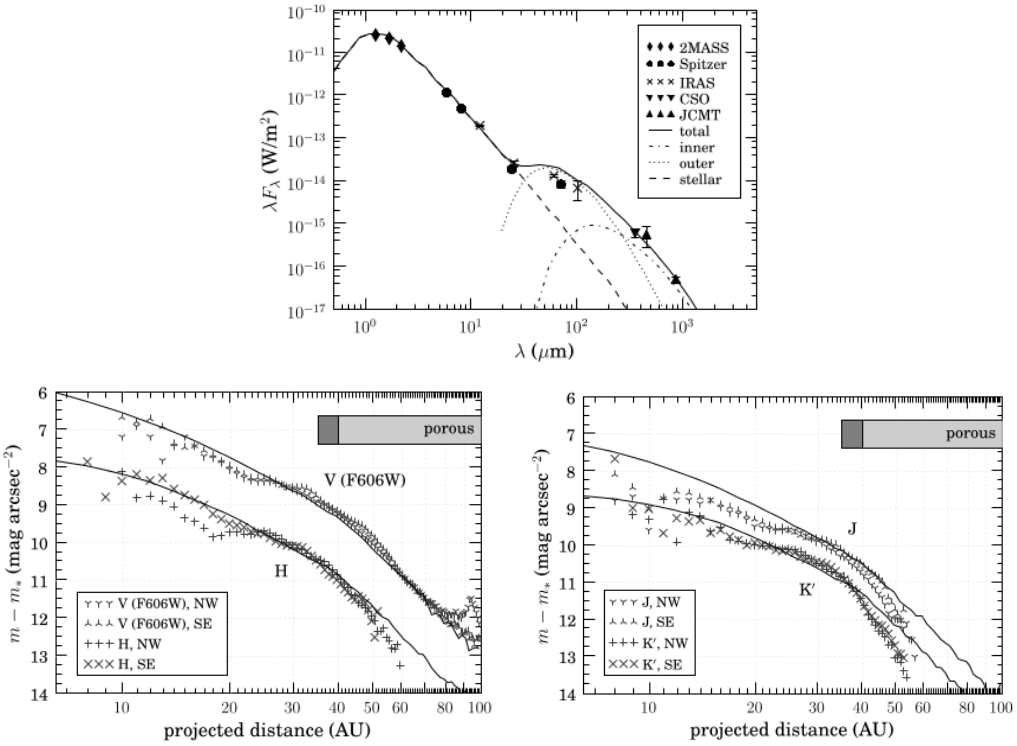

FIGURE 6.12: Surface brightness profiles for AU Mic in the F606W, H-band (left) and J and K' band (right) (Fitzgerald et al., 2007).

The models produced by F07 have provided the most robust examination of the AU Mic disc in scattered, polarized light and of its SED.

6.1.7 Discussion

While Liu et al. (2004) obtains a good fit with a modified black body, the model only fits to the SED and not the surface brightness or polarization. They also only consider a modified black body model to describe the dust. While this is useful in determining the mass of the disc, it does not provide any information and the scattered light or polarization of the disc.

The model produced by Krist et al. (2005) provides a good fit to the observed F606W band HST data, however, their model uses a modified HG function to describe the entire disc. Recent millimetre observations (MacGregor et al., 2013) show that the inner region of the disc is dominated by millimetre size grains. In addition, the shallow slope at the mm regime of the SED however is best fit with mm grains (Metchev et al., 2005). The model produced by GKM07 also suffers from the same problem as it uses a single size grain Mie model to describe the dust grains.

The models of most interest are the Monte Carlo models produced by Metchev et al. (2005) and F07. Both models assume a flat disc with no flaring, however they assume a very different a_{min} and a_{max}. Metchev et al. (2005) uses a grain size ranging from $0.5 - 300$ μm , however this constraint is only valid over the $50 - 60$ AU region (region for which the $R-H$ color data was available). Beyond 60 AU, only the R band data was available and the scattered light data becomes very noisy.

F07 provides the most robust SED and surface brightness fitting as they fit their model to more observational data and they also conduct an extensive χ^2 analysis. The observations in scattered light performed by F07 provided additional information (JHK' and F606W (GKM07)) to constrain the disc and dust parameters for a larger region of the disc. For this reason, this thesis will be using F07 disc models as a basis of the models created in Hyperion.

6.2 Modelling AU Mic with Hyperion

As previously mentioned, the disc models produced by F07 will be used as a basis for the models created in Hyperion. The full disc model used by F07 can be seen in Table

Table 6.6: Best fit disc models from Fitzgerald et al. (2007)

	Compact		Porous	
Parameter	Inner Disc	Outer Disc	Inner Disc	Outer Disc
r_{in} (AU)	28	32	35	40
r_{out} (AU)	32	300	40	300
p	1.5	-2.5	1.5	-2.5
β	0.0	0.0	0.0	0.0
R_0 (AU)	20	20	20	20
h_0 (AU)	0.8	0.8	0.8	0.8
M_{dust} ($M_\odot$)	8.1×10^{-8}	8.1×10^{-10}	3.0×10^{-8}	6.9×10^{-10}

6.6. The final stellar model used was also adopted from F07. The compact grain model used is a pure astrosilicate (Draine, 2000) grain model whose optical properties were already present in the BHMie wrapper provided with Hyperion. The RI for the porous grain model was taken from Mathis & Whiffen (1989). This involved creating an RI file for the BHMie wrapper to read so that the scattering properties could be calculated. As a sanity check, the albedo of the dust models were compared to those calculated by F07. The values can be seen in Table 6.7 and are found to be consistent with those determined by F07.

The aim in this Chapter will be to confirm F07 results by modelling AU Mic with the same disc/dust parameters and to improve on their results through parameter tests. First, the disc models produced in Hyperion will be fitted to the observational SED data. When a suitable fit is made, the best fit SED model will then be used to fit the surface brightness data. Adjustments, via parameter tests, will be made so that the final disc model simultaneously fits the SED, surface brightness and polarization.

Table 6.7: Summary of the dust grain models used

	F07		This Work	
Wavelength (μm)	g	A	g	A
Porous				
0.606	0.83	0.52	0.84	0.52
1.600	0.81	0.54	0.81	0.54
Compact				
0.606	0.66	0.83	0.66	0.83
1.600	0.60	0.81	0.59	0.82

6.2.1 SED

The initial parameter values used to model AU Mic are summarized in Table 6.6, however a parameter test was also conducted to determine whether the values from F07 actually produce the best fit for Hyperion. These parameter test were conducted changing one parameter at a time while the other parameters were fixed to the values summarized in Table 6.6.

It should be noted that a benchmark test comparing radiative transfer codes, including MCFOST, to Hyperion was conducted by Robitaille (2011), in which they found a maximum difference of $\approx$ 20 percent in the SED and surface brightness flux between the Radiative Transfer codes for a flared disc model. Robitaille (2011) does however mention that the results are within dispersion of results obtained from the other codes.

Metchev et al. (2005) has already showed that the SED flux will be lowered by decreasing M_{dust} or by increasing the size of a_{min} or a_{max}. The parameter tests conducted here will explore how surface density exponent (p), disc flaring parameter (β) and position of the inner radius (R_{min}) affect the SED.

Figure 6.13 shows the parameter tests conducted on the compact grain model and disc. Moving the location of the inner radius r_{min} closer to the star increases the flux in the mid-IR. This is to be expected as the grains are now hotter due to their close

proximity to the star. The surface density exponent for the inner region ($0.5 \leq p_{inner} \leq 2.5$) however, does not significantly change the SED flux. The inner region only spans from $28-32$ AU for the compact grains, therefore a change in p_{inner} is unlikely to have any significant effect on the SED flux. Conversely, the outer disc spans from $32-300$ AU, therefore any change in p_{outer} ($-1.0 \leq p_{outer} \leq -3.0$) will be seen in the SED flux due to the surface density falling off over a larger radius.

The flaring parameter ($0.0 \leq \beta \leq 1.0$) on the other hand has very little influence on the SED flux in this parameter test. The AU Mic disc is currently modelled as a continuous disc, so unlike the transitional disc HD 169142 from Chapter 2 and 4, there is no disc wall from an annular gap to intercept the star light. Varying β from 0-1 only changes the scale height from 0.8 to 12 AU respectively.

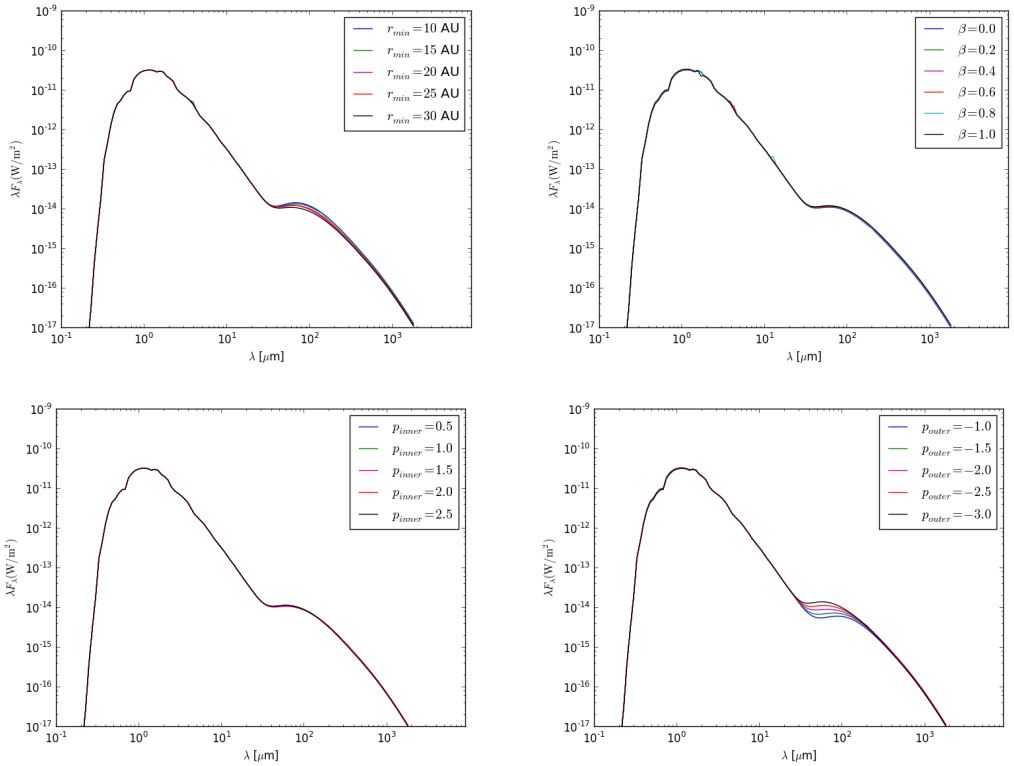

FIGURE 6.13: SED parameter tests conducted for the minimum radius of the disc R_{min} (top left), flaring parameter β (top right), surface density exponent for the inner disc p_{inner} (bottom left) and outer disc p_{outer} (bottom right).

The spectroscopic and imaging observations used to constrain the disc model include: Spitzer Chen et al. (2005), IRAS Faint Source Catalogue (Mathioudakis & Doyle, 1991), SMA (Wilner et al., 2012), optical spectra (Kiraga, 2012), 2MASS (Cutri et al., 2003) and JCMT (Liu, 2004).

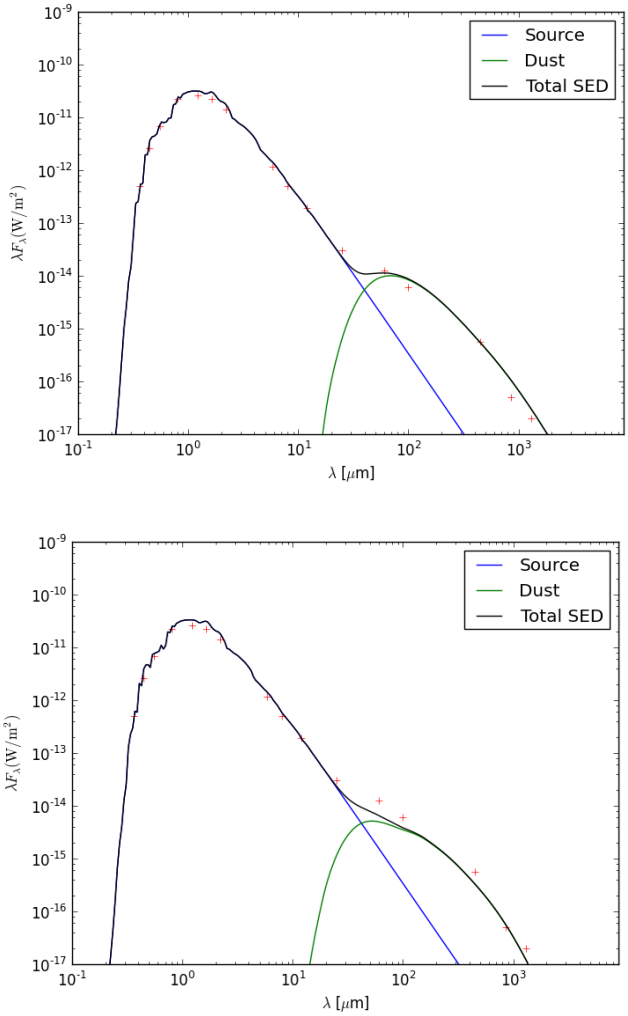

Figure 6.14: Best fit synthetic SED models created in Hyperion for the compact grains (top) and porous grains (bottom).

Both the compact and porous grain models visually fit the SED well. However, the SED for our porous model does not match the SED produced by F07 porous model. F07 sees an excess around $60 - 70$ μm while our model falls short in this wavelength range. In contrast the compact SED produced by F07 falls short in this wavelength

range while our model fits the data points very well. This could be explained by the mass of the disc being higher in the compact model which will mean a larger number of dust grains for thermal emission and by the compact grains having a size distribution of 0.15-50 μm in the outer disc.

6.2.2 Surface Brightness and Polarization

Once again, the parameters listed in Table 6.6 are used as initial values for our model. Similarly to the previous subsection, a parameter test will be conducted to see how the surface density exponent (p), disc flaring parameter (β) and position of the inner radius (R_{min}) affect the surface brightness profile. Figure 6.15 shows the results of the parameter tests conducted for the H-band.

The parameter test seen in Figure 6.15 were conducted in the H-band, however the tests on the F606W, J and K' behaved in a similar manner. The surface density exponent for the inner disc was varied from $0.5 \leq p_{inner} \leq 2.0$ and the for the outer disc was varied from $-1.0 \leq p_{outer} \leq -3.5$. Both parameters have little effect on the SBP due to the disc being edge on. Therefore the SBP seen will be from the midplane rather than the surface of the disc. The disc flaring parameter β was varied across both discs from $0.0 \leq \beta \leq 2.0$. Increasing β significantly decreases the flux of the SBP. During these parameter tests, h_0 and R_0 are kept constant, therefore as β increases the scaleheight increases ($h(R) \propto R^{\beta}$). This results in the already optically thin disc being spread vertically, due to the scale height increasing with radius, which decreases the optical depth and probability from scattering of a dust grain. Decreasing the dust mass M_{dust} and increasing the grain size were found to decrease the flux of the surface brightness profile (Metchev et al., 2005).

One important parameter that needs to be taken into account is the photon count. In the outer disc, the surface density is $\propto r^{-2.5}$, therefore the dust density at the edge of this disc (r_{out}) will be much less than that closer (r_{in})to the central star. As the disc is already optically thin, the chances of scattering off dust close to r_{out} will be very low, even with first forced scattering enabled. Therefore a sufficiently high photon count

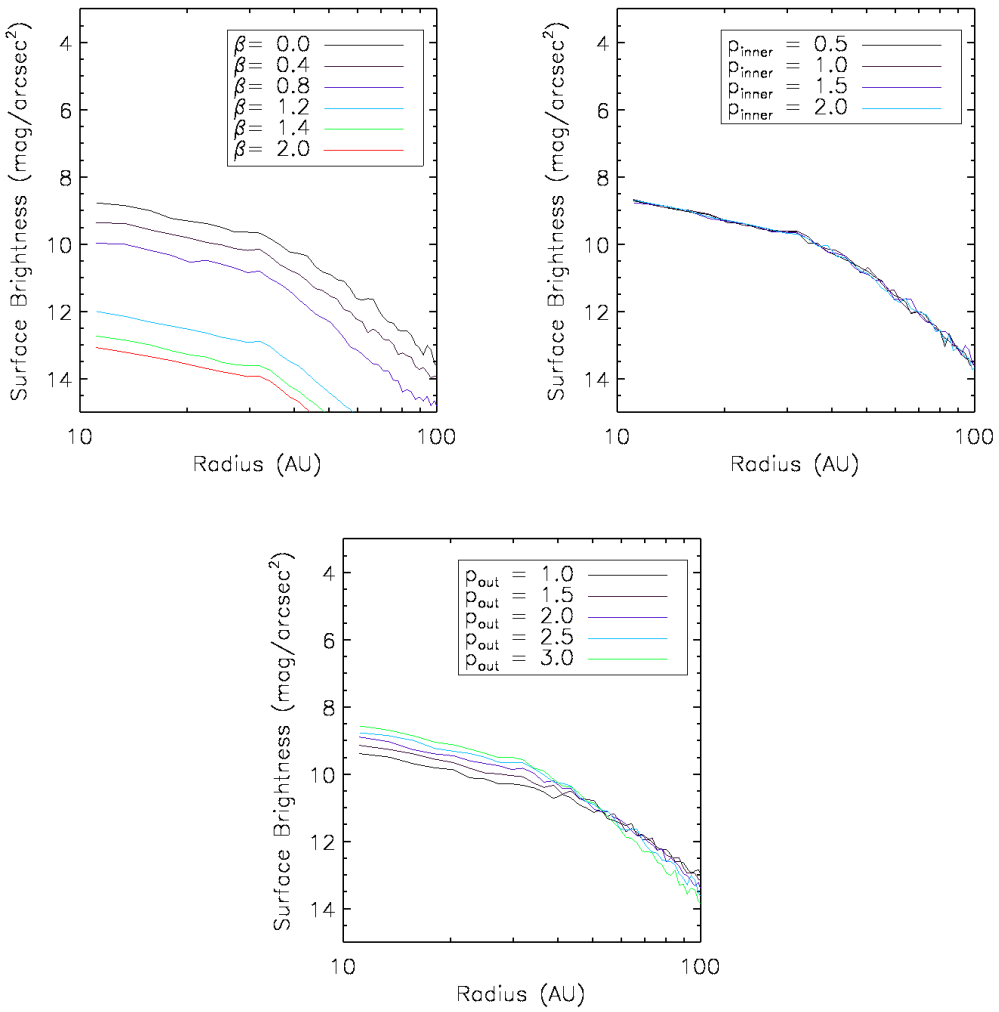

FIGURE 6.15: Surface brightness parameter tests conducted for the flaring parameter β (left), surface density exponent for the inner disc p_{inner} (right) and outer disc p_{outer} (bottom) in the H-band.

(1×10^7) was required to ensure that scattering occurred off the grains at r_{out}.

During the parameter test, an attempt was made to fit the split midplane surface brightness power law indices calculated by F07, however both the compact and porous models were unable to fit the observed power law indices. The power law index increased with the surface density exponent p, however β had no significant influence on the power law index. With the current two disc model, fitting the SED, surface brightness, polarization and surface brightness profile power law exponents was not possible. This could be an indication that a two disc model is too simple and a more

complex model is required.

Using the same models as in Figure 6.14, we now look at the surface brightness profiles in the JHK' and F606W bands and linear polarization in the F606W band of the disc .

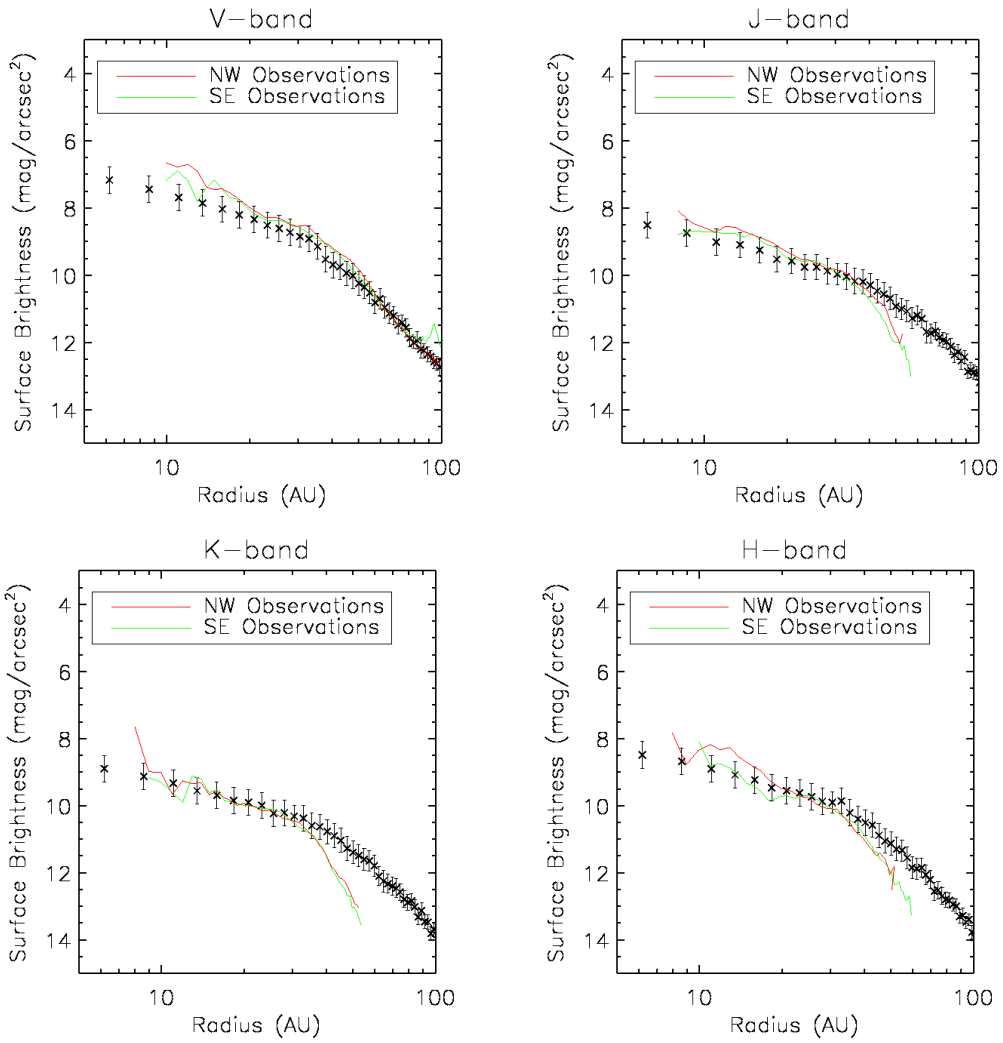

Figure 6.16: Plots showing the surface brightness in the JHK' (Fitzgerald et al., 2007) and F606W (Graham, Kalas & Matthews, 2007) band for the compact grain model.

Similar to F07, the porous grains are able to produce a reasonable fit to the observed surface brightness in the F606W and H band however, the porous model fails to drop off in brightness at distances greater than $\approx$ 40 AU. The compact grain also provides a

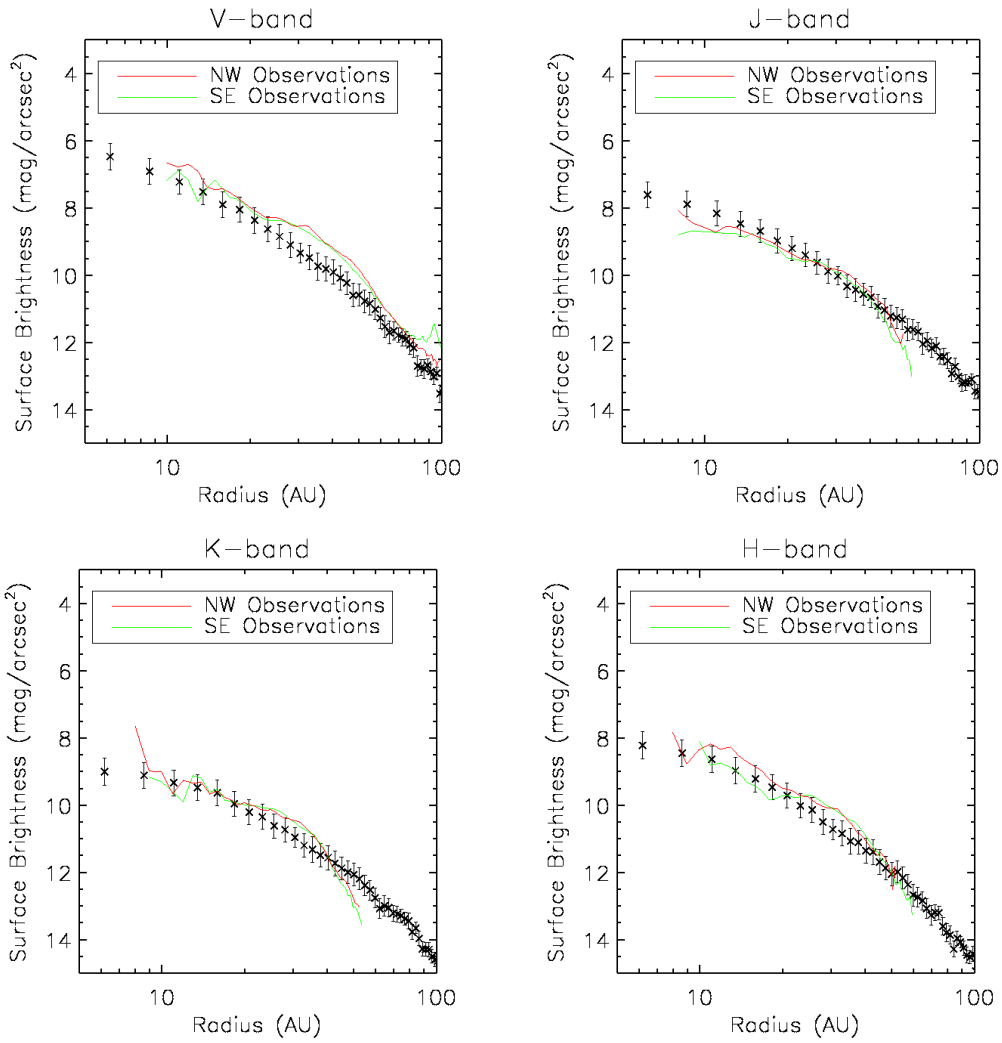

Figure 6.17: Plots showing the surface brightness in the JHK' (Fitzgerald et al., 2007) and F606W (Graham, Kalas & Matthews, 2007) band for the porous grain model.

good fit to the F606W data however overestimates the brightness at distances greater than ≈ 40 AU for the JHK' data. This could be due to the compact grains having a greater albedo than the porous grains and therefore are more reflective than the porous grains in the JHK' and F606W wavelength range.

The compact grains fail to match the observed polarization as a function of radius and instead the model values plateau at low polarization. The porous grain model is able to produce a better fit to the observed polarization. Similar to F07, the porous grains produce a polarization curve which plateaus at ≈ 40 AU at a higher polarization,

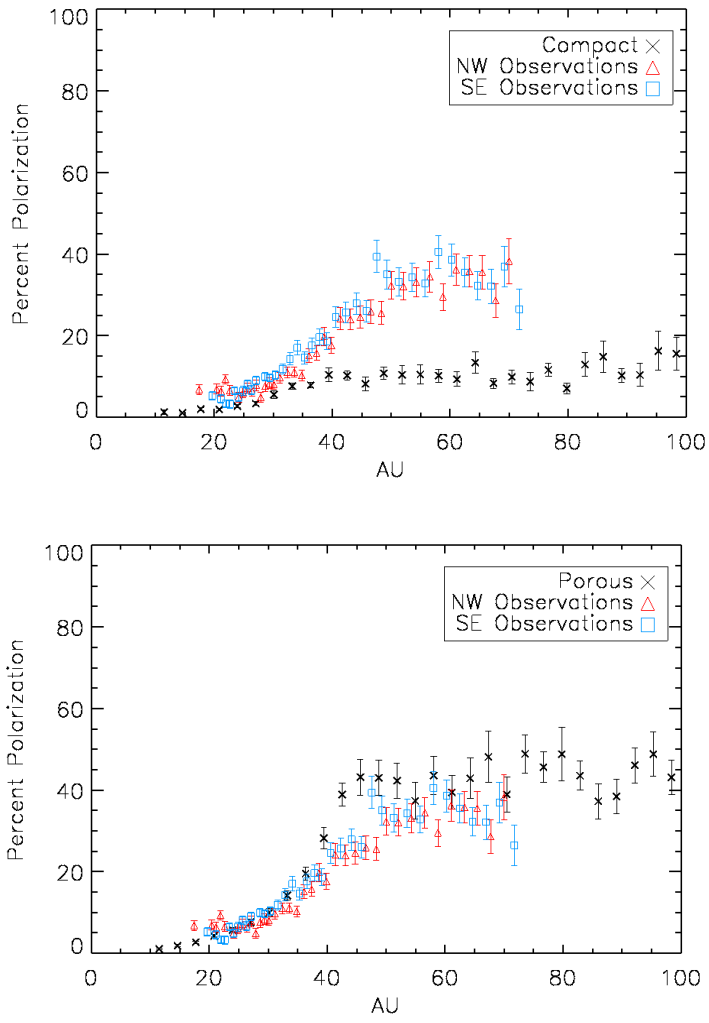

Figure 6.18: Plots showing the percent polarization in the F606W (Graham, Kalas & Matthews, 2007) band for the compact (top) and porous (bottom) grain model.

than the observed polarization, of ≈ 40 percent. This can be explained by examining the disc model. From 35-40 AU, the disc consists of millimetre grains and therefore they will not contribute to the polarization of the disc. Beyond 40 AU, the disc consists of micron size grains which will be the source of the polarized light. The scattering angle will become more obtuse and acute with radius starting at 0 and 180 degrees at 0 AU. However, Figure 6.19 shows that backscattering is far less likely to occur compared to forward scattering. As the radius approaches 40 AU the scattering angle will tend to 90 degrees at which the polarization peaks (Figure 6.19). Beyond 40 AU, the full

range of scattering angles (0-180) is possible, however the the forward scattering angle will still be favoured.

6.3 Discussion

While the compact grains fit the observed surface brightness reasonably well, they are unable to fit the polarization. The plane of polarization for spherical grains, with a size parameter $x \geq 1$, can flip by 90 degrees at certain scattering angles which results in the electric field being orientated parallel to the scattering plane (Kruegel, 2003). Figure 6.19 shows this clearly as the polarization becomes negative at ≈ 50 degrees for the compact spherical grains.

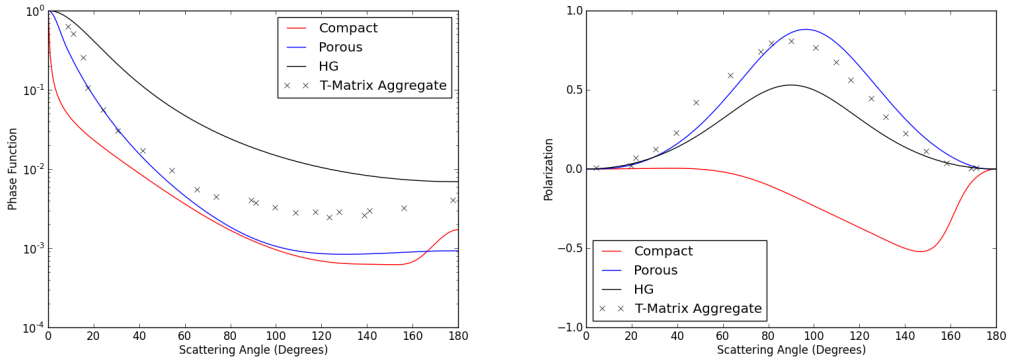

Figure 6.19: Plots showing the normalized phase function (left) and the degree of polarization against scattering angle for the compact, porous, T-matrix aggregate (GKM07) and HG function.

The porous grain models predict the surface brightness and polarization reasonably well, however Figure 6.19 shows that both the compact and porous grains are unable to simultaneously fit the best fit Henyey-Greeenstein (HG) model polarization and phase function (GKM07). Both the compact and porous grains are too forward throwing. To solve this problem, GKM07 used a large ($x = 10.2$) porous (90 percent) silicate grain, modelled using the T-Matrix method (Mackowski & Mishchenko, 1996), composed of 128 small ($x = 0.9$) monomers (Kimura, Kolokolova & Mann, 2006). This T-Matrix aggregate particle was more successful in recreating the HG polarization and phase

function. Therefore, the next step in improving the grain models would be to explore the use of porous and non-Mie grains.

6.4 Modelling AU Mic with DDSCAT + Hyperion

Shen, Draine & Johnson (2009) discuss how these aggregate models compare with the AU Mic data obtained by GKM07. Using a very porous BA model, such as the 90% porous aggregate used by GKM07, allows one to reproduce the phase function features of the disc, however, it over predicts the polarization. Shen, Draine & Johnson (2009) use a lower porosity (BAM2 model) and are able to better fit the observations of the AU Mic disc.

The BAM2 model was run at two wavelengths (0.5012 and 0.6310 μm) for two different grain types 100%, silicate and 50%-silicate/50%-graphite (Shen, Draine & Johnson, 2008, 2009). The purpose of modelling these specific grain types is to compare the output from DDSCAT with the results obtained from Shen, Draine & Johnson (2009).

The scattering matrices were calculated for 3 realizations of the BAM2 model; each realization was constructed with a different initial seed for the random ballistic agglomeration process. The scattering matrices were also calculated in 4 different scattering planes, which were then averaged to determine the final scattering matrix. Initial models were constructed by determining the scattering properties for a range of grain sizes and applying a simple size distribution, Equation 6.6 and 6.7, to them.

$$\int_{am_{min}}^{a_{max}} C.a^{-3.5}\mathrm{d}a = 1 \tag{6.6}$$

$$a_{\mathrm{eff}} = N^{1/3}.a \tag{6.7}$$

where $a_{max} = 0.060$, $a_{min} = 0.015$, C is a constant, a is the monomer size, a_{eff} is the effective radius of the grain and N is the number of monomers (356). These are then compared to the Henyey-Greenstein (HG) function produced by GKM07. The intensity and polarization are modelled as Equations 6.4 and 6.5.

Figure 6.20 shows the phase function and polarization produced by the scattering matrix by the individual grain models and the average grain model. These figures match up very well to the phase function and polarization produced by Shen, Draine & Johnson (2009) and to the HG function produced by GKM07.

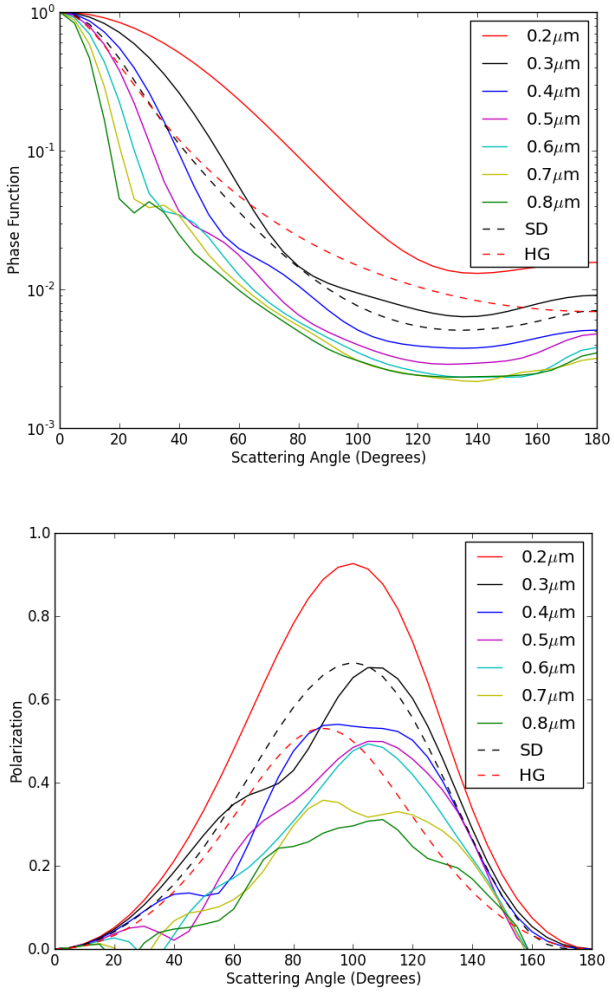

Figure 6.20: Phase function vs scattering angle (top) and Polarization vs scattering angle (bottom). The grains are modelled as 50%-silicate/50%-graphite and the wavelength of the incoming light is 0.5012 μm.

The size distribution described above is a simplistic approach to modelling over a range of grain sizes. A more complex power law size distribution would more accurately represent a range of grain sizes. A size distribution will be applied to the BAM2 grains

in a similar manner to the BHMie wrapper[1] (Appendix A.2). In order to do this efficiently, a script was created to extract the necessary data from the DDSCAT output files. Initially a size distribution similar to the porous grains (Table 6.6) was used to model the DDSCAT grains.

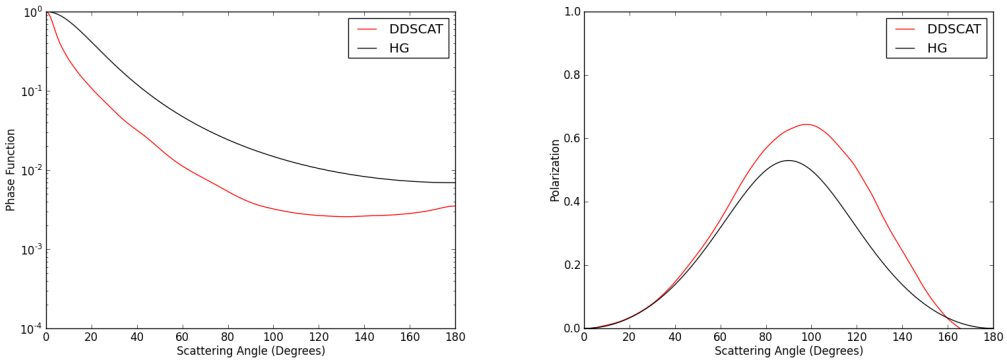

Figure 6.21: Plots showing the normalized phase function (left) and the degree of polarization against scattering angle for non-spherical grains (BAM2) modelled using DDSCAT.

Figure 6.21 shows the polarization and phase function produced by DDSCAT. The DDSCAT model fits the HG phase function well, however overestimates the polarization. This is due to the size distribution used and minimum grain size used. In the F606W band, a grain with an effective radius, $a_{eff} = 0.05$ will have a size parameter, $x \approx 0.5$. So far, it is seen that the BAM2 grains from DDSCAT produce a more comparable fit to the phase function and polarization from GKM. The next step will be to integrate DDSCAT into Hyperion.

6.4.1 DDSCAT/HDF5 Dust Model

The disc model will be loosely based on the porous grain model in terms of size distribution and location of the grains. The DDSCAT grain of choice was the BAM2 dust grain which was made up of 256 monomers (113696 dipoles in total). This dust grain is the most compact of the three grains (refer to Chapter 5.4) due to the higher number of points of contact the monomers have with each other. However creating millimetre

[1] https://github.com/hyperion-rt/bhmie

size grains in DDSCAT, for small wavelengths, produces very large size parameters, which causes DDSCAT to crash. Therefore, the millimetre grains are represented by the millimetre compact silicate grains.

In order to create an HDF5 dust file for the BAM2 model, a combination of the scattering properties from DDSCAT and Mie theory were used. For the wavelength range $0 - 300$ μm , DDSCAT was used to model the dust grains and for $\lambda > 300$ μm , Mie theory was used to model the grains. At $\lambda > 300$ μm , the size parameter becomes very small ($x_{max} = 0.02$ for a grain size $a_{max} = 1$ μm) and therefore enters the Rayleigh Scattering regime. Once the scattering properties of the dust grains from DDSCAT and BHMie were found, they were combined into a single file so that a single HDF5 could be made (Refer to Chapter 3.1.1 for detail on the HDF5 file). A summary of the grain models used can be seen in Table 6.8.

Table 6.8: Summary of the dust grain models for the best fit DDSCAT dust model

Dust Model	Radius of the Disc (AU)	Grain Size	Power Law Size Distribution
DDSCAT Inner Region	$35 - 40$	$3 - 6$ mm	-3.5
DDSCAT Outer Region	$40 - 300$	$0.05 - 1.0$ μm	-4.1

Once again, a parameter test was conducted for the BAM2 grains to determine the best fit values. The parameters changed the SED and surface brightness in the same way as they did for the compact and porous grain models.

6.5 Final Disc Model

6.5.1 Inner Planetesimal Belt

Recent millimetre observations by MacGregor et al. (2013) have provided more information on the millimetre size dust grains within 40 AU from the star. A mass estimate of 3.519×10^{-8} $M_{\odot}$ was calculated for the inner disc (< 40 AU) which is consistent with

both Liu et al. (2004), Fitzgerald et al. (2007). An additional peak is also detected in the disc, which MacGregor et al. (2013) suggests may be an unresolved planetesimal belt located witin < 3 AU with a mass estimated to be 4.525×10^{-10} $M_{\odot}$. The addition of this disc however, had no significant effect on the SED flux. The surface brightness flux on the other hand increased due to the inner planetesimal belt. Figure 6.22 shows an illustration of the new disc structure. The best fit disc model can be seen in Table 6.9.

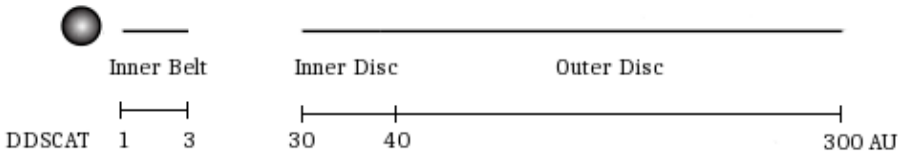

Figure 6.22: Illustration of the AU Mic disc model with the additional inner belt.

Table 6.9: Best fit disc model from Hyperion for the DDSSCAT BAM2 grains

Parameter	Inner Belt	Inner Disc	Outer Disc
r_{in}	1	30	40
r_{out}	3	40	300
Surface Density Exponent (p)	1.5	1.5	-2.5
Flaring exponent (β)	0.0	0.0	0.0
Radius R_0 (AU)	20	20	20
Disc scale height (AU) at r_0	0.8	0.8	0.8
M_{dust} ($M_{\odot}$)	4.5×10^{-10}	9.0×10^{-8}	6.9×10^{-10}

Other than the inclusion of the inner planetesimal belt, the mass of the inner disc was increased to 9.0×10^{-8} to fit the observed SED and the radius of the inner disc was extended from $30 - 40$ AU. This increase in mass is required to increase the far-IR flux to fit the observational data. The remainder of the model matches the porous model produced by F07. The SED, surface brightness and polarization plots for the BAM2

grains at F606W can be seen in Figure 6.23.

The SED for the DDSCAT model fits the observed SED better than the porous grains. The porous grain model underestimates the SED flux in the far-IR, however the BAM2 grains are able to produce a better fit in this region. The addition of the inner planetesimal belt also increases the surface brightness in the inner region of the disc. The porous grain model failed to fit the surface brightness in the 35-50 AU region and underestimates the flux. The BAM2 grain model is able to fit to the observations throughout the radius of the disc. The BAM2 grains also fit the observed polarization better than both the compact and porous grains. The polarization slowly increases to ≈ 38 % at which point it plateaus within the error bars of the observations.

6.5.2 JHK' Polarization Predictions

In addition to modelling the AU Mic disc in scattered light and polarized light in the F606W band, surface brightness data exists for the JHK'-bands Fitzgerald et al. (2007) and polarization predictions can be made for these bands. Using the best fit disc model for the BAM2 grains for the F606W, the surface brightness and percent polarization can be calculated in the JHK'-bands. Figure 6.24 shows the surface brightness fits and Figure 6.25 shows the predicted percent polarization in the JHK'-bands.

The DDSCAT model provide a good fit to the JH-band data, however it does not fit the K' data well. The DDSCAT model is composed of silicates and suffers similar problems as to the compact grain model. Silicates have a higher albedo than the porous grain model and therefore are more reflective. The silicate grains are also more isotropically scattering than the porous grains, so one would expect to see more scattered light at larger radius where there are a higher range of scattering angles.

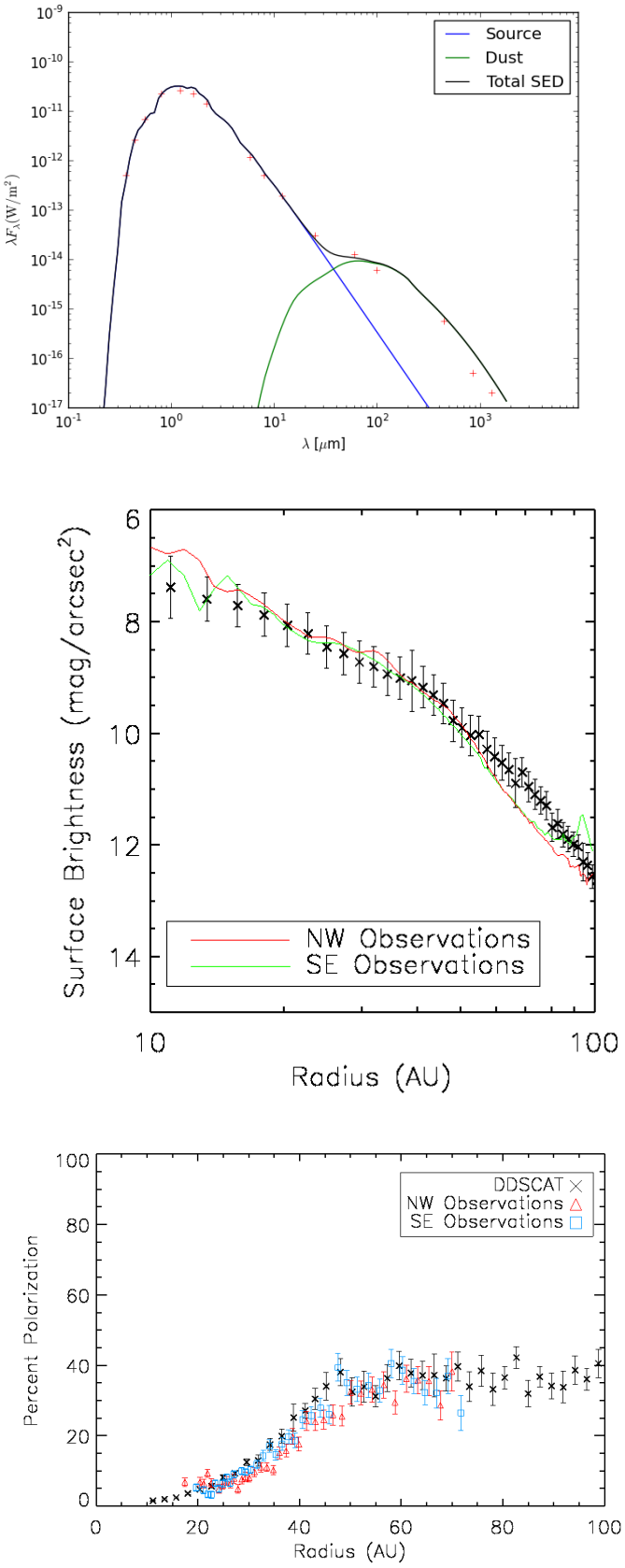

FIGURE 6.23: Plots showing the SED, surface bright (top) and percent polarization (bottom) for the BAM2 grains. Observational F606W data is taken from (Graham, Kalas & Matthews, 2007).

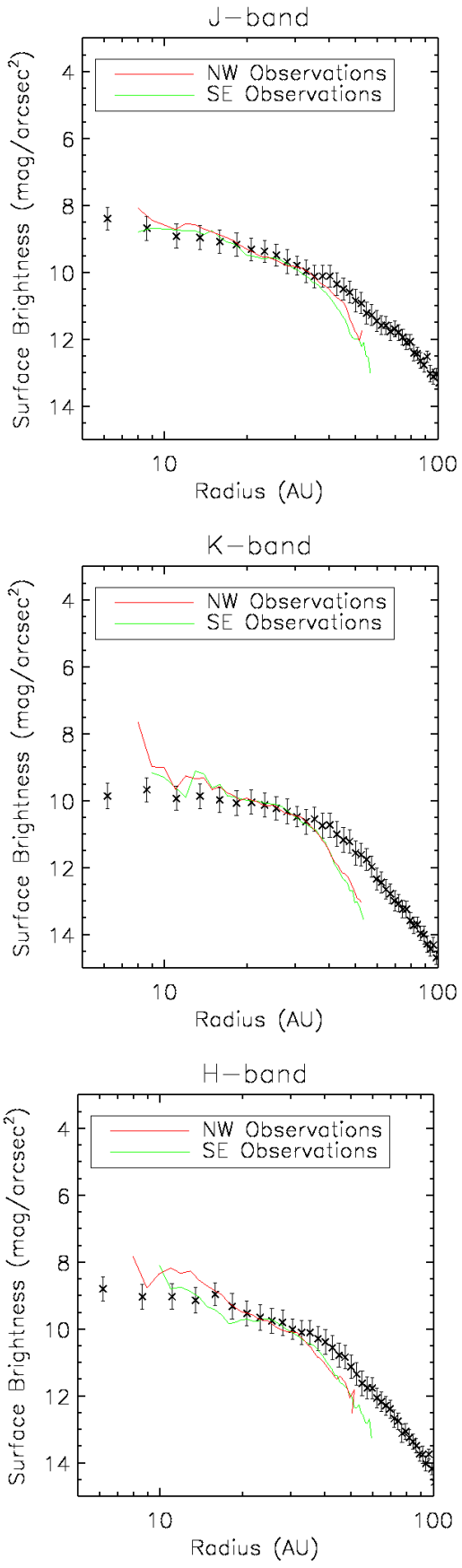

Figure 6.24: Plots showing the surface brightness in the JHK' (Fitzgerald et al., 2007) and F606W (Graham, Kalas & Matthews, 2007) band for the BAM2 DDSCAT grain model.

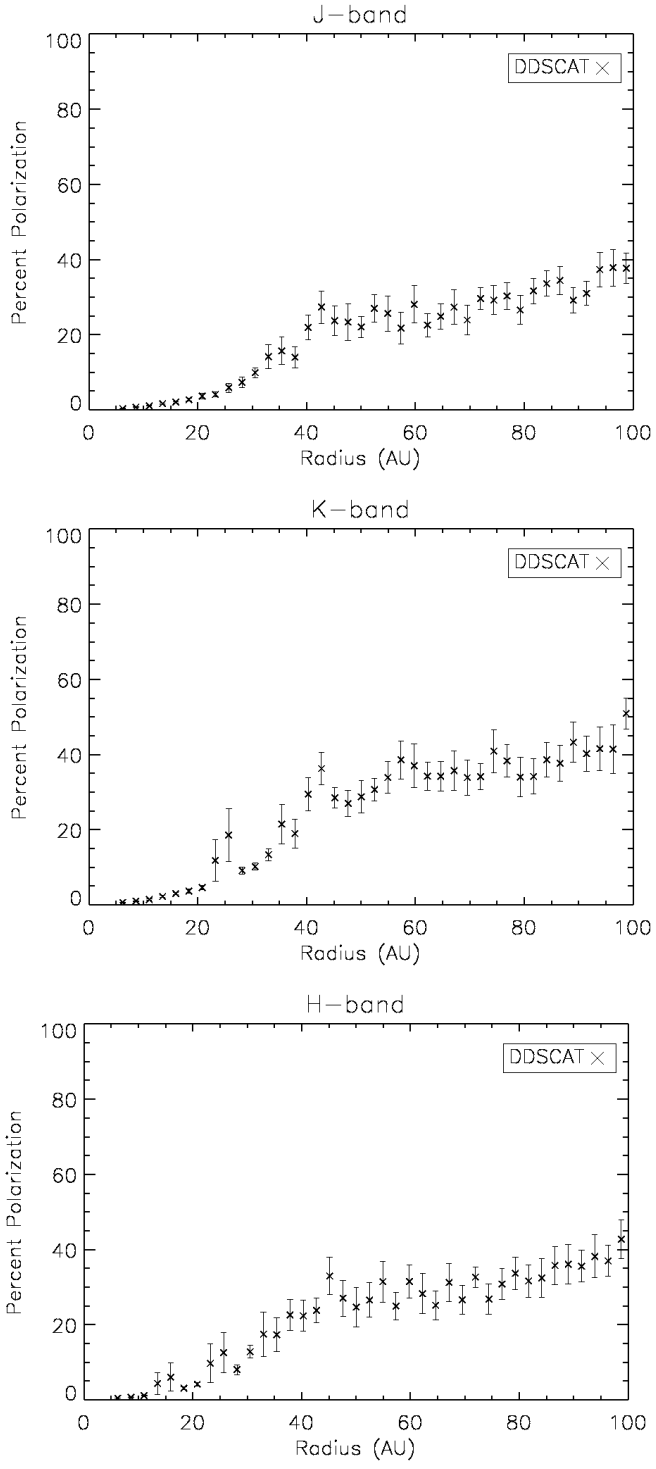

FIGURE 6.25: Plots showing the predicted percent polarization in the JHK'-band (Fitzgerald et al., 2007) for the BAM2 DDSCAT grain model.

6.6 Discussion

There is an abundance of evidence to show that dust grains are not spherical (Section 1.4), however, due to their computational inexpensive nature compared to more complex aggregates, they are still readily used when modelling dust grains. The work presented in this Chapter aimed to show a simple yet effective method to incorporate BAM2 grains into a Monte Carlo radiative transfer code. The results show an improvement to the fit presented by F07 who used EMT to model a porous spherical grain. The BAM2 model is able to simultaneously fit the SED, surface brightness (F606W (GKM07), H (F07)), polarization and HG model (GKM07).

While using a 4 element scattering matrix to model the scattering properties, from an optically thin disc where single scattering dominates, works as a first order approximation, one would need to consider increasing the number of independent scattering matrix elements to more accurately model these non-spherical BAM2 grains. This would involve removing the symmetry from the scattering matrix, resulting in 8 independent scattering elements. For an optically thick disc, where multiple scattering is dominant, would require even more independent scattering matrix elements.

Similar to the transitional disc around HD169142, grain growth in debris discs is a natural consequence of ballistic aggregation of smaller dust particles. We also see fragmentation play an important role in debris discs due to the abundance of micron size grains present in the disc. This is once again applied to our disk model as a power law size distribution, ranging from micron to centimetre grains, and is required to reproduce the observed SED, SB and polarization. However, here we explore how ballistic aggregation can create irregular particles. Shen, Draine & Johnson (2008) constructs three ballistic aggregate models with varying degrees of porosity. These are generated using three simple algorithms described in Chapter 5.4. Testing each grain model showed that the BAM2 model was the most suited for modelling the dust grains in AU Mic. This is due to grain being the most compact and having the lowest peak polarization of the three models. At the moment, the BAM2 grain is rotationally averaged around ϕ so that a single scattering matrix is used for each wavelength.

Future work may consider a dependency on ϕ, where each ϕ angle is either weighted or randomly chosen using a random number generator, however this will require heavy modification to the Hyperion code and HDF5 dust file.

The final best fit model is a three component disc model. The disc is modelled as a geometrically flat disc, therefore having no flaring and implying that the majority of the dust has settled to the midplane. This is further reinforced through observations of the disc (GKM07, F07). Similar to HD169142, there is an annular gap present in the disc (MacGregor et al., 2013). Once again we expect the annular gap to be a result of the presence of a planetary body. However, since the disc is edge on, any mass estimations using the SB or polarization are not possible.

The outer disc is split into two regions, an inner region consisting of millimetre grains and an outer region consisting of micron grains. This is comparable to dynamical models produced by Krivov, Mann & Krivova (2000) who consider two dust populations based on their blow out radius, α (large grains close to the star) and β meteoroids (smaller particles which are blown further away due to stellar radiation). Although their paper was focused on β Pictoris, their results are applicable to debris discs with low gas content and comparable optical depths.

7

Conclusion & Future Work

The main aim of this thesis is to examine the properties of circumstellar discs. This includes PDI observations and radiative transfer modelling of the transitional disc HD169142 and radiative transfer modelling of the debris disc AU Mic. Unfortunately, the PDI observations of HD169142 were not of sufficient quality to resolve any disc features or be used to compare to radiative transfer models. Therefore, a combination of previous scattered light and polarimetric images of HD169142 were used to help constrain the disc structure and dust properties of the disc. By comparing previous observations to radiative transfer models, one can begin to constrain the size, composition and structure of the dust grains in the disc.

Initially, the dust grains were modelled as spheres, however (for AU Mic), this was found to have limitations. Therefore a more realistic dust grain (BAM2) was examined to be used with Hyperion. This involved modifying Hyperion to incorporate the

scattering properties (calculated from DDSCAT) of the BAM2 grains into a readable HDF5 file for Hyperion.

7.1 PDI Observations of HD169142

The transitional disc around the Herbig Ae/Be star HD169142 has been well observed over the last decade (Acke & van den Ancker, 2004; Blondel & Djie, 2006; Grady et al., 2007; Honda et al., 2012; Quanz et al., 2013). One of the aims of this thesis was to expand the observations of the disc by conducting H band high contrast imaging on the VLT. The images were obtained through the polarimetric differential imaging technique with the adaptive optics system NACO. Previous polarimetric imaging of HD169142 has focused on the inner region of the circumstellar disc, while our observations use longer exposure times, with the intention of being able to examine the outer regions of the disc. However, the longer exposure times only allowed the disc to be traced up to $R \approx 250AU$, which is comparable to previous polarimetric observations as Quanz et al. (2013), which were able to trace the disc out to 250 AU. The results show distinct signs of polarization, within $R < 250$ AU, due to scattering in circumstellar material.

A maximum percent polarization value of 2 percent in the H-band and 1 percent in the K_s was measured. Due to the misaligned 'spider-frame' between the target and reference star, AO artefacts and waffle patterns, we were unable to successfully subtract the PSF of the star to reveal the intrinsic polarization of the disc. Therefore, the calculated polarization values act as a lower limit. Previous J-band imaging polarimetry (Hales et al., 2006) found the maximum polarization to be ≈ 2 percent. The J-band percent polarization also acts a lower limit as Hales et al. (2006) did not perform PSF subtraction to their observations. A single and split SBP was examined and compared to those found by Quanz et al. (2013). Our fits were found to be shallower than those found by Quanz et al. (2013) which we attribute to the presence of the PSF and AO waffle pattern.

Due to the long exposure times, the saturated region extends beyond the ring like structure seen at approximately 25 AU (Quanz et al., 2013). In addition to this,

the annular gap seen between 40 and 70 AU (Quanz et al., 2013) is not seen in our observations due to saturation. In all cases, the saturated region extends into the annular gap ($\approx 40 - 70$ AU).

Deconvolution was attempted with the Lucy-Richardson (Richardson, 1972; Lucy, 1974) method algorithm in IRAF and with the convolve routine in IDL in an attempt to reduce the affect of the PSF. However, both methods failed due to the reference and target star being affected by the waffle pattern in both the H and K_s-bands. An attempt was made to use the stars surrounding the target star, however a suitable star was not found. This resulted in any further information being unattainable.

7.2 Modelling of HD169142

The disc was then modelled using the 3D radiative transfer code Hyperion using the 1.1 μm (Grady et al., 2007) and H-band (Fukagawa et al., 2010) scattered light observations and H-band polarimetric (Quanz et al., 2013) observations.

Initial models were constructed using a two disc structure in which various dust models were tested and the observed SED was reproduced via a parameter test. The dust models tested included astronomical silicates and amorphous carbon with a power law size distribution ranging in size from 0.01-10000 μm and 20-10000 μm . Since HD169142 is a Group Ib Herbig star, it does exhibit any silicate features. In the two disc model, the observed SED could only be recreated by excluding silicate from the disc.

Recent polarimetric differential imaging (PDI) (Quanz et al., 2013) however has shown the existence of an annular gap. In addition to this, the annular gap is found not to be devoid of dust. Before the annular gap was included in the model, with dust, we assumed it to be devoid of dust grains. This therefore created a three-component disc structure. The dust models were once again tested and we were able to reproduce the observed SED and include silicates in the disc by placing them in the outer disc. The next step was to simultaneously fit the observed SBP in scattered and polarized light. Once again a parameter test was conducted to ensure that the final three disc

model was able to fit the observed SED and SBP in scattered (1.1 μm : -3.09 ± 0.0 (Grady et al., 2007), 3.09 ± 0.12 (this work), 1.65 μm : -3.00 ± 0.20 (Fukagawa et al., 2010), 3.16 ± 0.12 (this work)) and polarized light (1.65 μm : 3.31 ± 0.11 (Quanz et al., 2013), 3.39 ± 0.07 (this work)) within errors. This model also allowed us to predict the percent polarization in the H-band which was found to peak at ≈ 14 percent.

The inclusion of the annular gap, with dust, meant the final disc model constructed is a four-component disc structure. By performing a parameter test for the mass contained within the annular gap and by comparing the modelled surface brightness to the observed surface brightness within the gap, estimates of the mass of the annular gap (2.10×10^{-6} $M_{\odot}$) are made as well as for the planet ($\approx 1.53 \times 10^{-5}$ $M_{\odot}$ ($0.016 M_{Jupiter}$)) suspected to be responsible for causing the gap. However, using a gas/dust ratio of 22-50 (Meeus et al., 2010) the total mass of the disc is estimated to be between $3.52 - 7.80 \times 10^{-4}$ $M_{\odot}$ ($0.368 - 0.816$ $M_{Jupiter}$). This fits within the range of the total mass calculated by Reggiani et al. (2014). The final four disc model was able to reproduce the observed SED and SBP in scattered (1.1 μm : -3.09 ± 0.0 (Grady et al., 2007), 3.06 ± 0.18 (this work), 1.65 μm : -3.00 ± 0.20 (Fukagawa et al., 2010), 3.21 ± 0.17 (this work)) and polarized light (1.65 μm : 3.31 ± 0.11 (Quanz et al., 2013), 3.43 ± 0.13 (this work)) within errors.

7.3 Integrating DDSCAT and Hyperion

Prior to this study, spherical grains were prevalently used when modelling dust grains in circumstellar discs (Voshchinnikov & Krügel, 1999; Graham, Kalas & Matthews, 2007; Sauter et al., 2009), especially in Monte Carlo simulations (Metchev et al., 2005; Fitzgerald et al., 2007; Honda et al., 2012). The symmetrical nature of spheres allows for shorter CPU time when calculating the scattering properties compared to aggregate grain models and requires only four independent elements when describing the scattering matrix. However, spherical dust grains have limitations, although they can produce high polarization, they are often too isotropically scattering (GKM07).

In the case of AU Mic, two spherical dust models were tested, a compact silicate

model and a porous dirty ice model. Both grain models were able to reproduce the SED and surface brightness in the F606W and H-band but were unable to match the observed polarization and high degree of forward scattering. The compact silicate grain model underestimated the polarization, peaking at only $\approx$ 15 percent and the porous model overestimated the polarization peaking at 45 percent. Therefore, the use of more complex/realistic ballistic aggregate particles (BAM2) was explained to solve this problem.

Shen, Draine & Johnson (2009) have previously attempted to use DDSCAT with BAM2 grains to fit to the best fit HG model from GKM07. However, only a simple average was considered over a particle size ranging from $0.02 \leq a \leq 0.08$ μm . While Shen, Draine & Johnson (2009) was able to produce a good fit, taking an average does not accurately represent how dust grains exist in circumstellar discs. Due to processes such as collisional attrition of large parent bodies (Strubbe & Chiang, 2006), an increase of smaller grains is seen and best described by a power law size distribution. The study conducted in this thesis aimed to expand on this work by creating a script which can extract the necessary data from the DDSCAT output and apply a size distribution to it. This will be the first time DDSCAT has been used with a Monte Carlo radiative transfer scattering code and will the most realistic model of the dust grains in the AU Mic disc to date.

Currently, Hyperion uses four independent elements to define scattering matrix, therefore rotational averaging and a 50/50 percent population of grains and their enantiomers were used to reduce the number of non-zero independent scattering elements from DDSCAT to four. This worked as a good first order approximation when modelling BAM2 grains. Once the BAM2 scattering properties were contained in an HDF5 file, they could then be read into Hyperion. Applying these BAM2 grains to the AU Mic disc allowed us to simultaneously fit the observed SED, surface brightness and polarization in the H and F606W-band obtaining a better fit than using conventional spherical grains. The disc model using BAM2 grains plateaued and peaked at a distance offset and polarization comparable to that observed (47 AU at $\approx$ 35 percent polarization). Polarization predictions are also made in the JHK'-band for the BAM2

grains for the AU Mic debris disc which can be tested in future observations.

7.4 Future Work

The work conducted in this thesis represents a step towards modelling dust grains in Monte Carlo simulations in a more realistic way. It has been shown that a simple script can be used to extract the required data from DDSCAT and can apply a size distribution to the data. It has also shown that using more physically realistic grains, such as the BAM2 type grains, is necessary as spherical grains fail to completely fit all of the observational data. The improvements in matching observational data for AU Mic in scattered and polarized light are demonstrated to be better than spherical grains. This work also emphasizes the need to include polarimetric information in order to properly constrain the dust grain properties in circumstellar discs. The next step would be to increase the number of independent scattering matrix elements available for Hyperion to read.

While using a 4 element scattering matrix to model the scattering properties, from an optically thin disc (where single scattering dominates), works as a first order approximation, one would need to consider increasing the number of independent scattering matrix elements to more accurately model these BAM2 grains if multiple scattering is important. This would involve removing the symmetry from the scattering matrix, resulting in 8 rotationally averaged independent scattering elements. For an optically thick disc, where multiple scattering is dominant, even more independent scattering matrix elements would be required. However, due to time constraints, this part of the project was not completed.

Another aspect of the code that could be expanded is the need for rotational averaging. At the moment, the BAM2 grain is rotationally averaged around Φ (rotation angle of $\hat{\mathbf{a}}_1$ around k, refer to Figure 5.6) so that a single scattering matrix is used for each wavelength. Future work may consider a dependency on Φ, where each Φ angle is either weighted or randomly chosen using a random number generator therefore removing the need for rotational averaging. This will, however, require heavy modification

to the Hyperion code and HDF5 dust file.

A

Appendix

A.1 Mass calculations for HD169142 four component disc

The mass of the models constructed in Chapter 4 are based on the values determined by Meeus et al. (2010). The model was originally a two disc model with $M_{innerdisc} = 2 \times 10^{-9}$ $M_{\odot}$ and $M_{outerdisc} = 1.5 \times 10^{-4}$ $M_{\odot}$. Therefore, to add the annular gap, the outer disc must be split into three separate components (assuming a the same disc parameters for each component of the outer disc).

$$M_{Total} = \int_{r_{min}}^{r_{max}} \mathrm{d}^3 r \ \rho \tag{A.1}$$

$$M_{Total} = \rho_0 \int_0^{2\pi} \int_{-\infty}^{\infty} \int_{r_{min}}^{r_{max}} \mathrm{d}r\mathrm{d}z\mathrm{d}\phi \left(\frac{R_0}{R}\right)^{\beta-p} r \, \exp\left[-\frac{1}{2}\left(\frac{z}{h_0}\frac{R_0^\beta}{r^\beta}\right)^2\right] \tag{A.2}$$

let

$$\begin{aligned} t &= \frac{z}{\sqrt{2}}\frac{R_0^\beta}{r^\beta}\frac{1}{h_0} \\ \mathrm{d}t &= h_0 \mathrm{d}z\sqrt{2}\frac{R_0^\beta}{r^\beta} \end{aligned} \tag{A.3}$$

therefore

$$M_{Total} = 2\pi\rho_0 h_0 \int_{r_{min}}^{r_{max}} \mathrm{d}r r \, \left(\frac{R_0}{R}\right)^{\beta-p} \sqrt{2}\frac{R_0^\beta}{r^\beta} \int_{-\infty}^{\infty} \mathrm{d}t \exp(-t^2) \tag{A.4}$$

$$M_{Total} = (2\pi)^{3/2}\rho_0 h_0 \int_{r_{min}}^{r_{max}} R_0^{-p} r^{p+1} \mathrm{d}r \tag{A.5}$$

$$M_{Total} = (2\pi)^{3/2}\rho_0 h_0 R_0^{-p} \left[\frac{r^{p+2}}{p+2}\right] \tag{A.6}$$

$$M_{Total} = \frac{(2\pi)^{3/2}\rho_0 h_0 R_0^{-p}(r_{max}^{p+2} - r_{min}^{p+2})}{p+2} \tag{A.7}$$

therefore, splitting the outer disc into three components of radius (a = 28 AU, b = 42 AU), (b = 42 AU, c = 67 AU) and (c = 67 AU, d = 240 AU) results in:

$$M_{Outer} = \frac{(2\pi)^{3/2}\rho_0 h_0 R_0^{-p}((b^{p+2} - a^{p+2}) + (c^{p+2} - b^{p+2}) + (d^{p+2} - c^{p+2}))}{p+2} \tag{A.8}$$

This gives a value for $\rho_0 = 1.586 \times 10^{-8}$ and a disc mass of $M_{\mathrm{Disc2}} = 1.535 \times 10^{-5}$ $\mathrm{M}_\odot$, $M_{\mathrm{Disc2}} = 1.744 \times 10^{-5}$ $\mathrm{M}_\odot$ and $M_{\mathrm{Disc2}} = 1.172 \times 10^{-4}$ $\mathrm{M}_\odot$.

A.2 DDSCAT Extraction Script

```
import numpy as np

alpha = -4.1
density = 2.26
prefix = 'Si_SED'
directory = 'Si_SED/Complete/'

#wavelength, need to use the table option in ddscat.par

wavelength = np.loadtxt(directory+'wave.tab', skiprows=1,
   unpack=True)

no_wave = wavelength.size

#a_eff, need to use the table option in ddscat.par

a_eff = np.loadtxt(directory+'aeff.tab', skiprows=1, unpack
   =True)
no_sizes = a_eff.size
amax = 1.00
amin = 0.05

#averaging over the 4 scattering planes

skip = 43
theta, phi = np.loadtxt(directory+'w000r000.avg', usecols
   =(0,1), skiprows=skip, unpack=True)
```

```
total_scat_ang = (theta.size) #no of scat angles over 4
   scat planes
no_ang = theta.size/4 #number of theta values

S_11_rot = np.zeros((no_wave,no_sizes,no_ang))
S_12_rot = np.zeros((no_wave,no_sizes,no_ang))
#S_13_rot = np.zeros((no_wave,no_sizes,no_ang))
#S_14_rot = np.zeros((no_wave,no_sizes,no_ang))
S_21_rot = np.zeros((no_wave,no_sizes,no_ang))
S_22_rot = np.zeros((no_wave,no_sizes,no_ang))
#S_23_rot = np.zeros((no_wave,no_sizes,no_ang))
#S_24_rot = np.zeros((no_wave,no_sizes,no_ang))
#S_31_rot = np.zeros((no_wave,no_sizes,no_ang))
#S_32_rot = np.zeros((no_wave,no_sizes,no_ang))
S_33_rot = np.zeros((no_wave,no_sizes,no_ang))
S_34_rot = np.zeros((no_wave,no_sizes,no_ang))
#S_41_rot = np.zeros((no_wave,no_sizes,no_ang))
#S_42_rot = np.zeros((no_wave,no_sizes,no_ang))
S_43_rot = np.zeros((no_wave,no_sizes,no_ang))
S_44_rot = np.zeros((no_wave,no_sizes,no_ang))

#3D numpy array for different wavelength,size particles and
    angles

for ir in range(0,no_wave,1):
        for ik in range(0,no_sizes,1):
```

```
            s_11, s_12, s_21, s_22, s_33, s_34, s_43,
               s_44 = np.loadtxt(directory+'w'+str
               ('{0:0>3}'.format(ir))+'r'+str
               ('{0:0>3}'.format(ik))+'.avg', usecols
               =(3,4,5,6,7,8,9,10), skiprows=skip,
               unpack=True)

            for ij in range(0,total_scat_ang,no_ang):
                    S_11_rot[ir,ik,:] = S_11_rot[ir,ik
                       ,:] + s_11[ij:ij+no_ang]
                    S_12_rot[ir,ik,:] = S_12_rot[ir,ik
                       ,:] + s_12[ij:ij+no_ang]
#                   S_13_rot[ir,ik,:] = S_13_rot[ir,ik
   ,:] + s_13[ij:ij+no_ang]
#                   S_14_rot[ir,ik,:] = S_14_rot[ir,ik
   ,:] + s_14[ij:ij+no_ang]
                    S_21_rot[ir,ik,:] = S_21_rot[ir,ik
                       ,:] + s_21[ij:ij+no_ang]
                    S_22_rot[ir,ik,:] = S_22_rot[ir,ik
                       ,:] + s_22[ij:ij+no_ang]
#                   S_23_rot[ir,ik,:] = S_23_rot[ir,ik
   ,:] + s_23[ij:ij+no_ang]
#                   S_24_rot[ir,ik,:] = S_24_rot[ir,ik
   ,:] + s_24[ij:ij+no_ang]
#                   S_31_rot[ir,ik,:] = S_31_rot[ir,ik
   ,:] + s_31[ij:ij+no_ang]
#                   S_32_rot[ir,ik,:] = S_32_rot[ir,ik
   ,:] + s_32[ij:ij+no_ang]
                    S_33_rot[ir,ik,:] = S_33_rot[ir,ik
                       ,:] + s_33[ij:ij+no_ang]
```

```
                        S_34_rot[ir,ik,:] = S_34_rot[ir,ik
                            ,:] + s_34[ij:ij+no_ang]
        #               S_41_rot[ir,ik,:] = S_41_rot[ir,ik
           ,:] + s_41[ij:ij+no_ang]
        #               S_42_rot[ir,ik,:] = S_42_rot[ir,ik
           ,:] + s_42[ij:ij+no_ang]
                        S_43_rot[ir,ik,:] = S_43_rot[ir,ik
                            ,:] + s_43[ij:ij+no_ang]
                        S_44_rot[ir,ik,:] = S_44_rot[ir,ik
                            ,:] + s_44[ij:ij+no_ang]

#Extracting optical properties from DDSCAT output files

Q_ext = np.zeros((no_wave,no_sizes))
Q_abs = np.zeros((no_wave,no_sizes))
Q_sca = np.zeros((no_wave,no_sizes))
c_ext = np.zeros((no_wave,no_sizes))
c_abs = np.zeros((no_wave,no_sizes))
c_sca = np.zeros((no_wave,no_sizes))

Qext,Qabs,Qsca = np.loadtxt(directory+'qtable', usecols
   =(2,3,4), skiprows=16, unpack=True)

for ie in range(0,no_wave,1):
        for iq in range(0,no_sizes,1):
                Q_ext[ie,iq] = Qext[iq+ie*no_sizes] #Q_ext[
                   wave,aeff]
                Q_abs[ie,iq] = Qabs[iq+ie*no_sizes]
                Q_sca[ie,iq] = Qsca[iq+ie*no_sizes]
```

```
                c_ext[ie,iq] = Q_ext[ie,iq]*(np.pi*a_eff[iq
                   ]**2)*1.e-8 #from micron^2 to cm^2
                c_abs[ie,iq] = Q_abs[ie,iq]*(np.pi*a_eff[iq
                   ]**2)*1.e-8
                c_sca[ie,iq] = Q_sca[ie,iq]*(np.pi*a_eff[iq
                   ]**2)*1.e-8

#Applying the size distribution to the optical properties

S_11 = np.zeros((no_wave,no_ang))
S_12 = np.zeros((no_wave,no_ang))
#S_13 = np.zeros((no_wave,no_ang))
#S_14 = np.zeros((no_wave,no_ang))
S_21 = np.zeros((no_wave,no_ang))
S_22 = np.zeros((no_wave,no_ang))
#S_23 = np.zeros((no_wave,no_ang))
#S_24 = np.zeros((no_wave,no_ang))
#S_31 = np.zeros((no_wave,no_ang))
#S_32 = np.zeros((no_wave,no_ang))
S_33 = np.zeros((no_wave,no_ang))
S_34 = np.zeros((no_wave,no_ang))
#S_41 = np.zeros((no_wave,no_ang))
#S_42 = np.zeros((no_wave,no_ang))
S_43 = np.zeros((no_wave,no_ang))
S_44 = np.zeros((no_wave,no_ang))

C_ext = np.zeros(no_wave)
C_abs = np.zeros(no_wave)
C_sca = np.zeros(no_wave)
kappa_ext = np.zeros(no_wave)
```

```
#Determine particle dimensions and constants

abundance_mass = 1. #although there are 3 comp, there is
   only one type of grain present. need >1 for different
   BAM2 models in one dust file

avg_volume = 4.*np.pi/3. *((alpha+1.)/(alpha+4.))*(amax**(
   alpha+4.)-amin**(alpha+4.))*(amax**(alpha+1.)-amin**(
   alpha+1.))**(-1.)

avg_particle_mass = (avg_volume/1e12)*density #divide by 1
   e12 to get micron^3 to cm^3

abundance_number_mass = abundance_mass/avg_particle_mass

#abundance_number = abundance_number_mass/sum(
   abundance_number_mass) # renormalize abundances for >
   comp
abundance_number = abundance_number_mass/
   abundance_number_mass # renormalize for 1 comp

#bin sizes and looping over wave and size

logamin = np.log10(amin)
logastep = (np.log10(amax) - np.log10(amin))/no_sizes
a1 = np.zeros(no_sizes+1)
a = np.zeros(no_sizes+1)
a2 = np.zeros(no_sizes+1)
```

```
for ig in range(0,no_wave,1):
        for ia in range(1,no_sizes+1,1):
                a1[ia] =  10.**(logamin + logastep*(ia-1.))
                a[ia] =  10.**(logamin + logastep*(ia-0.5))
                a2[ia] =  10.**(logamin + logastep*(ia))

                distribution_weight_number = (a2[ia]**(
                   alpha+1.)-a1[ia]**(alpha+1.))/(amax**(
                   alpha+1.)-amin**(alpha+1.))
                weight = distribution_weight_number*
                   abundance_number

                S_11[ig,:] = S_11[ig,:] + weight*S_11_rot[
                   ig,ia-1,:]
                S_12[ig,:] = S_12[ig,:] + weight*S_12_rot[
                   ig,ia-1,:]
                #S_13[ig,:] = S_13[ig,:] + weight*S_13_rot[
                   ig,ia-1,:]
                #S_14[ig,:] = S_14[ig,:] + weight*S_14_rot[
                   ig,ia-1,:]
                S_21[ig,:] = S_21[ig,:] + weight*S_21_rot[
                   ig,ia-1,:]
                S_22[ig,:] = S_22[ig,:] + weight*S_22_rot[
                   ig,ia-1,:]
                #S_23[ig,:] = S_23[ig,:] + weight*S_23_rot[
                   ig,ia-1,:]
                #S_24[ig,:] = S_24[ig,:] + weight*S_24_rot[
                   ig,ia-1,:]
                #S_31[ig,:] = S_31[ig,:] + weight*S_31_rot[
                   ig,ia-1,:]
```

```
                #S_32[ig,:] = S_32[ig,:] + weight*S_32_rot[
                   ig,ia-1,:]
                S_33[ig,:] = S_33[ig,:] + weight*S_33_rot[
                   ig,ia-1,:]
                S_34[ig,:] = S_34[ig,:] + weight*S_34_rot[
                   ig,ia-1,:]
                #S_41[ig,:] = S_41[ig,:] + weight*S_41_rot[
                   ig,ia-1,:]
                #S_42[ig,:] = S_42[ig,:] + weight*S_42_rot[
                   ig,ia-1,:]
                S_43[ig,:] = S_43[ig,:] + weight*S_43_rot[
                   ig,ia-1,:]
                S_44[ig,:] = S_44[ig,:] + weight*S_44_rot[
                   ig,ia-1,:]
                C_ext[ig] = C_ext[ig] + weight*c_ext[ig,ia
                   -1]
                C_abs[ig] = C_abs[ig] + weight*c_abs[ig,ia
                   -1]
                C_sca[ig] = C_sca[ig] + weight*c_sca[ig,ia
                   -1]

#Opacity of the dust to extinction (Kappa_ext or chi)

        kappa_ext[ig] = C_ext[ig] * (abundance_mass/
           avg_particle_mass) # for 1 comp, need to sum(
           abun_mass/avg_part_mass) for > 1 comp

#Scattering angles: cosine of the scattering angle

mu = np.cos((np.pi/180)*theta[0:no_ang])
```

```
#write properties to files for hyperion python modules to
   read

np.savetxt(directory+prefix+'.f11', S_11, fmt="%11.4e") #in
    the bhmie .f11 file, there is a space at the begining
   of each wavelength
np.savetxt(directory+prefix+'.f12', S_12, fmt="%11.4e")
#np.savetxt(directory+prefix+'.f13', S_13, fmt="%11.4e")
#np.savetxt(directory+prefix+'.f14', S_14, fmt="%11.4e")
np.savetxt(directory+prefix+'.f21', S_21, fmt="%11.4e")
np.savetxt(directory+prefix+'.f22', S_22, fmt="%11.4e")
#np.savetxt(directory+prefix+'.f23', S_23, fmt="%11.4e")
#np.savetxt(directory+prefix+'.f24', S_24, fmt="%11.4e")
#np.savetxt(directory+prefix+'.f31', S_31, fmt="%11.4e")
#np.savetxt(directory+prefix+'.f32', S_32, fmt="%11.4e")
np.savetxt(directory+prefix+'.f33', S_33, fmt="%11.4e")
np.savetxt(directory+prefix+'.f34', S_34, fmt="%11.4e")
#np.savetxt(directory+prefix+'.f41', S_41, fmt="%11.4e")
#np.savetxt(directory+prefix+'.f42', S_42, fmt="%11.4e")
np.savetxt(directory+prefix+'.f43', S_43, fmt="%11.4e")
np.savetxt(directory+prefix+'.f44', S_44, fmt="%11.4e")

np.savetxt(directory+prefix+'.wav', wavelength, fmt="%11.4e
   ")
np.savetxt(directory+prefix+'.mu', mu, fmt="%11.4e")
np.savetxt(directory+prefix+'.alb', C_sca/C_ext, fmt="%11.4
   e")
```

```
np.savetxt(directory+prefix+'.chi', kappa_ext, fmt="%11.4e
   ")
```

References

Acke B., van den Ancker M. E., 2004, Astronomy and Astrophysics, 426, 151 80, 168

Adams F. C., Lada C. J., Shu F. H., 1987, The Astrophysical Journal, 312, 788 66

Allard F., Hauschildt P. H., Alexander D. R., Tamanai A., Schweitzer A., 2001, The Astrophysical Journal, 556, 357 135

Allard F., Hauschildt P. H., Schwenke D., 2000, The Astrophysical Journal, 540, 1005 135

Amdahl G. M., 1967, in Proceedings of the April 18-20, 1967, Spring Joint Computer Conference, AFIPS '67 (Spring), ACM, New York, NY, USA, pp. 483–485 75

Andre P., Ward-Thompson D., Barsony M., 1993, The Astrophysical Journal, 406, 122 6

Andrews S. M., Williams J. P., 2005, The Astrophysical Journal, 631, 1134 5

Apai D., Pascucci I., Brandner W., Henning T., Lenzen R., Potter D. E., Lagrange A.-M., Rousset G., 2004, Astronomy and Astrophysics, 415, 671 xvi, 48, 51

Apai D., Schneider G., Grady C. A., Wyatt M. C., Lagrange A.-M., Kuchner M. J., Stark C. J., Lubow S. H., 2015, The Astrophysical Journal, 800, 136 xiv, 13, 14

Armitage P. J., 2010, Astrophysics of Planet Formation xiii, 3, 7

Artymowicz P., Lubow S. H., 1994, The Astrophysical Journal, 421, 651 107

Augereau J.-C., Beust H., 2006, Astronomy and Astrophysics, 455, 987 134

Augereau J. C., Nelson R. P., Lagrange A. M., Papaloizou J. C. B., Mouillet D., 2001, Astronomy and Astrophysics, 370, 447 53

Babcock H. W., 1953, Publications of the Astronomical Society of the Pacific, 65, 229 35

Backman D. E., Paresce F., 1993, in Protostars and Planets III, Levy E. H., Lunine J. I., eds., pp. 1253–1304 10, 11

Bally J., Testi L., Sargent A., Carlstrom J., 1998, The Astronomical Journal, 116, 854 7

Barrado y Navascués D., Stauffer J. R., Song I., Caillault J.-P., 1999, The Astrophysical Journal, Letters, 520, L123 128

Basu S., 1998, The Astrophysical Journal, 509, 229 5

Biller B. A. et al., 2014, The Astrophysical Journal, Letters, 792, L22 57, 100

Bjorkman J. E., Wood K., 2001, The Astrophysical Journal, 554, 615 73

Blandford R. D., Payne D. G., 1982, Monthly Notices of the Royal Astronomical Society, 199, 883 4

Blondel P. F. C., Djie H. R. E. T. A., 2006, Astronomy and Astrophysics, 456, 1045 30, 80, 81, 82, 168

Blum J., Wurm G., 2000, Icarus, 143, 138 115

Bodenheimer P., Grossman A. S., Decampli W. M., Marcy G., Pollack J. B., 1980, Icarus, 41, 293 3

Bohren C. F., Huffman D. R., 1983, Absorption and scattering of light by small particles 16, 17, 19, 20, 23, 62, 63

Boley A. C., Payne M. J., Corder S., Dent W. R. F., Ford E. B., Shabram M., 2012, The Astrophysical Journal, Letters, 750, L21 xiv, 14, 15

Boss A. P., 1997, Science, 276, 1836 3

Brauer F., Dullemond C. P., Henning T., 2008, Astronomy and Astrophysics, 480, 859 107

Brogan C. L. et al., 2015, The Astrophysical Journal, Letters, 808, L3 xiii, 8

Brownlee D., Joswiak D., Matrajt G., 2012, Meteoritics and Planetary Science, 47, 453 xiv, 23, 24

Brownlee D. E., Tomandl D. A., Olszewski E., 1977, in Lunar and Planetary Science Conference Proceedings, Vol. 8, Lunar and Planetary Science Conference Proceedings, Merril R. B., ed., pp. 149–160 xiv, 23, 24

Bruggeman D. G., 1935, Annals of Physics, 24, 636 23

Calvet N. et al., 2005, The Astrophysical Journal, Letters, 630, L185 9

Canovas H., Ménard F., Hales A., Jordán A., Schreiber M. R., Casassus S., Gledhill T. M., Pinte C., 2013, Astronomy and Astrophysics, 556, A123 xiii, 9, 11, 39, 41

Canovas H., Rodenhuis M., Jeffers S. V., Min M., Keller C. U., 2011, Astronomy and Astrophysics, 531, A102 41

Chen C. H. et al., 2005, The Astrophysical Journal, 634, 1372 143, 149

Cieza L. A. et al., 2010, The Astrophysical Journal, 712, 925 9

Cieza L. A., Swift J. J., Mathews G. S., Williams J. P., 2008, The Astrophysical Journal, Letters, 686, L115 5

Clarke C. J., Gendrin A., Sotomayor M., 2001, Monthly Notices of the Royal Astronomical Society, 328, 485 5

Cutri R. M. et al., 2003, 2MASS All Sky Catalog of point sources. xiii, 10, 30, 80, 135, 149

D'Alessio P., Calvet N., Hartmann L., Franco-Hernández R., Servín H., 2006, The Astrophysical Journal, 638, 314 9, 64, 107

D'Alessio P., Calvet N., Hartmann L., Lizano S., Cantó J., 1999, The Astrophysical Journal, 527, 893 xiii, 10

D'Alessio P., Cantö J., Calvet N., Lizano S., 1998, The Astrophysical Journal, 500, 411 65

D'Alessio P., Merín B., Calvet N., Hartmann L., Montesinos B., 2005, Revista Mexicana de Astronomia y Astrofisica, 41, 61 85

Dent W. R. F., Greaves J. S., Coulson I. M., 2005, Monthly Notices of the Royal Astronomical Society, 359, 663 85

Dominik C., Dullemond C. P., 2008, Astronomy and Astrophysics, 491, 663 107

Draine B. T., 1988, The Astrophysical Journal, 333, 848 109

Draine B. T., 2000, The Discrete Dipole Approximation for Light Scattering by Irregular Targets, Mishchenko M. I., Hovenier J. W., Travis L. D., eds., p. 131 110, 136, 142, 146

Draine B. T., 2003a, The Astrophysical Journal, 598, 1017 87

Draine B. T., 2003b, The Astrophysical Journal, 598, 1026 15

Draine B. T., Flatau P. J., 1994, Journal of the Optical Society of America A, 11, 1491 109, 110

Draine B. T., Flatau P. J., 2012, ArXiv e-prints 110, 114

Draine B. T., Flatau P. J., 2013, ArXiv e-prints xix, 109, 119

Draine B. T., Goodman J., 1993, The Astrophysical Journal, 405, 685 110, 136

Draine B. T., Lee H. M., 1984, The Astrophysical Journal, 285, 89 67, 136

Dullemond C. P., Dominik C., 2004, Astronomy and Astrophysics, 417, 159 64, 66, 107

Dullemond C. P., Dominik C., 2005, Astronomy and Astrophysics, 434, 971 xiii, 10

Dullemond C. P., Hollenbach D., Kamp I., D'Alessio P., 2007, Protostars and Planets V, 555 65

Dunkin S. K., Barlow M. J., Ryan S. G., 1997a, Monthly Notices of the Royal Astronomical Society, 286, 604 30, 49

Dunkin S. K., Barlow M. J., Ryan S. G., 1997b, Monthly Notices of the Royal Astronomical Society, 286, 604 80, 86

Durisen R. H., Boss A. P., Mayer L., Nelson A. F., Quinn T., Rice W. K. M., 2007, Protostars and Planets V, 607 3

Elias J. H., Frogel J. A., Matthews K., Neugebauer G., 1982, The Astronomical Journal, 87, 1029 42

Espaillat C., Calvet N., D'Alessio P., Hernández J., Qi C., Hartmann L., Furlan E., Watson D. M., 2007, The Astrophysical Journal, Letters, 670, L135 9

Esplin T. L., Luhman K. L., Mamajek E. E., 2014, The Astrophysical Journal, 784, 126 15

Farihi J., 2011, ArXiv e-prints 1

Fitzgerald M. P., Kalas P. G., Duchêne G., Pinte C., Graham J. R., 2007, The Astrophysical Journal, 670, 536 xxi, xxii, xxiv, 53, 132, 134, 143, 144, 146, 152, 153, 160, 161, 163, 164, 170

Fukagawa M. et al., 2010, Publications of the Astronomical Society of Japan, 62, 347 54, 96, 106, 169, 170

Furlan E. et al., 2006, The Astrophysical Journals, 165, 568 xiii, 10

Golimowski D. A. et al., 2006, The Astronomical Journal, 131, 3109 13, 128

Goodman A. A., Benson P. J., Fuller G. A., Myers P. C., 1993, The Astrophysical Journal, 406, 528 4

Gorti U., Dullemond C. P., Hollenbach D., 2009, The Astrophysical Journal, 705, 1237 5

Grady C. A. et al., 2007, The Astrophysical Journal, 665, 1391 xvii, 31, 53, 54, 82, 85, 96, 104, 106, 168, 169, 170

Graham J. R., Kalas P. G., Matthews B. C., 2007, The Astrophysical Journal, 654, 595 xx, xxi, xxii, 3, 11, 24, 27, 111, 130, 131, 152, 153, 154, 162, 163, 170

Greene T. P., Wilking B. A., Andre P., Young E. T., Lada C. J., 1994, The Astrophysical Journal, 434, 614 5

Guimarães M. M., Alencar S. H. P., Corradi W. J. B., Vieira S. L. A., 2006, Astronomy and Astrophysics, 457, 581 80

Habart E., Natta A., Testi L., Carbillet M., 2006, Astronomy and Astrophysics, 449, 1067 31, 82

Haisch, Jr. K. E., Lada E. A., Lada C. J., 2001, The Astrophysical Journal, Letters, 553, L153 7, 11

Hales A. S., Gledhill T. M., Barlow M. J., Lowe K. T. E., 2006, Monthly Notices of the Royal Astronomical Society, 365, 1348 xv, 31, 33, 48, 51, 168

Hanner M. S., Lynch D. K., Russell R. W., 1994, The Astrophysical Journal, 425, 274 86

Harper D. A., Loewenstein R. F., Davidson J. A., 1984, The Astrophysical Journal, 285, 808 11

Hartmann L., Megeath S. T., Allen L., Luhman K., Calvet N., D'Alessio P., Franco-Hernandez R., Fazio G., 2005, The Astrophysical Journal, 629, 881 xiii, 10

Harvey P. M., Wilking B. A., Joy M., 1984, Nature, 307, 441 2

Hauschildt P. H., Allard F., Baron E., 1999, The Astrophysical Journal, 512, 377 xxiv, 134

Helou G., Khan I. R., Malek L., Boehmer L., 1988, The Astrophysical Journals, 68, 151 135

Hillenbrand L. A. et al., 2008, The Astrophysical Journal, 677, 630 1

Holland W. S. et al., 1998, Nature, 392, 788 xiii, 2

Hollenbach D., Johnstone D., Lizano S., Shu F., 1994, The Astrophysical Journal, 428, 654 8

Honda M. et al., 2012, The Astrophysical Journal, 752, 143 31, 82, 85, 87, 91, 104, 123, 168, 170

Houk N., Fuentes-Williams T. H., 1982, in Bulletin of the American Astronomical Society, Vol. 14, Bulletin of the American Astronomical Society, p. 615 80

Hughes A. M. et al., 2009, The Astrophysical Journal, 698, 131 9

Janson M., Carson J. C., Lafrenière D., Spiegel D. S., Bent J. R., Wong P., 2012, The Astrophysical Journal, 747, 116 14

Johnstone D., Hollenbach D., Bally J., 1998, The Astrophysical Journal, 499, 758 8

Kalas P. et al., 2008, Science, 322, 1345 xiv, 14, 15

Kalas P., Graham J. R., Clampin M., 2005, Nature, 435, 1067 13

Kalas P., Graham J. R., Fitzgerald M. P., Clampin M., 2014, in IAU Symposium, Vol. 299, IAU Symposium, Booth M., Matthews B. C., Graham J. R., eds., pp. 204–207 14

Kalas P., Liu M. C., Matthews B. C., 2004, Science, 303, 1990 xx, 12, 13, 127, 128, 132, 136, 137, 142

Kama M., Min M., Dominik C., 2009, Astronomy and Astrophysics, 506, 1199 64

Kemp J. C., Wolstencroft R. D., 1972, The Astrophysical Journal, Letters, 176, L115 23

Kenyon S. J., Hartmann L., 1987, The Astrophysical Journal, 323, 714 64, 65, 66

Kenyon S. J., Hartmann L., 1995, The Astrophysical Journals, 101, 117 xiii, 10

Kimura H., Kolokolova L., Mann I., 2006, Astronomy and Astrophysics, 449, 1243 24, 26, 155

Kiraga M., 2012, Acta Astronomica, 62, 67 149

Krist J. E. et al., 2005, The Astronomical Journal, 129, 1008 xiv, xx, xxiv, 13, 14, 130, 131, 132, 137, 138, 139, 142, 145

Krivov A. V., Mann I., Krivova N. A., 2000, Astronomy and Astrophysics, 362, 1127 166

Krivova N. A., Krivov A. V., Mann I., 2000, The Astrophysical Journal, 539, 424 53

Kruegel E., 2003, The physics of interstellar dust 25, 155

Kuhn J. R., Potter D., Parise B., 2001, The Astrophysical Journal, Letters, 553, L189 xv, 31, 33, 49, 79, 82

Kuiper G. P., 1951, Proceedings of the National Academy of Science, 37, 383 3

Kundu M. R., Jackson P. D., White S. M., Melozzi M., 1987, The Astrophysical Journal, 312, 822 133

Kwon W., Looney L. W., Mundy L. G., 2011, The Astrophysical Journal, 741, 3 xiii, 8

Lada C. J., 1987, in IAU Symposium, Vol. 115, Star Forming Regions, Peimbert M., Jugaku J., eds., pp. 1–17 5

Laughlin G., Bodenheimer P., 1994, Instabilities in protostellar disks., Franco J., Lizano S., Aguilar L., Daltabuit E., eds., p. 313 3

Liou J.-C., Zook H. A., 1999, The Astronomical Journal, 118, 580 128

Liseau R., Brandeker A., Fridlund M., Olofsson G., Takeuchi T., Artymowicz P., 2003, Astronomy and Astrophysics, 402, 183 xiii, 2

Liu M. C., 2004, Science, 305, 1442 xx, 53, 128, 129, 130, 132, 139, 149

Liu M. C., Matthews B. C., Williams J. P., Kalas P. G., 2004, The Astrophysical Journal, 608, 526 xx, 127, 135, 136, 137, 143, 145, 160

Lucas P. W., Roche P. F., 1998, Monthly Notices of the Royal Astronomical Society, 299, 699 23

Lucy L. B., 1974, The Astronomical Journal, 79, 745 57, 169

Lucy L. B., 1999, Astronomy and Astrophysics, 344, 282 73

MacGregor M. A. et al., 2013, The Astrophysical Journal, Letters, 762, L21 xx, 133, 134, 145, 159, 160, 166

Mackowski D. W., Mishchenko M. I., 1996, J. Opt. Soc. Am. A, 13, 2266 155

Makidon R. B., Sivaramakrishnan A., Perrin M. D., Roberts, Jr. L. C., Oppenheimer B. R., Soummer R., Graham J. R., 2005, Publications of the Astronomical Society of the Pacific, 117, 831 48

Manoj P., Bhatt H. C., Maheswar G., Muneer S., 2006, The Astrophysical Journal, 653, 657 30, 80, 81

Mariñas N., Telesco C. M., Fisher R. S., Packham C., 2011, The Astrophysical Journal, 737, 57 80, 81

Martin P., 1989, in IAU Symposium, Vol. 135, Interstellar Dust, Allamandola L. J., Tielens A. G. G. M., eds., p. 55 23

Mathioudakis M., Doyle J. G., 1991, Astronomy and Astrophysics, 244, 433 134, 135, 149

Mathis J. S., 1990, Annual Review of Astronomy and Astrophysics, 28, 37 15

Mathis J. S., Rumpl W., Nordsieck K. H., 1977, The Astrophysical Journal, 217, 425 141

Mathis J. S., Whiffen G., 1989, The Astrophysical Journal, 341, 808 143, 146

Matsuo T., Shibai H., Ootsubo T., Tamura M., 2007, The Astrophysical Journal, 662, 1282 3

Mattila K., 1970, Astronomy and Astrophysics, 9, 53 69

McKee C. F., Ostriker E. C., 2007, Annual Review of Astronomy and Astrophysics, 45, 565 4

Meeus G. et al., 2010, Astronomy and Astrophysics, 518, L124 xxiii, 80, 81, 82, 83, 85, 87, 89, 92, 103, 123, 170, 175

Meeus G., Waters L. B. F. M., Bouwman J., van den Ancker M. E., Waelkens C., Malfait K., 2001, Astronomy and Astrophysics, 365, 476 xiv, 29, 30, 31, 32, 85, 86

Merín B. et al., 2010, The Astrophysical Journal, 718, 1200 9

Merkle F. et al., 1989, The Messenger, 58, 1 35

Messenger S., Keller L. P., Stadermann F. J., Walker R. M., Zinner E., 2003, Science, 300, 105 24

Metchev S. A., Eisner J. A., Hillenbrand L. A., Wolf S., 2005, The Astrophysical Journal, 622, 451 xx, xxiv, 13, 128, 129, 130, 132, 134, 136, 137, 138, 139, 141, 143, 145, 147, 150, 170

Millar-Blanchaer M. A. et al., 2015, The Astrophysical Journal, 811, 18 13

Min M., Dullemond C. P., Dominik C., de Koter A., Hovenier J. W., 2009, Astronomy and Astrophysics, 497, 155 71

Min M., Jeffers S. V., 2010, in Electromagnetic and Light Scattering XII, K. Muinonen, A. Penttilä, H. Lindqvist, T. Nousiainen, & G. Videen, ed., p. 166 25

Mishchenko M. I., Travis L. D., Mackowski D. W., 1996, Journal of Quantitiative Spectroscopy and Radiative Transfer, 55, 535 26

Mizuno H., 1980, Progress of Theoretical Physics, 64, 544 3

Mundy L. G. et al., 1996, The Astrophysical Journal, Letters, 464, L169 xiii, 8

Muzerolle J., Allen L. E., Megeath S. T., Hernández J., Gutermuth R. A., 2010, The Astrophysical Journal, 708, 1107 9

Najita J. R., Carr J. S., Glassgold A. E., Valenti J. A., 2007, Protostars and Planets V, 507 xiii, 9, 10

Osorio M. et al., 2014, The Astrophysical Journal, Letters, 791, L36 xv, xvii, 32, 33, 34, 43, 55, 57, 79, 82, 91, 92, 100, 104

Owen J. E., Ercolano B., Clarke C. J., Alexander R. D., 2010, Monthly Notices of the Royal Astronomical Society, 401, 1415 5

Ozernoy L. M., Gorkavyi N. N., Mather J. C., Taidakova T. A., 2000, The Astrophysical Journal, Letters, 537, L147 129

Papaloizou J. C. B., Nelson R. P., Kley W., Masset F. S., Artymowicz P., 2007, Protostars and Planets V, 655 29

Pascucci I., Wolf S., Steinacker J., Dullemond C. P., Henning T., Niccolini G., Woitke P., Lopez B., 2004, Astronomy and Astrophysics, 417, 793 xvi, xxiii, 66, 67, 68

Perri F., Cameron A. G. W., 1974, Icarus, 22, 416 3

Perryman M. A. C. et al., 1997, Astronomy and Astrophysics, 323, L49 128

Pinte C., Harries T. J., Min M., Watson A. M., Dullemond C. P., Woitke P., Ménard F., Durán-Rojas M. C., 2009, Astronomy and Astrophysics, 498, 967 74

Pollack J. B., Hubickyj O., Bodenheimer P., Lissauer J. J., Podolak M., Greenzweig Y., 1996, Icarus, 124, 62 3

Purcell E. M., Pennypacker C. R., 1973, The Astrophysical Journal, 186, 705 27

Quanz S. P., Avenhaus H., Buenzli E., Garufi A., Schmid H. M., Wolf S., 2013, The Astrophysical Journal, Letters, 766, L2 xv, xvii, 9, 31, 33, 34, 41, 43, 53, 54, 55, 56, 57, 79, 91, 92, 98, 100, 101, 102, 106, 107, 168, 169, 170

Quanz S. P., Schmid H. M., Geissler K., Meyer M. R., Henning T., Brandner W., Wolf S., 2011, The Astrophysical Journal, 738, 23 40, 49

Raman A., Lisanti M., Wilner D. J., Qi C., Hogerheijde M., 2006, The Astronomical Journal, 131, 2290 49, 85

Reggiani M. et al., 2014, The Astrophysical Journal, Letters, 792, L23 57, 100, 102, 103, 108, 170

Richardson W. H., 1972, Journal of the Optical Society of America (1917-1983), 62, 55 57, 169

Robitaille T. P., 2010, Astronomy and Astrophysics, 520, A70 72

Robitaille T. P., 2011, Astronomy and Astrophysics, 536, A79 62, 68, 71, 75, 76, 147

Rosseland S., 1924, Monthly Notices of the Royal Astronomical Society, 84, 525 71

Saija R., Iatì M. A., Giusto A., Borghese F., Denti P., Aiello S., Cecchi-Pestellini C., 2003, Monthly Notices of the Royal Astronomical Society, 341, 1239 142

Sauter J. et al., 2009, Astronomy and Astrophysics, 505, 1167 23, 170

Schmid H. M., Joos F., Tschan D., 2006, Astronomy and Astrophysics, 452, 657 54

Schneider G. et al., 2014, The Astronomical Journal, 148, 59 133

Shen Y., Draine B. T., Johnson E. T., 2008, The Astrophysical Journal, 689, 260 xix, 15, 25, 115, 116, 117, 156, 165

Shen Y., Draine B. T., Johnson E. T., 2009, The Astrophysical Journal, 696, 2126 156, 157, 171

Shu F. H., Adams F. C., Lizano S., 1987, Annual Review of Astronomy and Astrophysics, 25, 23 4

Smith B. A., Terrile R. J., 1984, Science, 226, 1421 3, 13, 127

Smith T. L., Clayton G. C., Valencic L., 2004, The Astronomical Journal, 128, 357 16

Song I., Weinberger A. J., Becklin E. E., Zuckerman B., Chen C., 2002, The Astronomical Journal, 124, 514 127

Strom K. M., Strom S. E., Edwards S., Cabrit S., Skrutskie M. F., 1989, The Astronomical Journal, 97, 1451 7, 9

Strubbe L. E., Chiang E. I., 2006, The Astrophysical Journal, 648, 652 11, 171

Su K., 2005, in Nearby Resolved Debris Disks, Kamp I., Meixner M., eds., p. 36 12

Sylvester R. J., Skinner C. J., Barlow M. J., Mannings V., 1996, Monthly Notices of the Royal Astronomical Society, 279, 915 30, 80, 86

Takeuchi T., Artymowicz P., 2001, The Astrophysical Journal, 557, 990 11

Telesco C. M. et al., 2000, The Astrophysical Journal, 530, 329 xiv, 12

Temperton C., 1992, SIAM Journal of Scientific and Statistical Computing, 676 114

Terebey S., Shu F. H., Cassen P., 1984, The Astrophysical Journal, 286, 529 4

Tielens A. G. G. M., 2008, Annual Review of Astronomy and Astrophysics, 46, 289 16

Tinbergen J., 1996, Astronomical Polarimetry 40

Torres C. A. O., Quast G. R., da Silva L., de La Reza R., Melo C. H. F., Sterzik M., 2006, Astronomy and Astrophysics, 460, 695 134

Tsikoudi V., 1988, The Astronomical Journal, 95, 1797 127

van Boekel R., Min M., Waters L. B. F. M., de Koter A., Dominik C., van den Ancker M. E., Bouwman J., 2005, Astronomy and Astrophysics, 437, 189 xiv, 31, 32, 80, 81

van de Hulst H. C., 1957, Light Scattering by Small Particles 19, 63

van den Ancker M. E., 1999, PhD thesis, University of Amsterdam 80, 81

van der Veen W. E. C. J., Habing H. J., Geballe T. R., 1989, Astronomy and Astrophysics, 226, 108 xvii, 81

Vandenbussche B. et al., 2010, Astronomy and Astrophysics, 518, L133 xiii, 2

Voshchinnikov N. V., Krügel E., 1999, Astronomy and Astrophysics, 352, 508 24, 25, 170

Wagner K. R. et al., 2015, The Astrophysical Journal, 798, 94 101, 107

Waterman P. C., 1965, IEEE, 53, 805 25

Wehrse R., Baschek B., von Waldenfels W., 2000, Astronomy and Astrophysics, 359, 780 71

Whitney B. A., 2011, Monte Carlo radiative transfer, Saikia D. J., Trimble V., eds., World Scientific Publishing Co, pp. 151–176 61

Williams J. P., Cieza L. A., 2011, Annual Review of Astronomy and Astrophysics, 49, 67 5

Wilner D. J., Andrews S. M., MacGregor M. A., Hughes A. M., 2012, The Astrophysical Journal, Letters, 749, L27 149

Witzel G. et al., 2011, Astronomy and Astrophysics, 525, A130 xv, 35, 36, 45

Wolf S., 2003, Computer Physics Communications, 150, 99 136

Wolf S., Henning T., 2000, Computer Physics Communications, 132, 166 136

Wood K., Reynolds R. J., 1999, The Astrophysical Journal, 525, 799 69

Wurm G., Blum J., 1998, Icarus, 132, 125 24

Yusef-Zadeh F., Morris M., White R. L., 1984, The Astrophysical Journal, 278, 186 73

Zacharias N., Monet D. G., Levine S. E., Urban S. E., Gaume R., Wycoff G. L., 2004, in Bulletin of the American Astronomical Society, Vol. 36, American Astronomical Society Meeting Abstracts, p. 1418 80

Zubko V. G., Mennella V., Colangeli L., Bussoletti E., 1996, Monthly Notices of the Royal Astronomical Society, 282, 1321 87

Zuckerman B., Forveille T., Kastner J. H., 1995, Nature, 373, 494 11

Zuckerman B., Song I., Bessell M. S., Webb R. A., 2001, The Astrophysical Journal, Letters, 562, L87 10, 13, 128